Spin Transport in Insulating Altermagnets: From Hopping Conduction to Altermagnons

Edgar Felipe Galíndez Ruales

Spin Transport in Insulating Altermagnets: From Hopping Conduction to Altermagnons

Edgar Felipe Galíndez Ruales
geb. in Bogotá D.C. (Colombia)
Mainz, den Februar 03, 2026

Dissertation zur Erlangung des Grades
"Doktor der Naturwissenschaften"
am Fachbereich Physik, Mathematik und Informatik der
Johannes Gutenberg-Universität Mainz

Rigorosum: 27 of May 2026

Reviewer:	Prof. Dr.	Mathias Kläui
	Prof. Dr.	Gerhard Jakob
	Prof. Dr.	Alexander Mook
	Prof. Dr.	Randolf Pohl
Supervisor:	Prof. Dr.	Mathias Kläui

Edgar Felipe Galindez Ruales
Kläui lab
Johannes Gutenberg-Universität Mainz
Institut für Physik
Staudingerweg 7
D-55099 Mainz
galindez@uni-mainz.de

Abstract

Altermagnetism has recently emerged as a particular symmetry-defined magnetic phase that combines compensated magnetic order in real space with large spin polarization in reciprocal space. This thesis establishes consequences of the altermagnetic symmetry that are experimentally testable and have technologically potentially relevant transport functionalities, with an emphasis on insulating systems where magnons carry spin. A unified theoretical background is explored for spin injection, propagation, and detection in compensated magnets, combined with the symmetry constraints that govern altermagnetic spin splitting and altermagnon polarization.

Experimentally, the thesis implements from device fabrication to harmonic transport protocols, synchrotron photoemission electron microscopy, and magnon spin transport. In Ti-doped hematite, angle-dependent Hall measurements reveal a symmetry-controlled odd transverse response that emerges only in the spin flop phase, accompanied by crystal orientation-dependent sign inversions. XMLD and XMCD-based PEEM reconstruct the absolute Néel vector orientation and correlate real-space domain changes with changes of the transport pseudovector. In insulating orthoferrites, spin Hall magnetoresistance is established as a local electrical probe of the interfacial magnetic configuration. Non-local measurements then demonstrate altermagnetic magnon transport in d wave orthoferrites, including direction-dependent sign inversions between the Γ–U and Γ–U' directions, finite responses at zero magnetic field, and a non-monotonic distance dependence with sign reversal results from the competition between different exchange split magnon modes. Simulations reproduce these features and show that they vanish when the altermagnetic exchange splitting is removed, establishing a direct link between the observed transport signatures and altermagnetism.

These results identify insulating orthoferrites and hematite as concrete platforms for field-free, symmetry-defined, low-power magnon spin transport and for combined transport and microscopy diagnostics of altermagnetic order.

Keywords: altermagnetism, magnons, non-local spin transport, spin Seebeck effect, spin Hall magnetoresistance, orthoferrites, hematite, PEEM.

Zusammenfassung

Der Altermagnetismus hat sich in jüngster Zeit als eine symmetrie-definierte magnetische Phase herauskristallisiert, die eine kompensierte magnetische Ordnung im Realraum mit einer starken Spinpolarisation im reziproken Raum vereint. Diese Dissertation leitet Konsequenzen der altermagnetischen Symmetrie her, die experimentell überprüfbar sind und potenziell technologisch relevante Transporteigenschaften bieten, mit einem Schwerpunkt auf isolierenden Systemen, in denen Magnonen den Spin tragen. Es wird ein einheitlicher theoretischer Rahmen für Spin-Injektion, -Ausbreitung und -Detektion in kompensierten Magneten entwickelt, der mit den Symmetriebedingungen verknüpft ist, welche die altermagnetische Spinaufspaltung und die Polarisation von Altermagnonen bestimmen.

Experimentell umfasst die Arbeit den gesamten Ablauf von der Bauelementfertigung über harmonische Transportmessungen und synchrotronbasierte Photoemissions-Elektronenmikroskopie bis hin zu Untersuchungen des magnonischen Spintransports. In Ti-dotiertem Hämatit zeigen winkelabhängige Hallmessungen eine symmetriebestimmte ungerade transversale Antwort, die ausschließlich in der Spin-Flop-Phase auftritt und kristallorientierungsabhängige Vorzeichenwechsel zeigt. XMLD- und XMCD-basierte PEEM rekonstruiert die absolute Orientierung des Néel-Vektors und korreliert Änderungen der realräumlichen Domänenstruktur mit Variationen des Transport-Pseudovektors. In isolierenden Orthoferriten wird die Spin-Hall-Magnetowiderstandsmessung als lokale elektrische Sonde der interfacialen magnetischen Konfiguration eingeführt. Nichtlokale Messungen zeigen anschließend altermagnetischen Magnonentransport in d-Wellen-Orthoferriten, einschließlich richtungsabhängiger Vorzeichenwechsel zwischen den Richtungen Γ–U und Γ–U', endlicher Signale bei Nullfeld sowie einer nichtmonotonen Distanzabhängigkeit, deren Vorzeichenumkehr aus der Konkurrenz verschiedener austauschgespaltener Magnonenzweige resultiert. Simulationen reproduzieren diese Erscheinungen und zeigen, dass sie verschwinden, wenn die altermagnetische Austauschaufspaltung entfernt wird, wodurch eine direkte Verbindung zwischen den beobachteten Transportsignaturen und dem Altermagnetismus hergestellt wird.

Diese Ergebnisse identifizieren isolierende Orthoferrite und Hämatit als konkrete Plattformen für feldfreien, symmetrie-definierten, energieeffizienten magnonischen Spintransport sowie für eine kombinierte Diagnostik der altermagnetischen Ordnung mittels Transportmessungen und Mikroskopie.

Schlagwörter: Altermagnetismus, Magnonen, nichtlokaler Spintransport, Spin-Seebeck-Effekt, Spin-Hall-Magnetowiderstand, Orthoferrit, Hämatit, PEEM.

Resumen

El altermagnetismo ha surgido recientemente como una fase magnética definida por simetría que combina un orden magnético compensado en el espacio real con una gran polarización de espín en el espacio recíproco. Esta tesis establece consecuencias de la simetría altermagnética que son comprobables experimentalmente y que poseen funcionalidades de transporte potencialmente relevantes para la tecnología, con énfasis en sistemas aislantes donde los magnones transportan el espín. Se desarrolla un marco teórico unificado para la inyección, propagación y detección de espín en imanes compensados, integrado con las restricciones de simetría que gobiernan la separación de espín altermagnética y la polarización de los altermagnones.

En el plano experimental, la tesis abarca desde la fabricación de dispositivos hasta protocolos de transporte armónico, microscopía de fotoemisión de electrones con radiación de sincrotrón y mediciones de transporte de espín por magnones. En hematita dopada con Ti, las mediciones de Hall angulodependientes revelan una respuesta transversal asimétrica controlada por simetría que aparece únicamente desde la fase de spin flop, acompañada de inversiones de signo dependientes de la orientación cristalográfica. La PEEM basada en XMLD y XMCD reconstruye la orientación absoluta del vector de Néel y correlaciona cambios de dominio en el espacio real con cambios del pseudovector de transporte. En ortoferritas aislantes, la magnetorresistencia Hall de espín se establece como una sonda eléctrica local de la configuración magnética interfacial. Posteriormente, las mediciones no locales demuestran transporte magnonico altermagnético en ortoferritas de tipo onda d, incluyendo inversiones de signo dependientes de la dirección entre las direcciones Γ–U y Γ–U', respuestas finitas a campo magnético cero y una dependencia no monótona con la distancia cuyo cambio de signo resulta de la competencia entre diferentes ramas de magnones nodegenerados. Las simulaciones reproducen estas características y muestran que desaparecen cuando se elimina la separación de intercambio altermagnética, estableciendo un vínculo directo entre las firmas de transporte observadas y el altermagnetismo.

Estos resultados identifican a las ortoferritas aislantes y a la hematita como plataformas concretas para transporte de espín por magnones de bajo consumo, definido por simetría y operable sin campo externo, así como para una diagnóstica combinada de orden altermagnético mediante transporte y microscopía.

Palabras clave: altermagnetismo, magnones, transporte de espín no local, efecto Seebeck de espín, magnetorresistencia Hall de espín, ortoferritas, hematita, PEEM.

Declaration of Authorship

I hereby declare that the thesis submitted is my own unaided work. All direct or indirect sources used are acknowledged as references. The thesis, in whole or in part, has never been submitted to any other examination committee that is able to admit a doctoral degree.

Ich versichere, dass ich meine Dissertation selbstständig verfasst und keine anderen als die angegebenen Quellen und Hilfsmittel benutzt sowie Zitate kenntlich gemacht habe. Die Doktorarbeit ist weder abschnittsweise, noch in der vorliegender Form bei einer anderen Prüfungsbehörde zur Erlangung eines Doktorgrades eingereicht worden.

Mainz, June 3, 2026

Original signed

Edgar F. Galindez Ruales

"Au milieu de l'hiver, j'apprenais enfin qu'il y avait en moi un été invincible."
"In the midst of winter, I found there was within me an invincible summer."
— "Retour à Tipasa," in L'Été (Camus, 1952/1953).

To my *Schatzcito*, who has sacrificed the most in this project.

Contents

List of Figures

List of Tables

1. Introduction

In the modern era, electronics have become the backbone of human progress, driving everything from communication and healthcare to financial systems and artificial intelligence. However, traditional semiconductor-based electronics face critical limitations, particularly in energy consumption, scalability, and processing speed. The continued reliance on charge-based circuits leads to excessive power dissipation, reducing efficiency and increasing environmental impact. According to Puebla et al. (2020), data centers alone account for nearly 1% of global electricity consumption, a number expected to rise exponentially with the growing digital economy [1]. This energy demand has far-reaching consequences, including carbon emissions, resource depletion, and economic inefficiencies, making it clear that new energy-efficient computational paradigms are needed [2].

The world's data storage and computational needs are expanding at an unprecedented rate. With the exponential rise of artificial intelligence, cloud computing, and high-performance data centers, global computation is consuming more energy than entire nations. Studies estimate that global power demand from data centers will increase by 50 % by 2027 and by as much as 165 % by the end of the decade (compared with 2023) unless more energy-efficient alternatives are developed [3]. In response, spin-based electronics (spintronics) offer a potentially revolutionary alternative, leveraging electron spin rather than charge to process and store information. Unlike conventional semiconductor devices, spintronic components retain information without power, significantly reducing standby energy losses [1, 4–13]. This paradigm shift could reduce global computational energy consumption by orders of magnitude, making the transition to spin-based memory and logic a critical step toward sustainability.

The rate at which data is being created today surpasses the storage and processing capabilities of modern hardware. In 2024 alone, the world produced an estimated 330 exabytes of data per day, a trend that has grown exponentially since the Internet's inception [14]. Conventional storage technologies cannot keep pace with this data deluge, resulting in bottlenecks in cloud computing and high-performance computing environments. Moreover, the movement of such vast amounts of data requires ultrafast and highly robust processing architectures that traditional silicon-based circuits cannot provide. Antiferromagnetic spintronics emerges as a promising solution, offering terahertz-range processing speeds, non-volatility, and robustness against external perturbations [15]. By leveraging the unique properties of antiferromagnet (AFMs), researchers are exploring next-generation computing architectures that surpass conventional silicon-based logic in both speed and energy efficiency.

Beyond the technological imperative, the exploration of altermagnetism represents a fundamental leap in condensed matter physics. Until recently, altermagnetism remained unnoticed due to the historical binary classification of magnetic materials into ferromagnets (FMs) and AFMs This new class of materials exhibits zero net magnetization while simultaneously possessing strong spin-polarized band structures, enabling

exotic quantum transport properties [16]. Much like the discovery of superconductivity redefined our understanding of electron pairing and quantum coherence, altermagnetism challenges conventional paradigms by revealing the importance of symmetry-breaking [17–27]. This realization opens entirely new research directions, particularly in materials where real-space and reciprocal-space symmetry considerations are equally crucial for unveiling novel electronic and spintronic effects.

The classification of magnetic materials is being rewritten, and with it, the foundations of spintronics. Group theory and reciprocal space topology, central to the physics of superconductors, now play a defining role in understanding altermagnetic band structures and transport phenomena. The simultaneous investigation of real-space magnetic order and reciprocal-space band topology is essential in uncovering these materials' unique properties. Altermagnetism stands at the forefront of a new wave of magnetic research, bridging fundamental physics with practical applications in ultrafast, energy-efficient spintronics.

This convergence of societal needs, energy efficiency demands, high-speed computing, and fundamental physics breakthroughs defines the scientific motivation behind studying altermagnetic materials. In the next section, we will quantitatively explore the advancements, research trends, and key motivations driving the rapid rise of altermagnetic spintronics.

1.1. Scientific Motivation

Altermagnetic materials represent a potentially transformative advancement in spintronics, offering a unique combination of properties that address the limitations of traditional ferromagnetic and antiferromagnetic materials. Unlike FMs, which exhibit net magnetization and are susceptible to external magnetic fields, altermagnets (AMs) possess zero net magnetization, similar to AFMs, providing robustness against magnetic perturbations. However, AMs also exhibit strong spin polarization, a characteristic typically associated with FMs, enabling efficient spin current generation without the drawbacks of stray magnetic fields. This distinctive blend of attributes positions AMs as promising candidates for developing high-speed, energy-efficient spintronic devices [18, 21, 28].

The concept of altermagnetism has evolved significantly over the past few years. Initially, certain collinear antiferromagnetic materials exhibiting anomalous Hall effect (AHE) due to specific crystal symmetries were identified, suggesting unconventional magnetic behaviors [21]. A pivotal experimental breakthrough occurred with the observation of altermagnetic properties in ruthenium dioxide (RuO_2), providing concrete evidence of this new magnetic phase [22]. Subsequent research has expanded the list of known altermagnetic materials to include Mn_5Si_3 [29], MnTe [30–36], CrSb [37–40], hematite [41], among others, each demonstrating unique electronic and magnetic properties that align with theoretical predictions. Despite these advancements, several predicted altermagnetic materials have yet to be experimentally confirmed, highlighting the ongoing exploration in this field [13, 18, 27, 36, 37, 42–46].

Detecting and manipulating spin transport in AMs present notable challenges, particularly due to their compensated magnetic structures and the prevalence of insulating behavior. One promising approach involves utilizing magnons—quanta of spin waves—as carriers of spin information. In antiferromagnetic insulators, magnon-based

spin transport has been demonstrated, offering insights into potential mechanisms applicable to AMs [47–54]. However, efficiently generating, controlling, and detecting magnon currents in altermagnetic materials remains challenging, necessitating further research to harness their full potential in spintronic applications.
In this thesis, fundamental questions are addressed on how altermagnetic symmetry in compensated magnets translates into experimentally accessible transport functionalities, and how such symmetry-derived effects can be validated by complementary electrical, microscopic, and computational probes. The overarching goal is to establish a symmetry-based and reproducible methodology that connects symmetry constraints to measurable signatures in both transverse hopping-based transport and non-local magnon-mediated spin transport.

A first question concerns the direct experimental consequences of altermagnetic symmetry: which transport observables are uniquely enabled by momentum-dependent spin splitting in a compensated magnet, and how do these observables differ from responses driven by net magnetization or conventional spin–orbit mechanisms, particularly in insulating materials where spin information is transported by magnons rather than electrons?

A second set of questions focuses on hematite (α-Fe_2O_3) as an experimentally accessible model system for symmetry-controlled transverse transport. Under which symmetry conditions does hematite exhibit an odd transverse (Hall) response despite vanishing net magnetization, and how do crystallographic orientation and the spin-flop transition determine the sign and angular dependence of this response? Closely related is the question of whether the altermagnetic order parameter can be reconstructed unambiguously in real space using combining dichroism techniques, and whether changes in domain state can be correlated quantitatively with changes of the transport pseudovector.

A third topic addresses how to establish reliable baselines for interpreting non-local transport in insulating orthoferrites. Can magnetoresistances in Pt|$LuFeO_3$ and Pt|$YFeO_3$ provide a robust *local* electrical probe of the interfacial magnetic configuration, thereby fixing the symmetry-defined projection factors that control injection and detection efficiency? In parallel, what are the characteristic of diffusive non-local magnon spin transport in a canted orthoferrite ($YFeO_3$) along high-symmetry axes, including the decay length, magnetic-field dependence, and crystallographic anisotropy that serve as reference observables?

Building on the answers from this question, the central question is whether insulating *d*-wave orthoferrites support *field-free* non-local magnon transport that is selected by crystallographic direction, including sign inversion between different altermagnetic directions and suppression along high-symmetry control axes. A key mechanistic question follows: are the observed direction-dependent and distance-dependent sign changes explained by competition between *exchange-split altermagnon branches*, with distinct lifetimes, velocities, and polarizations, rather than by weak ferromagnetic canting alone?

1.2. State of the Art in Altermagnetic Spintronics

The concept of altermagnetism emerged from theoretical developments initially driven by unexpected experimental observations of AHEs (AHE) in materials traditionally considered collinear AFMs, where no net magnetization should exist [21, 55–57]. This

surprising discovery prompted a revision of established magnetic paradigms and led to the theoretical proposal of a novel magnetic phase termed "altermagnetism," characterized by compensated antiparallel magnetic order and momentum-dependent spin-splitting in the electronic band structure, despite zero net magnetization [23, 58–60]. Theoretical works such as those by Šmejkal et al. [19,20,24,61] introduced the concept of crystal symmetry-driven Anomalous Hall effect (AHE) in collinear AFMs, identifying extensive material families with altermagnetic characteristics. Subsequently, Šmejkal and colleagues proposed a unified symmetry-based framework describing nonrelativistic spin-splitting effects, elucidating their fundamental distinction from conventional spin-orbit coupling (SOC) mechanisms. Yuan et al. [62], and Hayami et al. [55,63] expanded the theoretical understanding by predicting substantial momentum-dependent spin splitting in centrosymmetric and low-atomic-number AFMs, further supported by models developed by Ahn et al. [56] and Roig et al. [64].

The first experimental validation of altermagnetism appeared with the observation of a large AHE in RuO_2 by Feng et al. [22], significantly advancing the field and inspiring further explorations in similar materials. Additional magneto-transport studies soon confirmed the AHE in MnTe [26] and Mn_5Si_3 [29], and hematite [41], verifying predictions of robust symmetries breaking without net magnetization. Angle-resolved photoemission spectroscopy experiments, notably by Fedchenko et al. [65], Lee et al. [66], and Osumi et al. [30], have directly visualized substantial spin splitting in RuO_2, MnTe, and CrSb, respectively, confirming the theoretical predictions of momentum-dependent spin textures intrinsic to AMs [40]. Additionally, direct imaging of altermagnetic domain structures using photoemission electron microscopy (PEEM) combined with x-ray magnetic circular dichroism (XMCD) techniques has been demonstrated clearly in MnTe by Amin et al. [33] and in hematite (α-Fe_2O_3) by the author [41], providing direct spatial visualization of the underlying altermagnetic order. Table **A.1** in appendix A summarizes the recent demonstration of altermagnetic properties in MnF_2 [67,68], $Rb_{1-\delta}V_2Te_2O$ [69], KV_2Se_2O [70], $CoNb_4Se_8$ [71], MnTe [25,26,30,33,36,42,66,72,73], Mn_5Si_3 [29,74,75], RuO_2 [65,76–80], CrSb [46,81–85], and hematite [41,86,87]. A more extended list of altermagnetic candidates is shown in appendix **B.1** [88,89].

Despite significant experimental progress, several key theoretical predictions remain experimentally unobserved. For instance, altermagnetic superconductivity, proposed to host unconventional pairing mechanisms and topological states [90, 91], remains unobserved. Moreover, the predicted altermagnetic-induced finite-momentum Cooper pairing [92] and Majorana enge states in heterostructures [93, 94] represent frontier opportunities that remain experimentally elusive. Additional predictions such as chiral magnons in RuO_2 [95] and MnTe [42], piezomagnetic effects [34], and topological transitions between nodal and nodeless Zeeman splitting [96] are yet to be confirmed experimentally. Exploring these phenomena will significantly advance understanding and the potential technological applications of altermagnetism.

Furthermore, the insulating nature of many altermagnetic materials presents challenges for practical spintronic device integration, necessitating efficient spin transport mechanisms beyond conventional electron conduction. Magnon transport offers a promising solution, as demonstrated in insulating AFMs like hematite [47–49] and $YFeO_3$ [97], where nonreciprocal and long-range spin-wave propagation was observed [51]. Theoretical predictions indicate significant potential for magnon-based spin transport and spin-caloritronic phenomena in AMs [98–100]. However, experimental

verification of these magnonic predictions, including giant anisotropies of magnon lifetimes and chiral altermagnonic excitations, remained a critical objective until now. Addressing these challenges and exploring these predictions will further solidify altermagnetic spintronics as a transformative field for future magnetic technologies.

2. Theoretical Background

The binary classification of *collinear* magnetic materials, between ferromagnets and antiferromagnets, is not anymore complete. A new class of magnetic materials has been discovered, the *AMs*: collinear sublattice, globally compensated orders that nevertheless host sizable spin-split electronic (and magnonic) bands due to symmetry constraints in their magnetic space groups. In contrast to both FMs and conventional Néel AFMs, AMs break $\mathcal{PT}$ symmetry while preserving sublattice compensation, yielding alternating spin splitting in **k**-space, nodal features protected by crystal symmetries, and resulting unconventional responses (Fig. **2.1**). This chapter, therefore, begins with a systematic account of altermagnetism: symmetry properties (magnetic space/group theory), reciprocal-space manifestations (alternating spin splitting, nodal lines/planes, and Weyl points), and a Landau-functional perspective that clarifies the altermagnetic order parameter and its coupling to fields, strain, and interfaces. Relevant compounds for this thesis are expanded (α-Fe_2O_3, and orthoferrites) with emphasis on their symmetry classes and predicted/observed responses [24, 88, 95].

Having established the altermagnetic foundation, the chapter turns to *spin transport in insulating compensated magnets*, which provides the tools to interpret both altermagnetic and non-altermagnetic case studies in later chapters. We begin with spin injection and detection at normal-metal/insulator interfaces, covering electrical and thermal routes: the spin Hall (SHE) and inverse spin Hall (ISHE) effects for charge–spin interconversion [101, 102] and the spin Seebeck effect (SSE) for thermally driven spin currents [103, 104]. We develop the frequency-dependent spin-mixing conductance formalism and discuss how interfacial symmetry, disorder, and the imaginary part of the spin-mixing conductance impact phase and torque transfer across the interface.

We then address *magnons as angular momentum carriers* in magnetically compensated insulators: polarization, dispersion, coherence, and their roles across the diffusive and the high-density/coherent regimes. Particular attention is given to how crystalline anisotropy, magnetic domain distribution, finite temperature, and damping control experimentally accessible observables such as non-local resistances and spin Hall magnetoresistance (SMR) [105–107]. Where relevant, we highlight how altermagnetic symmetry modifies magnon band topology (e.g., altermagnons) and anisotropies, with direct implications for directionally selective magnon transport and domain-wall dynamics [95, 108].

Together, these sections provide the theoretical foundation necessary to understand the experimental results presented in the subsequent chapters, as well as to appreciate the significance of recent advances in the field of compensated spintronics. Throughout, we connect symmetry principles to transport observables, providing the theoretical basis for later chapters on the AHE in doped hematite, local interfacial magnetoresistances in orthoferrites, and non-local magnon transport in $YFeO_3$ and $LuFeO_3$.

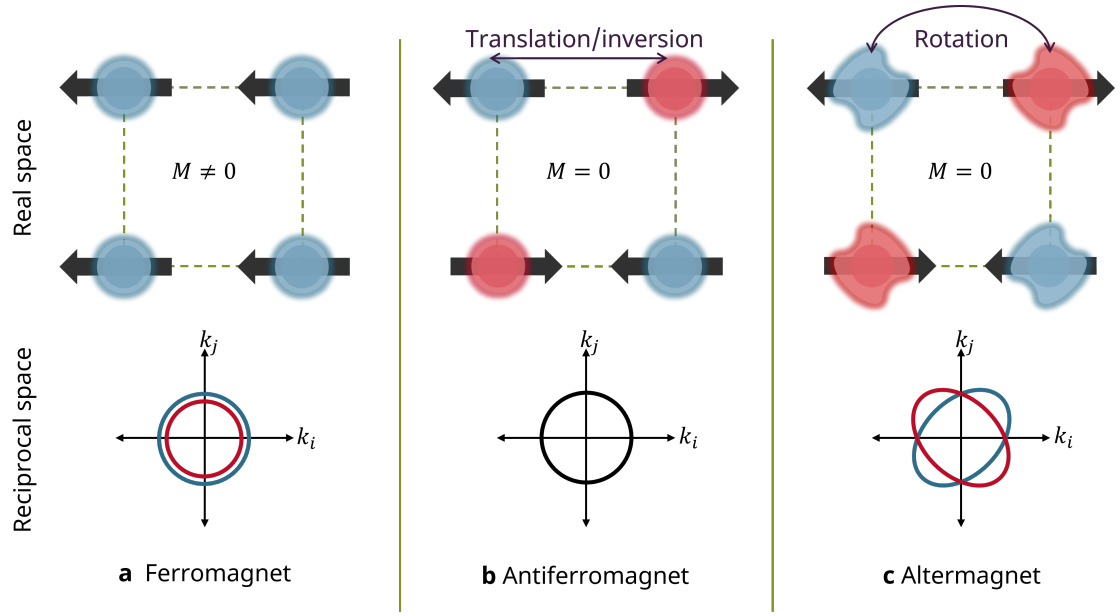

Figure 2.1.: Schematic comparison of collinear magnets clasification in real and reciprocal space. Top row: real-space spin configurations. In FMs, all spins align parallel, yielding a finite net magnetization $M \neq 0$. In AFMs, spins align antiparallel and cancel under translation or inversion, resulting in $M = 0$. In AMs, spins are also compensated ($M = 0$), but the symmetry of their arrangement (e.g., under rotations) leads to alternating spin orientations in momentum space. Bottom row: reciprocal-space (k_i vs k_j) consequences. FMs exhibit spin-split Fermi surfaces of opposite spin character. AFMs retain spin degeneracy in momentum space. AMs, in contrast, show a characteristic alternating spin splitting of the bands in **k**-space despite zero net magnetization, reflecting the unique symmetry-protected nature of altermagnetic order.

2.1. Altermagnetism: Fundamentals and Theoretical Models

Altermagnetism is a recently identified third elementary magnetic phase distinct from conventional ferromagnets (FM) and antiferromagnets (AFM) [19]. In an altermagnet (AM), spins form a collinear, compensated magnetic order (zero net magnetization like an AFM) but produce, along certain directions, a band spin-splitting in momentum space reminiscent of a FM [59] (See Fig. **2.1**). This seemingly paradoxical combination, i.e., no net moment and strong time-reversal symmetry-breaking effects, is enabled by the inequivalence of the sublattice due to special symmetry conditions of the crystal and magnetic order [59]. Below, we outline the symmetry criteria for altermagnetic ordering, how these symmetries imprint on the band structure (nodal surfaces and alternating spin splitting), the representation-theoretic description (magnetic space groups and Berry phase properties), and concrete examples like α-Fe_2O_3, and orthoferrites.

2.1.1. Symmetry-Based Identification of Altermagnetic Materials

AMs can be understood through a symmetry classification of collinear magnets (Fig. **2.1c**). In symmetry terms, they occupy a remaining class of collinear order that is distinct from ferromagnetism and conventional Néel antiferromagnetism [19, 20, 109]. In a traditional collinear AFM, there is typically a combined space-inversion ($\mathcal{P}$) and time-reversal ($\mathcal{T}$) symmetry (or an equivalent translation τ symmetry) that maps each up-spin to a down-spin site. This $\mathcal{PT}$ symmetry forces every electronic state to be Kramers spin-degenerate [25], despite the individually broken time-reversal symmetry (Fig. **2.1b**). In contrast, an altermagnetic order is forbidden from having such inversion or half-translation symmetries combined with time reversal [19, 20, 109]. The magnetic space group of an AM must lack centrosymmetry (no inversion center in the magnetic group) and instead includes only proper or improper rotations that relate opposite spins [19, 20, 109]. In group-theoretic language, the magnetic point group of an AM is a halving subgroup of the paramagnetic point group that does not contain inversion (in other words, the spin order parameter transforms as a non-trivial even-parity representation) [19, 20, 109]. This allows for the spin-up and spin-down sublattices to be related by a rotation or mirror operation (with or without a translation) rather than by inversion. For example, a two-sublattice collinear AFM on a centrosymmetric lattice (like bipartite inversion-related sites) is usually not altermagnetic because inversion combined with $\mathcal{T}$ remains a symmetry (enforcing degenerate bands). But suppose the lattice or spin arrangement breaks that inversion symmetry while maintaining other crystalline symmetries. In that case, a compensated collinear order can still emerge that lacks any $\mathcal{PT}$-type symmetry, fulfilling the AM criteria. Notably, even some centrosymmetric crystals can host altermagnetism if the magnetic order breaks inversion (as seen in MnTe) [25]. In summary, to identify an AM, one inspects the magnetic space group for the absence of any antiunitary symmetry that would enforce global spin degeneracy (like $\mathcal{PT}$ or a glide τ-symmetry), and the presence of only rotations/mirrors relating opposite spins.

Role of Time-Reversal and Spin-Symmetry Groups:

By definition, AMs break time-reversal symmetry ($\mathcal{T}$) (since they are magnets), but they are spin-compensated (net moment zero) by symmetry. This means the magnetic order parameter is an even-parity "multi-pole" in spin space rather than a uniform polar vector. One way to classify this is by analogy to spherical harmonics or pairing symmetry: a collinear FM corresponds to an s-wave ($l = 0$) spin configuration (uniform spin polarization in real-space), while a conventional Néel AFM on two sublattices is like a p-wave ($l = 1$, odd parity) order (spin polarization changes sign under inversion) [19, 20, 109]. AMs realize higher even-parity analogues; for instance, d-wave ($l = 2$, Fig. **2.2a** and **c**) or g-wave ($l = 4$, Fig. **2.2b** and **d**) spin arrangements, which have an even number of sign changes in the spin distribution [19, 20, 109].

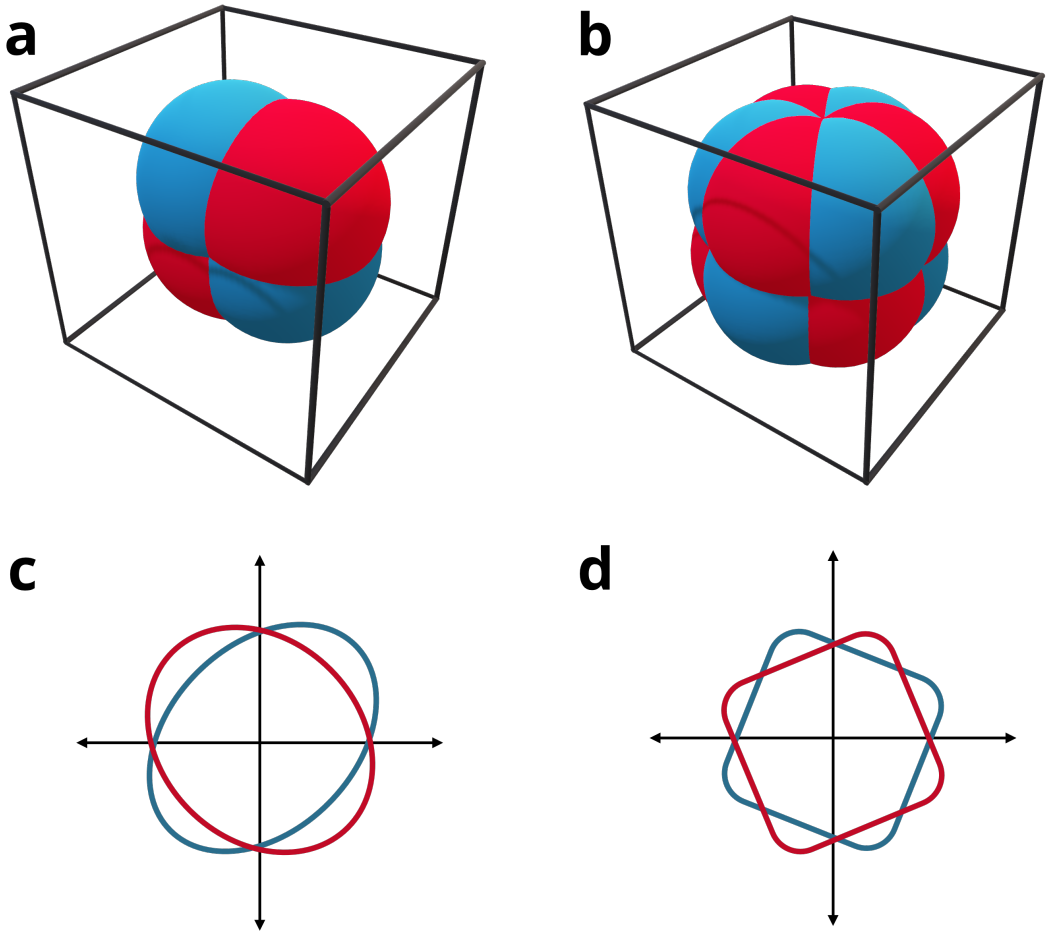

Figure 2.2.: ***d*- and *g*-wave altermagnetic spin splitting in reciprocal space.** Energy iso-surface of a 3D **a** d-wave and a **b** g-wave AM. The red/blue lobes encode the sign of the nonrelativistic spin splitting $\Delta E(\mathbf{k}) = E_{\uparrow}(\mathbf{k}) - E_{\downarrow}(\mathbf{k})$. Iso-energy (Fermi) contours for a 2D **c** d-wave and a **d** g-wave AM; colors indicate opposite spin polarization, not magnetization magnitude.

In real space, this means the staggered spin polarization pattern is more complex than a simple bipartite alternation: it may change sign under certain 90° or 60° rotations (as a d- or g-wave-like form), but remains symmetric under inversion (hence even-parity) [19, 20, 109]. For example, a d-wave altermagnetic order can be visualized as a spin density with two opposite lobes (up vs. down) separated by nodal planes (zero spin), analogous to a $d_{x^2-y^2}$ orbital shape [19, 20, 109] (Fig. **2.1c**). Such an order parameter is *even under inversion* (since $\phi_d(-\mathbf{r}) = \phi_d(\mathbf{r})$ for $d_{x^2-y^2}$), but *changes sign under exchanging x and y* (equivalently, under a 90° rotation in a tetragonal setting).

In summary, the symmetry-based identification comes down to checking that: (i) $\mathcal{T}$ is broken (magnetism present); (ii) net moment is zero (compensated spins); (iii) no combined $\mathcal{PT}$ or τ-translation symmetry remains; (iv) at least one non-trivial unitary symmetry (rotation/mirror) relates the spin sublattices. The material's magnetic space group permits altermagnetic ordering if all are satisfied [9, 18–20, 109, 110].

2.1.2. Reciprocal Space Manifestations of Altermagnetism

By using symmetry principles (magnetic group theory and representation analysis), one can identify candidate AMs and predict their nodal points/lines in the band structure and physical responses. The theoretical formalism rests on understanding how real-space even-parity spin order leads to momentum-space alternating spin splitting, protected by crystal symmetry [25, 59].

Alternating Spin Splitting in k-Space

The unique symmetry conditions of AMs lead to a very characteristic pattern in reciprocal space: an anisotropic, sign-changing spin splitting of electronic (magnonic) bands. In a ferromagnet, exchange coupling shifts spin-↑ and spin-↓ bands apart by a roughly constant energy (spin splitting is the same sign throughout the Brillouin zone, Fig. **2.1a**). In a conventional AFM (with $\mathcal{PT}$ symmetry), bands remain two-fold degenerate (no spin splitting anywhere in k, Fig. **2.1b**). An AM lies between these extremes: it exhibits spin-split bands, but the magnitude and sign of the splitting depend on crystal momentum (Fig. **2.1c**) [16, 88, 110]. In other words, the spin polarization of the bands alternates in different regions of the Brillouin zone, such that overall there are equal numbers of spin-↑ and spin-↓ states (ensuring zero total moment). Crucially, there are certain high-symmetry momenta (surfaces in k-space) where the spin splitting vanishes altogether: these are the "nodal surfaces" characteristic of AMs. Across a nodal surface, the sign of the splitting inverts (e.g., the spin-up band is higher in energy on one side, and the spin-down band is higher on the other side). This produces a plaid-like or "checkerboard" spin polarization pattern in momentum space, as often depicted for AMs (Fig. **2.2**) [19, 20, 109].

Origin of Nodal Lines and Planes

The existence of spin-degenerate nodal planes in the band structure is enforced by the real-space magnetic symmetries. An altermagnetic space group typically includes one or multiple operations that map an up-spin site to a down-spin site and send momentum $\mathbf{k}$ to an equivalent point. When $\mathbf{k}$ lies on the invariant subspace of that operation, the Bloch states must form degenerate pairs (one from each sublattice/spin); i.e., a band crossing along a line or plane in k-space is protected.

For example, consider hematite, a hexagonal AM (Fig. **2.3**). There a 120° spin rotation around $\hat{\mathbf{c}}$ combined with the crystallographic 120° rotation results in an effective C_3 symmetry in the spin–space group. This operation sends $(k_x, k_y, k_z) \mapsto \big(R_{2\pi/3}(k_x, k_y),\, k_z\big)$ and simultaneously exchanges the two magnetic sublattices (opposite spins), then any $\mathbf{k}$ lying on the invariant manifolds of this action (namely the three vertical planes that contain $\hat{\mathbf{c}}$ and one of the $\Gamma - K_{1,2,3}$ directions) has a partner state with opposite spin at the same $\mathbf{k}$; these are *three* spin-degenerate nodal planes parallel to k_z. In addition, a non-symmorphic mirror parallel to the basal plane, which can be written schematically as $\tilde{M}_z = \{m_z \,|\, 0, 0, \frac{1}{2}\}$ composed (in the spin group) with the appropriate spin rotation, maps $(k_x, k_y, k_z) \mapsto (k_x, k_y, -k_z)$ while swapping spins; therefore for any state with $k_z = 0$ it produces an opposite-spin partner at the same $\mathbf{k}$, enforcing the *fourth* nodal plane at $k_z = 0$ (Fig. **2.3**). With spin–orbit coupling, this k_z=0 plane remains symmetry constrained by the relativistic non-symmorphic mirror

(only the S_z component is allowed), whereas bands away from the four planes display the characteristic strong g-wave alternation of the nonrelativistic spin splitting [25,66].

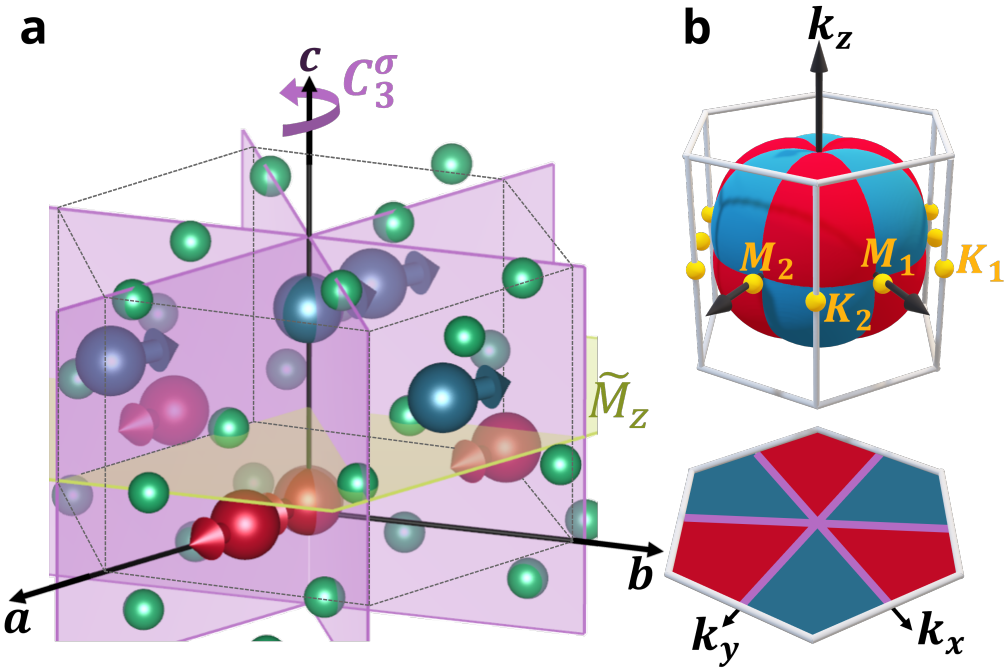

Figure 2.3.: Symmetry origin of the four nodal planes in hematite as a *g*-wave altermagnet. **a** Real-space lattice with compensated magnetic sublattices (red/blue arrows perpendicular to $\pm\hat{c}$). The effective spin–space threefold rotation $C_3^{\text{spin–space}}$ about $\hat{c}$ (together with the crystallographic C_3) relates three vertical invariant manifolds represented as vertical planes (purple) parallel to k_z and with a 120° symmetry. A nonsymmorphic mirror parallel to the basal plane, $\tilde{M}_z = \{m_z \,|\, 0, 0, \frac{1}{2}\}$, is indicated by the plane (green) protected by $\tilde{M}_z$. **b** Hexagonal Brillouin zone with the four spin-degenerate nodal planes through Γ and one of the $\Gamma - M_{1,2,3}$ directions. Their intersections with constant-k manifolds produce the nodal lines; sectors away from the planes exhibit the characteristic sign alternation of the nonrelativistic spin splitting $\Delta E(\mathbf{k})$ for a g-wave AM. A $k_z \neq 0$ *projection* is represented in the bottom with the purple nodal lines.

In general, each symmetry operation that half-turns the spins will generate one nodal surface in momentum space (the locus of $\mathbf{k}$ fixed by that symmetry). Therefore, the parity (wave character) of the spin order determines how many nodal surfaces exist: d-wave AMs have two nodal surfaces (Fig. **2.1a**), g-wave have four (Fig. **2.3**), and i-wave have six distinct spin-degenerate planes cutting through Γ in the Brillouin zone. These can be visualized as multiple mirror or glide planes in momentum space along which spin-↑ and spin-↓ bands coincide. For instance, a d-wave order on a square lattice might enforce degeneracy along $k_x = 0$ and $k_z = 0$ planes (yielding two orthogonal nodal planes). Off those planes, spin splitting grows and reaches opposite-sign quadrants between them.

Symmetry Protection

The symmetry protection of the nodal features (nodal planes, lines, points, and Weyl fermions) means that as long as the magnetic order preserves the relevant crystal symmetry, the degeneracies (and sign of spin polarization) are robust. For instance, in a tetragonal d-wave AM, the combination of a 90° rotation and spin inversion might enforce that $E_\uparrow(k_x, k_z) = E_\downarrow(k_z, -k_x)$, guaranteeing two nodal planes ($k_x = \pm k_z$) crossing the Brillouin zone center (Fig. **2.4**). If the protecting symmetry is lowered (for example, by strain that breaks the relevant mirror/glide or by a rotation of the Néel vector), a symmetry-allowed gap-opening coefficient in the low-energy (Dirac-like) $k \cdot p$ Hamiltonian becomes finite and *lifts the degeneracy across the entire nodal plane*. Depending on which symmetry elements survive, the former nodal plane generically collapses to nodal lines or points, or is fully lifted. However, as long as the magnetic space group remains in the altermagnetic class, the nodal surfaces are a universal feature; their exact orientation may depend on the details of the symmetry operation, but some spin-degenerate surfaces will still exist. In summary, the reciprocal-space hallmark of AMs is an anisotropic, sign-changing spin splitting with band degeneracies along specific symmetry planes/lines, directly reflecting the real-space magnetic symmetry operations [16, 19, 20, 109, 110].

2.1.3. Mathematical Formalism and Consequences

The altermagnetic order parameter can be rigorously described by the magnetic space group's irreducible representations (irreps). Essentially, one asks how a collinear spin configuration transforms under the crystal's symmetry operations. For a ferromagnet, the spin orientation is usually aligned with a high-symmetry axis and transforms as the fully symmetric (trivial) irrep of the point group (since all spins are identical under symmetry). A Néel AFM often corresponds to an odd-parity irrep. For example, the order parameter might transform like a polar vector that flips sign under inversion (this is analogous to a p-wave or dipolar symmetry). Altermagnetic orders belong to even-parity, higher-order irreps, often the same ones that would describe a d-wave or g-wave nematic order parameter. Indeed, altermagnetic spin order can be viewed as a kind of spin-space nematic: it breaks certain crystal rotations by the spin-up vs spin-down arrangement pattern, without producing a net dipole moment. For example, in a d-wave AM (as $LuFeO_3$ or $YFeO_3$) the collinear AFM spin arrangement has been identified with a B_{2g}-like representation (analogous to $x^2 - y^2$ symmetry); this corresponds to the "d-wave" character, changing sign under 90° rotation. Group theory dictates that such an order parameter will have two distinct domains (related by a 90° rotation) and will enforce two nodal planes in k-space (as discussed). In general, one can classify collinear magnetic orders by their symmetry (s-, p-, d-, f-, g-wave, etc.), and AMs are those in the even-l (even parity, $l \geq 2$) categories [16, 19, 20, 109, 110]. A possible new type could arise with the high-order odd parity, the so-called anti-altermagnets [111–114].

In practice, to use representation theory for identifying AMs requires a specific notion of group theory. The power of this classification is that it rigorously shows that AMs are a distinct symmetry category that had been overlooked historically, and only recently have theorists pointed out that such nonrelativistic, spin-split AFM states are symmetry-allowed and indeed realized in materials [16, 19, 20, 109, 110]. However, more recently, effective, phenomenological, and practical descriptions have been developed.

$\mathbf{k} \cdot \mathbf{p}$ Model and Band Structure Formalism

An effective Hamiltonian capturing the altermagnetic spin splitting can also be derived from symmetry analysis, and the same symmetry arguments can be transferable to the magnon hamiltonians. Consider a simple case: a tetragonal crystal with a collinear AFM order of d-wave symmetry (like $LuFeO_3$ or $YFeO_3$). To the lowest order in $\mathbf{k}$ (about Γ), the spin-dependent part of the Hamiltonian must transform like the same d-wave irrep. This leads to a term in the $k \cdot p$ Hamiltonian of the form:

$$H_{spl}(\mathbf{k}) = \Delta f(\mathbf{k}) \sigma_x, \tag{2.1}$$

where σ_x is the Pauli matrix for spin (assuming the spin quantization axis is x) and $f(\mathbf{k})$ is an invariant polynomial with the symmetry of the magnetic order. For a $d_{x^2-z^2}$-like order (Fig. **2.4**), one finds approximately $f(\mathbf{k}) \propto k_x^2 - k_z^2$ (in 2D) or analogous forms in 3D (involving k_y as needed).

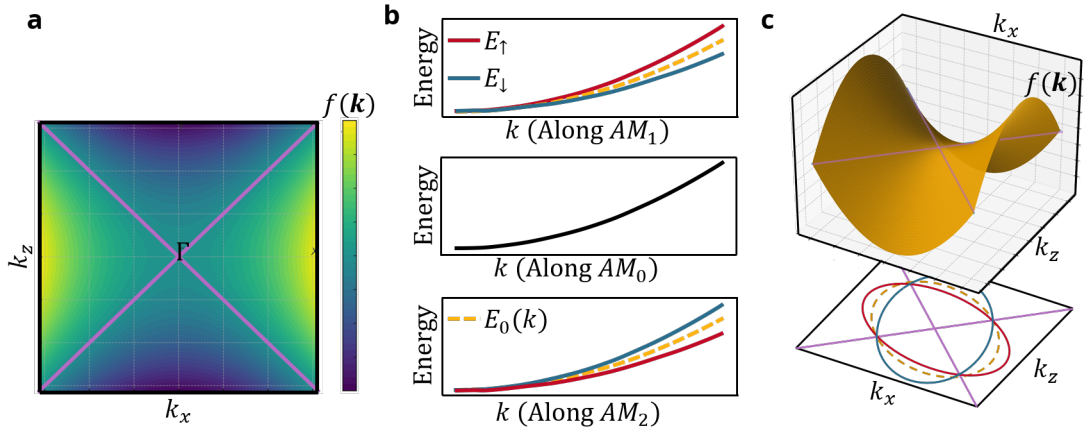

Figure 2.4.: **$\mathbf{k} \cdot \mathbf{p}$ $\mathbf{d_{x^2-z^2}}$-wave form model.** **a** Basal-plane symmetry form factor $f(\mathbf{k}) \propto k_x^2 - k_z^2$ for a tetragonal d-wave AM. The nodal lines $k_x = \pm k_z$ (diagonals) enforce $\Delta E(\mathbf{k}) = \pm \Delta f(\mathbf{k}) = 0$, while the lobes along k_x (k_z) correspond to $f > 0$ ($f < 0$). **b** Band dispersions for the effective Hamiltonian $H_{\text{spl}} = \Delta f(\mathbf{k}) \sigma_z$, on 3 AM directions: along AM_1 ($f > 0$) the spin-split branches $E_{\uparrow,\downarrow} = E_0 \pm \Delta f$ open with one sign, along AM_2 ($f < 0$) they open with the opposite sign, and along AM_0 ($f = 0$) the splitting vanishes (dashed curve shows the paramagnetic reference E_0). **c** Top: 3D saddle surface $k_y = f(\mathbf{k})$ highlighting the zero sets on the diagonals; bottom: symmetry-projected Fermi contours—relative to the paramagnetic contour (dashed), the spin-up (spin-down) sheet expands (contracts) in sectors where $f > 0$ and contracts (expands) where $f < 0$.

This implies an exchange splitting that is positive for states along the k_x axis and negative along the k_z axis, with $f(\mathbf{k}) = 0$ along $k_x = \pm k_z$; exactly the alternating pattern described earlier. In more complex cases (lower symmetry), $f(\mathbf{k})$ might involve higher-order terms or mixed k components. Still, the key feature is that it is an odd function under the symmetry that swaps spin sublattices (so that f changes sign under that operation). The full band structure of an AM can then be understood as an ordinary (paramagnetic) band structure plus such a momentum-dependent spin-splitting term. Away from the nodal planes ($f(\mathbf{k}) \neq 0$), the magnitude of splitting

respects the crystal's point group symmetry, while the sign of $\Delta f(\mathbf{k})$ alternates according to the irrep. Ab initio calculations confirm this. Such calculations also show that the largest splitting tends to occur along directions that maximize $|f(\mathbf{k})|$ (e.g., the Brillouin-zone boundaries mid-way between nodal planes), and it vanishes along the symmetry-enforced degenerate planes [16, 19, 20, 59, 109, 110].

Altermagnetic order parameter in the Landau functional.

The Landau tensor U^A introduced above is the continuum surrogate of the same sublattice odd, direction dependent hopping anisotropy that we identified microscopically as the origin of the altermagnetic spin splitting [55, 64]. In tight binding language, inequivalent Fe–O–Fe pathways on the two sublattices generate a k dependent, sign changing spin texture with nodal sets fixed by the magnetic space group; in the long wavelength limit this alternation reduces to the cross gradient term $w_{\mathrm{AM}} \propto A_{\mathrm{ani}}\big(\partial_x\mathbf{m}\cdot\partial_y\mathbf{n}+\partial_y\mathbf{m}\cdot\partial_x\mathbf{n}\big)$, that is, to an *anisotropic altermagnetic exchange interaction* controlled by U^A [108]. The same coefficient A_{ani} then appears in the small k expansion of the magnon Hamiltonian as the symmetry allowed k_xk_z splitting of the counter rotating branches, recovering the altermagnetic wave angular structure of the dispersion and its nodes discussed earlier, and providing a direct bridge between symmetry, band level alternation, and continuum dynamics [64, 107]. For the thesis, this connection is essential in two ways. First, for $YFeO_3$ and $LuFeO_3$ it furnishes a minimal parameterization of *magnon* transport anisotropy, since A_{ani} fixes the directions of enhanced or suppressed interfacial spin pumping and the direction dependence of diffusion lengths that underlie our non-local measurements [97, 115]. Second, on the *hopping* side, the same sublattice odd anisotropy encoded by U^A explains why altermagnetism is present even in the hopping regime. In practice, we will use A_{ani} as the continuum fitting knob that captures the microscopic alternation, allowing us to compare symmetry dictated trends across spectroscopy, transport, and our device geometries in a single, consistent model.

Following Gomonay *et al.* [108], the altermagnetic (AM) order parameter is introduced as a *staggered, symmetric second–rank tensor* that encodes the inequivalent local (bond) environments of the two magnetic sublattices. Concretely, one defines tensors $\hat{U}^{(1,2)}$ for sublattices $1, 2$ and forms the sublattice-odd, point-group–invariant combination

$$U^A \equiv U^{(1)}_{xy} - U^{(2)}_{xy}, \tag{2.2}$$

which is even under time reversal (structural) but odd under the sublattice exchange generated by the combined spin–space/real–space symmetry (e.g. $[C_2||C_4]$ in d–waves). In the simplest realization relevant for d-wave altermagnets the only nontrivial components are $U^{(1)}_{xy}$ and $U^{(2)}_{xy}$; under C_4 they map as $U^{(1)}_{xy} \leftrightarrow -U^{(2)}_{xy}$, rendering U^A invariant in the AM phase [108].

The Landau free-energy density contains the lowest-order scalar that couples this AM tensor to gradients of the magnetization $\mathbf{m}$ and Néel vector $\mathbf{n}$:

$$w_{\mathrm{AM}} \;\propto\; (U^{(1)}_{xy} - U^{(2)}_{xy})\big(\partial_x\mathbf{m}\cdot\partial_y\mathbf{n} + \partial_y\mathbf{m}\cdot\partial_x\mathbf{n}\big). \tag{2.3}$$

Setting $U^A = 1$ (absorbing its magnitude into a coefficient) yields the *anisotropic altermagnetic exchange interaction* term

$$w_{\mathrm{AM}} \;=\; A_{ani}\,\big(\partial_x\mathbf{m}\cdot\partial_y\mathbf{n} + \partial_y\mathbf{m}\cdot\partial_x\mathbf{n}\big), \tag{2.4}$$

which is the symmetry-distinct contribution responsible for AM-specific texture energetics and dynamics [108].

Equivalently, in the sublattice magnetization $\mathbf{M}_{1,2}$ the inhomogeneous exchange reads

$$w_{inh} \;=\; A_{iso}\big(|\nabla \mathbf{M}_1|^2 + |\nabla \mathbf{M}_2|^2\big) + 2A_{ani}(\partial_x \mathbf{M}_1 \cdot \partial_y \mathbf{M}_1 - \partial_x \mathbf{M}_2 \cdot \partial_y \mathbf{M}_2)\,, \tag{2.5}$$

so that each sublattice acquires a *direction-dependent* effective exchange interaction $A_{iso} \pm A_{ani}$ (maximal along [110]/[1$\bar{1}$0], vanishing along [100]/[010]), which is the continuum fingerprint of the AM spin-split band texture [108].

The tensorial altermagnetic order parameter U^A manifests in the free energy through additional gradient terms that couple the magnetization $\mathbf{m}$ and the Néel vector $\mathbf{n}$. This cross-term is symmetry-allowed in AMs but absent in collinear AFMs. The AM order parameter is thus (i) **mathematically** a rank-2, sublattice-odd tensor U^A; (ii) **symmetry** transforms according to the AM spin symmetry (e.g. $[C_2||C_4]$) and is time-reversal even; (iii) **couples** to $\mathcal{T}$-odd magnetic gradients to yield $\mathcal{T}$-even energy terms; (iv) **measurable** via its induced anisotropic exchange interaction A_{ani}, which controls magnon mode splitting, domain-wall internal magnetization gradients, and anisotropic Walker breakdown. A complementary, general Landau formulation identifying the AM order as a multipolar (secondary) order parameter and its linear couplings to observables is also possible to formulate with equivalent consequences [116].

Magnon Splitting In Fourier space, the AM gradient term contributes as $\propto A_{ani} k_x k_z$, giving rise to a momentum-direction-dependent splitting of the magnon modes. The resulting dispersion takes the form.

$$\omega_{\pm}(\mathbf{k}) = \sqrt{\omega_{AFMR}^2 + c^2 k^2} \;\pm\; 2\gamma M_s A_{ani}\, k_x k_z, \tag{2.6}$$

where ω_{AFMR} is the antiferromagnetic resonance (AFMR) frequency, c the spin-wave velocity, γ the gyromagnetic ratio, and M_s the sublattice magnetization. The angular dependence is given by $k_x k_z = k^2 \sin(2\phi)/2$, such that the splitting vanishes along the principal axes [100] and [001] and is maximal along the diagonals [101] and [10$\bar{1}$] (Fig. **2.5**). This anisotropy is a direct fingerprint of the AM order parameter and can be probed by inelastic neutron scattering. The anisotropic splitting in Eq. (2.6) reshapes the low energy spin transport through three coupled channels. First, it makes the magnon velocity and density of states angle dependent, so that the diffusion tensor becomes anisotropic, $\sigma_{\mathrm{m}}^{ij}(\phi)$, and the spin diffusion length acquires a directional form, $\lambda_{\mathrm{m}}(\phi) = \sqrt{D_{\mathrm{m}}(\phi)\,\tau_{\mathrm{m}}(\phi)}$ (with $D_{\mathrm{m}}(\phi)$ being the magnon diffusivity and $\tau_{\mathrm{m}}(\phi)$ the magnon relaxation time) [107]. Second, because the two branches $\omega_{\pm}$ carry opposite circular polarizations, interfacial spin transfer becomes polarization selective, with the efficiency set by the relative orientation between the injected spin accumulation and the eigenpolarization picked by $k_x k_z$ [117,118]. Along nodal directions, where $k_x k_z = 0$, the branches are degenerate and the net transverse spin current tends to cancel, while along diagonal directions one branch dominates, enhancing injection and detection. Third, the sign change of $k_x k_z$ across quadrants produces angular sign reversals in non-local thermoelectric signals and enables mode competition over distance, yielding non monotonic separations and even sign inversions when detector orientation samples

opposite quadrants in **k** space [115]. In practice, these effects manifest as characteristic rotations and amplitude modulations of electric and thermoelectric angular patterns through spin reorientation transitions, and as direction dependent propagation lengths in non-local geometries, all reproducible with a diffusive model that includes A_{ani} in the small k magnon Hamiltonian and the usual interfacial boundary conditions with $g_{\uparrow\downarrow}$ [107, 118, 119].

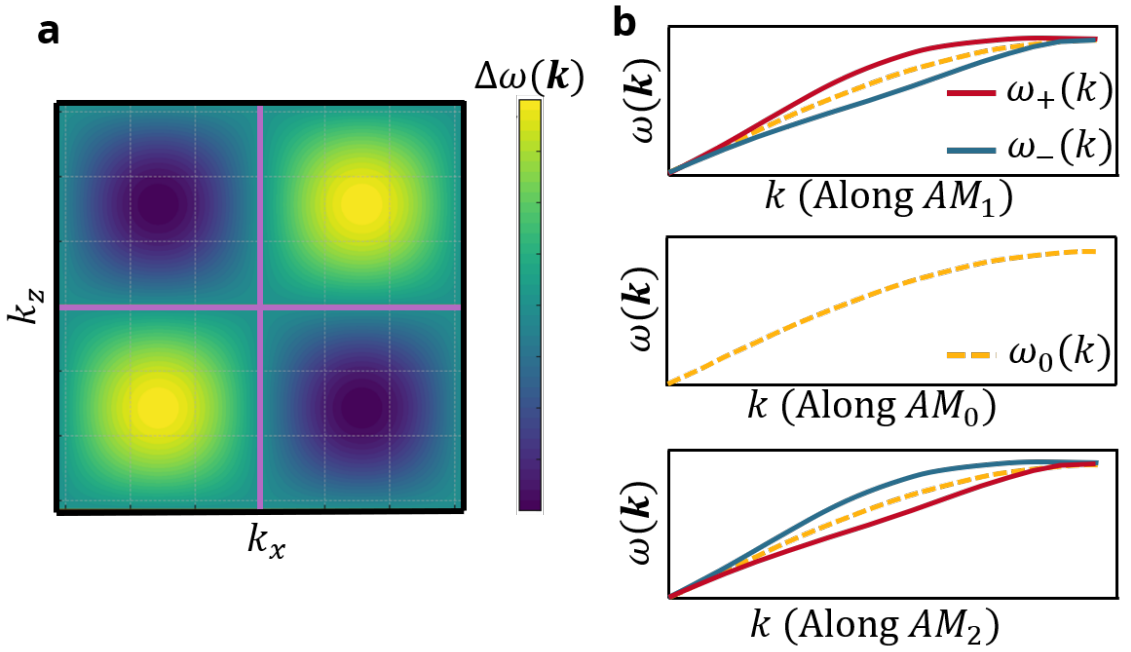

Figure 2.5.: **Altermagnetic *d*-wave magnon spin splitting from an anisotropic gradient term.** **a** Map of the frequency splitting in orthoferrites $\Delta\omega(\mathbf{k}) = \omega_+ - \omega_- = 4\gamma M_s A_{ani}\, k_x k_z$ on the $k_x - k_z$ plane: the splitting changes sign between quadrants and vanishes on the principal axes [100] and [001]. **b** Dispersions along symmetry lines for Eq. (2.6). Along AM_0, AM_1, and AM_2, the branches remain degenerate along high symmetry lines and split quadratically with k and opposite sign, $\omega_\pm = \sqrt{\omega_{AFMR}^2 + c^2k^2} \pm \gamma M_s A_{ani} k^2$. The AFMR gap is set to zero, $\omega_{AFMR} = 0$ (exchange/Goldstone limit). Lattice-periodic invariants are used so that the dispersion and splitting respect Brillouin-zone (BZ) periodicity.

In conventional collinear AFMs with negligible anisotropy and no external field, the long-wavelength magnon spectrum is gapless and linear, so near the Brillouin-zone center one finds [107, 120],

$$\omega(\mathbf{k}) \;\approx\; c\,|\mathbf{k}| \qquad (|\mathbf{k}| \to 0), \tag{2.7}$$

Expanding 2.6 at $|\mathbf{k}| \ll \omega_{\mathrm{AFMR}}/c$ gives

$$\omega_\pm(\mathbf{k}) \;\simeq\; \omega_{\mathrm{AFMR}} \;+\; \frac{c^2k^2}{2\,\omega_{\mathrm{AFMR}}} \;\pm\; 2\,\gamma M_s A_{\mathrm{ani}}\, k_x k_z, \tag{2.8}$$

so the leading k-dependence is *quadratic*, not linear. A linear, acoustic-like regime near Γ is recovered only in the gapless limit $\omega_{\mathrm{AFMR}} \to 0$ (ideal Heisenberg AFM). This quadratic-onset, directionally split spectrum is therefore a fingerprint of altermagnetic magnon kinematics and stands in sharp contrast to the gapless, isotropic linear dispersion of conventional AFMs. Relative to conventional collinear AFMs, AMs combine inversion symmetry with a sublattice odd hopping anisotropy. The result is a *nonrelativistic*, symmetry protected, sign changing spin splitting that fixes nodal sets and diagonal lobes in momentum space without net magnetization [55, 64]. Transport inherits these constraints. Linear magnon spectra of gapless AFMs become gapped with a quadratic onset and a d-wave polarization splitting, so that the most transparent directions for spin flow are rotated away from crystal axes to the diagonals, while nodes act as symmetry enforced dark directions for pumping and detection. Because the splitting term is even under inversion but odd under C_4 like rotations, its angular pattern is robust to weak spin orbit coupling (SOC) or weak canting, yet it reorients under spin reorientation transitions as the Néel vector rotates, providing a direct symmetry handle on transport anisotropies [55, 121, 122]. Finally, the polarization selectivity encoded by $\omega_{\pm}$ permits net spin flow even in a fully magnetically compensated lattice by unbalancing counter rotating modes through interface alignment or thermal gradients, a mechanism that naturally explains the pronounced directional non-local magnon transport observed in $YFeO_3$ and $LuFeO_3$ [115].

Berry Curvature and Anomalous Responses

One of the most significant consequences of altermagnetism is its impact on Berry curvature and related response functions. Berry curvature in momentum space, $\mathbf{\Omega}(\mathbf{k})$, acts like a "magnetic field" in k-space and is the source of anomalous Hall, optical, and magnetoelectric effects in crystals. In a collinear AFM with $\mathcal{PT}$ symmetry, $\mathbf{\Omega}(\mathbf{k})$ is exactly odd under $\mathcal{PT}$, causing a complete cancellation, thus no AHE or Kerr rotation occurs in such AFMs (their responses are often identically zero by symmetry). AMs, however, break $\mathcal{PT}$ symmetry, so Berry curvature has no fundamental requirement to cancel out. In fact, the alternating spin-split band structure can produce substantial Berry curvature in each spin channel. The symmetry operations relating spin-up and spin-down in an AM typically send $\mathbf{k}$ to a different point (e.g., rotate $\mathbf{k}$ by 90° or send $(k_x, k_y, k_z) \to (-k_x, -k_y, k_z)$). This means that the Berry curvature of a spin-↑ state at a $\mathbf{k}$ might equal the Berry curvature of a spin-↓ state at a different momentum $\mathbf{k}'$. If the Fermi surface or occupancy is symmetric, some cancellations can still occur, but not the guaranteed pairwise cancellation of a $\mathcal{PT}$-symmetric AFM. In many cases, the Berry curvature contributions actually reinforce rather than cancel, leading to nonzero integrated effects, such as a finite anomalous Hall conductivity (AHC) [16, 109, 110].

Because AMs are collinear, one might expect their Berry curvature distribution to come in equal and opposite patches (since for every spin-up state there is a spin-down state somewhere in the zone). However, those patches are crucially rotated or shifted in k-space such that the net doesn't vanish if the symmetry doesn't mandate it. If the crystal retains a high symmetry (like four-fold rotation), some components of the anomalous Hall tensor may cancel, e.g., a C_4 symmetry could force σ_{xy} to equal σ_{yx} with opposite sign, canceling net Hall in specific directions. This is why the orientation of the spin axis matters: for RuO_2, if the spin quantization is along the c-axis (preserving a C_{4z} axis), the AHE in the ab plane might cancel by symmetry; but if the easy axis

is in-plane (IP), the symmetry is lower and a Hall effect can emerge. Indeed, first-principles studies emphasize the importance of magnetization direction (easy axis) for anomalous transport in AMs [19, 20, 109].

Beyond the Hall effect, other TR-breaking responses, such as the magneto-optical Kerr effect or optical chirality, can occur in AMs depending on the Hall pseudo-vector. These are usually forbidden in a $\mathcal{PT}$-AFM but allowed here. For example, MnTe, RuO_2, and hematite have been examined for Kerr rotation signals and magnetic linear dichroism arising from their spin-split band structure. The Berry curvature distribution in AMs can also give rise to spin Berry phases and spin currents. For example, a spin-splitting that alternates with k effectively generates opposite spin Hall currents from different parts of the Fermi surface, which may or may not cancel. In some cases, a spin Hall effect (SHE) (shedding spin currents transverse to an applied electric field) can occur alongside or instead of a charge Hall effect, depending on symmetry. Detailed analysis has shown that Hall and spin Hall conductivities are possible in AMs. In summary, the Berry curvature in AMs is generally nonzero. This value can be considerable in magnitude due to the proximity of band degeneracies (gapped nodal surfaces acting like sources of Berry flux). These Berry curvature hotspots can lead to prominent experimental signatures, including the anomalous Hall effect, Kerr effect, anisotropic magnetoresistance, and orbital magnetization in each spin channel, all in a nominally zero-net-moment material. The theoretical formalism for computing these is the same as for FMs (integrating the Berry curvature over occupied states), but with the symmetry constraints of the altermagnetic space group used to determine which tensor components survive. Collinear AMs can display an anomalous Hall effect without SOC, purely from the nonrelativistic exchange splitting and broken $\mathcal{PT}$ symmetry. This was counterintuitive to decades of belief that AHE in collinear magnets required either a net magnetization or relativistic inversion-breaking (Rashba-type) splitting. The new symmetry classification shows that a non-relativistic exchange mechanism can lift Kramers degeneracy and produce Hall currents in the altermagnetic phase [16, 19, 20, 25, 109, 110].

2.1.4. Examples of Altermagnets

To solidify the concepts, we highlight some examples of AMs, explaining their symmetry and band-structure features. For a more complete list of candidates, their crystal symmetry, and their expected altermagnetic symmetry, see Anex **B.1**. In this thesis, we focus on Hematite and orthoferrites, as altermagnetic candidates.

Hematite (α-Fe_2O_3)(Hexagonal, corundum-type structure, $\mathrm{R}-3c$)

Hematite represents a prominent example of a g-wave AM characterized by a subtle interplay between crystallographic symmetry and magnetic order (Fig. **2.6a**), leading to a non-relativistic spin splitting of its electronic and magnonic bands. From the symmetry perspective, the underlying magnetic order in hematite below the Morin transition is collinear antiferromagnetic with spins oriented along the trigonal c-axis (Fig. **2.6c**), whereas above this transition, a spin reorientation occurs, forming an easy-plane canted antiferromagnetic state with the spins primarily oriented in the basal plane (Fig. **2.6b**). The emergence of the altermagnetic spin splitting in hematite is associated with the breaking of spin-rotation symmetry while preserving certain crystal

symmetries, notably the threefold rotational symmetry C_{3z}, the twofold rotation C_{2x}, and mirror symmetries (M_x, M_y, M_d) [41, 99, 123].

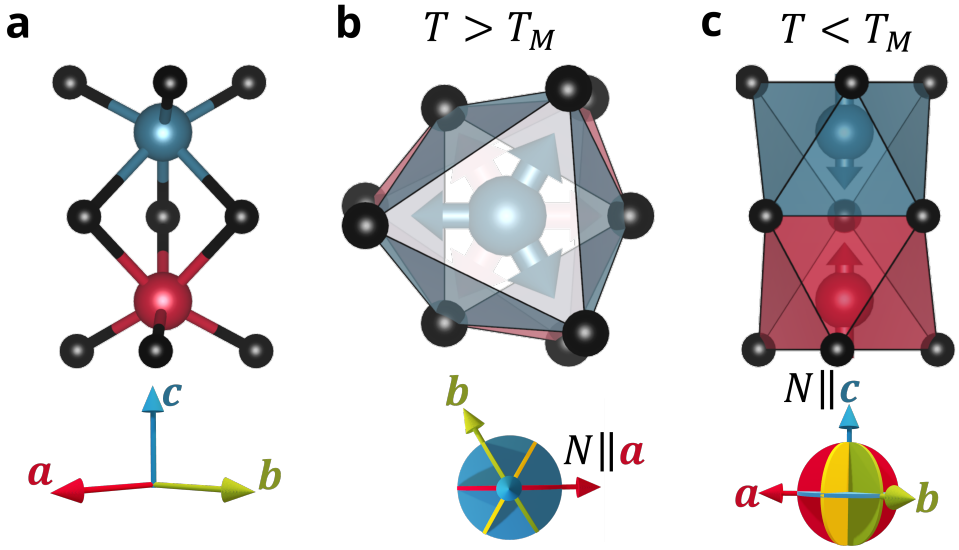

Figure 2.6.: **Crystal symmetries in hematite.** **a** Local Fe–O network of α-Fe_2O_3 ($R\bar{3}c$) showing two adjacent Fe sites with antiparallel spins (blue/red). The antiferromagnetic order breaks $\mathcal{PT}$ as the lattice is centrosymmetric, and the oxygen atoms break the $\tau\mathcal{T}$ symmetry. The (a, b, c) triad determines the crystallographic orientation. **b** $T > T_M$: easy-plane canted AFM; The FeO_6 sublatice octahedra show the breaking of the $\mathcal{PT}$symmetry, the Néel vector **N** confined to the basal plane (blue plane) along one of the three equivalent axes a, b, $a - b$ axis. A small canted moment in the $a - b$ plane is present, perpendicular to the Néel vector. A small $\hat{c}$ oriented external magnetic field can force the canted magnetization out-of-plane (OOP), within the high symmetry planes (green, yellow, red) **c** $T < T_M$: collinear easy-axis AFM with $\mathbf{N} \parallel c$; FeO_6 octahedra shown for reference. Blue/red shading denotes opposite Fe-sublattice spin orientations; black spheres indicate O atoms.

Magnetic point groups and allowed responses. Below the Morin transition ($T < T_M$), the collinear AFM order with $\mathbf{N} \parallel c$ belongs to magnetic class $\bar{3}m'$ and forbids a uniform magnetization and linear AHC. Above T_M, the easy–plane canted AFM selects a basal direction and lowers the symmetry to a monoclinic class compatible with $C2/c$ or $C2'/c'$ in each domain, which *allows* a basal-plane weak moment and Hall-like odd tensors. These assignments are consistent with SMR and X-ray dichroism imaging that read out the Néel vector orientation, and with room-temperature magnon transport in the easy-plane phase [47, 124, 125].

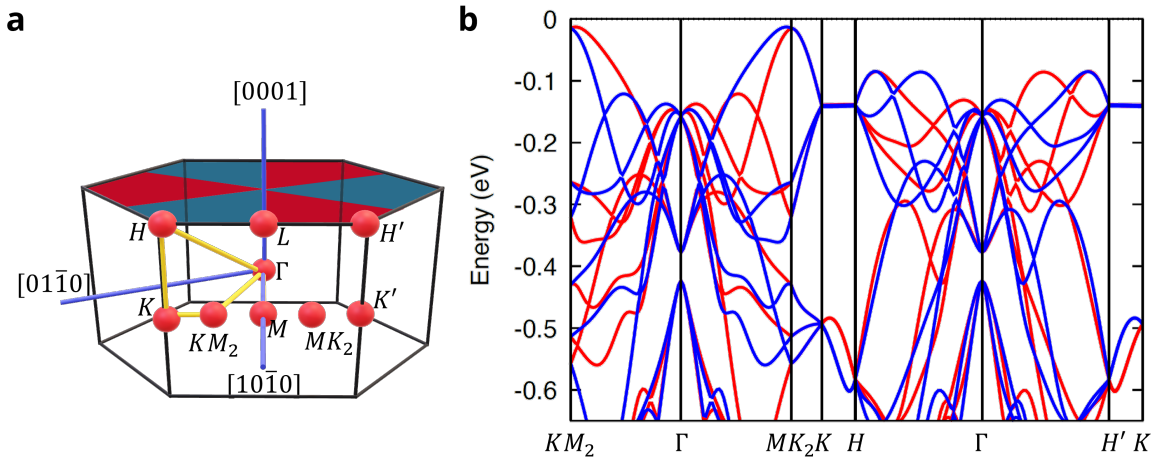

Figure 2.7.: **Altermagnetic signatures of hematite.a** Hexagonal Brillouin zone of α-Fe_2O_3; the spin texture slice at $k_z \neq 0$ in the top indicates the characteristic g-wave alternation. Yellow lines show the band-paths used. **b** Calculated bands along the indicated paths; red/blue denote opposite spin-split branches. The electronic bands are non-degenerate in two paths in the reciprocal space $\Gamma - H$ and $\Gamma - KM_2$. Adapted from Galindez-Ruales et al. [41], licensed under CC BY 4.0.

Magnetic structure and canting. The Fe^{3+} ($S = 5/2$) moments form two interpenetrating sublattices. Within each basal double layer, spins are parallel; adjacent double layers stack antiparallel along the c-axis. Above $T_M \simeq 260$ K (bulk), the easy–plane state exhibits a minute sublattice canting ($\theta \sim 0.4°$–$0.6°$ at low fields) producing $m \sim 10^{-3}$–10^{-2} μ_B/Fe, whereas below T_M the net moment vanishes by symmetry [126, 127].

Anisotropic exchange and DMI geometry. Dominant Fe–O–Fe superexchange between adjacent layers is antiferromagnetic; intralayer couplings are weaker and effectively ferromagnetic, yielding the double-layer motif. Symmetry-allowed Dzyaloshinskii–Moriya vectors are predominantly along c, enforcing $\mathbf{m} \propto \mathbf{L} \times \mathbf{D}$ in the basal plane only when $\mathbf{N} \perp c$. Thus, on cooling through T_M, the *allowed canting* vanishes (although microscopic DMI persists), restoring a strictly collinear state [126, 128, 129].

Multipolar origin of nonrelativistic spin splitting. The g-wave altermagnetic splitting can be formulated as ferroic rank-5 magnetic triakontadipole order coupled to antiferroic rank-4 charge hexadecapoles on Fe sites. This multipolar order breaks spin degeneracy without invoking strong SOC and is tunable by small oxygen displacements (strain, epitaxy, isovalent substitution) [41, 123].

Nodal manifolds and low-k scaling. In reciprocal space, hematite exhibits well-defined nodal planes, which are intrinsic to its symmetry. Specifically, the spin splitting of magnons exhibits a k^4 dependence at low wave vectors, displaying four distinct nodal surfaces. Three of these nodal surfaces are aligned precisely with crystallographic mirror planes (Fig. **2.7**). Remarkably, while the first three nodal surfaces

coincide with these mirror symmetries, the fourth nodal surface deviates from a non-symmorphic plane, creating additional nodal points in the $k_z = 0$ plane, resulting in a total of twelve nodal points instead of the six anticipated initially. These nodal surfaces emerge naturally from the symmetry conditions imposed by the magnetic and crystalline structure and serve as fingerprints for identifying the altermagnetic nature of the material experimentally [99].

Nonreciprocal magnon transport. In the canted (easy-plane) phase, broken inversion and time-reversal symmetries allow k-odd terms in the dispersion, yielding direction-dependent frequencies and amplitudes for counter-propagating spin waves. Time-of-flight spectroscopy and non-local detection show ultra-fast packets with group velocities up to ~ 20 km/s for bulk-like modes and ~ 6 km/s for surface-guided modes; the nonreciprocal contrast reverses with domain inversion (sign of $\mathbf{m}$ relative to $\mathbf{N}$) and can be controlled by the propagation direction relative to $\mathbf{N}$ [51]. These measurements use both inductive transduction and inverse spin Hall readout, confirming that nonreciprocity persists from GHz to the lower-THz dipolar–exchange regime and constitutes an intrinsic, symmetry-allowed transport asymmetry in α-Fe_2O_3.

Field–temperature phase diagram and spin flop. In the easy-axis phase ($T < T_M$), an IP (transverse) magnetic field drives a spin-flop of the Néel vector into the basal plane at a critical field H_{SF} that is largest at low T (tens of Tesla at liquid-helium temperatures) and collapses on approaching T_M [48]. Quantitatively, non-local transport and SMR experiments identify $H_{SF} \approx 8$ T at $T \sim 150$ K; near T_M, the softening makes the flop accessible at at couple of Tesla, producing sharp features in transport and resonance [47]. Above T_M, a small reorientation field of order 0.3–0.5 T appears within the easy plane, set by a weak threefold (sixth-order) anisotropy that maintains a finite gap and imprints a 60° angular periodicity in response functions [47]. In epitaxial films exceeding a critical thickness, T_M re-emerges and is *anisotropically* suppressed by fields applied parallel vs. perpendicular to the DM vector; the DM-related field scale extracted this way is essentially thickness-independent over orders of magnitude, enabling a transport-based quantification of interfacial vs. bulk anisotropies [125, 130].

Experimental fingerprints across $\mathbf{T_M}$. SMR in Pt/α-Fe_2O_3 provides an electrical symmetry readout: the angular harmonic content and phase shift by $\sim \pi/2$ across T_M directly reflect the reorientation of $\mathbf{N}$ from $\parallel c$ to IP, with SMR efficiencies up to $\sim 0.1\%$ in optimized stacks [124]. The SMR amplitude is enhanced near T_M due to the soft anisotropy and increased susceptibility [125]. X-ray linear dichroism (XMLD) and x-ray magnetic circular dichroism (XMCD) imaging (PEEM) resolves AFM domains and their temperature/field evolution; combined imaging–transport has recently been used to visualize the altermagnetic symmetry breaking and domain selection rules in hematite-based heterostructures [41].

Magnon transport and spin caloritronics. Non-local experiments with Pt injectors/detectors demonstrate room-temperature spin transport in α-Fe_2O_3 over micrometer distances. The non-local signal evolves continuously across T_M, with the largest signals when the magnon gap is minimized near the spin-flop; above T_M, transport persists via correlated pairs of linearly polarized magnons [47]. Ultra-low damping

($\alpha_{eff} \lesssim 10^{-5}$) and large group velocities account for these long dephasing lengths and enable electrical or optical driving of coherent dynamics (including THz spin-current emission into Pt) [47,131]. Together with the predicted nonrelativistic g-wave magnon splitting—dominant above $\sim$ 30 meV—these properties make hematite a promising platform for field-free, symmetry-controlled caloritronic effects and nonlinear magnon spin-splitter responses [99].

Thin films vs. bulk properties. In epitaxial α-Fe_2O_3(0001), the spin–reorientation temperature is set by the sign change of an *effective* uniaxial anisotropy $K_{\rm eff}(T)$ that combines bulk and film-specific terms,

$$K_{\rm eff}(T) \;=\; K_1(T) \;-\; |K_{\rm MD}| \;+\; K_{\rm me}(\varepsilon) \;+\; \frac{2K_s}{t} \;+\; K_{\rm int},$$

where $K_1(T)$ is the single–ion (easy–axis) term that *decreases* with T, $K_{\rm MD} < 0$ is the magnetodipolar (easy–plane) term that is only weakly T–dependent [132, 133], $K_{\rm me}(\varepsilon) \approx \frac{3}{2}\lambda\sigma$ is the magnetoelastic contribution from epitaxial strain ε (via stress σ), K_s is a surface/interface anisotropy (Néel type; $1/t$ scaling), and $K_{\rm int}$ collects interface-specific terms (e.g., clamping/destressing or exchange to overlayers). The Morin transition solves $K_{\rm eff}(T_M)=0$. In ultrathin or highly strained films, $K_{\rm me}+2K_s/t+K_{\rm int}$ can offset $K_1(T)$ *at all temperatures*, yielding $K_{\rm eff}(T) < 0$ and thus an easy–plane, canted state for the entire range up to T_N; operationally this means *no* Morin transition is observed down to base temperature (an effective $T_M \leq 0$ K) [124, 134].

Epitaxial strain provides a direct handle on $K_{\rm me}$. Fe L–edge XMLD on α-Fe_2O_3(0001) demonstrated that compressive in–plane strain (via a Cr_2O_3 buffer on Al_2O_3(0001)) *raises* T_M to $\sim$ 360 K for $\sim$ 3 nm films; T_M then decreases towards the bulk value as the film relaxes with thickness [135]. Conversely, in many sputtered/PLD films T_M is strongly *suppressed* or absent below $\sim$ 100 nm because size/strain and surface terms keep $K_{\rm eff} < 0$; optimizing oxygen stoichiometry can recover a finite T_M [134]. SMR shows that the anisotropy landscape in films also acquires a basal triaxial term (sixfold in hexagonal setting), visible as a 60° angular periodicity that selects in–plane **N** directions and shifts with growth conditions [124, 136].

In films thicker than a critical value, a *finite* T_M is recovered, and its field suppression is markedly anisotropic: H applied parallel vs. perpendicular to the DM vector shifts T_M by different amounts, enabling a transport–based extraction of the DM field and uniaxial anisotropies [130]. The DM scale is essentially thickness–independent over orders of magnitude [130], consistent with its bulk origin, whereas $K_{\rm me}$ and K_s/t control the thickness/strain trends of T_M.

Cation substitution and light–ion insertion provide reversible tuning of $K_{\rm eff}$. In (0001) films, Ti substitution *enhances* T_M well above the bulk value, consistent with a strengthened easy–axis term [137]. In contrast, hydrogen spillover into epitaxial α-Fe_2O_3 thin films reversibly *modifies* the anisotropy (via electron donation and local distortions), switching **N** between out–of–plane and in–plane at room temperature and shifting T_M correspondingly [138]. These results demonstrate that films can be engineered to realize $T_M \gg 300$ K (robust easy–axis) or $T_M \leq 0$ K (permanent easy–plane) by balancing K_1, $K_{\rm me}$, and surface/interface terms.

As summary, when comparing to bulk: (i) quantify strain to estimate $K_{\rm me}$, (ii) give t and interfaces to parameterize $2K_s/t$ and $K_{\rm int}$, (iii) use SMR angular harmonics to extract basal anisotropy and domain selection, and (iv) specify oxygen

stoichiometry/defect proxies that correlate with the presence or absence of a Morin anomal [124, 134, 136].

Rare earth Orthoferrites ($YFeO_3$, $LuFeO_3$, etc.) (Orthorhombic, Pbnm structure)

Orthoferrites are exemplary materials exhibiting d-wave altermagnetism. Their altermagnetic nature arises due to a unique combination of lattice distortions and antiferromagnetic (AFM) ordering, resulting in distinct non-relativistic spin splitting even without SOC.

Structural and magnetic setting Rare earth orthoferrites $RFeO_3$ crystallize in the distorted perovskite structure with space group $Pnma$ ($Pbnm$, No. 62) and point group D_{2h}, described by cooperative octahedral tilts of the Glazer type $a^-a^-c^+$ (Fig. **2.8 a**) [139, 140]. The $GdFeO_3$ type distortion produces sublattice-dependent Fe–O–Fe bond angles and anisotropic hopping paths that reduce cubic symmetry while preserving global inversion. Magnetically, the Fe^{3+} sublattice orders in a robust G type AFM with a high Néel temperature, typically 620 to 740 K, and for many members the room temperature spin structure is the Bertaut Γ_4 state (G_x, A_y, F_z), namely collinear G_x antiferromagnetism with a weak ferromagnetic canting F_z and a small A_y component (Fig. **2.9a**) [121, 122, 128, 141].

Symmetry and d-wave spin splitting In the Γ_4 state, time reversal is broken, inversion is retained, and a subset of nonsymmorphic operations survives. Within this magnetic space group, the combination of staggered exchange and sublattice dependent hopping enforces a momentum dependent, nonrelativistic spin splitting that transforms as a d-wave type irrep of D_{2h}, leading to symmetry protected nodal manifolds where the splitting vanishes and lobes where it is maximal [55, 62, 64, 96]. In minimal tight binding terms the leading form factor is odd under $k_x \leftrightarrow k_z$, for example $\cos(k_x a) - \cos(k_z a)$ or orthorhombic generalizations, which fixes nodal lines or planes along glide or mirror invariant directions in the Brillouin zone and yields alternating signs under the C_2 rotations of D_{2h} [55, 64]. Admitting SOC and DMI adds small, symmetry allowed corrections, such as crystal Hall and magneto optical responses, and can tilt or weakly shift the nodal structure, yet the primary d-wave splitting remains of nonrelativistic origin set by the magnetic space group and the anisotropic Fe–O–Fe pathways [57, 96, 121, 128]. The spectroscopic fingerprint is a $d_{x^2-z^2}$ like pattern in $\mathbf{k}$ space with degeneracies restored along mirror or glide invariant lines. See Fig. **2.8 b** for an example in $LuFeO_3$. Crucially, this d-wave altermagnetic splitting *does not* require SOC: it arises from sublattice-dependent *hopping anisotropies* (set by the octahedral tilts) combined with the G-type exchange field, which together break the combined antiunitary symmetry that would otherwise enforce Kramers-like degeneracy in a compensated AFM [55, 62].

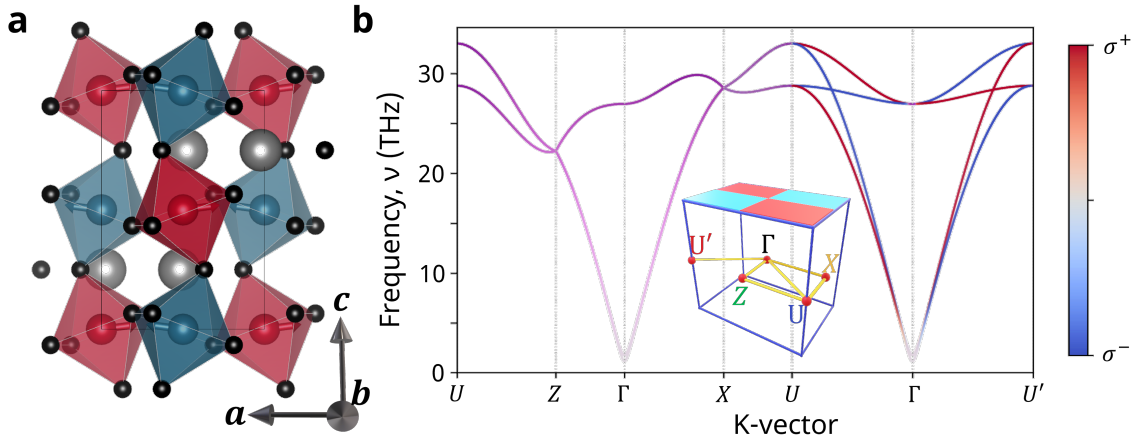

Figure 2.8.: Crystal and magnon signatures of d-wave altermagnetism in orthoferrites. **a** Orthorhombic $LuFeO_3$ (Pbnm) viewed along b, showing corner-sharing FeO_6 octahedra (blue/red for the two Fe sublattices). The weak ferromagnetic canting (exaggerated for clarity) arises from Dzyaloshinskii–Moriya interaction (DMI) and the antiferromagnetic order breaks the combined $\mathcal{T}\tau$ symmetry; oxygen atoms are black and the (a, b, c) triad is indicated. **b** Magnon dispersion along the different paths (inset: orthorhombic Brillouin zone with the path highlighted). Color encodes circular magnon polarization (σ^+/σ^-), revealing a chiral splitting characteristic of AMs. Degeneracies are restored on mirror-invariant (nodal) directions, e.g., along Γ–Z and Γ–X—while away from these lines a finite $\sigma^{\pm}$ splitting appears. Adapted from Galindez-Ruales et al. [115], arXiv:2508.14569 (2025), licensed under CC BY 4.0.

Weak ferromagnetism and DMI The weak ferromagnetic component F originates from the DMI permitted by the $a^-a^-c^+$ tilt geometry, which bends Fe–O–Fe bonds away from 180° and allows a DM vector perpendicular to the Fe–O–Fe plane [122, 128, 142]. The canting angle is small, yet it enables field tunability of the antiferromagnetic state and provides additional, SOC-mediated channels for optical and transport responses without being the primary source of the nonrelativistic d-wave splitting [121]. In symmetry terms, DMI and SOC act as weak knobs that couple the altermagnetic texture to Berry curvature effects while preserving the underlying d-wave momentum structure [57, 96].

At a Pt|$RFeO_3$ interface, the longitudinal spin magnetoreistivity (SMR) primarily probes the orientation of the Néel vector **n** through the antiferromagnetic spin mixing conductance, while the weak ferromagnetic canting **F** supplied by DMI adds a smaller ferromagnet–like channel. In the diffusive SMR theory, the antiferromagnetic selection rule makes the SMR *maximal* when the spin accumulation is perpendicular to the Néel vector and *minimal* when parallel, producing a characteristic 90° phase shift with respect to a ferromagnet. The imaginary part g_i^{AF} introduces a quadrature component that can tilt the angular traces and modify the field dependence through interfacial spin precession. In orthoferrites, DMI fixes **F** relative to the crystal axes, so across a $\Gamma_4 \to \Gamma_2$ spin reorientation the rotation of **n** drives a corresponding rotation

of the SMR lobes, while the **F**–term provides a small symmetry–allowed asymmetry in selected geometries. These expectations have been verified, which show an antiferromagnetic SMR angular phase and its evolution with temperature, and are consistent with SMR observations in other magnetic compensated oxides including α–Fe_2O_3. The altermagnetic d–wave anisotropy further implies that the SMR amplitude depends on the current and $\hat{\sigma}$ orientation with respect to the crystal diagonals, because interfacial spin transfer into magnons is enhanced on the altermagnetic lobes and suppressed along nodal directions [143–145].

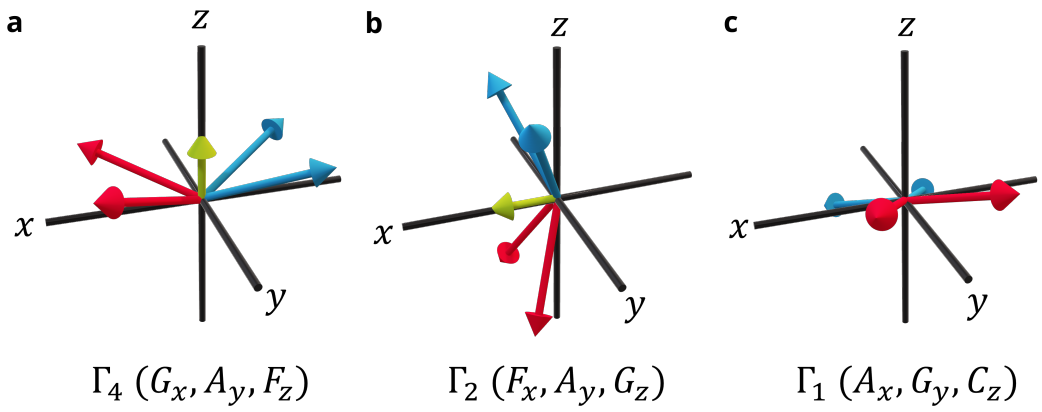

Figure 2.9.: Schematics of common magnetic spin configurations in orthoferrites. **a** Γ_4 configuration ($G_xA_yF_z$): Fe spins aligned predominantly along the x-axis with weak canting along z. **b** Γ_2 configuration ($F_xA_yG_z$): Fe spins aligned along z with canting along x. **c** Γ_1 configuration ($A_xG_yC_z$): collinear AFM order with no net ferromagnetic moment. Arrows represent Fe moments and canting directions exaggerated for clarity.

Because the nonrelativistic altermagnetic splitting is set by sublattice-dependent Fe–O–Fe hopping, any knob that tunes the $a^-a^-c^+$ tilt pattern (biaxial strain, substrate orientation, or hetero-octahedral connectivity) modulates the *magnitude* and even the *orientation* of the d-wave form factor [139,140]. Epitaxial strain can selectively enhance (suppress) the lobes of the $d_{x^2-y^2}$-like texture and shift nodal planes, offering a route to rotate magnon and electronic anisotropies without changing chemical composition.

Spin reorientation transitions and rare earth coupling Across the $RFeO_3$ series, spin reorientation transitions are common (Table **2.1**), typically $\Gamma_4 \rightarrow \Gamma_2$ upon cooling, driven by the temperature dependent competition between Fe magnetocrystalline anisotropy and the $3d$–$4f$ exchange with the rare earth sublattice [121,122,146]. Landau descriptions with two competing anisotropies capture continuous, mixed Γ_{24}, or abrupt transitions [122,146]. Because SRTs rotate the Néel vector, they reselect which nonsymmorphic operations remain active and thereby reorient the d-wave nodal sets rather than destroying the altermagnetic mechanism. Table **2.1** lists representative Γ_i ground states and transition windows across the series [121,142,147–151].

Table 2.1.: **Properties of rare-earth orthoferrites.** Γ_i labels follow Bertaut notation with $(G_xA_yF_z)$ for Γ_4, $(F_xA_yG_z)$ for Γ_2, and $(A_xG_yC_z)$ for Γ_1. Where a two-step reorientation occurs, the interval is shown as $T_1! \rightarrow T_2$ and the intermediate Γ_{24} phase is implicit. The column **RE Ord.** lists the rare-earth sublattice ordering temperature T_N^{R} (if present). $\mathbf{R^{3+}}$ **Gnd.** gives the $4f^n$ configuration and Russell–Saunders ground term; the last three columns report the corresponding quantum numbers L, S, and J [151]. For diamagnetic $\mathrm{R^{3+}} = \mathrm{La^{3+}}, \mathrm{Y^{3+}}, \mathrm{Lu^{3+}}$ and for $\mathrm{Eu^{3+}}$ (J=0), no RE ordering is expected. T_{SR} values refer to stoichiometric bulk single crystals at ambient pressure; ranges indicate onset → completion of the reorientation [121, 142, 147–150].

RE FeO_3	**Spin Conf.**	**T_{SR} [K]**	**RE Ord.**	**R^{3+} Gnd.**	L	S	J
$LaFeO_3$ [152, 153]	Γ_4	–	–	Dia. ($4f^0$)	0	0	0
$CeFeO_3$ [154, 155]	$\Gamma_4 \rightarrow \Gamma_1$	240→220	–	$4f^1$	3	1/2	5/2
$PrFeO_3$ [152, 156]	$\Gamma_2 \rightarrow \Gamma_4$	200→172	–	$4f^2$	5	1	4
$NdFeO_3$ [157]	$\Gamma_4 \rightarrow \Gamma_2$	170→100	–	$4f^3$	6	3/2	9/2
$SmFeO_3$ [153, 158]	$\Gamma_2 \rightarrow \Gamma_4$	480→450	∼4 K	$4f^5$	5	5/2	5/2
$EuFeO_3$ [153]	Γ_4	–	–	$4f^6$ (J=0)	3	3	0
$GdFeO_3$ [153, 159]	Γ_4	–	2–4 K	$4f^7$	0	7/2	7/2
$TbFeO_3$ [153, 160, 161]	$\Gamma_4 \rightarrow \Gamma_2 \rightarrow \Gamma_4$	8.5→3→5	∼5 K	$4f^8$	3	3	6
$DyFeO_3$ [153, 162, 163]	$\Gamma_4 \rightarrow \Gamma_1$	∼50	4.5 K	$4f^9$	5	5/2	15/2
$HoFeO_3$ [164–167]	$\Gamma_4 \rightarrow \Gamma_2$	55→ 35	5–6 K	$4f^{10}$	6	2	8
$ErFeO_3$ [152, 160, 168, 169]	$\Gamma_4 \rightarrow \Gamma_2$	93→85	∼4 K	$4f^{11}$	6	3/2	15/2
$TmFeO_3$ [170]	$\Gamma_4 \rightarrow \Gamma_2$	94→82	∼3 K	$4f^{12}$	5	1	6
$YbFeO_3$ [171]	$\Gamma_4 \rightarrow \Gamma_2$	∼8	∼2 K	$4f^{13}$	3	1/2	7/2
$LuFeO_3$ [152]	Γ_4	–	–	Dia. ($4f^{14}$)	0	0	0
$YFeO_3$ [172, 173]	Γ_4	–	–	Dia.	0	0	0

Altermagnons: magnon nodal splitting effects due to altermagnetism In AMs, the magnon Hamiltonian transforms under the same magnetic space-group operations that govern the electronic Bloch Hamiltonian; therefore, the symmetry-imposed alternating spin splitting in the electronic bands has a direct magnon analogue. Antiunitary operations (e.g., $\mathcal{T}$ combined with mirrors or rotations) enforce nodal lines/planes where the chirality-resolved magnon branches $\sigma^{\pm}$ are degenerate. In contrast, away from those invariant manifolds, the branches split with opposite sign on symmetry-related $\mathbf{k}$-paths—precisely mirroring the electronic k-space alternation. This correspondence is particularly consequential in orthoferrites, which are wide-gap insulators: low-energy spin transport is entirely magnonic, so the altermagnetic symmetry must be diagnosed and exploited in the magnon spectrum rather than via itinerant electrons. In Fig. **2.8b** the magnon bands of $LuFeO_3$ are shown; degeneracies re-emerge along mirror-invariant directions (e.g., $\Gamma-Z$, $\Gamma-X$), whereas finite $\sigma^{\pm}$ splitting appears on generic paths (e.g., near U and U'), providing a spectroscopic fingerprint of altermagnetic order and the basis for chiral-magnon transport in an insulating platform.

Beyond the electronic bands, the same magnetic space-group constraints imprint a d-wave structure on the magnon sector. In the collinear limit, two counter-rotating

magnon modes are symmetry-degenerate on nodal directions but *split* away from them, with the leading anisotropy transforming as a d-wave form factor (e.g. $\propto \sin k_x a \sin k_z a$ at small k, reducing to $\propto k_x k_z$ in the continuum) [55, 64]. DMI adds a small chiral (nonreciprocal) component consistent with $Pnma$ tilts, slightly shifting frequencies for $\pm\mathbf{k}$ and enabling direction-selective magnon transport without net magnetization [121, 128]. These predictions rationalize polarization-resolved magnon spectra such as those sketched in Fig. **2.8b** and connect directly to anisotropic non-local magnon transport and SMR/SSE angular fingerprints anticipated in $YFeO_3$ and $LuFeO_3$ [107].

Implications for spin transport In the wide gap $RFeO_3$, the low-energy spin transport is magnonic. The d-wave symmetry fixes directions in which the interfacial spin pumping and the diffusive propagation are enhanced or suppressed, depending on whether wave vectors align with nodal sets or with lobes of the altermagnetic form factor. Across an SRT, the reorientation of the Néel vector, and thus of the active nonsymmorphic operations, rotates these anisotropies, which should manifest as characteristic changes in SMR and SSE angular dependences (Sec. 2.2 and 2.2.1), as well as in the polarization selectivity of pumped or detected magnon modes [55, 64, 107].

2.2. Spin Transport in Insulating Compensated Magnets

Spin transport in insulating compensated magnets, such as collinear AFMs and AMs, has emerged as a cornerstone of next-generation spintronic research due to its potential to combine high-frequency operation with low power dissipation and robustness against external magnetic perturbations. These materials, characterized by zero net magnetization but long-range magnetic order, support the propagation of spin information via magnons—quanta of collective spin excitations—rather than charge carriers. As a result, they circumvent the Joule heating limitations inherent to metallic spintronic systems and open pathways for ultrafast and energy-efficient signal processing [15, 105, 107].

In these systems, spin currents can be generated and detected through a variety of interfacial mechanisms coupling the dynamics of itinerant electrons in heavy metals to localized spins in insulating magnets (Fig. **2.10**) [101, 119]. The interplay between interface effects, magnon dispersion, magnetic symmetry, and anisotropy defines the fundamental physics governing spin transport and the SMR.

The following subsections develop the theoretical models describing spin injection, detection, and magnon-mediated transport in compensated insulating magnets. We explore both well-established mechanisms and open challenges, addressing how magnetic anisotropy, symmetry constraints, interface spin-mixing conductance, and magnon polarization modes determine the efficiency and directionality of spin currents.

2.2.1. Spin Injection and Detection Mechanisms

Spin transport phenomena in insulating compensated magnets rely fundamentally on efficient methods for injecting and detecting spin currents [174]. Typically, spin injection into insulating magnets occurs at interfaces with heavy metals, such as Pt,

that exhibit significant SOC. The SHE, for instance, facilitates electrical spin injection into insulators, where an electric current in a heavy metal generates a transverse spin current due to spin-dependent scattering processes (extrinsic SHE) or intrinsic band structure properties (intrinsic SHE) [101]. Another well-known injection mechanism is the SSE, where thermal gradients across interfaces between insulating magnets and heavy metals result in spin current generation [104].

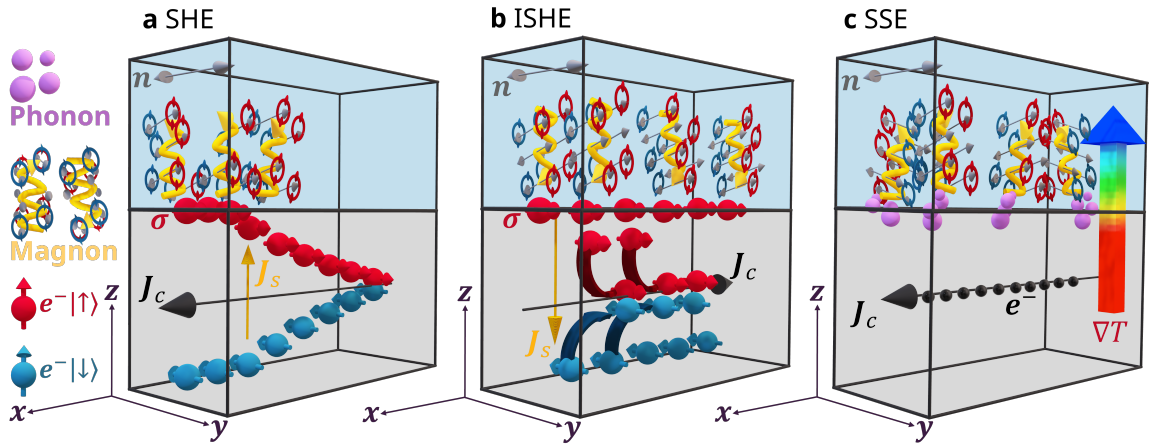

Figure 2.10.: **Spin injection and detection mechanisms in insulating compensated magnets. a** SHE: an IP charge current j_c in a heavy metal (Pt) generates a transverse spin current j_s that injects spins into the adjacent insulating magnet. **b** Inverse Spin Hall Effect (ISHE): a spin current j_s flowing from the magnet into Pt is converted into a measurable transverse charge voltage V_{ISHE}. **c** SSE: a temperature gradient ∇T across the magnet–Pt interface drives a spin current j_s, which is detected electrically in Pt via the ISHE. Black arrows indicate charge currents, spins by red (blue) arrows, and heat flow by a color-gradient arrow.

Conversely, the ISHE enables spin detection by converting a spin current into a measurable transverse charge voltage [102]. Complementing these phenomena, spin pumping emerges when magnetization dynamics, induced either via external fields or resonant excitations, generate a spin current that flows from the insulating magnet into an adjacent heavy metal layer, which is beyond our scope [117, 175, 176]. In all these injection and detection mechanisms, the role of the spin mixing conductance ($g_{\uparrow\downarrow}$) at the interfaces remains crucial. The real part, g_r, determines the magnitude of spin transfer, while the imaginary component, g_i, is linked to spin accumulation and precessional dynamics at interfaces [119, 177].

Spin Injection from an electrically generated spin-accumulation

The generation of spin currents in nonmagnetic metals adjacent to insulating magnets primarily relies on the SHE, which is a cornerstone of electrical spin injection in spintronics. When a charge current is applied through a nonmagnetic metal with strong SOC, spin-dependent transverse deflection of charge carriers occurs, generating

a pure spin current orthogonal to the charge flow, this transverse spin flow can be efficiently injected into an adjacent magnetic insulator, provided the interface conditions permit angular momentum transfer (Fig. **2.10a**). The SHE can be broadly classified into extrinsic and intrinsic mechanisms, based on whether it originates from impurity scattering or band structure topology, respectively.

Extrinsic SHE The extrinsic SHE describes spin-current generation via spin-dependent scattering processes occurring in nonmagnetic metals with strong SOC, such as Pt or Ta. In these systems, spin currents arise from asymmetric scattering (skew scattering) and side-jump mechanisms. This mechanism depends critically on impurity concentration and scattering potentials [101].

Intrinsic SHE In contrast to the extrinsic mechanism, the intrinsic SHE arises directly from the electronic band structure of the material. Here, the Berry curvature $\Omega(\mathbf{k})$ of the occupied states acts as an effective magnetic field in momentum space, deflecting electrons based on their spin.Unlike the extrinsic case, the intrinsic SHE is robust against disorder and largely independent of scattering processes. Materials with broken inversion symmetry and strong spin-orbit coupling exhibit large intrinsic spin Hall angles, as first described in p-doped semiconductors and extended to transition metals [101, 178, 179].

Inverse Spin Hall Effect

The ISHE is the reciprocal (time-reversal) phenomenon of the SHE, enabling the detection of spin currents via their conversion into measurable transverse charge voltages in materials with strong spin-orbit coupling, such as Pt, Ta, or W (Fig. **2.10b**).

The resulting voltage V_{ISHE} is commonly used as the readout in non-local spin transport experiments, in SSE setups, or as a detection mechanism for spin pumping signals [101].

The ISHE is a bulk effect, but its manifestation at interfaces depends on multiple factors, including the spin dephasing length, spin diffusion length, and the nature of the spin accumulation at the interface. Particularly in collinear AFMs and AMs, where the net magnetization is zero, the symmetry of the spin current polarization plays a critical role. The ISHE remains robust provided the injected spin current has a component orthogonal to both the spin polarization and charge flow axes allowed by the material's symmetry.

In insulating compensated magnets, the ISHE signal is usually measured in adjacent heavy metal layers. In these systems, the spin current originates from thermally or electrically excited magnons and transmits angular momentum across the interface via exchange coupling. The measured charge voltage in the heavy metal layer is then interpreted as a direct consequence of spin injection from the insulating magnet and its subsequent conversion by the ISHE.

Quantitative modeling of ISHE signals often involves solving coupled spin-diffusion equations within the metal layer, incorporating boundary conditions that include the spin mixing conductance $g_{\uparrow\downarrow}$ and the spin diffusion length λ_s. This is crucial for distinguishing between the spin current generated by bulk spin accumulation and that produced by interface proximity effects or parasitic contributions [106].

Spin Seebeck Effect due to thermal gradients

The SSE describes the generation of spin currents in magnetic insulators driven by temperature gradients applied perpendicular to the magnet-metal interface [104, 177]. From a microscopic viewpoint, the SSE can be understood in terms of thermally excited magnons. A temperature gradient ∇T induces a non-equilibrium magnon distribution within the insulating magnet, creating a magnon chemical potential gradient (μ_m). This gradient drives magnons to diffuse towards the cooler side of the interface, producing spin accumulation at the interface with a heavy metal such as Pt (Fig. **2.10c**) [106]. The diffusive magnon spin current density (J_s) generated due to a temperature gradient can be theoretically described by a linear-response model as:

$$\mathbf{J}_s = -\sigma_m \left(\nabla \mu_m + S_m \nabla T\right), \tag{2.9}$$

where σ_m is the magnon spin conductivity, and S_m is the magnon Seebeck coefficient characterizing the efficiency of thermal-to-spin conversion [180]. The magnon chemical potential gradient ($\nabla \mu_m$) accounts for the magnon number imbalance generated by thermal excitation, thus reflecting the magnon population dynamics in the insulating magnet [106].

Theoretically, the SSE at a metal|AFM interface is described within the same magneto-electronic-circuit model as for FMs, but with the Néel order parameter $\mathbf{n}$ replacing the magnetization and with AFM-specific spin-mixing conductances. In a compensated, collinear AFM the interfacial spin current contains a coherent, *pumping* contribution from Néel dynamics and an incoherent, *thermal* contribution associated with a magnon chemical potential generated by ∇T [117, 118, 177, 181]. The coherent part reads

$$\mathbf{J}_s^{\mathrm{pump}} = \frac{\hbar}{4\pi}\Big[g_r^{\mathrm{AF}}\ \mathbf{n}\times\dot{\mathbf{n}} + g_i^{\mathrm{AF}}\ \dot{\mathbf{n}}\Big], \tag{2.10}$$

where $g_r^{\mathrm{AF}} = \mathrm{Re}\, g_{\uparrow\downarrow}^{\mathrm{AF}}$ and $g_i^{\mathrm{AF}} = \mathrm{Im}\, g_{\uparrow\downarrow}^{\mathrm{AF}}$ quantify the dissipative and reactive interfacial spin transfer for a compensated interface. The thermal SSE contribution is captured by a boundary condition that couples the metal spin accumulation $\boldsymbol{\mu}_s$ and the AFM magnon bias (or chemical potential) μ_m to the interfacial spin current:

$$\mathbf{J}_s^{\mathrm{th}} = -\frac{1}{4\pi}\Big[g_r^{\mathrm{AF}}\ \mathbf{n}\times(\mathbf{n}\times\boldsymbol{\mu}_s) + g_i^{\mathrm{AF}}\ \mathbf{n}\times\boldsymbol{\mu}_s\Big]\ +\ \mathcal{G}_T^{\mathrm{AF}}\ \nabla T, \tag{2.11}$$

where $\mathcal{G}_T^{\mathrm{AF}}$ is the interfacial spin Seebeck coefficient that encodes the stochastic, thermally driven spin pumping by incoherent AFM magnons. In equivalent μ_m-based formulations, one writes $J_s^{\parallel\mathbf{n}} = \mathcal{G}_\mu^{\mathrm{AF}}\,\mu_m + \mathcal{G}_T^{\mathrm{AF}}\,\Delta T$, which is microscopically consistent with the fluctuation–dissipation approach of the SSE [118, 177, 181]. Equations (2.10)–(2.11) make explicit that, despite zero net magnetization, compensated AFMs pump and absorb spin with an efficiency set by $g_{\uparrow\downarrow}^{\mathrm{AF}}$, and that the SSE appears as a thermal source term at the interface on equal footing with the coherent Néel dynamics [117, 118].

Spin Mixing Conductance and Spin Transfer

The *spin-mixing conductance* $g_{\uparrow\downarrow} = g_r + i g_i$ is the central interfacial parameter governing how efficiently transverse spin angular momentum is transmitted across a normal-metal|magnetic-insulator (N|MI) interface. It compactly encodes both the *dissipative*

(damping-like) absorption of transverse spin (g_r) and the *reactive* (field-like) interfacial phase shifts (g_i) experienced by spin-dependent scattering. As such, $g_{\uparrow\downarrow}$ sets the scale of spin pumping, spin-transfer torque (STT), and SMR, and it enters on equal footing in injection and detection problems by Onsager reciprocity [119, 182]. For magnetic *compensated* two-sublattice collinear insulators (AFMs and related compensated magnets), the natural slow collective coordinate is the Néel vector $\mathbf{n} = (\mathbf{m}_1 - \mathbf{m}_2)/(2M_s)$, while the net magnetization $\boldsymbol{\ell} = (\mathbf{m}_1 + \mathbf{m}_2)/(2M_s)$ is small and, in the strong-exchange limit, slaved to $\mathbf{n}$ via

$$\boldsymbol{\ell} \simeq \frac{\chi_\perp}{\gamma}\, \mathbf{n} \times \dot{\mathbf{n}}. \tag{2.12}$$

A key theoretical result is that the *same* spin-mixing construct applies with the replacement $\mathbf{m} \mapsto \mathbf{n}$ and with antiferromagnet-specific parameters $g_{r,i}^{AF}$: there is *no* cancellation between sublattices at a magnetically compensated interface, so $g_{\uparrow\downarrow}^{AF}$ can be comparable to FMs [117]. The pumped spin current and reciprocal STT become

$$\mathbf{J}_s^{pump} = \frac{\hbar}{4\pi}\left(g_r^{AF}\, \mathbf{n} \times \dot{\mathbf{n}} + g_i^{AF}\, \dot{\mathbf{n}}\right), \qquad \boldsymbol{\tau}_{STT} = \frac{1}{4\pi s}\left[g_r^{AF}\, \mathbf{n} \times (\mathbf{n} \times \boldsymbol{\mu}_s) + g_i^{AF}\, \mathbf{n} \times \boldsymbol{\mu}_s\right], \tag{2.13}$$

with selection rules fixed by symmetry: $\boldsymbol{\mu}_s \parallel \mathbf{n}$ produces no damping-like torque, whereas $\boldsymbol{\mu}_s \perp \mathbf{n}$ is maximally effective [15, 117]. The boundary condition mirrors with $\mathbf{m} \to \mathbf{n}$ and $g_{r,i} \to g_{r,i}^{AF}$, and provides the interface closure for both coherent (spin pumping) and incoherent (thermal magnon) spin transport theories [118, 183].

2.2.2. Magnons as Spin Carriers in magnetically Compensated Insulators

In insulating magnets, spin transport is mediated by collective excitations of the spin lattice, namely, magnons. These quasiparticles represent quantized spin waves and serve as the primary carriers of angular momentum in the absence of mobile charge carriers [105, 106].

The magnetic ground state symmetry and exchange interactions dictate the intrinsic properties of magnons in compensated systems. For instance, in bipartite collinear AFMs, two degenerate magnon branches often carry opposite spin angular momentum, yielding zero net spin current in equilibrium. However, when driven out of equilibrium by thermal gradients, spin pumping, or spin-orbit interactions at interfaces, these modes can support net spin flow with distinctive polarization textures and transport lengths [107, 118, 184, 185].

A key distinction between magnons in FMs and those in compensated magnets lies in their polarization and dispersion characteristics. In FMs, spin-wave modes are circularly polarized and energetically nondegenerate. In contrast, collinear compensated magnets can host linearly or elliptically polarized magnons, often degenerate in energy, with spin angular momentum that can be encoded in the sublattice pseudospin structure. This duality introduces opportunities for pseudospin-dependent transport and information processing at THz frequencies, along with challenges in detection and control.

Moreover, recent work has revealed that altermagnetic materials, despite their zero net magnetization, can exhibit symmetry-protected non-degenerate magnon branches due to their lower magnetic space group symmetries. This leads to spin-polarized magnon bands even in the absence of net moment, enabling anisotropic spin transport and magnon-mediated spin-orbit torques [42, 186].

Magnons as information carriers

These collective excitations of the spin lattice carry spin angular momentum without accompanying charge motion, making them ideal candidates for low-dissipation spintronic devices. Unlike electronic spin currents, magnonic currents are not limited by Joule heating, and their transport properties are governed by exchange interactions, magnetic anisotropy, and thermal fluctuations rather than impurity scattering or carrier mobility [105, 107].

For ideal easy-axis collinear AFMs, the two magnon branches are degenerate and linearly dispersing near the Brillouin zone center, carrying opposite spin angular momentum $\pm\hbar$. However, in materials with broken inversion or certain non-symmorphic symmetries (such as AMs), the degeneracy of the magnon branches can be lifted. This results in non-degenerate magnon modes with distinct polarization and group velocity, enabling a net spin current even in a fully compensated magnetic lattice [95, 186].

The spin current density carried by magnons can be expressed as:

$$\mathbf{J}_s = \sum_{\mathbf{k},\lambda} \hbar \sigma_\lambda \mathbf{v}_{\mathbf{k},\lambda} n_{\mathbf{k},\lambda}, \tag{2.14}$$

where λ indexes the magnon branches, σ_λ is the spin angular momentum per magnon mode (typically ± 1), $\mathbf{v}_{\mathbf{k},\lambda}$ is the group velocity, and $n_{\mathbf{k},\lambda}$ is the Bose–Einstein magnon occupation number. The direction and magnitude of $\mathbf{J}_s$ depend on the population imbalance between modes of opposite spin, which can be driven by thermal gradients (SSE), spin pumping, or interfacial torques. The magnitude of the imbalance determines the transport regime, which can be classified as either linear or non-linear.

Linear Transport (Diffusive Magnon Flow)

In the linear response regime, spin transport in insulating compensated magnets is dominated by the diffusive flow of thermally excited magnons. These magnons, polarized through interfacial processes such as spin pumping or thermal gradients (i.e., the SSE), propagate over characteristic distances determined by scattering processes and intrinsic relaxation mechanisms. This transport is governed by the magnon chemical potential μ_m, a thermodynamic parameter introduced to describe the non-equilibrium population of magnons [106, 187] (Fig. **2.11a**).

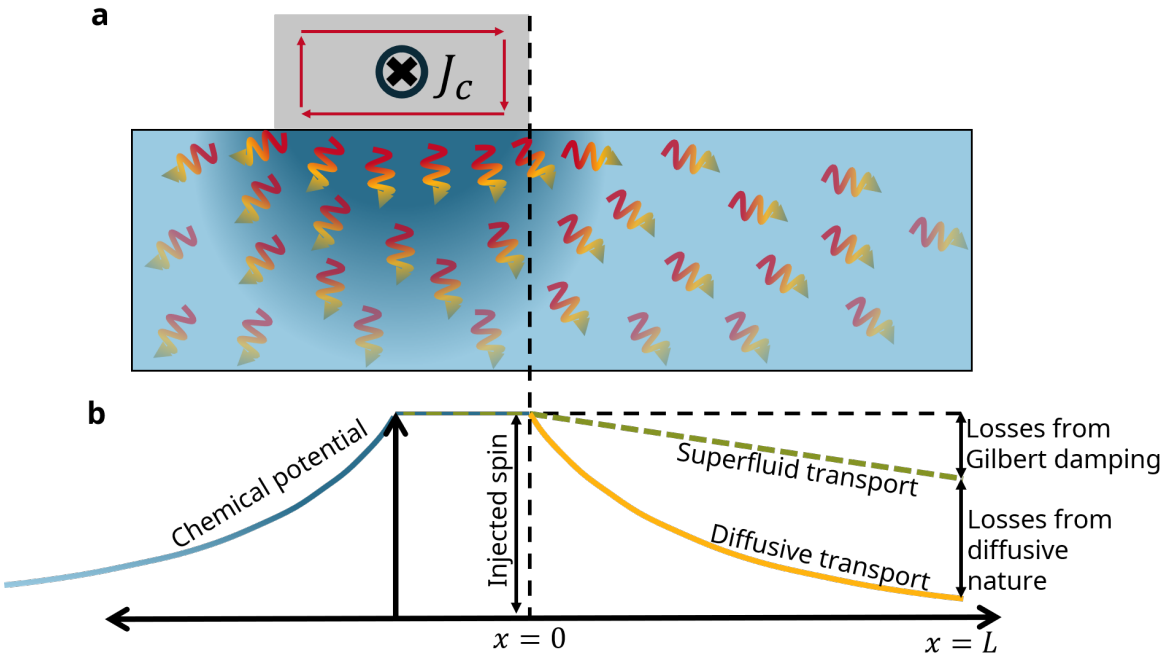

Figure 2.11.: **Injector-driven magnon generation and spatial decay.** **a** A heavy–metal injector (Pt) carries a charge current J_c along the strip. The SHE creates a spin accumulation at the interface that injects magnons into the magnetic insulator. Blue shading encodes the magnon chemical potential $\mu_m(x, y)$, maximal beneath the injector and decaying away in plane, while wavy traces depict propagating magnons. **b** One-dimensional profiles versus distance x of the injector. To the right, a comparison of a diffusive regime with exponential attenuation, $\mu_m(x) = \mu_0 e^{-x/\ell_m}$ with diffusion length ℓ_m, and a superfluid, nearly linear attenuation representative of drift or quasiballistic transport limited mainly by Gilbert damping. To the left, the chemical potential decays from the wire toward equilibrium within the source region.

The diffusion of magnons can be modeled analogously to particle diffusion, using a spin diffusion equation that takes the form [106]

$$\frac{\partial \mu_m}{\partial t} = D_m \nabla^2 \mu_m - \frac{\mu_m}{\tau_m}, \tag{2.15}$$

where D_m is the magnon diffusion constant, and τ_m is the magnon relaxation time. In a steady state, this yields an exponential decay of the magnon chemical potential away from the point source (Blue shading in Fig. **2.11**):

$$\mu_m(x) \propto \exp\left(-\frac{x}{\lambda_m}\right), \tag{2.16}$$

with $\lambda_m = \sqrt{D_m \tau_m}$ defining the magnon spin diffusion length. The spin current carried by diffusive magnons is then given by:

$$\mathbf{J}_s = -\sigma_m \nabla \mu_m, \tag{2.17}$$

where σ_m is the magnon spin conductivity (Fig. **2.11b**). In linear response, the relaxation time τ_m includes a Gilbert-controlled channel arising from the finite linewidths of the thermally occupied magnon modes:

$$\tau_m^{-1}(T) \;=\; \tau_\alpha^{-1}(T) \;+\; \tau_{\mathrm{mp}}^{-1}(T) \;+\; \tau_{\mathrm{mi}}^{-1} \;+\; \tau_{\mathrm{mm}}^{-1}(T), \qquad \tau_\alpha^{-1}(T) \simeq \left\langle \alpha\, \omega_{\mathbf{k}} \right\rangle_T, \tag{2.18}$$

where $\tau_{\mathrm{mp}}, \tau_{\mathrm{mi}}, \tau_{\mathrm{mm}}$ denote magnon–phonon, magnon–impurity and magnon–magnon channels, respectively [105, 107]. Interfacial spin pumping (sp) enhances dissipation:

$$\alpha_{eff} = \alpha_0 + \alpha_{sp}, \qquad \alpha_{sp} = \frac{\gamma \hbar\, g_r}{4\pi\, s\, t}, \tag{2.19}$$

which renormalizes τ_α and thereby the spin diffusion length $\lambda_m = \sqrt{D_m \tau_m}$ [119, 187]. In collinear AFMs, the same expressions hold with $g_r \to g_r^{\mathrm{AF}}$ and the mode frequencies $\omega_{\mathbf{k}}$ taken for the two AFM branches [107, 117].

This model has proven essential in interpreting non-local magnon transport experiments, where a spin current injected at one Pt contact diffuses through an insulating magnet and is detected at a separate contact via the ISHE [47, 48, 97, 106].

Magnon polarization in AFMs

In antiferromagnetic (AFM) insulators, the spin polarization of magnons is governed by the symmetry and topology of the magnetic lattice, that determines the direction of the Néel vector. Unlike in FMs, where spin waves typically exhibit circular polarization with a single handedness corresponding to the net magnetization, AFMs host two counter-rotating magnon modes due to the presence of two (or more) antiparallel sublattices (Fig. **2.12a**). These modes, often referred to as acoustic and optical branches, are typically degenerate in energy in collinear AFMs with inversion symmetry and no net magnetization, each carrying opposite spin angular momentum $\pm\hbar$ [107, 188].

The magnon polarization in AFMs can be classified based on their symmetry properties and the corresponding eigenstates of the spin Hamiltonian. In the long-wavelength limit, the two magnon branches correspond to circular polarized spin precession in opposite directions on each sublattice. This leads to zero net spin angular momentum for the system as a whole, but allows for spin transport when an imbalance between the modes is induced by external stimuli such as interfacial spin injection [189], an external magnetic field (Fig. **2.12a**), or thermal gradients [187].

Furthermore, the character of magnon polarization strongly depends on the material's magnetic anisotropy. In easy-axis AFMs, magnons are typically circular polarized, particulary at the relevant small $\mathbf{k}$ values, with the two modes being degenerate at zero external magnetic field [48, 190]. At the same time, in easy-plane systems, they may exhibit elliptical or linear polarization depending on $\mathbf{k}$ and the details of exchange and anisotropy interactions [107]. Importantly, these polarization properties determine the interaction of magnons with external fields and with spin currents from adjacent metals.

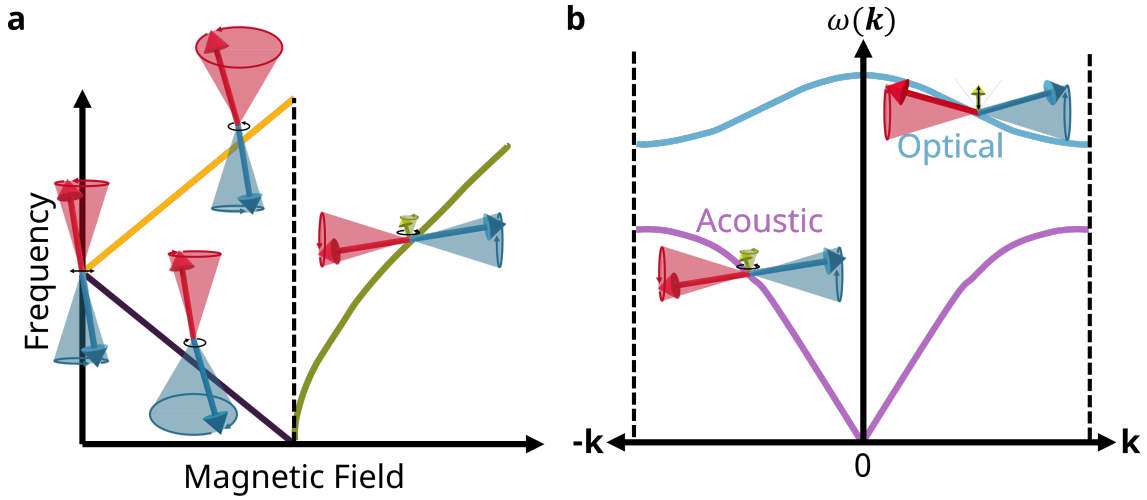

Figure 2.12.: **Field–induced chirality and dispersion of AFM magnons. a** Magnon resonance frequency versus magnetic field H applied along the easy axis. At $H = 0$ the eigenmodes are *circular* polarized but the two branches are spin degenerate (no net magnon angular momentum) A finite field lifts this degeneracy and the modes split into counter–rotating states, σ^+ (CR) and σ^- (CL); one hardens while the other softens as H increases. At the spin–flop field H_{SF} (vertical dashed line) the soft branch approaches zero frequency and the ground state reorients to an easy–plane configuration; beyond H_{SF} an EP mode is stabilized with a small canted magnetization (green). **b** Magnon dispersion $\omega(k)$ highlighting the acoustic (purple) and optical (blue).

In recent years, the notion of magnon polarization has been extended to include the concept of "pseudospin", a formalism that treats the two degenerate magnon modes as a spin-1/2 system in a pseudospin space. This perspective has been employed to describe magnonic phenomena such as spin Nernst effects and the generation of pure spin currents in AFMs [191]. In altermagnetic systems, where symmetry breaking lifts the degeneracy of magnon modes across specific directions in momentum space, this polarization asymmetry enables net spin transport despite zero net magnetization [95, 186]. In general, the polarization of magnons in AFMs determines the nature of spin transfer, damping, and detection at interfaces, and underpins the design of magnon-based logic devices and spin current diodes.

Easy-Axis vs. Easy-Plane Magnon Modes

In compensated collinear magnets, the magnetic anisotropy plays a crucial role in determining the symmetry, energy spectrum, and polarization of magnon modes. Two distinct cases commonly arise: easy-axis and easy-plane AFMs. These two categories exhibit fundamentally different spin dynamics and magnon transport, which are relevant to both theoretical modeling and spintronic applications [107, 117].

Easy-Axis AFMs (Ising-like) In easy-axis AFMs, the magnetic sublattices align antiparallel along a preferred crystallographic axis (e.g., the z-axis), stabilized by uniaxial

anisotropy. The linearized spin-wave analysis of such systems yields magnon modes that are typically circular polarized and degenerate in energy (the left-most mode in Fig. **2.12a**). The two sublattices precess out of phase with equal amplitude, resulting in zero net dynamic magnetization [117].

The magnon dispersion for easy-axis AFMs, derived using the Holstein-Primakoff transformation or sigma-model approaches, takes the form:

$$\hbar\omega_k = \sqrt{(\Delta + Ak^2)^2 - (Bk^2)^2}, \tag{2.20}$$

where Δ is the anisotropy gap, A is the spin exchange interaction, and B is a coupling coefficient related to inter-sublattice exchange. These magnons are typically high-frequency (THz range) and short-wavelength excitations, offering prospects for ultrafast spin manipulation; however, their spin transport is often symmetric and short-ranged, without external fields or asymmetry-inducing mechanisms [192].

Easy-Plane AFMs (XY-like) In contrast, easy-plane anisotropy systems, the magnons are linearly polarized, although the polarization is also often **k**-dependent. Here, the IP rotational symmetry gives rise to a gapless Goldstone mode associated with the spontaneous breaking of U(1) symmetry. This results in a low-energy, long-wavelength acoustic magnon mode with linear polarization (Lower branch in Fig. **2.12b**) [189].

The Goldstone mode allows for coherent and long-range spin transport, even at low temperatures. In certain symmetry-broken conditions, these systems can host spin superfluidity—macroscopic phase-coherent transport of spin angular momentum without dissipation—driven by phase gradients of the Néel vector [183].

The presence or absence of a gap in the magnon spectrum, as well as the polarization type, critically influences mode coupling with spin currents at interfaces. For instance, easy-plane AFMs are more susceptible to spin pumping and spin-orbit torques because the transverse components of the magnetization are dynamically active and interact with adjacent metals more efficiently [188].

Understanding the distinction between easy-axis and easy-plane is also essential for characterizing the spin dynamics in AMs. In materials such as $YFeO_3$ and $LuFeO_3$, the weak ferromagnetic canting due to DMI coexists with easy-axis behavior. At the same time, symmetry constraints in AMs allow splitting of otherwise degenerate magnon branches, even in the absence of net magnetization [88, 97].

Magnon-Mediated Spin Transfer

Magnon-mediated spin transfer at the interface between a heavy metal (typically Pt) and an insulating compensated magnet represents a central mechanism for spin injection and detection in spintronic devices (Fig. **2.13**). This mechanism relies on the interconversion between electronic spin currents and magnonic excitations at the interface, a process governed by exchange interactions and the interfacial spin mixing conductance [175, 182].

At the microscopic level, a spin current polarized perpendicular to the magnetic order parameter, when it arrives at the interface, can stimulate the creation or annihilation of magnons in the magnetic insulator. In AFMs and AMs, due to the compensated nature of the spin lattice, this process involves exciting specific combinations of sublattice

precessions in combination with thermal excitations, that match the symmetry and polarization of the incident spin current [117,189]. The transfer of angular momentum across the interface occurs without net charge transport and is the fundamental base of SMR.

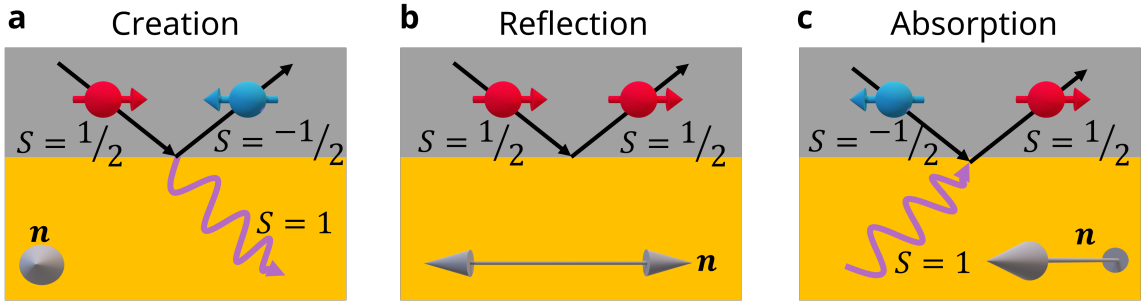

Figure 2.13.: **Interfacial magnon mediated spin transfer at a Pt/compensated–insulator interface.** **a** *Creation:* a transverse electronic spin current in Pt with electron spin $S = \frac{1}{2}$ arrives at the interface, flips its spin, and transfers angular momentum to the lattice, creating a magnon of spin $S = 1$ in the insulator. **b** *Reflection:* for spin accumulation parallel to the Néel vector $\mathbf{n}$, the interfacial torque vanishes, electrons are reflected, and no magnon is emitted. **c** *Absorption:* an incoming magnon with $S = 1$ is absorbed at the interface, flipping the interfacial electron spin and injecting spin back into the metal. These processes are governed by the antiferromagnetic spin mixing conductance $g_{\uparrow\downarrow}^{\mathrm{AF}}$ and obey symmetry selection rules set by $\mathbf{n}$, maximizing transfer for spin polarization transverse to $\mathbf{n}$.

In the linear regime, the magnon–mediated interfacial spin current pumped into an adjacent standard metal has the same structure as in FMs upon the replacement $\mathbf{m} \mapsto \mathbf{n}$, with an antiferromagnetic spin–mixing conductance $g_{\uparrow\downarrow}^{\mathrm{AF}} = g_r^{\mathrm{AF}} + \mathrm{i}\, g_i^{\mathrm{AF}}$ [117,119]:

$$\mathbf{J}_s = \frac{\hbar}{4\pi} g_r^{\mathrm{AF}} \left(\mathbf{n} \times \frac{d\mathbf{n}}{dt} \right) + \frac{\hbar}{4\pi} g_i^{\mathrm{AF}} \frac{d\mathbf{n}}{dt}. \tag{2.21}$$

The first term is the damping–like spin–pumping contribution set by $\mathrm{Re}\, g_{\uparrow\downarrow}^{\mathrm{AF}}$, while the second is the reactive, field–like component governed by $\mathrm{Im}\, g_{\uparrow\downarrow}^{\mathrm{AF}}$. A key theoretical result is that, for a compensated interface, the two sublattices add rather than cancel in $g_{\uparrow\downarrow}^{\mathrm{AF}}$, yielding magnitudes comparable to FMs, with symmetry selection rules that suppress pumping for $\boldsymbol{\mu}_s \parallel \mathbf{n}$ (Fig. **2.13b**) and maximize it for transverse spin accumulation (Fig. **2.13a**) [117].

The interfacial selection rule in Fig. **2.13** highlights a *torque* maximum for transverse spin accumulation, i.e., absorption $\propto \mathbf{n} \times (\boldsymbol{\mu}_s \times \mathbf{n})$ is largest for $\boldsymbol{\mu}_s \perp \mathbf{n}$. However, that perturbation drives a small precession of the Néel vector or local damping, but this angular momentum is dissipated locally as heating, not transmitted as a magnon flow. Decomposing the interfacial spin accumulation as $\boldsymbol{\mu}_s = \mu_\parallel \mathbf{n} + \boldsymbol{\mu}_\perp$, the $\perp$ component produces local damping–like absorption (no long–range spin flow), whereas the $\parallel$ component establishes a magnon chemical potential (Fig. **2.11**) $\mu_m \propto \mu_\parallel$ that diffuses

into the AF, yielding

$$\mathbf{j}_s^{\mathrm{AF}} = -\,\sigma_m\,\boldsymbol{\nabla}\mu_m,$$

with σ_m the magnon spin conductivity [106,117,118]. In easy–axis AFMs the low–energy eigenmagnons carry spin $\pm\hbar$ *along* $\mathbf{n}$; thus a finite $\mu_{\parallel}$ injects an imbalance between the two branches (net spin current collinear with $\mathbf{n}$), while $\boldsymbol{\mu}_{\perp}$ excites a symmetric (zero–spin) combination that is absorbed locally at the injector. Consistently, non–local experiments find an "on" state for $\boldsymbol{\mu}_s \parallel \mathbf{n}$ and an "off" state for $\boldsymbol{\mu}_s \perp \mathbf{n}$ [48, 97].

At finite temperatures, the occupation of magnon modes follows Bose-Einstein statistics. Thermally activated magnons significantly influence both the spin injection efficiency and the spin decay length within the insulator [106,118]. The interfacial coupling becomes temperature-dependent through the magnon spectral density $N(\omega, T)$, which modifies both the spin current amplitude and the angular response.

Finite-Temperature Considerations in AFMs Temperature has a profound effect on spin transport in insulating compensated magnets. Thermal magnons dominate the spin current at room temperature in most practical systems, where the magnon population follows the Bose-Einstein distribution. The number of thermally excited magnons increases with temperature, enhancing the amplitude of spin currents generated via the SSE or detected via ISHE [106].

However, temperature also introduces increased magnon-magnon and magnon-phonon scattering, leading to enhanced damping and reduced magnon propagation length. In AFMs, thermal fluctuations can destabilize the Néel order near the Néel temperature T_N, reducing spin coherence and spin pumping efficiency [107, 118], efficiently decreasing the magnitude of the SMR effects.

In the low-temperature regime, where magnon populations are suppressed, coherent magnon transport and quantum effects such as magnon condensation or interference may become dominant. The efficiency of magnon–mediated spin transfer exhibits a pronounced temperature dependence because the interfacial spin current is carried by thermally populated magnons. In a kinetic picture, the available magnon population scales with the Bose factor,

$$n_m(T) \;\propto\; \int \mathrm{d}\omega\, \mathcal{D}(\omega)\, n_{\mathrm{B}}(\hbar\omega, T),$$

so that in gapped AFMs one finds an activated behavior $n_m(T) \sim e^{-\hbar\omega_{\mathrm{AFMR}}/k_{\mathrm{B}}T}$, which suppresses interfacial spin transfer as T is lowered. Within the diffusive model, the interfacial spin conductance into the magnet and the bulk magnon spin conductivity scale as

$$G_{\mathrm{s}}(T) \propto \int \mathrm{d}\omega\, \mathcal{D}(\omega) \left(-\frac{\partial n_{\mathrm{B}}}{\partial \omega}\right), \qquad \sigma_m(T) \propto n_m(T)\, D_m(T),$$

so even if the magnon diffusivity D_m and the diffusion length $\lambda_m = \sqrt{D_m \tau_m}$ increase upon cooling, the strong reduction of n_m dominates and the net spin current decreases with temperature. Practically, this yields smaller SMR and SSE amplitudes at low T in compensated insulators, especially when $\hbar\omega_{\mathrm{AFMR}}$ is sizable, while near room temperature the larger thermal population enhances interfacial spin transfer and non-local magnon signals [106, 107, 117, 118, 177].

Moreover, the magnon-mediated spin transfer is sensitive to the magnetic domain configuration and the applied magnetic field. Multi-domain effects can introduce averaging over different magnon polarizations and dispersions, reducing the net spin signal or introducing phase shifts in the angular dependence of the SSE and SMR responses [48, 97].

Field Dependence and Multi-Domain Effects In compensated magnets such as orthoferrites and hematite, the spin transport response is highly sensitive to the magnetic domain structure and applied external fields. At low fields, multiple magnetic domains can coexist with different Néel vector orientations, leading to spatial averaging of the magnon signal and reduction of the net spin current detected in non-local measurements [47, 48]. This effect is particularly significant near spin-flop transitions or Morin transitions, where abrupt reorientation of the Néel vector occurs.

The application of external magnetic fields enables partial or complete alignment of domains, thereby enhancing the spin signal and revealing the anisotropic nature of magnon transport. Field-induced reorientation also modifies the magnon spectrum, activating specific magnon branches and potentially suppressing symmetry-protected degeneracies (Fig. **2.12a**). The field dependence thus serves as a diagnostic tool for disentangling different transport regimes and for probing domain-wall contributions to magnon scattering.

2.2.3. Other Considerations

Beyond the standard mechanisms of magnon-mediated spin transport in insulating compensated magnets, several additional physical phenomena can critically influence spin dynamics, coherence, and spin-transfer efficiency. These include subtle effects arising from spin–orbit coupling, microscopic exchange anisotropies, topological features in magnon bands, and interfacial symmetry breaking. Of particular relevance are the DMI, intrinsic spin splitting in AMs, and effects such as magnon coherence and condensation. These factors do not just perturb the magnon dispersion or modify relaxation rates: they fundamentally alter the nature of the spin excitations, their polarization, and their coupling to electronic reservoirs. Understanding these contributions is essential for designing next-generation spintronic devices that exploit the full symmetry and dynamical complexity of compensated magnetic insulators.

Dzyaloshinskii–Moriya Interaction Effects

The DMI is a relativistic correction to the exchange interaction that arises in magnetic systems lacking inversion symmetry at the atomic or interfacial level. It takes the form:

$$\mathcal{H}_{\mathrm{DMI}} = \sum_{\langle i,j \rangle} \mathbf{D}_{ij} \cdot (\mathbf{S}_i \times \mathbf{S}_j), \tag{2.22}$$

where $\mathbf{D}_{ij}$ is the DMI vector determined by the symmetry of the lattice, and $\mathbf{S}_i$ and $\mathbf{S}_j$ are neighboring spin vectors. This interaction favors a non-collinear spin arrangement, leading to canting in otherwise collinear AFMs and compensated magnets [119, 192].

In insulating collinear magnets, particularly those with weak inversion symmetry breaking, such as orthoferrites ($YFeO_3$) and hematite (Fe_2O_3), the DMI induces a

small canting angle between sublattice magnetizations. This weak ferromagnetism opens new spin wave channels and allows for spin pumping and SMR even in zero external field [48, 97].

The presence of DMI introduces chirality into the magnon modes. It lifts the degeneracy between clockwise and counterclockwise spin wave precessions, resulting in non-reciprocal magnon propagation, where magnons with wavevector $+\mathbf{k}$ and $-\mathbf{k}$ possess different energies [193]. This can be formally expressed as:

$$\omega(\mathbf{k}) \neq \omega(-\mathbf{k}), \tag{2.23}$$

which leads to spatially asymmetric magnon transport, a phenomenon increasingly exploited in nonreciprocal magnonic devices and in directional spin-current routing.

From a symmetry perspective, DMI is allowed in systems where the inversion symmetry is broken either globally (non-centrosymmetric crystals) or locally (e.g., at interfaces or due to distortions). In AFMs, the form and strength of DMI depend on the magnetic space group and the orientation of the magnetic sublattices. In altermagnetic systems, DMI can coexist with altermagnetism, potentially enhancing the anisotropic magnon propagation and giving rise to hybrid symmetry-protected and chiral excitations [95].

2.3. Summary

This chapter presented a model for spin transport in insulating, compensated magnets and integrated it with the symmetry principles of altermagnetism. We began with the mechanisms for spin injection and detection at metal|insulator interfaces, covering electrical routes via the SHE and ISHE, thermal routes via the SSE, and dynamic routes via spin pumping. Throughout, the complex spin mixing conductance governed the reciprocity between pumped and backflow spin currents, setting the interfacial selection rules for damping-like and field-like channels. We formulated magnons as the relevant spin carriers in collinear compensated systems, establishing the diffusive, linear regime in terms of a magnon chemical potential and its continuity equation, then extending to coherent and nonlinear regimes where mode competition, interaction-driven linewidths, and threshold phenomena emerge. The role of magnetic anisotropy, DMI, and Gilbert damping was made explicit in both the Néel vector dynamics and the kinetic descriptions, providing direct links to non-local geometries, frequency-dependent spin pumping, and temperature-dependent decay lengths. A central contribution was the explicit incorporation of altermagnetic symmetry into transport. In AMs, sublattice-dependent hopping combined with compensated order produces a non-relativistic, momentum-dependent spin splitting with d- or g-wave form factors, nodal manifolds fixed by the magnetic space group, and chirality-resolved magnon branches, all in the absence of net magnetization. These symmetry constraints select preferred axes for spin injection and diffusion, control polarization conversion at interfaces, and generate robust anisotropies in spin decay that persist in wide gap insulators such as $LuFeO_3$ and $YFeO_3$. We connected these principles to recent predictions and observations across electronic and magnonic sectors, including chiral altermagnons, large anisotropies of magnon lifetimes, and efficient spin caloritronic responses in AMs, as well as to materials discovery in two-dimensional platforms. Taken together, the chapter establishes

how magnetic space group symmetry, interfacial spin conversion, and magnon kinetics combine to determine spin transport in compensated magnets, and how the altermagnetic class embeds these elements into a single, symmetry-anchored picture that is directly testable in orthoferrites and related compounds.

3. Methods

This chapter details the integrated experimental methods used to quantify spin transport in insulating compensated magnets, focusing on $YFeO_3$, $LuFeO_3$, and α-Fe_2O_3. We describe the sample growth, their structural and magnetic verification, and micro/nanofabrication of Pt-based bilayer devices for local and non-local measurements [97, 174, 194, 195]. Transport protocols employ first/second-harmonic detection and current-reversal symmetrization to separate electrically driven from thermally driven magnon populations, while crystallographic alignment enables symmetry-resolved tests of altermagnetism. Synchrotron microscopy techniques provide element-specific imaging of domains and 180° walls that cross-check transport-derived order parameters [196]. Computational details are detailed in Appendix E. Together, these methods establish a reproducible set of methods from materials growth to quantitative inference of interfacial spin transfer, magnon diffusion, and altermagnetic symmetry fingerprints.

3.1. Experimental Techniques

The realization of spin transport experiments in insulating compensated magnets requires a rigorous combination of high-quality material synthesis, structural and magnetic characterization, and precise micro- and nanofabrication methods. In particular, the orthoferrites $YFeO_3$ and $LuFeO_3$, together with doped hematite (α-Fe_2O_3), form the material basis of this thesis. These compounds were prepared either as bulk single crystals or epitaxial thin films, depending on the requirements of the transport experiments. Structural quality and stoichiometry were assessed through X-ray diffraction (XRD), while static magnetic properties were characterized using Superconducting quantum interference device (SQUID) magnetometry. Device fabrication was carried out using electron-beam lithography (EBL) and thin-film deposition of metallic electrodes to define both local and non-local transport geometries. The measurement strategies were tailored to probe spin Hall magnetoresistance (SMR), anomalous Hall effect (AHE), and magnon-mediated non-local spin transport. Furthermore, synchrotron-based photoemission electron microscopy (PEEM) was employed to directly visualize the domain structure of altermagnets, particularly the 180° domain walls in hematite. The following subsections provide detailed descriptions of the synthesis routes, fabrication protocols, and characterization techniques that underpin this work.

3.1.1. Sample Preparation: Material Synthesis and Characterization

The preparation of high-quality samples is a prerequisite for reliable investigations of spin transport in compensated magnetic insulators. Thin films of hematite were grown by pulsed laser deposition (PLD), following optimized protocols to achieve epitaxial strain control, smooth surfaces, and stoichiometric composition [41, 195, 197].

Bulk single crystals of $LuFeO_3$ and $YFeO_3$ were grown using the optical floating-zone technique, enabling large, high-purity crystals with well-defined crystallographic orientations [97, 115]. For the fabrication of electrical devices, thin metallic layers, such as Pt or Cr/Au, were deposited via magnetron sputtering to define ohmic contacts [198]. Structural, magnetic, and morphological characterization of the resulting samples was performed using XRD, SQUID magnetometry, and IPorce microscopy , ensuring the necessary crystalline quality and domain stability required for subsequent spin transport experiments. An experimental run-table (Table **D.1**) with the set-up and parameters specification, as well as internal eLabFTW numbers can be found in Appendix D.

Growth of the Samples

The samples studied in this thesis fall into two principal categories: (i) epitaxial thin films of α-Fe_2O_3 grown by PLD, and (ii) single crystals of $LuFeO_3$ and $YFeO_3$ grown via the optical floating-zone method. Metallic top contacts (e.g., Pt, Au) were deposited by sputtering for the fabrication of electrical devices. In this section, contributions performed by third parties are explicitly outlined. The optimization of α-Fe_2O_3 was performed by E. Baek under the author's supervision. The growth of α-Fe_2O_3 on sapphire substrates was performed by E. Baek and A. Akashdepp at JGU-Mainz, and the group of Prof. Avner Rothschild at the Technion-Israel Institute of Technology, in Haifa, Israel. Bulk single crystals of $LuFeO_3$ and $YFeO_3$ were prepared at the International Center for Quantum and Molecular Structures in the group of Prof. Shixun Cao. Optimization of growth and final high-quality crystal growth was performed by W. Yang and X. Ma under the supervision of Prof. Cao. Calibration of deposition rates and the sputtering process was performed at JGU Mainz by D. M. Tran and M. A. Syskaki under the supervision of Prof. Gerhard Jakob. In Table **D.2** a list of the samples, with internal eLabFTW numbers, fabricator, internal name and associated measurements can be found in Appendix D.

Pulsed Laser Deposition: Epitaxial thin films of α-Fe_2O_3 (doped and undoped) were synthesized by PLD, yielding atomically smooth films with mosaic spreads below 1° and root-mean-square roughness of only a few Å [197].

In pulsed–laser deposition, nanosecond ultraviolet pulses (typically KrF, $\lambda = 248$ nm) are focused onto a rotating ceramic target at a fluence above the ablation threshold. Each pulse deposits its energy within the optical absorption depth, driving an explosive, near-congruent ejection of atoms, ions, small clusters, and electrons that form a forward–directed plasma plume [199–202]. The plume expands toward the heated substrate ($T_{sub} \sim$ 700–800°C here); at low background pressure its species travel quasi–ballistically with kinetic energies of a few–tens of eV, whereas at mTorr oxygen the mean free path shortens and a shock front develops that thermalizes part of the plume [199, 203]. The reactive background (oxygen) also replenishes anion content and promotes the correct oxidation state on the surface, which is crucial for complex oxides like α-Fe_2O_3 and $LuFeO_3$ [200–203]. On arrival, energetic species nucleate at terraces/steps; subsequent surface diffusion and incorporation determine the growth mode (layer–by–layer vs. step flow vs. island), which is tuned by the laser fluence/repetition rate, substrate temperature, oxygen pressure, and target–substrate distance [203]. In

situ reflection high-energy electron diffraction (RHEED) provides a real–time metric of the growth mode: specular–spot intensity oscillations track monolayer completion (period $\propto$ one unit–cell layer), enabling calibration of the deposition rate used here before growing thicker films [200–203]. Advantages of PLD for complex oxides include good transfer of cation stoichiometry from a multicomponent target and high instantaneous growth rates; practical considerations such as particulate suppression are addressed by target rotation/translation, off–axis geometries, and operating fluences below the splashing threshold [199–202]. Growth windows were optimized to control oxygen stoichiometry. The deposition rates were calibrated by X-ray reflectometry in thinner samples (5-10 nm), and then extrapolated until reaching the desired thickness of 150 nm for α-Fe_2O_3.

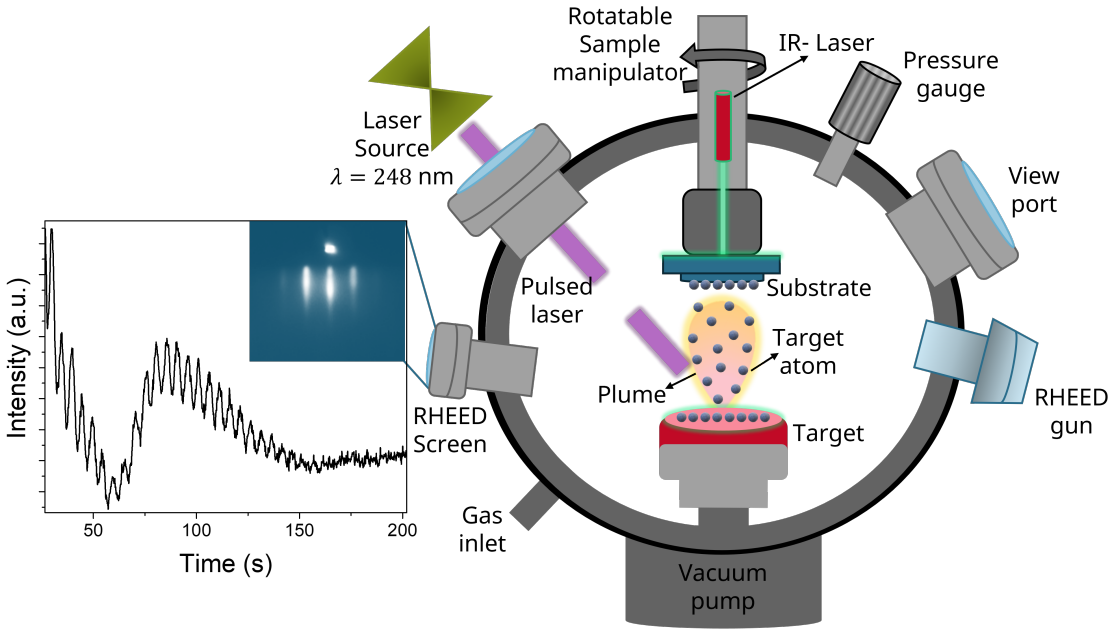

Figure 3.1.: Pulsed-laser-deposition schematic and in-situ RHEED. Schematic of the ultra high vacuum PLD chamber used to synthesize epitaxial α-Fe_2O_3 and $LuFeO_3$ thin films: a KrF excimer laser (red beam) ablates a rotating ceramic target, producing an oxide plume in a controlled oxygen background; the heated substrate faces the plume on a rotating/tilting stage. A RHEED gun and phosphorous screen are aligned at grazing incidence for real-time monitoring. *Inset:* representative RHEED pattern from hematite showing streaks indicative of 2D epitaxy, and RHEED intensity oscillations used to track layer-by-layer growth and to calibrate deposition rates.

Optical Floating-Zone Single Crystals: Bulk single crystals of $LuFeO_3$ and $YFeO_3$ were prepared using the optical floating-zone method [97,115]. Stoichiometric polycrystalline feed rods were synthesized by conventional solid-state reaction, and growth was carried out in a four-mirror floating-zone furnace under controlled oxygen atmosphere. In the optical floating–zone (OFZ) method, infrared/visible radiation from high–power lamps is collected by four opposing elliptical mirrors and focused onto the neck between a dense polycrystalline *feed* rod and a *seed* rod, creating a small crucible–free molten

zone held by surface tension [204, 205]. As the seed and feed are counter–rotated (typically a few rpm) and translated downward at a prescribed rate, fresh material from the feed continuously melts while the lower side of the zone solidifies epitaxially on the seed, thus pulling a single crystal. Zone stability, and ultimately crystalline quality, is controlled by (i) lamp power (zone temperature), (ii) growth rate ($\mathrm{mm\,h^{-1}}$), (iii) counter–rotation speeds (mixing), (iv) gas composition and pressure (oxygen activity for oxides), and (v) the thermal gradient across the zone [206]. The crucible–free configuration minimizes contamination, enables high melting temperatures, and allows for precise control of oxygen stoichiometry by operating in flowing O_2/air or under elevated p_{O_2} when required [204].

Growth rates of 2–5 mm/h were combined with counter-rotation of seed and feed rods to homogenize the melt. The method yielded centimeter-scale, twin-free single crystals with well-defined crystallographic orientations , which were subsequently cut and polished for transport and magnetometry experiments.

Sputtering of Metallic Contacts: For electrical devices, metallic electrodes were deposited onto the oxide films or polished bulk crystals by direct current (DC) magnetron sputtering (Fig. **3.2**).

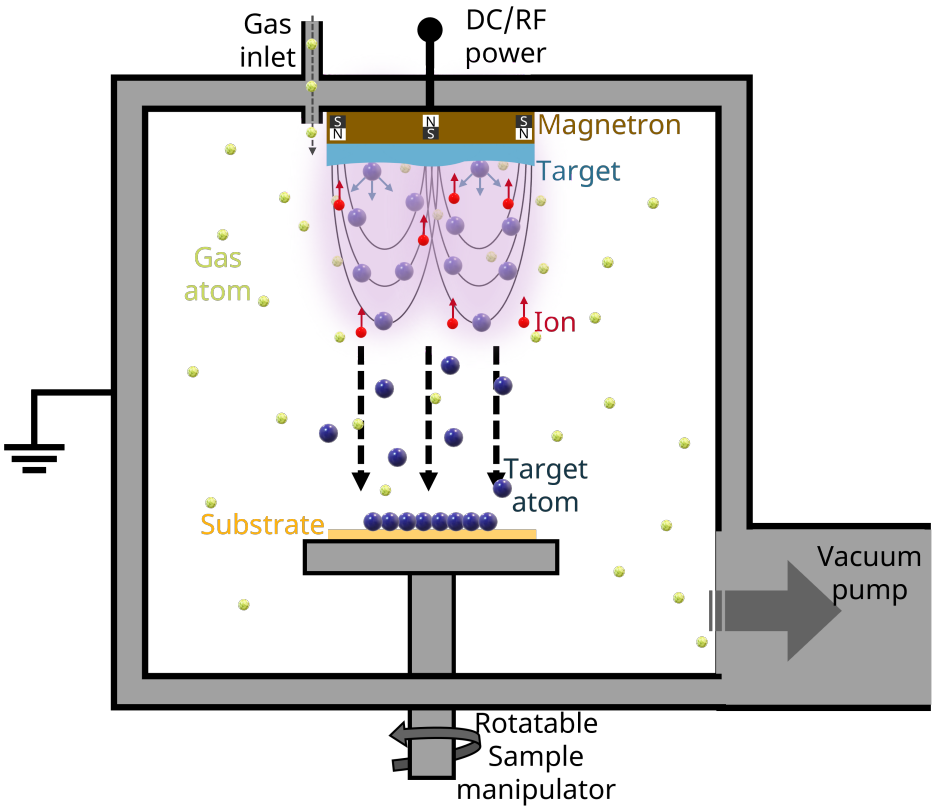

Figure 3.2.: DC magnetron sputtering of metallic contacts. Schematic of a magnetron source in Ar (green balls) showing electron confinement by the magnetron field, ion bombardment of the target (red balls), and the flux of sputtered neutrals (blue balls) that condense on a rotating substrate.

A low–pressure Ar discharge is ignited between a negatively biased metal target

(cathode) and the grounded chamber/substrate. Electrons emitted from the target are trapped by the electromagnetic field of the magnetron (permanent magnets behind the target), increasing their path length and ionization probability and thereby sustaining a dense plasma adjacent to the target [207, 208]. Ar^+ ions accelerated across the cathode sheath sputter surface atoms from the target; these neutrals traverse the gas and condense on the substrate to form a film. Deposition kinetics (rate, adatom energy and momentum flux, microstructure) are set primarily by process pressure and power, target–substrate distance, and substrate temperature/rotation [209]. Prior to metallization, a brief Ar plasma (30 s) cleaning removes weakly bound surface species. For spin–orbit devices, Pt thicknesses $t_{\mathrm{Pt}} \sim 5$–8 nm maximize interfacial spin transparency while retaining sizable spin Hall response [210, 211]. Platinum films of 7 nm thickness were used for the devices, while Cr/Au bilayers (5 nm Cr / 50 nm Au) were used for bonding pads and low-resistance current leads. The deposition was performed in high-vacuum chambers with base pressures below 10^{-6} Torr, and the rates were calibrated by X-ray reflectometry.

Basic Characterization Techniques

The crystalline quality, magnetic ordering, and surface morphology of the thin films and single crystals were verified by a combination of structural, magnetic, and surface-sensitive techniques. These measurements ensured that the samples possessed the necessary epitaxial quality, compensated magnetic nature, domain stability, and stoichiometry for spin transport studies.

XRD: XRD was employed to confirm phase purity, epitaxial growth, and strain state in both thin films and bulk crystals. The measurements were performed using a four-circle Bruker D8 Discover thin-film diffractometer (Fig. **3.3**).

XRD probes periodic order through elastic scattering of monochromatic X-rays with wavevectors $\mathbf{k}_{\mathrm{i}}$ and $\mathbf{k}_{\mathrm{f}}$. The scattering vector $\mathbf{q} = \mathbf{k}_{\mathrm{f}} - \mathbf{k}_{\mathrm{i}}$ selects reciprocal-lattice vectors $\mathbf{G}_{hkl}$; constructive interference occurs when the Laue condition $\mathbf{q} = \mathbf{G}_{hkl}$ is met [212, 213]. In the common Bragg formulation, peak positions satisfy

$$2d_{hkl} \sin\theta = n\lambda, \tag{3.1}$$

with magnitude $|\mathbf{q}| = 4\pi \sin\theta/\lambda$. For symmetric θ–2θ scans on OOP (00ℓ) reflections, the lattice spacing $d_{00\ell}$ yields the perpendicular lattice parameter and strain, via

$$\varepsilon_{\perp} = \frac{d_{00\ell} - d_{00\ell}^{\mathrm{bulk}}}{d_{00\ell}^{\mathrm{bulk}}}. \tag{3.2}$$

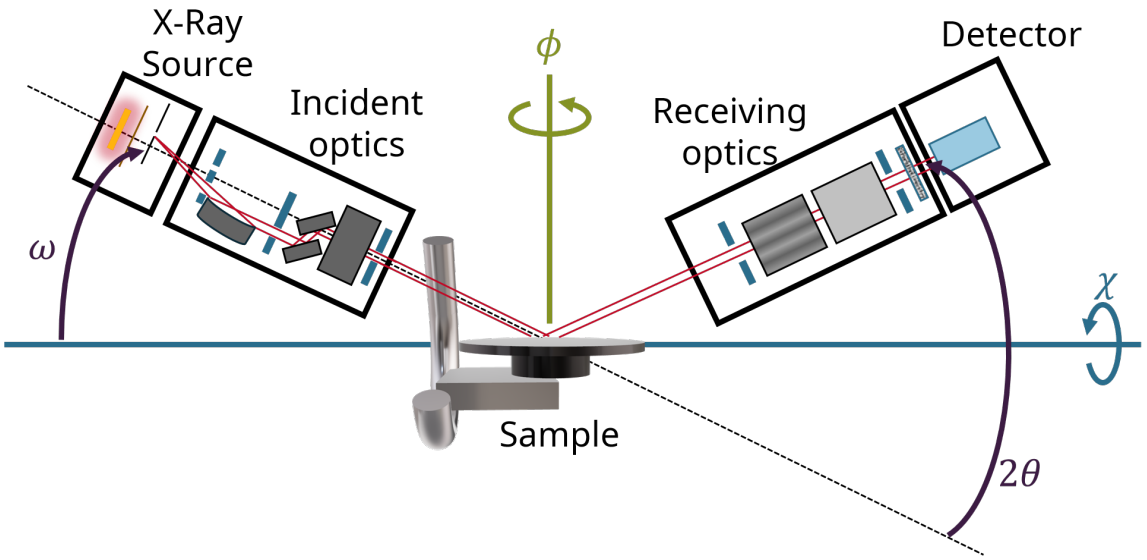

Figure 3.3.: Four-circle X-ray diffractometer geometry (Bruker D8 Discover). Schematic of the diffractometer showing the incident and diffracted beams and the four goniometer axes: incident angle ω, detector angle 2θ, azimuthal rotation ϕ, and sample tilt χ. Symmetric θ–2θ scans (with $\omega = \theta$) were used to determine out-of-plane lattice parameters (phase purity/epitaxy), rocking curves (ω-scans at fixed 2θ) quantified crystalline mosaicity, and ϕ-scans at fixed θ–2θ and χ established IP epitaxial relationships. Off-specular reflections are accessed by a nonzero χ. The figure illustrates the definitions of ω, 2θ, ϕ, and χ used throughout the text.

Rocking curves (ω-scans at fixed 2θ) measure the distribution of crystalline tilt/mosaicity through the peak width. Azimuthal ϕ-scans of asymmetric reflections at fixed θ–2θ and χ resolve IP epitaxial relationships and twin variants. ϕ-scans at a fixed θ-2θ and χ on off-specular peaks allowed us to identify the orientations of the IP directions. Fig. **3.3** shows the geometry of the four-circle diffractometer and the corresponding ω, 2θ, ϕ and χ angles.

In the case of hematite, sharp diffraction peaks and narrow rocking curves confirmed the high structural quality of films grown on sapphire substrates [197].

SQUID Magnetometry: Magnetic characterization was performed using SQUID magnetometry from Quantum Design, covering the temperature range from 2 to 360 K and magnetic fields up to 7 Tesla. The technique was primarily used for the quantitative measurement of the canted moment on the samples, as well as for detecting possible temperature transitions (Morin temperature in hematite). Hematite films exhibite a Morin transition at temperatures consistent with literature values (260 K for bulk, 200 K for 100 nm thin films), approaching the 0 K value with a reduction in thickness and increasing its value with Ti doping. The Morin transition of the films was observed and characterized by a decrease in the magnetic moment to effectively zero above the background substrate contributions. As a volumetric technique, the measurements were always normalized to the volume of the sample after background subtraction and expressed in emu/f.u. In Table **3.1**, practical conversions between magnetic moment and

magnetization units are presented. Converting from emu/f.u. to volume magnetization requires the number density of formula units, $n_{\text{f.u.}}$, which can be computed either from mass density and molar mass, or from crystallographic data, with the number of formula units per unit cell (Z) and the volume of the unit cell (V_{cell}).

Table 3.1.: **Conversions among CGS and SI units for magnetic *moment* and *magnetization*.** Here, ρ is the density in g/cm^3, $n_{\text{f.u.}}$ the number density, and Z the number of formula units per unit cell. In SI, H is in A/m and $B = \mu_0(H + M)$ (with $\mu_0 = 4\pi \times 10^{-7}$ H/m). The CGS relation 1 Oe $= 10^3/(4\pi)$ A/m ≈ 79.5775 A/m may be useful when converting H.

Quantity	Relation
Magnetic moment (m)	$m\,[\text{emu}] = 10^3\, m\,[\text{A m}^2]$
Magnetization (M)	$M\,[\text{emu/cm}^3] = 10^{-3}\, M\,[\text{A/m}]$
From emu/f.u. to emu/cm^3	$M\,[\text{emu/cm}^3] = m\,[\text{emu/f.u.}] \times n_{\text{f.u.}}\,[\text{f.u./cm}^3]$
$n_{\text{f.u.}}$ via ρ, M_{mol}	$n_{\text{f.u.}} = \dfrac{\rho}{M_{\text{mol}}} N_{\text{A}}$
$n_{\text{f.u.}}$ via Z	$n_{\text{f.u.}} = \dfrac{Z}{V_{\text{cell}}}$
From emu/f.u. to A/m	$M\,[\text{A/m}] = 10^3\, m\,[\text{emu/f.u.}] \times n_{\text{f.u.}}$

Note: 1 Bohr magneton: 1 $\mu_{\text{B}} = 9.274\,010\,0783 \times 10^{-24}\ A\,\text{m}^2 = 9.274\,010\,0783 \times 10^{-21}$ emu.

Atomic Force Microscopy: To ensure reliable spin-transport readout, the sputtered top electrodes (Pt) must form a continuous, pinhole-free layer on the oxide surface. In the early stages of metal growth on oxides, island nucleation and geometrical shadowing can leave voids and pinholes, especially when the surface topography is comparable to the film thickness, so continuity is only reached after depositing a sufficiently thick layer [214]. A practical way to ensure continuous metallization is therefore to verify that the electrode thickness comfortably exceeds the characteristic surface-roughness scale; in this work, we required the Pt thickness to be at least one order of magnitude larger than the RMS roughness measured by atomic force microscopy. This criterion places our electrodes well above reported continuity thresholds for sputtered Pt films, which can be as low as 0.4-1.0 nm depending on deposition conditions [215]. Surface morphology was assessed using tapping-mode atomic force microscopy [216], which yielded root-mean-square (RMS) roughness values of 1–3 Å for the optimized thin films. Such low roughness is consistent with step-flow growth on atomically flat sapphire substrates and is critical for ensuring reproducible interfacial quality in spin-transport devices [197]. The single crystals were commercially polished to <3 Å RMS roughness and orientation (crystallographic) accuracy $< 1°$, as the initial cut and polishing had 3-8° offset and 50–60 Å RMS roughness. Fig. **3.4** shows the different atomic force microscopy micrographs before and after re-polishing.

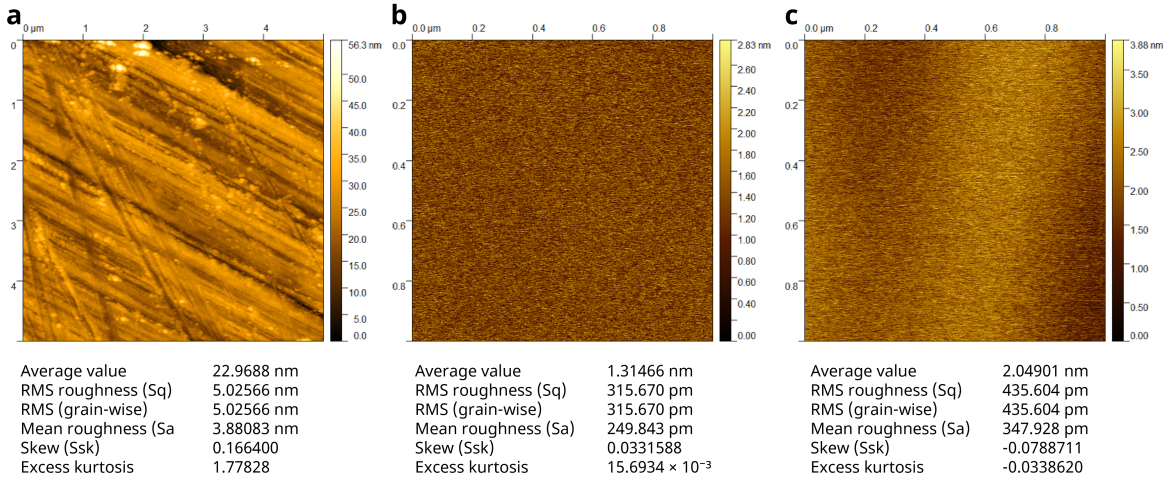

Figure 3.4.: Atomic force microscopy micrographs and root-mean-square (RMS) roughness values. Tapping mode atomic force microscopy for **(a)** $YFeO_3$ single crystal hand polished, **(b)** commercially polished and **(c)** α-Fe_2O_3 100 nm (0001) hematite thin film on Al_2O_3(0001) substrate.

3.1.2. Device fabrication: patterning, electrode deposition.

Device micro- and nanofabrication followed a standardized process flow optimized for insulating oxides (Fig. **3.5**): (i) definition of metal features by EBL on resist-coated (PMMA A4/AR-N 7520.17) samples, (ii) electrode formation by thin-film deposition and lift-off, and (iii) argon ion milling for mesa isolation or edge cleaning prior to metallization. The overall goal was to realize low-resistance, stable interfaces for local SMR devices and low-noise injector–detector structures for non-local magnon transport, while preserving the magnetic order and surface quality of the underlying oxides [97, 174, 194, 210].

Lithography and pattern transfer. Before lithography, samples were cleaned in an ISO 5 (ISO 14644-1) or class 100 (FED-STD-209E) cleanroom (no more than 100 particles bigger than 0.5 µm per cubic foot or 3,520 particles/m^3). The cleaning procedure consisted of two consecutive ultrasonic baths in acetone and isopropanol, each for one minute. Then, samples were coated with PMMA A4 and baked at 85°C for 180 seconds. Patterning was performed on an EBL from Pioneer at 20 kV and an exposure current of 160-250 µC/cm^2. To suppress charging during exposure, a transient conductive overlayer (polymeric e-spacer) was applied and removed prior to development. Positive-tone resist (PMMA A4) enabled high-fidelity transfer of sub-micron features suitable for Hall bars, non-local three-wire geometries, and bonding pads. Development in methyl isobutyl ketone:isopropanol (1:3) yielded reproducible undercut profiles for lift-off. For a better undercut, bilayer resists can be used to ensure clean lift-off with well-defined edges. Negative-tone (AR-N7520.17) resist was used with an AR300-47 developer for structures requiring dielectric or oxide etch definition (e.g., isolation trenches or alignment fiducials). A subsequent low-energy Ar^+ ion milling was used with conservative ion energies and duty cycles to minimize surface amorphization. Alignment marks defined in an initial lithography level enabled multi-level registration

for subsequent steps.

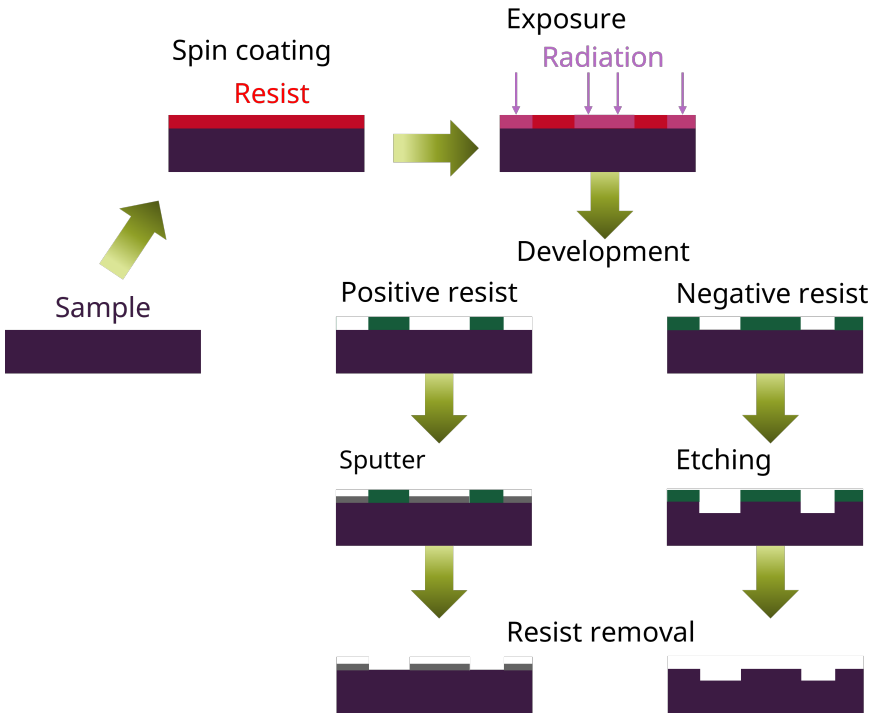

Figure 3.5.: **Lithography workflow.** Generic sequence for pattern transfer starting from a clean sample: spin coat and soft-bake a resist layer, expose to spatially confined radiation, and develop. **Left branch (positive resist, lift-off)**: development opens windows down to the substrate; a metal film is deposited conformally; lift-off removes the resist and overlying metal, leaving metal only in the exposed regions (used for Pt and Cr/Au contacts). **Right branch (negative resist, etch transfer)**: development leaves a resist stencil; the underlying film is subsequently removed in the open regions by ion milling or wet etch; resist stripping completes the subtractive transfer (used for mesas or isolation).

Electrode deposition and interfaces. Heavy-metal electrodes (Pt) were deposited by magnetron sputtering onto freshly developed resist patterns. Typical Pt thicknesses were in the range relevant for SMR and efficient spin injection/detection (7 nm), balancing electrical resistivity, spin diffusion length, and signal-to-noise [194, 210]. For robust wire-bonding and low contact resistance, we employe Cr/Au and Ti/Au bilayers for large-area pads, using as adhesion layer Cr or Ti, (5 nm) beneath the Au (50 nm). No significant difference was found between Cr and Ti in the measurements. Base pressures were kept in the 10^{-7}–10^{-6} Torr range with calibrated deposition rates (thickness obtained by X-ray reflectometry [217]). Always, a brief in situ Ar^{+} soft pre-clean (30 seconds) removed adventitious adsorbates immediately before metal deposition, thereby enhancing spin transparency without measurably roughening the oxide.

Lift-off and post-processing. Metals were patterned by lift-off in a heated solvent (acetone) with gentle manual agitation, without the use of ultrasonics. To prevent redeposition and maintain line-edge integrity in closely spaced injector–detector pairs,

we used soak–rinse cycles and filtered solvents. No high-temperature post-anneals were applied after metallization to avoid oxygen off-stoichiometry or interdiffusion at the oxide/metal interface. Electrical continuity and contact resistance were verified on test structures prior to low-noise measurements. The resulting device set included: (i) local Hall bars for SMR, (ii) non-local injector–detector geometries (three-wire layouts, Fig. **3.6**) with variable wire-to-wire spacing for extracting magnon transport lengths, and (iii) without any metal deposited, etched Hall bars for transport experiments in conductive hematite.

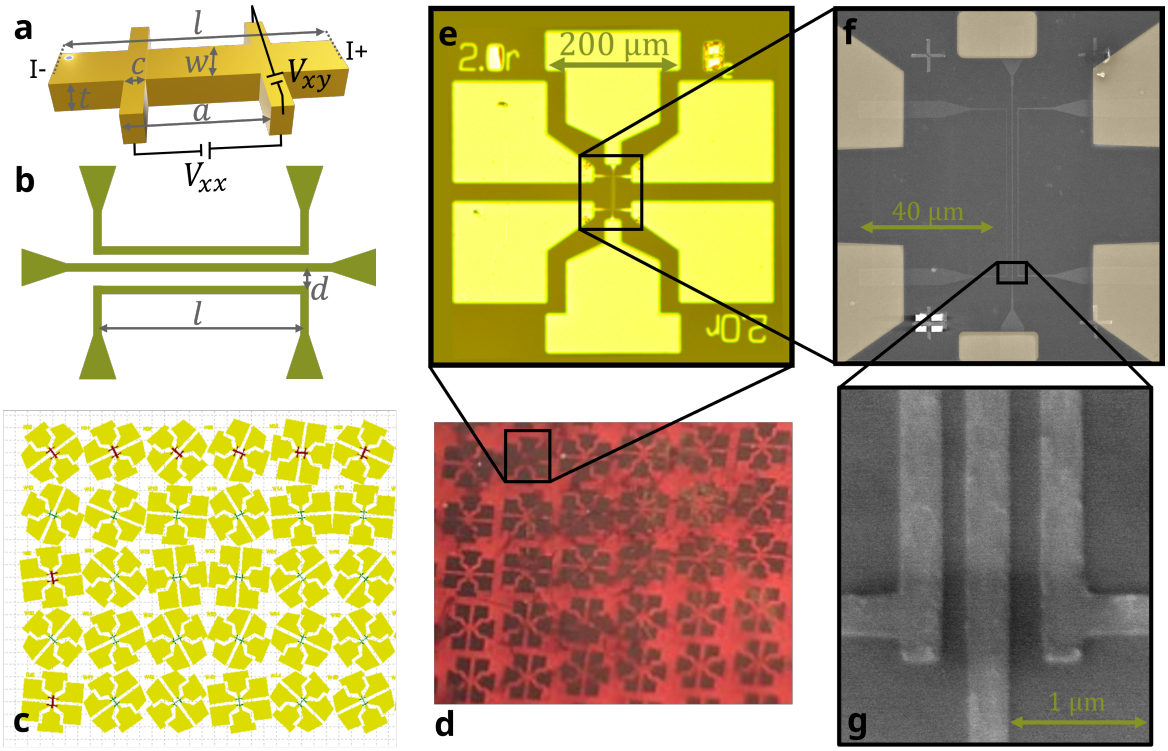

Figure 3.6.: Device designs, chip layout, and fabricated structures. (**a**) Schematic of a local Hall bar (used for SMR/AHE) indicating channel thickness t, width w, and cross width c. (**b**) Schematic of a non-local magnon-transport device of length l and separation distance d with injector and detector strips connected to tapered pads. (**c**) Photomask layout of the multi-device chip. (**d**) Optical micrograph of the patterned sample showing the device array after lithography/lift-off. (**e**) Optical micrograph of a single selected device with bonding pads. (**f**) Micrograph of a completed non-local device highlighting the active region. (**g**) Close-up of the injector–detector gap showing the wire separation.

Non-local and local transport device architectures. Local devices are patterned as Hall bars for SMR, with Pt channels of thickness (t) 7 nm, width (w) 200-250 nm, and length (l) 50-80 µm, oriented along different crystallographic axes. Non-local architectures employ three-wire layouts atop the magnetic insulator, and wire-to-wire

separation d between 400-1000 nm, facilitating reliable extraction of the magnon diffusion length λ_m [48, 174]. To suppress parasitic capacitive coupling and thermoelectric cross-talk, leads are routed symmetrically with ground shielding where possible, and current-reversal protocols are implemented during measurement. Crystallographic alignment is established via substrate edges and XRD fiducials and transferred to the lithography coordinate frame using high-contrast alignment marks; injector/detector axes are then placed at defined angles (ϕ) with respect to the easy axes.

3.2. Measurement Techniques

This thesis focuses on electrical transport measurements of spin transport in insulating and slightly conducting compensated magnets, using (i) hopping transport AHE, (ii) *local* bilayer measurements (SMR), and (iii) *non-local* magnon-mediated transport geometries on single-crystal and epitaxial orthoferrites and hematite. Across all measurements, we employ low-noise current sources, a nanovoltmeter, and rotatable stages, combined with a cryogenic variable-temperature insert (VTI) inside a superconducting magnet (Figure **3.7**).

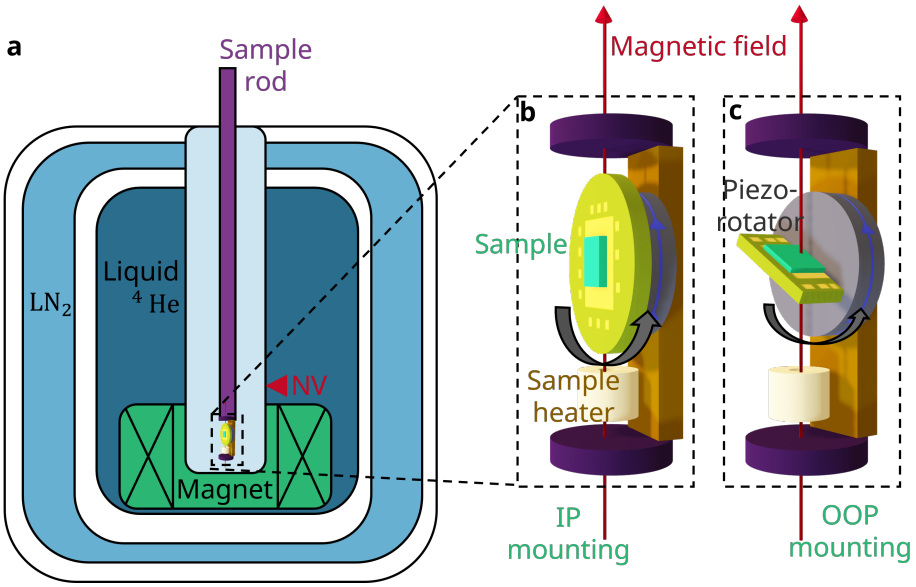

Figure 3.7.: Cryostat and sample mounting for angle-dependent transport measurements. **(a)** Schematic of the cryogenic insert and superconducting magnet: a VTI is immersed in a liquid-^{4}He bath (with an outer liquid-N_2 shield), and the sample is introduced on a sample rod into the magnet bore. The temperature of the VTI is controlled by a closed-loop heater and a needle valve (NV), and is monitored with a Cernox sensor. **(b)** IP and **(c)** OOP mounting configuration, where the device plane is oriented with respect to the applied magnetic field and the sample temperature is controlled by a local heater and another Cernox sensor closer to the sample.

All this to acquire temperature, field, and angle-dependent datasets that enable quantitative extraction of spin-transport lengths, interfacial spin conductance, and

altermagnetism-specific symmetry signatures. The base electrical noise level of the cryostat was pre-characterized as a function of frequency, resistance, and temperature using surface-mounted resistors in the sample holder, as shown in Appendix C [218–230].

3.2.1. Anomalous Hall effect

The AHE was probed on Hall-bar devices patterned on conducting α-Fe_2O_3 (1% Ti-doped). The device geometry follows a six–contact Hall bar with transverse voltage probes placed symmetrically about the current channel; the out-of–plane (OOP) field direction was determined by a pre-measurement angle scan to suppress in–plane planar Hall contributions [41]. Measurements were performed using low–noise current excitation and voltage reading with a nanovoltmeter; odd/even-in-current components were separated by current–reversal averaging. The first–harmonic (1ω) transverse response contains the ordinary Hall term and the symmetry–allowed anomalous Hall term, which was separated into symmetric and antisymmetric with respect to the external magnetic field. Due to the high electrical resistance of the devices, a DC current source, a nanovolmeter (transverse voltage), and a potentiometer (longitudinal voltage) were used.

Resistivity derivation. With the current I along $\hat{\mathbf{x}}$ and the OOP field B_z, the transverse voltage V_{xy} is measured between opposing side contacts. Longitudinal resistivity is obtained from the longitudinal voltage V_{xx} while the Hall resistivity is obtained from the transverse V_{xy}:

$$\rho_{xx}(B,\varphi) \;=\; \frac{t\cdot w}{a\cdot I}\,V_{xx}(B,\varphi), \tag{3.3}$$

$$\rho_{xy}(B,\varphi) \;=\; \frac{t}{I}\,V_{xy}(B,\varphi), \tag{3.4}$$

where t is the magnetic layer thickness, φ is the in–plane angle between the current direction and a crystallographic reference axis, and $w = 10$ µm and $a = 50$ µm are our design-specific distances (Fig. **3.6a**) [41].

First/second harmonic and current–symmetry protocols. Using DC current reversal, we define

$$V_{xy}^{\mathrm{odd}}(B,\varphi) = \frac{V_{xy}(+I) - V_{xy}(-I)}{2}, \qquad V_{xy}^{\mathrm{even}}(B,\varphi) = \frac{V_{xy}(+I) + V_{xy}(-I)}{2}, \tag{3.5}$$

which is (neglecting terms of order I^3) equivalent to the harmonic measurements:

$$V_{xy}^{1\omega}(B,\varphi) \;=\; I_0\,R_{xy}(B,\varphi), \qquad V_{xy}^{2\omega}(B,\varphi) \;\propto\; I_0^2\,\mathcal{S}(B,\varphi), \tag{3.6}$$

where R_{xy} captures the resistive Hall terms (ordinary and anomalous), while $\mathcal{S}$ represents thermoelectric sources driven by I^2 heating (Table **3.2**) [179]. Experimentally, V_{xy}^{even} (or $V_{xy}^{2\omega}$) was at least an order of magnitude smaller than the odd (first–harmonic) component under our conditions (I <3 µA) [41].

Table 3.2.: **Hall-effect measurement voltages contributions.** Combinations of readings taken with opposite current I and magnetic field B eliminate all spurious terms except the true Hall (V_H) and Ettingshausen (V_E) voltages [231]. Signs indicate the parity of each contribution under I and/or B reversal. *Legend:* V_M: misalignment (odd in I, even in B); V_S: thermoelectric (even in I, B); V_E: Ettingshausen (odd in I and B); V_N: Nernst (even in I, odd in B); V_R: Righi–Leduc (even in I, odd in B); V_O: voltmeter offset (independent of I, B). The final combination cancels all but V_H and V_E.

Voltage	I	B	V_H	V_M	V_S	V_E	V_N	V_R	V_O
V_1	+	+	+	+	+	+	+	+	+
V_2	−	+	−	−	+	−	+	+	+
$(V_1 - V_2)$			$2V_H$	$-2V_M$	0	$2V_E$	0	0	0
V_3	+	−	−	+	+	−	−	−	+
V_4	−	−	+	−	+	+	−	−	+
$(-V_3 + V_4)$			$2V_H$	$2V_M$	0	$2V_E$	0	0	0
$(V_1 - V_2 - V_3 + V_4)$			$4V_H$	0	0	$4V_E$	0	0	0

Symmetry analysis tailored to altermagnets. For collinear AMs, the AHC transforms as a pseudovector constrained by the magnetic point group. In α-Fe_2O_3 (space group $R\bar{3}c$), the basal–plane three–fold symmetry enforces a leading threefold angular anisotropy of the anomalous Hall resistivity when the Néel vector lies in plane [24, 41]. We therefore parameterize the transverse response measured in the first harmonic as

$$\rho_{xy}^{1\omega}(B,\varphi) \;=\; R_0\, B_z \;+\; \rho_{xy}^{\mathrm{AM}}(\varphi) \;+\; \rho_{xy}^{\mathrm{PHE}}(\varphi), \tag{3.7}$$

with ordinary Hall coefficient R_0, an altermagnetic anomalous Hall term

$$\rho_{xy}^{\mathrm{AM}}(\varphi) \;\approx\; K_3 \sin\big[3(\varphi - \varphi_0)\big] \;+\; K_1 \sin(\varphi - \varphi_1), \tag{3.8}$$

and a planar Hall background captured by

$$\rho_{xy}^{\mathrm{PHE}}(\varphi) \;=\; \Delta\rho_{\mathrm{PHE}} \sin 2(\varphi - \varphi_{\mathrm{PHE}}), \tag{3.9}$$

where $\varphi_0, \varphi_1, \varphi_{\mathrm{PHE}}$ are phase offsets set by crystallography and probe placement. The 3φ harmonic reflects the threefold crystal symmetry of hematite and the altermagnetic order parameter's transformation properties; the 1φ term accounts for weak-ferromagnetic canting above the Morin transition and any residual misalignment [24, 41]. In metallic altermagnets like RuO_2 or Mn_5Si_3, analogous symmetry–locked AHE anisotropies have been reported, supporting the altermagnetic origin of the Hall response [22, 29]. The transverse conductivity σ_{xy} is calculated as:

$$\sigma_{xy} = \frac{\rho_{xy}}{\rho_{xx}^2 + \rho_{xy}^2} \tag{3.10}$$

To extract the Hall-like signal from other contributions (planar Hall, anisotropic magneto resistance, contact misalignment, etc), the transverse contribution (in our local

coordinate system) is symmetrized/antisymmetrized (Fig. **3.8**) with respect to the external magnetic field using the equation (equivalent for resistivity as well):

$$\sigma_{xy}^{A} = \frac{\sigma_{xy}(H) - \sigma_{xy}(-H)}{2}. \tag{3.11}$$

$$\sigma_{xy}^{S} = \frac{\sigma_{xy}(H) + \sigma_{xy}(-H)}{2}. \tag{3.12}$$

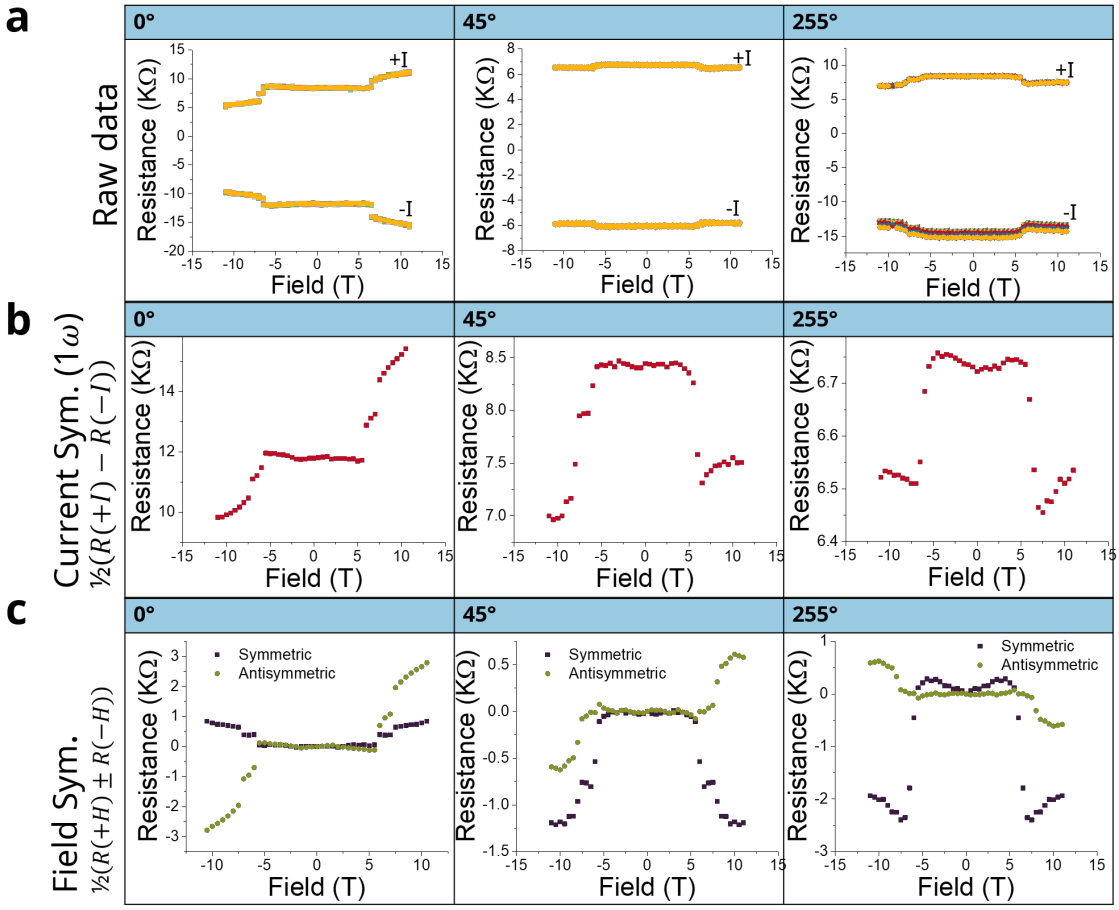

Figure 3.8.: **Transverse resistance as a function of the magnetic field in different parts of the field symmetrization process.** **(a)** Raw data (20 cycles), **(b)** Hall-like (1ω), **(c)** and symmetric (minus the average zero field offset) and antisymmetric part of the resistance for the Hall bars with 0°, 45°, and 255° with respect to the crystallographic axis **a**. Reproduced from Galíndez et al. [41], licensed under CC BY 4.0.

Unlike conventional ferromagnets—where the AHC is effectively a single pseudovector governed by the magnetization direction and thus primarily sensed as an out-of-plane (OOP) response—collinear altermagnets permit symmetry-allowed *in–plane* components of the AHC that depend on the Néel vector orientation and the crystal

axes [22,24]. Consequently, rotating the Hall bar (equivalently, rotating the current direction relative to the crystallographic frame while maintaining the same field protocol) projects different tensor components of the AHC into the measured transverse voltage. In hematite, the threefold basal-plane symmetry enforces a leading 3φ harmonic of the AHE when the Néel vector lies in plane; by choosing Hall bars at distinct angles φ with respect to a crystallographic reference, one can resolve the symmetry-locked $\sin(3\varphi)$ (and phase-shifted) components already in the first harmonic, while separating the planar Hall background $\propto \sin 2\varphi$ [41]. More generally, because the anomalous Hall *current* need not be strictly orthogonal to the charge current in crystals of low symmetry, Hall bars at multiple orientation angles provide complementary projections of the underlying AHC tensor and help disambiguate OOP from in–plane contributions [232]. Practically, we implement angle series with several lithographically defined Hall bars rotated by fixed increments and fit the odd-in-current (or 1ω) transverse resistivity to the sum of altermagnetic 3φ harmonics and a $\sin 2\varphi$ planar term.

In our measurement scheme, a current density $\mathbf{J} = (J_x, J_y, 0)$ confined to the x-y plane can be expressed as:

$$\mathbf{J} = J_A(\cos\phi, \sin\phi, 0), \tag{3.13}$$

where J_A is the current amplitude and ϕ is the angle between the direction of the current and the crystallographic a axis, which is aligned with the x axis. The electric field $\mathbf{E}$ produced by this current, considering the conductivity tensor σ_{ij}, is given by:

$$\mathbf{J} = \sigma_{ij}\mathbf{E}. \tag{3.14}$$

In our altermagnetic system, the non-diagonal conductivity components depend strongly on the orientation of the Néel vector [21]. While an external OOP magnetic field would yield a constant contribution related to the canted magnetic moment, the non-zero components σ_{xz} and σ_{yz} introduce a ϕ-dependent transverse electric field $\mathbf{E}$, even with constant OOP magnetization. Writing explicitly the tensor equations (with Hall symmetry ($\sigma_{xy} = -\sigma_{yx}$), we have:

$$\begin{aligned} \sigma_{xx}\,E_x \;+\; \sigma_{xy}\,E_y \;+\; \sigma_{xz}\,E_z \;&=\; J_A\cos\phi, \\ -\sigma_{xy}\,E_x \;+\; \sigma_{yy}\,E_y \;+\; \sigma_{yz}\,E_z \;&=\; J_A\sin\phi, \\ -\sigma_{xz}\,E_x \;-\; \sigma_{yz}\,E_y \;+\; \sigma_{zz}\,E_z \;&=\; 0. \end{aligned} \tag{3.15}$$

Assuming for simplicity J_A =1 A/m^2, and an isotropic longitudinal conductivity ($\sigma_{xx} = \sigma_{yy} = \sigma_{zz}$), the perpendicular electrical field, defined as $E_\perp = -E_x \cdot \sin(\phi) + E_y \cdot \cos(\phi)$, takes the form:

$$E_\perp = \frac{\sigma_{xx}\sigma_{xy} \;-\; \sigma_{xz}\sigma_{yz}\cos(2\phi) \;+\; (\sigma_{xz}^2 - \sigma_{yz}^2)\cos\phi\,\sin\phi}{\sigma_{xx}\big(\sigma_{xx}^2 + \sigma_{xy}^2 + \sigma_{xz}^2 + \sigma_{yz}^2\big)} \tag{3.16}$$

Similarly, the longitudinal component, defined as $E_\parallel = E_x \cdot \cos(\phi) + E_y \cdot \sin(\phi)$, is:

$$E_\parallel = \frac{(\sigma_{xx}^2 + \sigma_{yz}^2)\cos^2\phi \;-\; 2\,\sigma_{xz}\sigma_{yz}\cos\phi\,\sin\phi \;+\; (\sigma_{xx}^2 + \sigma_{xz}^2)\sin^2\phi}{\sigma_{xx}\big(\sigma_{xx}^2 + \sigma_{xy}^2 + \sigma_{xz}^2 + \sigma_{yz}^2\big)} \tag{3.17}$$

The resulting electric field inherits its angular dependence from the Néel-vector-sensitive conductivity tensor components σ_{ij} (which depends on the Energy $E - E_\mathrm{F}$,

in the σ_{ij} calculations). The exact form of this angular dependence is dictated by the relative magnitudes of the tensor components σ_{ij}, which themselves depend on the electronic structure and Fermi level positioning in the conduction bands. Our measured Hall voltage is then a convolution of the AHC, which depends on the Néel vector orientation with respect to the crystallographic axis, a contribution from the AHE due to the canted moment, and the Hall bar symmetry.

3.2.2. Local spin Hall magnetoresistance

SMR measurements were performed on heavy–metal(Pt)/insulating–magnet bilayers. A charge current $I \parallel \hat{\mathbf{x}}$ in Pt generates, via the SHE, a transverse spin accumulation $\boldsymbol{\mu}_{\mathrm{s}} \parallel \hat{\mathbf{y}}$ at the interface. The interfacial spin transfer depends on the projection of the magnetic order (magnetization $\mathbf{m}$ or Néel vector $\mathbf{n}$) onto $\boldsymbol{\mu}_{\mathrm{s}}$, which modulates the Pt resistivity and leads to a characteristic angular magnetoresistance [143, 194, 210]. In collinear antiferromagnets and altermagnets, the replacement $\mathbf{m} \to \mathbf{n}$ captures the symmetry of the interfacial spin mixing and yields the same leading $\cos 2\alpha/\sin 2\alpha$ harmonics when the field forces $\mathbf{n}$ to track the rotation plane.

Device geometry and angular protocols. Hall–bar structures (Pt thickness chosen comparable to or below the Pt spin–diffusion length) were patterned atop polished single crystals or epitaxial films. We define the in–plane rotation angle α between the current direction $\hat{\mathbf{x}}$, and ϕ the angle between the current direction and the crystallographic reference axis. Rotations were performed in three standard planes: (i) IP (in the film plane), (ii) j–N plane, and (iii) t–N plane, where $\hat{\mathbf{t}} \parallel \hat{\mathbf{y}}$ is the transverse in–plane axis and N (here) denotes the film normal [143, 210]. The longitudinal and transverse responses then follow the canonical SMR form:

$$\rho_{xx}(\alpha) = \rho_0 + \Delta\rho_1 \left[1 - (\hat{\mathbf{n}}\cdot\hat{\mathbf{t}})^2\right], \tag{3.18}$$

$$\rho_{xy}(\alpha) = \Delta\rho_2 \, (\hat{\mathbf{n}}\cdot\hat{\mathbf{j}})(\hat{\mathbf{n}}\cdot\hat{\mathbf{t}}), \tag{3.19}$$

which reduce to $\rho_{xx} = \rho_0 + \Delta\rho_1 \cos 2\alpha$ and $\rho_{xy} = \frac{1}{2}\Delta\rho_2 \sin 2\alpha$ for an in–plane rotation with $\mathbf{n}$ rigidly following the field. The amplitudes $\Delta\rho_{1,2}$ encode the interfacial (real) spin–mixing conductance $g_r^{\uparrow\downarrow}$, Pt spin Hall angle θ_{SH}, spin–diffusion length λ_{Pt}, and thickness t_{Pt} [143]. The samples were mounted on a piezo-rotating stage (ANR51 from Attocube) within a variable-temperature insert installed in a superconducting magnet capable of fields up to 12 T (Oxford Instruments) and a temperature range of 2-350 K.

First/second–harmonic and current–reversal readout. SMR is odd in neither current nor field; the *magnetoresistive* signal appears at the first harmonic (1ω) in lock–in detection. Thermoelectric backgrounds scale with I^2 and are isolated in the second harmonic (2ω). Equivalently, in DC measurements, we separate even/odd–in–current voltages via current reversal:

$$V_{xx}^{1\omega} \equiv V_{xx}^{\mathrm{odd}} = \frac{V_{xx}(+I) - V_{xx}(-I)}{2} \approx I\, R_{xx}(\alpha), \tag{3.20}$$

$$V_{xx}^{2\omega} \equiv V_{xx}^{\mathrm{even}} = \frac{V_{xx}(+I) + V_{xx}(-I)}{2} \propto I^2\, \mathcal{S}(\alpha), \tag{3.21}$$

and fit $R_{xx}(\alpha)$ to Eqs. (3.18)–(3.19) while monitoring $V_{xx}^{2\omega}$ to quantify and subtract thermal artifacts [194,210]. For the SMR measurement, a Keithley 6221 current source applied a square-wave charge current with alternating polarity to the current channel, while a transverse/longitudinal probe measured the voltage with a Keithley 2182A nanovoltmeter. The voltmeter was synchronized with the current source, operating in Delta Mode (Fig. **3.9**), to acquire 1000 data points at around 50 ms per data point. A 4 ms delay between current reversals (24 Hz) and data acquisition was applied to mitigate transient effects (see Sec. 3.2.3), ensuring stability against rise-time artifacts or capacitor-like effects in the nanostructures.

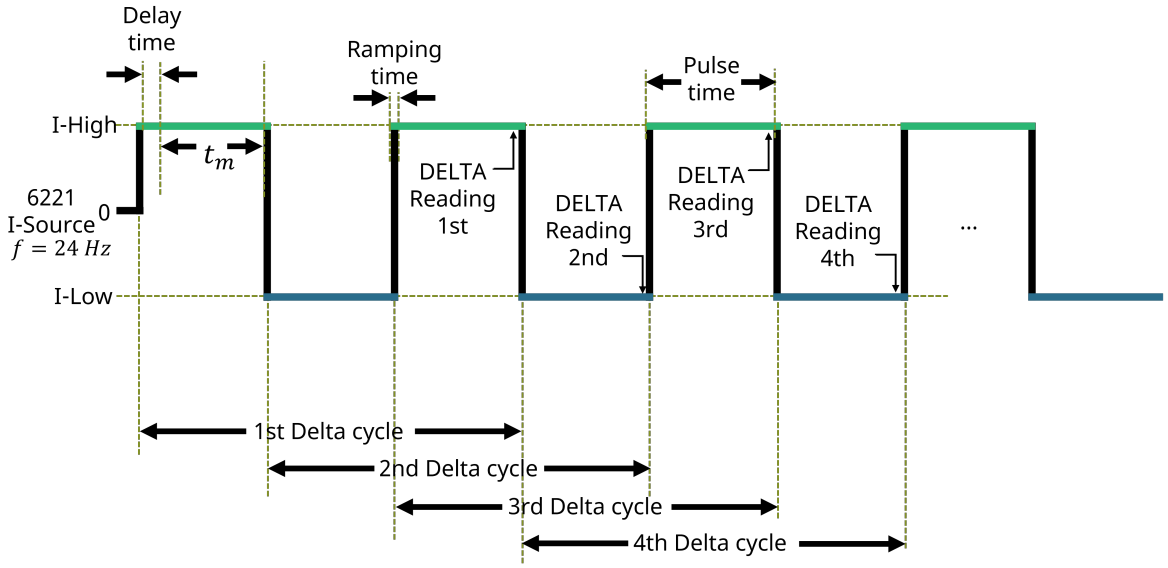

Figure 3.9.: **Delta–mode timing diagram.** The source current is alternated between $+I$ and $-I$ with period $T_r = 1/f_r$. After each reversal, a settling delay t_s precedes the measurement window t_m, during which the nanovoltmeter averages the voltage. The two averaged plateaus $\bar{V}_+$ and $\bar{V}_-$ form one *delta pair*, yielding $V_\Delta = (\bar{V}_+ - \bar{V}_-)/2$ (odd in current) and $V_\Sigma = (\bar{V}_+ + \bar{V}_-)/2$ (even in current). Repeating multiple pairs and averaging suppresses $1/f$ drift and random noise. Using integer–line–cycle t_m (one power line cycle) provides mains–frequency rejection.

Data quality and controls. Before analysis, we (i) confirm reversibility upon clockwise/counterclockwise rotation, (ii) subtract any residual misalignment offsets by symmetrization/antisymmetrization, (iii) check the invariance of the 1ω amplitude under current inversion, and (iv) verify that 2ω signals remain at least an order of magnitude smaller than 1ω in the linear regime.

Altermagnetic impact. In altermagnets, the leading symmetry of the SMR in a heavy metal, insulating magnet bilayer can remain identical to the standard antiferromagnetic case, namely a dominant dependence on the projection of the interfacial spin accumulation $\boldsymbol{\mu}_s$ onto the order parameter $\mathbf{n}$, giving the familiar $\cos 2\alpha$ and $\sin 2\alpha$ harmonics when $\mathbf{n}$ is coherently rotated by an external field [143,194,210]. However, altermagnetism can introduce additional, experimentally relevant modifications through

symmetry locked spin splitting in momentum space, which can make the interfacial spin transfer efficiency, often parameterized by an effective real spin mixing conductance $g_r^{\uparrow\downarrow}$ and a spin transparency, depend on the crystallographic azimuth of the Pt strip relative to the altermagnetic axes. Practically, this can appear as a device orientation dependent SMR amplitude $\Delta\rho$ for Hall bars patterned along different crystal directions, phase shifts in angular scans due to symmetry locked easy axes, and, depending on the magnetic point group, the emergence of higher order angular harmonics beyond the pure 2α terms, for example $A_4 \cos 4\alpha$ or $A_6 \cos 6\alpha$, reflecting crystalline symmetry filtering rather than wiring artifacts [24, 88]. In addition, because the field driven rotation of $\mathbf{n}$ in compensated magnets is governed by anisotropy and susceptibility rather than simple ferromagnetic alignment, altermagnets may show direction dependent characteristic fields for the onset and saturation of the SMR modulation, which can vary between scan planes and between symmetry inequivalent transport axes, providing a route to disentangle interfacial anisotropy from purely geometric or resistive background effects [143, 210].

3.2.3. Non-local spin transport: geometry, electrical detection schemes.

Non-local transport geometries (Fig. **3.6(b)**) spatially separate spin injection and detection to probe diffusive magnon currents in insulating magnets. In our devices, narrow Pt strips (injector/detector) are patterned on top of the samples with a center-to-center spacing of d. A charge current through the injector generates an interfacial spin accumulation $\hat{\boldsymbol{\sigma}}_{\mathrm{SH}}$ via the SHE as well as a thermal gradient via Joule heating; the interfacial spin and the temperature gradient excite a nonequilibrium magnon chemical potential $\mu_{\mathrm{m}}(\mathbf{r})$ in the magnet. At the remote detector stripe, the arriving μ_{m} is converted into a voltage via the ISHE. The approach allows one to ascertain the magnon diffusion length λ_{m} and symmetry filtering by the Néel/canted vector in altermagnets [48, 97, 106, 115, 174].

Device geometry and angular conventions. Injector and detector strips (width $w \sim 300$nm, thickness $t_{\mathrm{Pt}} = 7$ nm) are oriented at fixed azimuthal angles relative to crystallographic axes to project symmetry components of the magnetic order. We denote by α the IP angle between $\hat{\boldsymbol{\sigma}}_{\mathrm{SH}} \parallel \hat{\mathbf{t}}$ and the magnetic order. In the drift–diffusion picture, the electrically generated signal scales with the *product* of creation and detection projections,

$$V_{\mathrm{NL}}^{\mathrm{el}}(\alpha) \;\propto\; \left(\hat{\boldsymbol{\sigma}}_{\mathrm{SH}}\cdot\mathbf{n}\right)_{\mathrm{inj}} \left(\hat{\boldsymbol{\sigma}}_{\mathrm{SH}}\cdot\mathbf{n}\right)_{\mathrm{det}} \;\Rightarrow\; \text{canonical } \cos^2\alpha \text{ or } \sin^2\alpha, \tag{3.22}$$

whereas thermally generated signals pick up only the *detection* projection [97, 174]. By patterning bars at multiple azimuths, we isolate altermagnetism-specific angular harmonics, with ϕ the angle between the current injector and the crystallographic magnetic easy axis.

Diffusion model and distance dependence. In the steady state, the magnon chemical potential obeys

$$D_{\mathrm{m}}\nabla^2\mu_{\mathrm{m}} - \frac{\mu_{\mathrm{m}}}{\tau_{\mathrm{m}}} = 0, \qquad \lambda_{\mathrm{m}} = \sqrt{D_{\mathrm{m}}\tau_{\mathrm{m}}}, \tag{3.23}$$

with interfacial boundary conditions set by the real spin-mixing conductance and spin Hall source at the injector [106]. For $d \gtrsim w$ on extended films, the detector voltage decays approximately exponentially,

$$V_{\mathrm{NL}}(d) \;\propto\; \exp(-d/\lambda_{\mathrm{m}}), \tag{3.24}$$

while in a strictly two-dimensional diffusion, a modified Bessel function dependence $K_0(d/\lambda_{\mathrm{m}})$ may appear; over practical distances both reduce to an exponential law used to extract λ_{m} [48, 106].

Electrical vs. thermal channels: AC (1ω/2ω) and DC protocols. Electrically driven magnons are *linear* in current, whereas Joule-heating-driven magnons scale as I^2. With AC excitation $I(t) = I_0 \sin \omega t$,

$$V_{\mathrm{NL}}^{1\omega}(\alpha, d) \;\propto\; I_0\, e^{-d/\lambda_{\mathrm{m}}} \left(\hat{\boldsymbol{\sigma}}_{\mathrm{SH}} \cdot \mathbf{n}\right)_{\mathrm{inj}} \left(\hat{\boldsymbol{\sigma}}_{\mathrm{SH}} \cdot \mathbf{n}\right)_{\mathrm{det}}, \tag{3.25}$$

$$V_{\mathrm{NL}}^{2\omega}(\alpha, d) \;\propto\; I_0^2\, e^{-d/\lambda_{\mathrm{m}}} \left(\hat{\boldsymbol{\sigma}}_{\mathrm{SH}} \cdot \mathbf{n}\right)_{\mathrm{det}}, \tag{3.26}$$

cleanly separating electrical (first harmonic) and thermal (second harmonic) contributions [174]. In our pseudo-DC variation (Delta mode), we use current reversal to form

$$R_{\mathrm{NL}}^{\mathrm{el}} = \frac{V_{\mathrm{NL}}(+I) - V_{\mathrm{NL}}(-I)}{2I}, \qquad R_{\mathrm{NL}}^{\mathrm{th}} = \frac{V_{\mathrm{NL}}(+I) + V_{\mathrm{NL}}(-I)}{2I^2}, \tag{3.27}$$

which are directly comparable to $1\omega/2\omega$ lock-in readouts and robust to small drifts [174].

We suppress capacitive pickup by symmetric wiring and verify linearity of $V_{\mathrm{NL}}^{1\omega} \propto I_0$ at fixed α and d. The thermal channel is benchmarked via I_0^2 scaling. Distance series are fitted on a device-by-device basis to extract λ_{m} with confidence intervals determined by error bars.

In the delta-mode current-reversal protocol, the voltage is sampled after a defined settling delay t_s following each polarity switch. If t_s is chosen shorter than the relevant electrical settling times of the injector and detector circuits, the recorded plateaus still contain transient contributions arising from parasitic RC constants of the wiring and contact pads, inductive switching artifacts, and recovery of the nanovoltmeter input stage. These transients can be comparable to the nano-volt to micro-volt non-local signals and, because their parity under current reversal is not guaranteed, they can leak into both the odd channel $V_\Delta = (\bar{V}_+ - \bar{V}_-)/2$ and the even channel $V_\Sigma = (\bar{V}_+ + \bar{V}_-)/2$, thereby biasing $R_{\mathrm{NL}}^{\mathrm{el}}$ and $R_{\mathrm{NL}}^{\mathrm{th}}$. This is particularly critical in non-local geometries, where capacitive cross-talk between injector and detector can generate decaying voltage tails after each reversal that mimic a distance-dependent signal; strong dependence on t_s (or on reversal frequency) is therefore a diagnostic of electrical pickup rather than genuine spin transport. The delay t_s should be set long enough that V_Δ and V_Σ become independent of t_s, i.e., after the transient has fully decayed.

3.2.4. Photoemission Electron Microscopy imaging

Synchrotron-based X-ray PEEM [196] is employed to directly visualize antiferromagnetic and altermagnetic domain textures with element specificity and nanoscale spatial resolution. Fig. **3.10** summarizes the experimental concept: polarization-tunable soft X-rays generated in an undulator are monochromatized and focused onto the sample at the PEEM endstation, where the resulting photoelectrons are energy filtered and imaged by an electron-optical column.

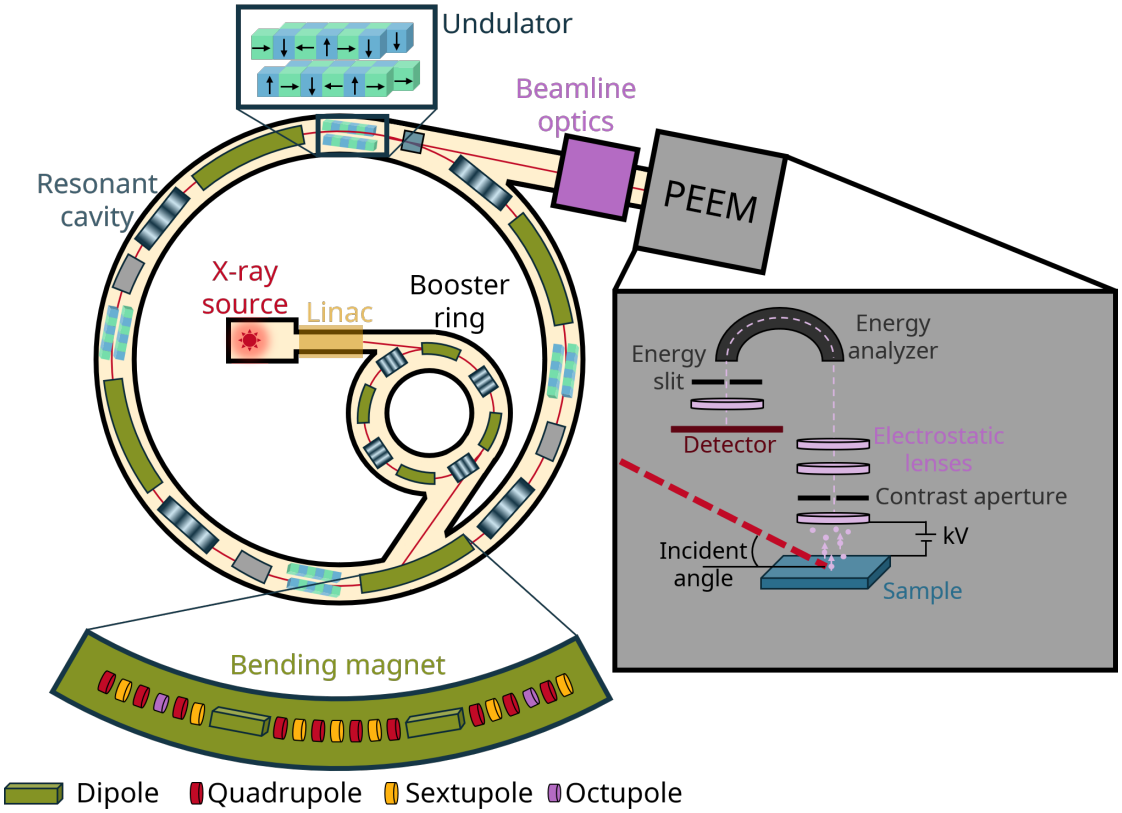

Figure 3.10.: **Synchrotron radiation source and imaging principle.** Schematic overview of a synchrotron light source and a PEEM endstation. An electron bunch is generated in the linac and stored in the ring, where bending magnets and insertion devices (undulators) produce intense, tunable soft X-rays that are transported through beamline optics to the PEEM. The undulator enables polarization control, which is exploited for XMLD/XMCD contrast in magnetic imaging. **Inset:** In the PEEM, the sample is illuminated at a certain incidence angle; photoelectrons emitted from the surface are accelerated by a high extraction field (∼kV), energy-filtered by an analyzer (energy slit/analyzer), and imaged onto a detector by an electron-optical column. A contrast aperture selects the desired electron trajectories and suppresses aberrations, while magnetic/electrostatic lenses form a real-space image with nanoscale (ideally 5 nm) spatial resolution.

Magnetic contrast is obtained by exploiting XMLD and XMCD at the transition-metal $L_{2,3}$ edges. XMLD is sensitive to the *axis* of the Néel vector (even under $\mathbf{n} \to -\mathbf{n}$),

while XMCD probes time-reversal symmetry breaking and thus lifts the $\pm\mathbf{n}$ ambiguity [33, 233, 234]. In practice, polarization-resolved PEEM image stacks acquired at photon energies selected from the XAS line shapes are combined into dichroic asymmetries, yielding quantitative maps of domain orientation and wall morphology. The measurements are carried out under ultrahigh vacuum with full polarization control at a modern spectromicroscopy beamline (MAXPEEM), whose brilliance and stability enable temperature- and angle-dependent imaging compatible with the transport experiments presented in this thesis [33, 196].

Setup and imaging conditions. X-ray PEEM measurements were carried out at aberration-corrected soft X-ray spectromicroscopy endstations with full polarization control, enabling both XMCD- and XMLD-PEEM at the transition-metal $L_{2,3}$ edges (schematically depicted in Fig. **3.10**). For XMLD contrast, we used linear polarization with the electric-field vector predominantly IP, while XMCD contrast was obtained by acquiring images at opposite circular helicities. Image sequences were recorded at photon energies chosen from XAS line shapes near the Fe $L_{2,3}$ edges, and processed as drift-corrected dichroic asymmetries to suppress topographic and intensity fluctuations [33, 196, 234]. The microscope operates in UHV and in an energy-filtered mode to reduce the secondary-electron background. To minimize charging on insulating films, conductive caps or ultrathin metallic overlayers are used when required and verified not to perturb the AFM texture [49]. At MAXPEEM (MAX IV), the elliptically polarizing undulator and plane-grating monochromator provide high flux over the soft X-ray range (tens to ∼keV-scale photon energies are not required here), enabling nanometre-scale spatial resolution and rapid acquisition of polarization- and angle-dependent image stacks [196].

Image formation and asymmetry definitions. For linear dichroism, two images with different energies and same polarization (equivalent to two orthogonal linear polarizations [196]) are recorded and combined as

$$A_{\mathrm{XMLD}}(\mathbf{r}) = \frac{I_{E_1}(\mathbf{r}) - I_{E_2}(\mathbf{r})}{I_{E_1}(\mathbf{r}) + I_{E_2}(\mathbf{r})}, \tag{3.28}$$

which is sensitive to the local Néel-vector axis through the $\cos 2\theta$ dependence between the E-field and the spin axis [234]. For circular dichroism,

$$A_{\mathrm{XMCD}}(\mathbf{r}) = \frac{I_{+}(\mathbf{r}) - I_{-}(\mathbf{r})}{I_{+}(\mathbf{r}) + I_{-}(\mathbf{r})}, \tag{3.29}$$

with $I_{\pm}$ acquired at fixed energy and opposite helicities (equivalent to the two energies imageing) the XMCD is proportional to the net canting moment and the anomalous Hall vector (that are not necessary collinear in an altermagnet), while XMLD remains sensitive to the antiferromagnetic axis in both easy-plane and easy-axis phases [49, 233, 234].

Vector mapping and rotational protocols. Because XMLD is even under $\mathbf{n} \to -\mathbf{n}$, 180° domains are indistinguishable by XMLD alone. We therefore combine (i) XMLD-PEEM taken while rotating the linear polarization (or the sample) to fit the expected

$\sin[2(\theta + \phi)]$ angular dependence and extract the IP axis angle ϕ, with (ii) XMCD-PEEM at a fixed energy/helicity pair to break the $\mathbf{n}$ vs. $-\mathbf{n}$ sign degeneracy and obtain full vector maps [33]. This workflow has become standard at modern PEEM beamlines [33, 196].

Imaging 180° altermagnetic domain walls in hematite. In α-Fe_2O_3, XMLD-PEEM resolves micrometre-scale AFM domains separated by sharp 180° walls across a broad temperature range that includes both easy-axis and easy-plane phases [49, 235]. Angle-resolved XMLD identifies the local Néel-vector axis, while the XMCD channel (finite in the canted state) lifts the sign ambiguity, allowing direct visualization of $\mathbf{n} \rightarrow -\mathbf{n}$ reversals—i.e., 180° altermagnetic walls in the easy-plane phase—consistent with transport signatures such as the sign-alternating anomalous Hall response predicted for altermagnets [24]. Practically, we acquire XMLD images at two energies (near the XMLD maxima/minima at the Fe L_3 edge) and at multiple polarization angles, compute A_{XMLD}, then use an XMCD mask (A_{XMCD} at Fe L_2 or L_3) to assign a unique Néel-vector orientation to each pixel [33]. The resulting PEEM vector maps reproduce the expected domain topology and wall orientations determined by crystalline anisotropy and strain fields.

3.3. Summary

The *Methods* chapter explain the methods used to obtain reproducible materials properties, structural information and measurements configurations that links materials synthesis, device engineering, metrology, and computation to quantify spin transport in insulating compensated magnets. High-quality epitaxial films and single crystals of α-Fe_2O_3 and $LuFeO_3$ were prepared (*via* PLD and optical floating-zone growth), structurally and magnetically tested (XRD, SQUID, atomic force microscopy), and integrated into lithographically defined local (SMR/AHE) and non-local architectures with sputtered Pt contacts optimized for spin–orbit transduction. Transport protocols combined first/second-harmonic readout and current-reversal symmetrization to disentangle electrical from thermal channels and to extract symmetry-resolved responses characteristic of altermagnets. Synchrotron PEEM (XMLD/XMCD) provided nanoscale, element-specific domain mapping that cross-validates transport-derived order-parameter orientations and wall morphology. The methods used underpin the following chapters, where we leverage the same symmetry-aware measurement geometry to demonstrate anisotropic and robust spin transport in orthoferrites and hematite.

4. Symmetry-controlled Hall conductivity in hematite: from angle dependent transport to Néel vector imaging

This chapter establishes experimental evidence that hematite (α-Fe_2O_3) realizes an altermagnetic state with symmetry-driven transverse transport, despite compensated sublattice moments [21]. Using angle-dependent Hall measurements on low-doped (1% Ti) (0001)-oriented thin films, an anomalous Hall response is observed only when the magnetic point group symmetry becomes compatible with a Hall pseudovector [24], namely above the spin-flop transition in the easy-axis phase, where the Néel vector is forced away from a high-symmetry direction. The extracted odd transverse conductivity exhibits a pronounced dependence on the crystallographic orientation of the Hall bar, including periodic sign inversions at specific current directions, which cannot be explained by the fixed canted moment or by a positively defined sixfold IP anisotropy energy [126, 236]. These observations provide a symmetry fingerprint consistent with g-wave altermagnetism and directly link the sign of the Hall response to the underlying altermagnetic order parameter.

The central strategy is to combine symmetry-resolved electrical transport [22] with real-space XPEEM imaging [33] to access complementary information that is not obtainable by either technique alone. Transport on C-cut Ti-doped hematite provides the orientation dependence of the odd transverse response in a controlled monodomain spin-flop state. However, it does not uniquely determine the absolute direction of the Néel vector. XPEEM on R-cut hematite resolves this ambiguity by mapping the IP Néel vector via XMLD contrast and by detecting XMCD contrast that tracks the projection of the altermagnetic Hall pseudovector, enabling a boolean combination that reconstructs the absolute Néel vector orientation in real space. Together, these measurements demonstrate that a 180° reversal of the Néel vector is associated with an inversion of the altermagnetic Hall vector, providing a direct bridge between the nodal, sign-changing Hall response observed in transport and the domain-resolved spin structure imaged by XPEEM. This chapter contains first principles calculations performed by Prof. Dr. Rafael Gonzalez Herrera from Universidad del Norte in Barranquilla, Colombia, as part of a collaboration with the group of Prof. Dr. Jairo Sinova at JGU Mainz. Details of the simulations can be found in the Appendix E.1 [41, 177, 237–251].

The interpretation in this chapter relies on the symmetry framework for altermagnetism and for Hall pseudovectors in compensated magnets, as introduced in the Chapter 2, including the dependence of the allowed components of the AHC tensor on the orientation of the Néel vector and on the magnetic point group. This chapter focuses on the hematite-specific implementation, the resulting datasets, and the symmetry-driven

conclusions drawn from their combined analysis.

4.1. Film quality and magnetic phase identification

Reliable symmetry-resolved conclusions require that the structural reference frame, the magnetic phase, and the relevant transport regime of the hematite films be established independently of the Hall data analysis. In particular, the interpretation of the angular dependence of the transverse response rests on a well-defined IP crystallographic axis used to define the Hall-bar orientation angle ϕ, and on knowing the temperature window in which the Ti-doped films reside in the easy-axis (collinear) phase at zero field [133]. Moreover, because the anomalous Hall response discussed below becomes sizable only once the spin configuration is driven away from the high-symmetry collinear state by an OOP magnetic field, the characteristic spin-flop field scale must be identified. Finally, the electronic conduction mechanism determines whether the data can be compared quantitatively to intrinsic Berry-curvature conductivities, or only at the level of symmetry-imposed angular trends. The following subsections, therefore, summarize the structural, magnetic, and transport-regime characterization required for the remainder of this chapter.

4.1.1. Structural quality and epitaxy

The symmetry resolved transport analysis requires a well-defined crystallographic reference frame in the film plane, because the Hall bar orientation angle ϕ is defined with respect to the hematite **a**-axis. The crystallographic purity and epitaxy of the (0001) oriented Ti-doped hematite films were therefore verified by XRD before device fabrication. A $\theta - 2\theta$ scan confirms the single-phase nature of the thin-film and the (0001) OOP orientation, with no secondary phases detected within the sensitivity of the measurement (Fig. **4.1a**). The (0006) rocking curve is narrow (inset of Fig. **4.1a**), indicating high crystalline quality and a small mosaic spread, which is relevant for ensuring that the IP reference directions are well defined across the patterned Hall bar array. The slight shift of the hematite diffraction peak compared with bulk reference values is consistent with homogeneous incorporation of Ti-dopants in PLD-grown hematite thin films, as reported in the thin film literature [252, 253].

To define the IP axes used throughout this chapter, a ϕ scan of the $[10\bar{1}4]$ reflection was used to identify crystallographically equivalent IP directions separated by 120° (Fig. **4.1c**). This procedure fixes the IP projection of the hematite **a**-axis and provides the angular origin for the Hall bar patterning angles ϕ discussed in Section 4.2. In the remainder of this chapter, $\phi = 0°$ denotes one chosen **a**-axis projection, and all other device angles are defined counterclockwise relative to this reference, while acknowledging that this choice is arbitrary within the threefold crystal equivalence.

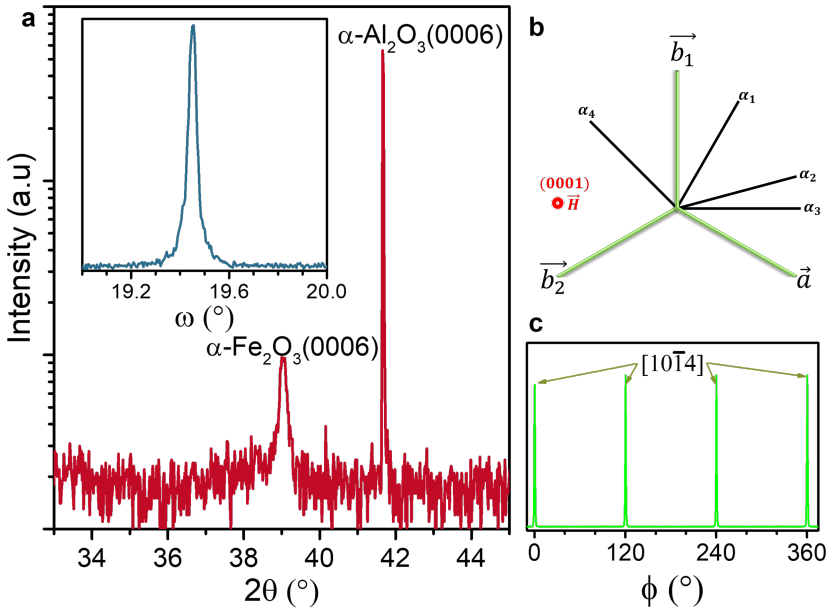

Figure 4.1.: Structural characterization of Ti-doped α-Fe_2O_3 films with (0001) orientation. **a** $\theta - 2\theta$ scans around the (0006) peak, no secondary phases are observed. The inset shows the rocking curve of the (0006) reflection, indicating narrow mosaic spread and high epitaxial quality. **b** Schematic illustration of the threefold symmetry of the (0001) surface plane, highlighting crystallographic equivalent IP directions used to define the Hall bar patterning angles. **c** In plane ϕ scan of an off-axis reflection, showing peaks separated by 120°, used to determine the IP projection of the hematite **a**-axis and to define the angular reference $\phi = 0°$ for device orientations. Adapted from Galíndez et al., *Adv. Mater.* **37**(2025): e05019, licensed under CC BY 4.0 [41].

4.1.2. Magnetic phase, Morin transition, and spin flop

The altermagnetic Hall response discussed in this chapter is conditional on the magnetic phase and on the field-driven spin reorientation; therefore, the relevant phase window of the Ti-doped films is established here using SQUID magnetometry (Fig. **4.2**). The temperature-dependent magnetization shows a Morin transition at $T_M \approx 330$ K for the 1% Ti-doped (0001) films (Fig. **4.2b**), which places measurements at 300 K in the easy-axis, collinear phase in zero field. Relative to bulk hematite, the transition is shifted upward and broadened, which is consistent with prior reports on doped and strained thin films, where competing anisotropies are modified by lattice and epitaxial effects [132, 254, 255]. Field-dependent magnetization loops taken below and above T_M reproduce the expected weak ferromagnetic moment magnitude in the high temperature phase and a negligible net moment in the collinear phase (Fig. **4.2a**), indicating that the low Ti concentration preserves hematite's intrinsic compensated ordering while enabling electrical conduction.

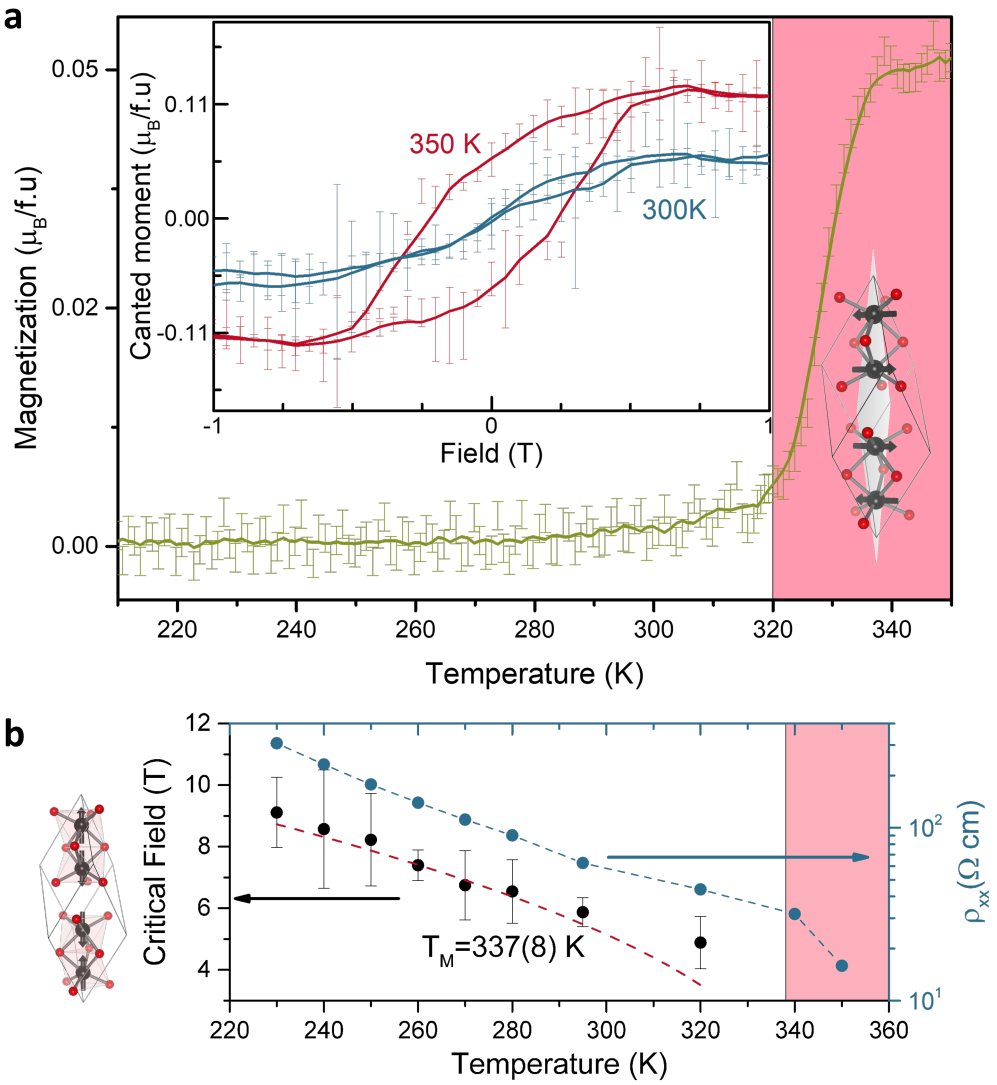

Figure 4.2.: SQUID magnetometry of Ti-doped (0001) α-Fe_2O_3 thin films for a magnetic field applied perpendicular to the c-axis. a Magnetization vs external magnetic field for the easy-axis phase at 300 K and the weak ferromagnetic phase at 350 K. Temperature dependent magnetization measured under a small applied magnetic field ($\mu_0 H = 20$ mT), revealing a Morin transition at $T_M \approx 330$ K. **b** Characteristic field scale associated with the field-driven spin reorientation as a function of temperature, plotted together with the temperature dependence of the longitudinal resistivity. Adapted from Galíndez et al., *Adv. Mater.* **37**(2025): e05019, licensed under CC BY 4.0 [41].

For the transport measurements, the key magnetic-field scale is the onset of spin-flop-driven reorientation under an OOP magnetic field applied along [0001], because the odd transverse signal becomes sizable only once the symmetry is lowered from the high-symmetry collinear configuration. In the easy-axis phase near room temperature, the transverse signal begins to increase strongly at fields of order 6 T, which is used

later as the operational marker for entering the symmetry allowed regime for a finite Hall pseudovector. The temperature evolution of this characteristic field scale, and its correspondence to the Morin transition physics, is discussed together with the transport data in Section 4.2.

4.1.3. Transport regime checkpoint

Before comparing the experimental results with first-principles AHC tensors, it is necessary to identify the electronic transport regime in the doped hematite films, as this determines which aspects of the theory can be meaningfully compared with the data. The longitudinal resistivity exhibits a strongly activated temperature dependence. Still, the extracted activation energy does not correspond to the hematite band gap, indicating that the conduction does not occur via simple band transport. Together with the magnitude of the conventional Hall coefficient observed in the low-field regime, these trends are consistent with hopping-dominated transport [256] in an impurity-derived conduction channel, as previously reported for doped hematite in the low-doping limit [257–260]. In this regime, the absolute magnitude of the experimentally extracted σ_{xy} is not expected to be quantitatively comparable to intrinsic Berry-curvature conductivities computed from a band description. The comparison performed in this chapter, therefore, focuses on symmetry-controlled trends, in particular the angular node structure and sign inversions, which are governed by the same magnetic point-group constraints that control the band spin splitting and the allowed Hall tensor components.

4.2. Electrical evidence for symmetry-controlled Hall response

This section presents the electrical transport evidence for a symmetry-controlled transverse response in Ti-doped (0001) hematite, measured on a single film patterned into an array of Hall bars with different IP orientations ϕ relative to the crystallographic **a**-axis. The analysis focuses on the field-odd transverse conductivity, extracted from the measured transverse voltage by antisymmetrization with respect to the OOP magnetic field, following the protocol defined in the Chapter 3. The central observation is that a sizable odd transverse signal emerges only after the system is driven through the field-induced spin reorientation, at which the magnetic symmetry becomes compatible with a finite Hall pseudovector; see Table **4.1**. In the following, the field dependence across the spin flop transition is established first, because it defines the field window in which the angular dependence and sign inversions reported later are physically meaningful.

Table 4.1.: The different magnetic phases of altermagnetic hematite below the Néel temperature range (bulk values). Here, $SO(2)$ is a continuous rotation around the axes of spins, C_2T is spin rotation around the axes perpendicular to the spins, and T is time-reversal symmetry. Reproduced from Galíndez et al., *Adv. Mater.* **37**(2025): e05019, licensed under CC BY 4.0 [41].

Primary Magnetic Order	Spin Space Group	Spin Point Group	Spin Orientation (T (K), Secondary Order)	Magnetic Space Group	Magnetic Point Group	Hall Vector (Néel dep.)
AM	$1-32c$ $\times SO(2)$ $\times C_2T$	$1-32m$ $\times SO(2)$ $\times C_2T$ (g-wave)	(100) ($T > 259$, canted WF)	C_2'/c'	$2'/m'$	$(\sigma_{yz}, \sigma_{xz}, \sigma_{xy})$
			(001) ($10 < T < 259$, perfectly compensated)	R-3c	-31m	(0,0,0)
			Tilted (T <10, ferrimagnet)	P-1	-1	$(\sigma_{yz}, \sigma_{xz}, \sigma_{xy})$

4.2.1. Field dependence across the spin flop transition

In the easy-axis phase at 300 K, the transverse response is weak at low fields and becomes strongly enhanced only in proximity to the spin flop transition under an OOP magnetic field applied along [0001] (Fig. **4.3a**). Representative traces of the field odd transverse conductivity for three Hall bars patterned at different orientations ϕ show a clear onset of the odd signal at fields of order 6 T. This onset is used in this chapter as the operational marker for entering the symmetry-allowed regime, in which the spin configuration is forced away from the high-symmetry collinear state and the Hall pseudovector becomes permitted by the magnetic point group. Consistent with this symmetry picture, the odd transverse conductivity remains small below the onset field, whereas above the transition, it increases rapidly and reaches a large amplitude at high fields.

The emergence of the odd transverse signal at the spin flop scale is a key prerequisite for the symmetry-resolved analysis, because it separates a low-field regime where the Hall response is symmetry-suppressed from a high-field regime where transverse transport is symmetry allowed. In the remainder of this section, the high field regime is used to extract the angular dependence of the odd transverse response across the full Hall bar array, including the characteristic sign inversions that constitute the primary transport signature of the altermagnetic order parameter.

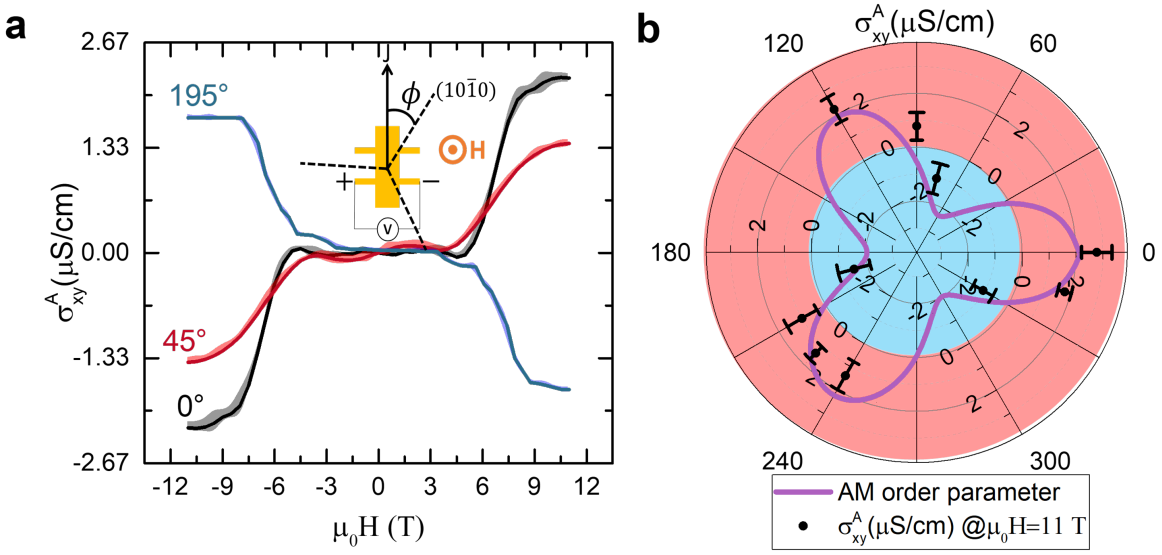

Figure 4.3.: Field odd transverse conductivity of Ti-doped (0001) α-Fe_2O_3 at 300 K. a Three representative Hall bars patterned at selected in plane angles ϕ relative to the crystallographic **a**-axis. The shaded bands denote the standard deviation obtained from six repeated field cycles. A pronounced increase in the odd transverse signal appears at fields of order 6 T, consistent with the onset of the spin flop-driven reorientation that enables a finite Hall pseudovector by symmetry. **b** Amplitude of the extracted odd transverse conductivity at $\mu_0 H = 11$ T for the full set of Hall bar orientations, illustrating the strong dependence on ϕ and the presence of symmetry-related sign changes.

For completeness, the full Hall-bar array dataset and the even/odd decomposition are shown in Appendix F (Fig. **F.1**), together with additional temperature-dependent transport data across the Morin transition (Fig. **F.2**) and the corresponding first-principles comparison (Fig. **F.3**).

4.2.2. Angular dependence and sign inversions, the core transport signature

Having established the high field regime in which a finite Hall pseudovector is symmetry allowed, we now analyze the dependence of the odd transverse response on the Hall bar orientation ϕ. Fig. **4.3b** summarizes the extracted odd transverse conductivity amplitude at $\mu_0 H = 11$ T for the full set of Hall bars patterned on the same film. A pronounced modulation with ϕ is observed, with extrema aligned to crystallographic directions and, crucially, periodic sign inversions that occur upon rotating the current direction by 60°. Crystallographically equivalent orientations exhibit comparable amplitudes, for example, $\phi = 0°$ and 120°, and likewise $\phi = 90°$ and 210°, demonstrating that the observed pattern is locked to the crystal symmetry rather than to fabrication-specific variations between devices. The existence of alternating signs at symmetry-related angles constitutes the central transport fingerprint of this chapter, because a sign change cannot be generated by a purely scalar IP anisotropy energy that is positive definite.

In addition to the field-odd Hall-like response analyzed in this subsection, a field-even transverse contribution is also present for Hall bars patterned away from the principal device axes. Fig. **4.4**shows the symmetric component σ_{xy}^{S} under an OOP magnetic field, displayed as a polar plot. The dominant fourfold modulation, with enhanced magnitude for orientations deviating from the nominal transverse probes, is consistent with geometric pickup of the longitudinal magnetoresistance due to a small non-orthogonality of the voltage electrodes, rather than an intrinsic Hall signal. Planar Hall contributions are excluded at the level required for the present interpretation, because each dataset is preceded by a β-scan that aligns the magnetisation along the OOP direction with an angular uncertainty below 0.5°, suppressing the IP component required for a planar Hall effect. Consequently, the symmetry analysis in this chapter is based exclusively on the antisymmetric, field-odd component σ_{xy}^{A}, which captures the Hall-like transverse signal used to extract the sign-inverting angular fingerprint.

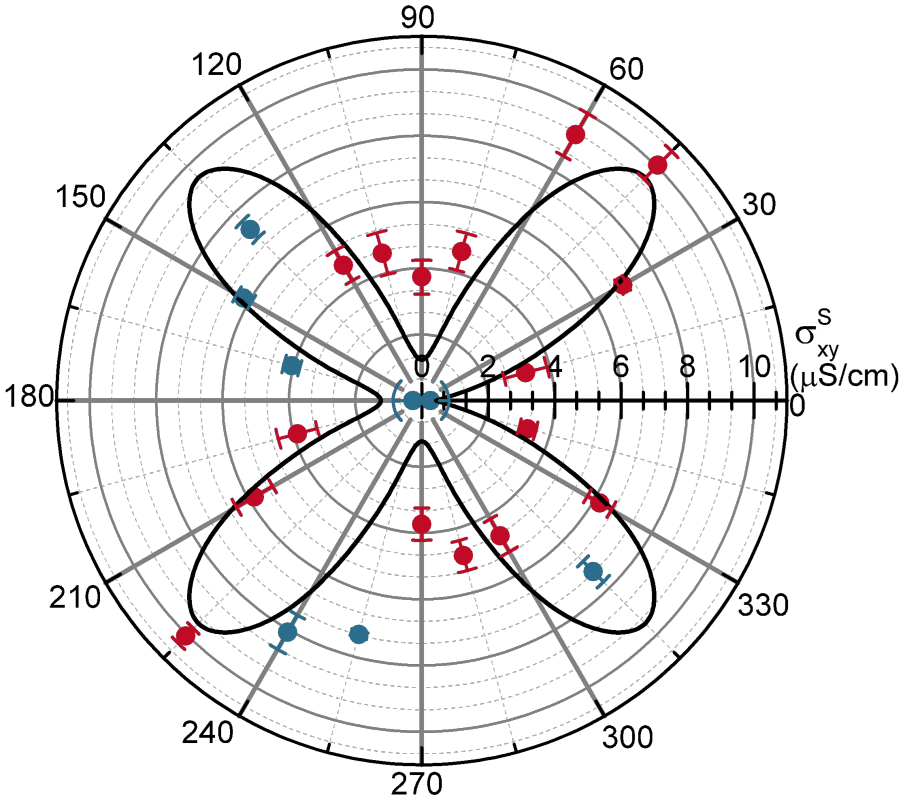

Figure 4.4.: **Field-even transverse conductivity component σ_{xy}^{S}.** Polar plot of the symmetric component of the conductivity, under an OOP magnetic field of $\mu_0 H = 11$ T, showing a dominant fourfold modulation attributed to non-Hall contributions (geometric pickup of longitudinal magnetoresistance). Adapted from Galíndez et al., *Adv. Mater.* **37**(2025): e05019, licensed under CC BY 4.0 [41].

Several trivial origins for the sign inversions can be excluded on symmetry and control grounds using only the arguments essential for the remainder of the chapter. First, a conventional AHE driven solely by the canted moment would not produce a sign change upon rotating the Hall bar, because the OOP magnetic field fixes the sign of the axial response associated with the moment. At the same time, the IP longitudinal resistivity

of the hexagonal (0001) surface is isotropic within the experimental resolution. Second, the field-even transverse contributions observed away from high-symmetry axes, which follow a distinct fourfold pattern, are attributed to geometric pickup of longitudinal magnetoresistance and do not enter the antisymmetric, Hall-like component used here. Third, the sixfold IP magnetic anisotropy of hematite can modulate the magnitude of a response through the energy landscape $K_6(1 - \cos 6\phi)$. Still, it cannot invert its sign because it is a scalar that remains non-negative for all ϕ. Therefore, the periodic sign alternation of the odd transverse conductivity requires an axial quantity that changes sign under rotation relative to the crystallographic axes, consistent with an altermagnetic Hall pseudovector whose orientation and sign are governed by the Néel vector and the crystal symmetry.

Two internal consistency checks are used in the main narrative to verify that the angular sign alternation of the odd transverse response is intrinsic and not introduced by the Hall bar geometry or data processing. First, the geometric symmetry of the Hall bar implies that two devices patterned 180° apart are equivalent and must yield the same transverse voltage when plotted in the local coordinate system of the bar. When the symmetric (field even) and antisymmetric (field odd) components of the transverse conductivity are displayed in polar form under an OOP magnetic of $\mu_0 H = 11$ T, the 180° rotated dataset appears at opposite angles but retains the same electrical sign, as expected from geometry. Importantly, when interpreted relative to the crystallographic reference axis, this mapping corresponds to an altermagnetic order parameter of opposite sign, while preserving the same nodal directions, consistent with the nodal structure inferred from Fig. **4.3b**.

Second, the sign of the odd transverse response can be switched reproducibly by reversing the Néel order at a fixed OOP field above the spin flop transition. Fig. **4.5** shows the transverse resistivity measured while maintaining a strong OOP field of $\mu_0 H = 10$ T and sweeping an IP magnetic field angle applied perpendicular to the Hall bar.

In this configuration, the system remains in the high-field spin-reoriented state where the odd transverse response is finite, while the IP field drives a 180° reversal of the Néel vector. The resulting hysteretic switching and sign inversion of the transverse resistivity provide a transport level confirmation that the odd transverse signal changes sign under a 180° Néel reversal, in agreement with the altermagnetic symmetry expectation used later in the combined transport and XPEEM analysis. Additional trace-level demonstrations of the symmetrization procedure, as well as extended datasets of the field's even-transverse contributions, are provided in the Chapter 3.

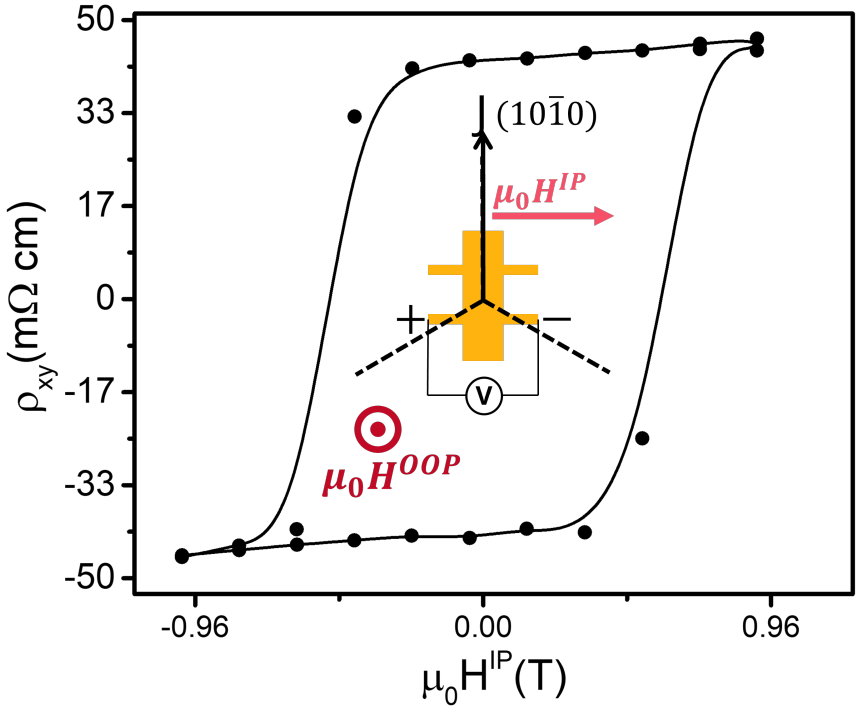

Figure 4.5.: Transverse resistivity under Néel vector inversion. Transverse resistivity hysteresis as a function of an IP magnetic field angle applied perpendicular to the Hall bar, measured at 300 K while maintaining an OOP field of $\mu_0 H = 10$ T. The strong OOP field keeps the system above the spin flop transition, while the IP field induces a 180° reversal of the Néel order, leading to a sign inversion of the transverse resistivity.

4.2.3. Consistency check in the weak ferromagnetic phase

The symmetry-controlled sign behavior is not restricted to the easy-axis phase above the spin flop scale. In the weak ferromagnetic phase above the Morin transition, where a canted moment exists already at small magnetic applied fields, the Hall-like response still depends on the crystallographic orientation of the Hall bar. Fig. **4.6** compares representative transverse conductivities for a device patterned along a high symmetry crystallographic axis and for a device oriented along an altermagnetic direction. While the high symmetry device shows a conventional anomalous Hall-like signal that saturates at the same field scale as the weak ferromagnetic moment, the altermagnetic orientation exhibits an odd component that inverts its sign relative to the high symmetry case. This behavior indicates that the transverse response cannot be reduced to a contribution from the canted moment alone [129], and supports the conclusion that the crystal symmetry and the Néel order determine the sign of the Hall-like signal.

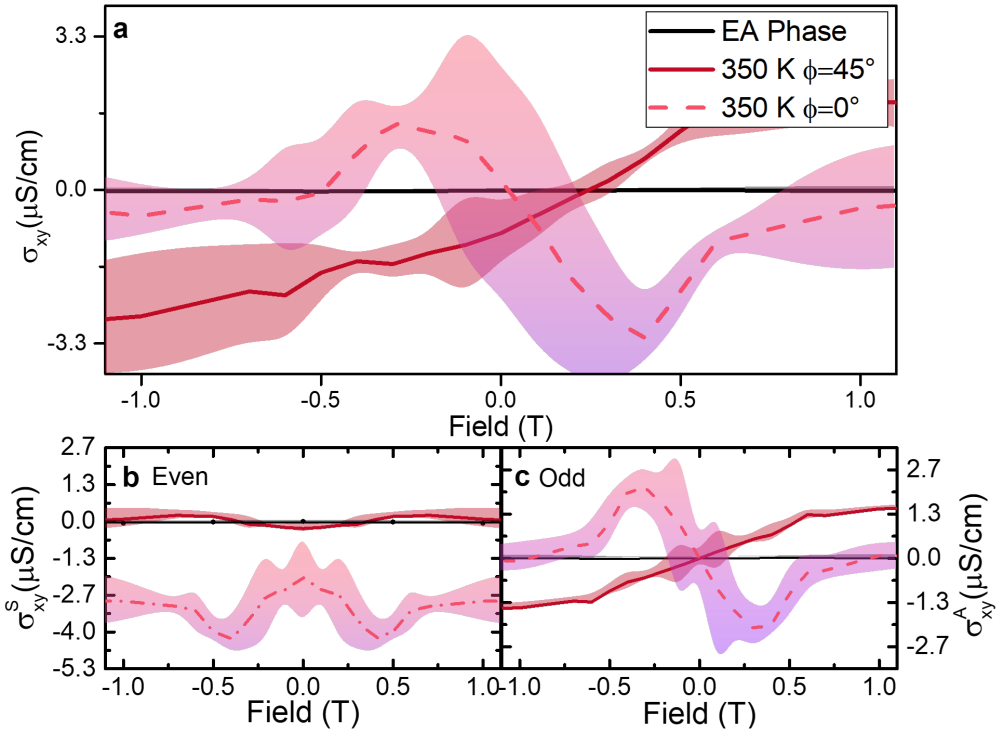

Figure 4.6.: **High temperature Transverse conductivities in hematite.** **a** Transverse conductivities measured in the weak ferromagnetic phase, comparing a Hall bar aligned along a high symmetry crystallographic axis and a Hall bar oriented at a relative angle of 45°. **b** Symmetric, field even component of the transverse conductivity. **c** Antisymmetric, field odd component of the transverse conductivity, showing a sign inversion between the two orientations. Adapted from Galíndez et al., *Adv. Mater.* **37**(2025): e05019, licensed under CC BY 4.0 [41].

4.3. Symmetry interpretation

The transport results above demonstrate that the transverse response is both field-selective, turning on at the spin flop scale, and strongly locked to the crystallographic orientation of the current, including periodic sign inversions. These observations are placed within the minimal-symmetry context required for interpretation and then compared qualitatively with first-principles calculations of the AHC tensor. The full altermagnetism symmetry framework and the classification of allowed Hall pseudovectors in compensated magnets are developed in the Chapter 2 and are not repeated here.

Hematite is theoretically classified as an altermagnet, because its crystal symmetry combined with collinear magnetic order breaks PT and $T\tau$ while preserving a combined real space and spin space rotation, leading to an altermagnetic band spin splitting [20, 21]. Within this symmetry setting, whether an anomalous Hall response is allowed is determined not by the presence of a net magnetization but by the magnetic point group associated with the Néel vector orientation and the relativistic spin structure. In the perfectly compensated collinear configuration with the Néel vector aligned along a high symmetry direction, the magnetic point group forbids a Hall pseudovector, and the AHC vanishes by symmetry (Table **4.1**). In contrast, when the spin

configuration is driven away from this high symmetry state, for example, by the field-induced spin reorientation above the spin flop transition, the magnetic point group changes to one compatible with a Hall pseudovector, enabling finite anomalous Hall tensor components.

For the present (0001) transport geometry, this symmetry constraint implies that a sizable odd transverse response is not expected in the low field easy-axis phase, but can appear once the OOP field enforces the spin reoriented state, consistent with the onset behavior in Fig. **4.3a**. Moreover, the Hall pseudovector in an altermagnet is not generally constrained to be parallel to the canted moment or strictly perpendicular to the Néel vector, and its allowed tensor components change sign under a 180° reversal of the Néel order. This provides the minimal symmetry basis for interpreting the angular sign inversions in Fig. **4.3b** and the Néel reversal switching in Fig. **4.5**.

To place the symmetry-controlled transport signatures on a microscopic footing, we compare the experimentally observed angular trends to first-principles calculations of the AHC (AHC) tensor in hematite. The calculations yield the three independent components of the AHC pseudovector, $(\sigma_{yz}, \sigma_{xz}, \sigma_{xy})$, as functions of the IP Néel vector orientation. Fig. **4.7** summarizes the calculated angular dependence and shows that all components exhibit characteristic sign changes and extinctions at specific angles, reflecting the symmetry constraints of the altermagnetic state. The calculations were performed by Prof. Dr. Rafael González-Hernández; details of the simulations can be found in the Appendix E and in Ref. [41].

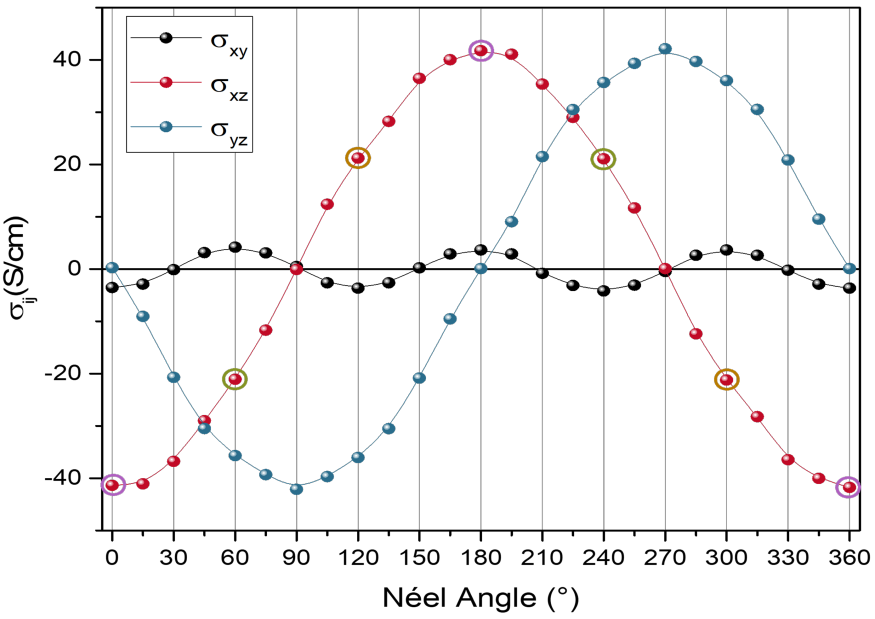

Figure 4.7.: AHC vector components angular dependence. Calculated $(\sigma_{yz}, \sigma_{xz}, \sigma_{xy})$ as a function of the IP orientation of the Néel vector. A 180° reversal of the Néel vector produces a sign inversion of the AHC components, while the different tensor components show phase-shifted angular dependence and symmetry-enforced nodes. Adapted from Galíndez et al., *Adv. Mater.* **37**(2025): e05019, licensed under CC BY 4.0 [41].

In the present experiments, transport occurs in a low-conductivity regime consistent with hopping-dominated conduction; therefore, comparisons between experiment and theory are made at the level of symmetry-controlled angular trends rather than absolute magnitudes. Within this scope, the calculations capture the key qualitative features required to interpret the transport data: the existence of symmetry-enforced suppressions of the AHC for particular Néel vector alignments and the sign inversion under a 180° Néel reversal. These properties provide the minimal theoretical context for the observed periodic sign alternations of the odd transverse response across Hall bar orientations in Fig. **4.3b**, and for the Néel reversal induced switching observed in Fig. **4.5**. A quantitative comparison of absolute conductivities is not attempted here, because the experimentally extracted σ_{xy} reflects hopping transport and thus is not expected to match intrinsic Berry curvature conductivities derived from a band description.

4.4. XPEEM validation of real space Néel order and Hall pseudovector

The transport measurements establish a symmetry-controlled, sign-changing odd transverse response that is consistent with an altermagnetic Hall pseudovector. Still, transport alone cannot uniquely determine the absolute direction of the Néel vector in real space. In particular, the 180° symmetry of the Hall bar and the threefold symmetry of the AHC limit the distinction of electrically equivalent magnetic states. To access the domain structure directly and to connect the sign changes inferred from transport to a real-space order parameter, we employ XPEEM imaging on R-cut hematite films, combining XMLD and XMCD contrast. General principles of XMLD and XMCD contrast formation, definitions of asymmetry, and acquisition and fitting procedures are described in the Chapter 3. Here, we focus solely on the geometry-specific interpretation required to validate the hematite results presented in this chapter.

4.4.1. XPEEM measurement geometry on R-cut hematite

To interpret the XMLD and XMCD contrast in terms of the Néel order and the altermagnetic Hall pseudovector, the measurement geometry must be fixed explicitly for the R-cut films used for imaging. Fig. **4.8** summarizes the coordinate system and the X-ray incidence used at the MAXPEEM beamline. Linear horizontal and linear vertical polarizations are used for XMLD to map the IP Néel axis, while circular polarization is used for XMCD, which is sensitive to the projection of an axial quantity onto the X-ray propagation direction. In the present chapter, this axial quantity is the symmetry allowed Hall pseudovector associated with the altermagnetic state. The geometry in Fig. **4.8** is therefore the reference used in the next subsections to connect XMLD-based Néel axis mapping, XMCD sign contrast, and the reconstructed absolute Néel direction [125].

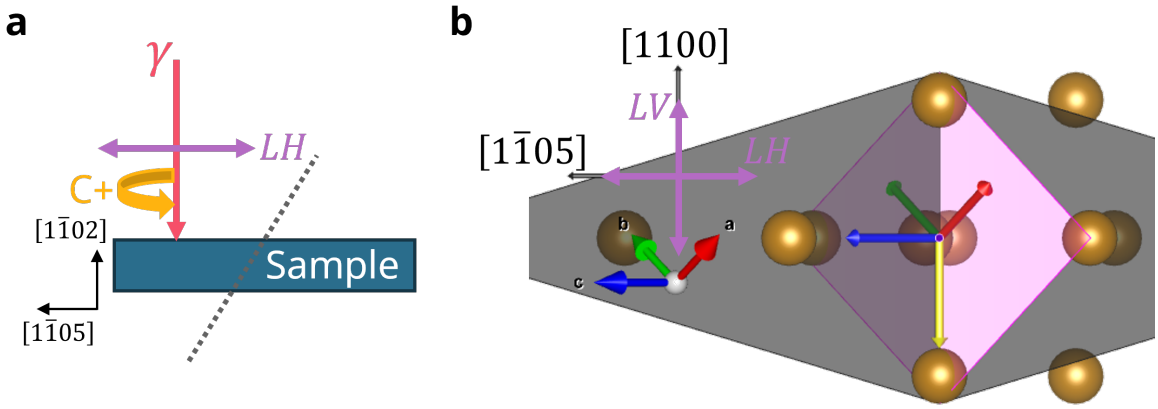

Figure 4.8.: Schematic representation of the experimental geometry for hematite imaging. **a** The R-cut oriented sample is illuminated with X-rays in linear horizontal, linear vertical, and circular polarization. The sample coordinate system is defined relative to the crystallographic axes, with the incident-beam direction indicated by γ **b** Visualization of the local crystallographic structure of hematite, showing the oxygen octahedra surrounding iron atoms and the alignment of the crystal axes. The Néel vector orientation relative to the X-ray polarization enables domain mapping and symmetry analysis via XMLD and XMCD. Adapted from Galíndez et al., *Adv. Mater.* **37**(2025): e05019, licensed under CC BY 4.0 [41].

4.4.2. XAS at the Fe edges

The XMLD and XMCD contrast mechanisms used for domain mapping are corroborated by X-ray absorption spectra recorded at the Fe $L_{2,3}$ edges. Figure **4.9a** shows XAS spectra acquired with opposite circular helicities and the corresponding XMCD signal, demonstrating a dichroic response at the Fe L_3 edge in the present geometry. The XMCD trace exhibits alternating positive and negative lobes across the absorption edge, a characteristic energy-dependent dichroic line shape at the Fe $L_{2,3}$ from altermagnets [33]. Because XMCD is obtained as the small difference between two large XAS signals, it is much smaller in magnitude than the absorption background and is therefore plotted with a constant factor for visibility, without changing its sign or spectral positions.

Figure **4.9b** shows XAS spectra taken with linear horizontal and linear vertical polarization and their difference, confirming a sizable XMLD response that is sensitive to the Néel axis orientation. These spectra provide the spectral basis for selecting the photon energies used to compute the XMLD and XMCD asymmetries employed in the imaging results discussed below.

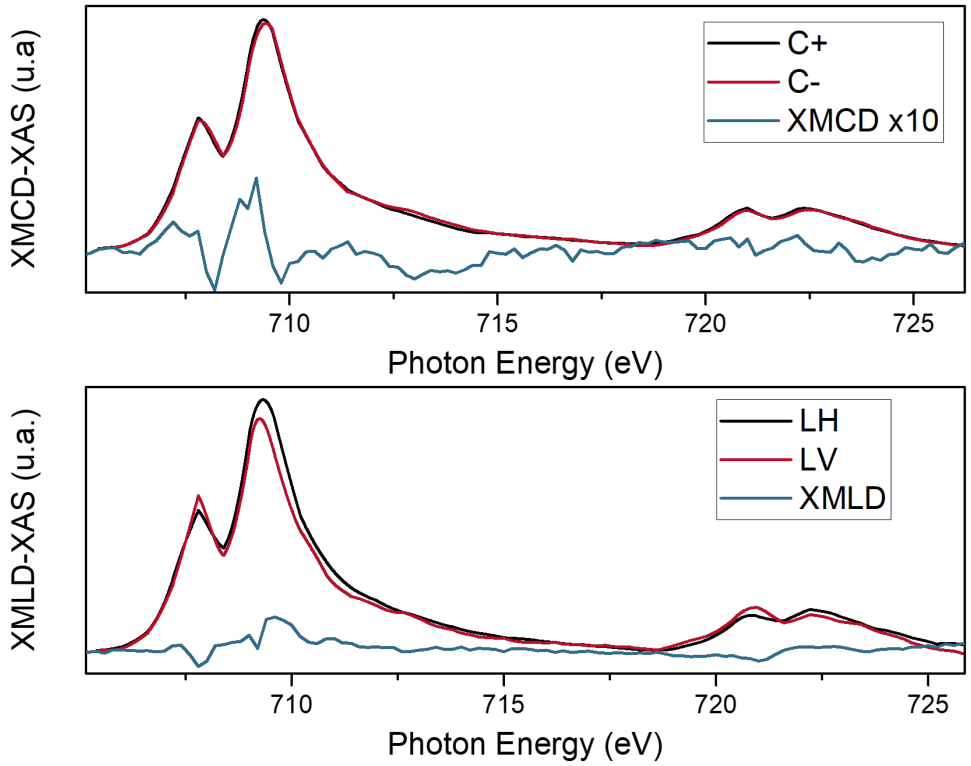

Figure 4.9.: **XAS spectra of hematite in the easy plane phase. a** X-ray absorption spectra acquired using circularly polarized light (C^+ and C^-) at the Fe $L_{2,3}$ edges, with the corresponding XMCD signal ($C^+ - C^-$) shown and multiplied by a constant factor for visibility. **b** XAS spectra taken with linear horizontal and linear vertical polarization, with the resulting XMLD signal ($LH - LV$) also magnified for clarity. Adapted from Galíndez Ruales et al., *Adv. Mater.* **37**(2025): e05019, licensed under CC BY 4.0 [41].

4.4.3. XMLD contrast in Ti-doped hematite

To verify that Ti-doping at the level used for transport does not suppress XMLD-based magnetic contrast, XMLD-PEEM measurements were also performed on Ti-doped hematite. Fig. **4.10a** shows a representative XMLD micrograph with clear domain contrast on the micrometer scale. Fig. **4.10b** shows the corresponding polarization-dependent XAS spectra and their difference, confirming that the XMLD signal remains robust in the doped system. This observation supports the use of low-level Ti-doping as a route to enable electrical transport measurements while maintaining the magnetic contrast required for symmetry-resolved Néel order imaging.

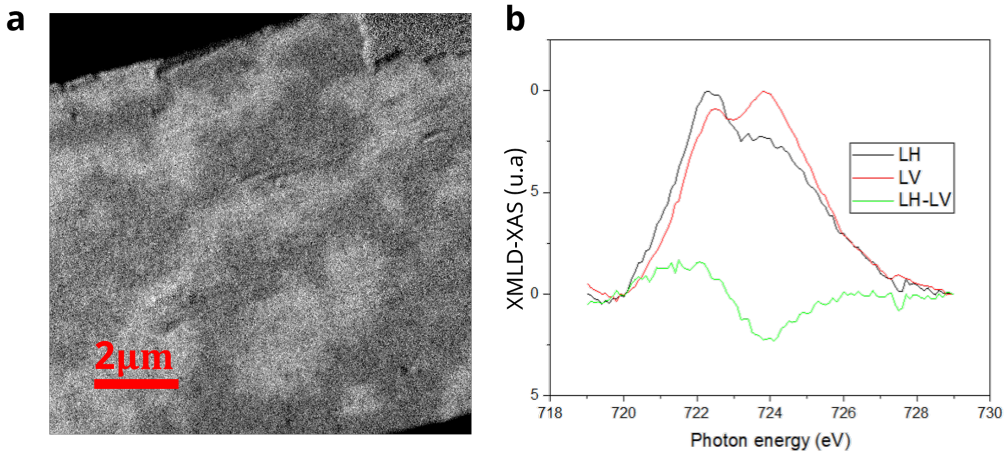

Figure 4.10.: **XMLD and XAS spectra at the easy plane phase of Ti-doped hematite. a** XMLD-PEEM micrograph of Ti-doped hematite obtained using linearly polarized light at the Fe L_2 edge, showing magnetic domain contrast. **b** XAS spectra acquired with linear horizontal and linear vertical polarization and their difference, confirming the XMLD signal used for imaging. Adapted from Galíndez et al., *Adv. Mater.* **37**(2025): e05019, licensed under CC BY 4.0 [41].

4.4.4. Mapping of absolute Néel domains

XMLD-PEEM provides a direct map of the IP Néel order in hematite, because the XMLD intensity depends on the orientation of the Néel vector relative to the polarization plane of the incident X-rays. Fig. **4.11** shows the XMLD-based Néel vector map obtained by rotating the linear polarization and fitting the local angular dependence. The domain pattern is consistent with the multi-domain structure expected for hematite in the high-temperature phase. Importantly, XMLD is insensitive to a 180° reversal of the Néel vector, therefore domains with $\mathbf{n}$ and $-\mathbf{n}$ are indistinguishable in XMLD and appear with identical contrast. This intrinsic 180° ambiguity motivates the complementary XMCD measurements.

XMCD-PEEM probes time reversal symmetry breaking through the projection of an axial quantity onto the incident X-ray direction. In the present context, the relevant axial quantity is the altermagnetic Hall pseudovector, whose components depend on the Néel vector orientation and can invert under a 180° reversal. Fig. **4.11b** shows the XMCD PEEM contrast map acquired at the Fe L_3 edge for the same field-free domain state imaged in XMLD. Strikingly, opposite XMCD contrast levels are observed for domains that share the same XMLD inferred Néel axis, indicating that XMCD resolves the 180° ambiguity of XMLD by providing sensitivity to the sign of the underlying axial response in this measurement geometry.

A Boolean combination of XMLD and XMCD contrasts enables full reconstruction of the absolute IP orientation of the Néel vector. Fig. **4.11c** shows the resulting combined map, where the XMLD-derived Néel axis and the XMCD sign together assign the absolute Néel direction within each domain. This real-space reconstruction directly supports the transport-based interpretation of sign-changing transverse responses, because it establishes that a 180° reversal of the Néel vector is accompanied by an inver-

sion of the XMCD contrast, consistent with a sign reversal of the altermagnetic Hall pseudovector projected onto the X-ray direction. For general contrast mechanisms and data-processing steps,see Chapter 3.

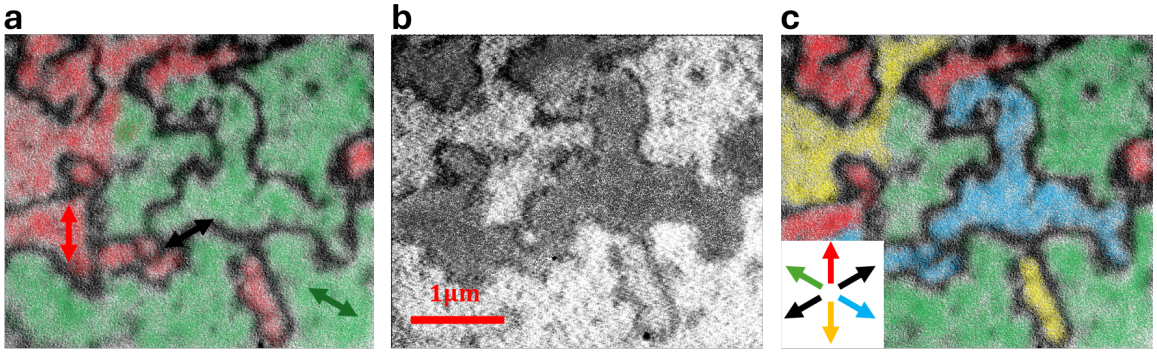

Figure 4.11.: XPEEM micrographs of hematite altermarnetic magnetic domains. **a** XMLD-PEEM Néel vector map of hematite at the Fe L_3 edge, reconstructed from polarization-dependent XMLD contrast. The map resolves the IP Néel vector orientation across domains, but it is intrinsically insensitive to a 180° reversal, so $\mathbf{n}$ and $-\mathbf{n}$ domains are equivalent in XMLD. **b** XMCD PEEM contrast map of hematite at the Fe L_3 edge. Domains that are equivalent in XMLD can show opposite XMCD contrast, providing sensitivity to the sign of the axial response in the present geometry. **c** Boolean combination of XMLD and XMCD contrast, yielding a full real-space reconstruction of the absolute Néel vector orientation across the domain pattern. Adapted from Galíndez et al., *Adv. Mater.* **37**(2025): e05019, licensed under CC BY 4.0 [41].

The transport and imaging results together establish a direct and internally consistent sign relation between the Néel order and the altermagnetic transverse response. In transport, once the system is driven above the spin flop transition where a finite Hall pseudovector is symmetry allowed, a 180° reversal of the Néel vector induced by an IP magnetic field produces a reproducible sign inversion of the transverse resistivity, while the OOP field polarity and the device geometry are kept fixed (Fig. **4.5**). In real space, XMLD-PEEM identifies domains that share the same Néel axis but cannot distinguish $\mathbf{n}$ from $-\mathbf{n}$, whereas XMCD PEEM splits these XMLD equivalent domains into two classes with opposite contrast (Fig. **4.11b**), and the boolean combination yields the absolute Néel vector direction (Fig. **4.11c**). The invariant quantity across this inversion is the crystallographic reference frame and the Néel axis extracted by XMLD, while the sign-changing quantity is the axial contrast associated with the Hall pseudovector projection, which flips upon $\mathbf{n} \rightarrow -\mathbf{n}$. This correlation provides the experimental basis for interpreting the periodic sign alternations of the odd transverse conductivity with Hall bar orientation as a symmetry-driven altermagnetic effect rather than a consequence of the fixed canted moment.

4.5. Summary

This chapter establishes symmetry-controlled transverse transport and real-space magnetic imaging signatures of altermagnetism in hematite (α-Fe_2O_3). Using low-level Ti-doping (1%) to enable electrical conduction while preserving compensated order, angle-dependent Hall measurements on (0001) oriented films reveal that a sizable odd transverse response emerges only once the spin configuration is driven through the spin flop transition, where the magnetic point group becomes compatible with a finite Hall pseudovector. In this symmetry-allowed regime, the odd transverse conductivity exhibits a pronounced dependence on the crystallographic orientation of the current, including periodic sign inversions at specific Hall-bar angles. These sign changes are inconsistent with a response governed solely by the fixed canted moment or by a positively defined IP anisotropy energy, and instead constitute a transport fingerprint of the altermagnetic order parameter. Complementary XPEEM imaging on R-cut hematite resolves the 180° ambiguity of XMLD and provides a full reconstruction of the absolute Néel vector orientation by combining XMLD and XMCD contrast. The observation of XMCD contrast in a compensated magnet, and its correlation with the Néel vector reversal, directly supports the existence of an altermagnetic Hall pseudovector, demonstrating that XMCD and Hall transport probe the same underlying symmetry allowed axial response, but at different energies and with distinct experimental access. More broadly, the results show that controlled doping of insulating altermagnets provides a practical route to expand the experimental materials space for symmetry-resolved electrical transport diagnostics.

Several aspects remain open within the scope of the present study. First, the Ti-doped films are in a low-conductivity regime consistent with hopping-dominated transport, which restricts comparisons to first-principles calculations to symmetry-controlled angular trends rather than absolute conductivities. Accessing a more metallic regime via alternative dopants, higher carrier densities without structural distortion, or different growth conditions would enable a more quantitative comparison with intrinsic Berry curvature conductivities and may yield larger measurable anomalous Hall signals. Second, exploring other crystallographic cuts would provide access to different projections of the AHC tensor components and may yield greater direct transport sensitivity for the larger calculated IP components. Finally, systematic control of the Fermi level position via doping or electrostatic tuning would enable optimization of the magnitude and anisotropy of the AHC and testing of the predicted energy dependence of the AHC components in hematite.

5. Local spin probe in orthoferrites

Local electrical probes based on SOC provide direct access to magnetic order in insulating AFMs, without charge transport through the magnetic layer [101, 143, 194, 210]. In heavy metal/magnet bilayers, a charge current in the metal generates a transverse spin accumulation at the interface via the SHE. The associated spin current is partially absorbed and reflected by interfacial spin transfer, thereby modifying the longitudinal resistance via inverse spin Hall conversion in the metal. This feedback constitutes the SMR, first demonstrated in Pt-ferrimagnetic insulator heterostructures and quantitatively captured by spin diffusion models in terms of the spin Hall angle and the interfacial spin mixing conductance [143, 194, 210].

A central advantage of SMR is that its symmetry is determined by the relative orientation between the current-induced interfacial spin polarization and the magnetic order parameter governing spin-current absorption. SMR therefore remains a sensitive electrical readout and it has become an established probe of AFM order and its field-driven reorientation in insulating systems [261, 262]. In this thesis, SMR plays a dual role. First, it provides a local, symmetry-sensitive reference that identifies the equilibrium orientation of the order parameter and tracks its evolution under applied fields in orthoferrites. Second, it establishes the local probe required to interpret non-local magnon-transport experiments, since injection and detection efficiencies, as well as the sign of the measured response, follow the same interfacial spin-polarization selection rules at the Pt-magnet interface [97].

This chapter is organized as follows. We first summarize the crystallographic conventions and magnetic order of $YFeO_3$ and $LuFeO_3$, which define the symmetry axes relevant for angular-dependent SMR. We then develop the local transport analysis, emphasizing the separation of genuine SMR from spurious magnetotransport contributions of the Pt layer and device geometry, which is essential for a robust symmetry assignment. Finally, we use the background-corrected SMR to electrically track the field-driven reorientation of the magnetic configuration, establishing a local spin probe that is directly comparable to, and consistent with, the non-local magnon-transport signatures discussed in the following chapters.

5.1. Orthoferrites: $YFeO_3$ and $LuFeO_3$

Orthoferrites are wide gap insulating perovskites in which spin angular momentum is carried by magnons rather than itinerant electrons. This makes them a suitable platform to connect crystallographic symmetry, magnetic order, and magnon propagation within a single device geometry. Pt-based heterostructures were patterned in top of high-quality bulk single crystals with well-defined orientations relative to the orthorhombic axes, enabling direct comparisons of transport along symmetry-equivalent and symmetry-inequivalent directions.

5.1.1. Crystal structure and crystallographic axes

Throughout this thesis, device orientations and rotation angles are reported with respect to the orthorhombic **a**-axis. The practical alignment workflow, including the transfer of the crystallographic frame to the lithography frame, is described in Chapter 3. Here, the axis convention is kept fixed, and only the specific orthorhombic directions probed by each device set are stated explicitly. Both materials crystallize in the orthorhombic *Pbnm* structure with oxygen octahedral tilts as shown in Fig. **2.8**. Structural quality and the absence of secondary phases are verified by high-resolution X-ray diffraction (XRD) along the surface normal. Figure **5.1** shows θ–2θ scans measured along the (010) direction for both crystals. For $YFeO_3$, only the expected (020) and (040) reflections are observed, confirming a single oriented phase in the probed volume. For $LuFeO_3$, the θ–2θ scan similarly demonstrates a single-phase orientation along the (020) plane, and together with the IP directions provide the crystallographic directions for assigning device axes relative to the orthorhombic frame.

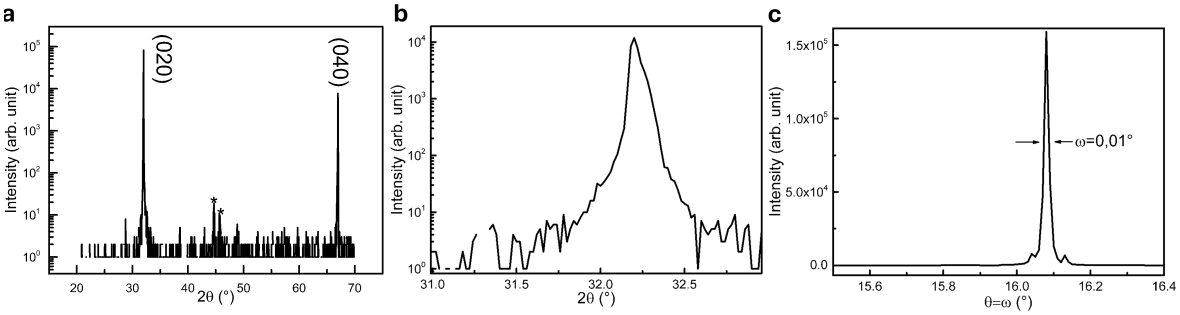

Figure 5.1.: **Structural characterization of the orthoferrite single crystals used for Pt device fabrication.** **a** $YFeO_3$ θ–2θ scan measured along the (010) direction perpendicular to the sample plane. Only (020) and (040) reflections are observed, consistent with single-phase orientation. Peaks marked with a star arise from the aluminium sample holder. **b** $LuFeO_3$ high-resolution θ–2θ scan demonstrating single-phase orientation along the (020) plane. **c** Rocking curve (ω scan) of the $LuFeO_3$ (020) reflection, highlighting the small mosaic spread and high structural coherence. Data in **a** Adapted from S. Das et al., *Nat. Commun.* **13**, 6140 (2022), licensed under CC BY 4.0 [97]. Data in **b,c** adapted from Galíndez et al., arXiv:2508.14569 (2025), licensed under CC BY 4.0 [115].

Beyond phase purity, the mosaic spread is quantified for $LuFeO_3$ by the rocking curve (ω scan) of the (020) reflection, Fig. **5.1(c)**. The narrow rocking curve indicates a small distribution of crystallographic tilt within the illuminated volume, implying a high structural coherence and a well-defined surface normal. For the SMR analysis, this is important because it minimizes uncontrolled admixture between IP and OOP field components during angular scans, and it reduces sample-dependent broadening that can otherwise obscure symmetry-based assignments of the equilibrium configuration.

5.1.2. Magnetic order and weak canting

At room temperature, the Fe sublattice in both $YFeO_3$ and $LuFeO_3$ is well described by the Bertaut Γ_4 configuration, (G_x, A_y, F_z), shown in Fig. **2.9(a)**. Although the weak ferromagnetic canting is small, it provides a practical handle for reproducibly preparing the magnetic configuration and for rotating it with an external field during angle-dependent transport measurements. The role of the DMI, and its relation to the *Pbnm* tilt pattern, is discussed in the orthoferrite subsection of Chapter 2 and is used when interpreting field and angle trends in the transport signals.

An additional advantage of $YFeO_3$ and $LuFeO_3$ is that Y^{3+} and Lu^{3+} are nonmagnetic. The magnetic response at room temperature is therefore dominated by the Fe sublattice, without rare-earth ordering or rare-earth-driven reorientation phenomena that would complicate the interpretation of transport anisotropies [121, 148]. At the same time, the degree of structural distortion varies systematically with the rare earth ionic radius. Orthorhombic $LuFeO_3$ consequently exhibits a larger orthorhombicity and a stronger magnetic anisotropy than $YFeO_3$ [163]. This provides a controlled material axis within the same structural prototype, allowing generic orthoferrite transport features to be separated from those enhanced by distortion and anisotropy. Consistent with this picture, orthorhombic $LuFeO_3$ has been reported to be magnetically hard, with unusually large anisotropy compared with less distorted orthoferrites, highlighting the sensitivity of the magnetic energy landscape to lattice geometry [263].

5.2. Different contributions in Pt/insulator bilayers

In Pt/insulating magnet bilayers, the measured longitudinal and transverse resistances contain several contributions that can share similar field and angular symmetries. Besides the genuine SMR, the metal itself can exhibit field-dependent magnetoresistance terms originating from spin-orbit mediated spin accumulation and orbital transport, and the interface can add proximity-induced galvanomagnetic signals [264]. Since the SMR amplitude in Pt on insulating AFMs can be comparable to these backgrounds, a reliable symmetry assignment of the magnetic configuration requires an explicit separation of the different terms [143, 194, 210].

5.2.1. Spin Hall magnetoresistance

SMR originates from the conversion between charge and spin currents in Pt via the spin Hall and ISHE, combined with spin current absorption and reflection at the Pt-insulator interface, quantified by the interfacial spin mixing conductance [143,194,210]. In the analysis below, we use SMR solely as a symmetry-selective electrical readout of the interfacial spin absorption, set by the magnetic order parameter, whereas the microscopic derivation and fitting formalism are presented in Chapter 2 and Chapter 3. Experimentally, we implement three orthogonal rotation scans, denoted α, β, and γ, as a harmonic filter for the SMR symmetry. In our convention, the γ scan is expected to be constant for ideal SMR, whereas α and β exhibit the characteristic sinusoidal modulation. This internal consistency check is essential because several Pt-based backgrounds can produce field-dependent signals with similar magnitudes but incompatible angular systematics [145].

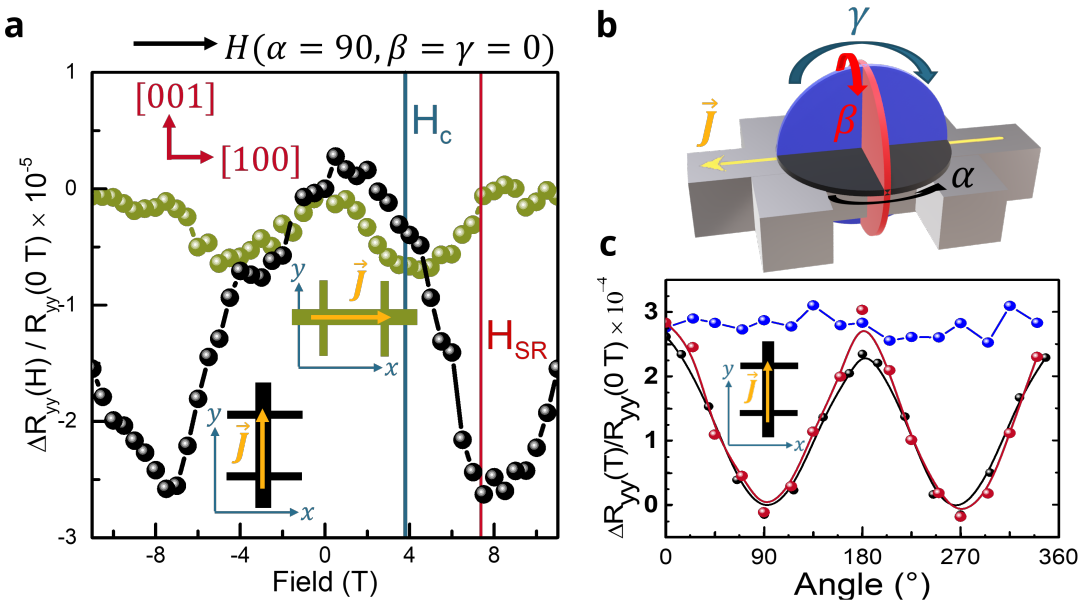

Figure 5.2.: Hallmarks of the magnetoresistance in Pt-orthoferrite bilayers. **a** Comparison of nominally identical Hall bars oriented parallel and perpendicular to the orthorhombic **a**-axis probed in the reorientation experiment. The magnetic reorientation feature is reproduced in both devices, while the parabolic field background differs, indicating a device-dependent Pt contribution. **b** Definition of the α, β, γ rotations with respect to the Hall bar current direction and sample normal. **c** α, β, γ scans of the longitudinal resistance after background correction, illustrating the characteristic SMR harmonics used for the symmetry analysis.

5.2.2. Hanle magnetoresistance in Pt and ordinary magnetoresistance

A dominant nonmagnetic background in thin Pt is Hanle magnetoresistance (HMR). Here, the spin Hall generated spin accumulation in Pt is dephased by Larmor precession in an applied magnetic field, leading to a field-dependent resistance even in the absence of any magnetic layer [265]. Because its angular dependence can resemble SMR-like harmonics, HMR is a critical confounding factor in Pt-insulator bilayers. The effect is conceptually related to earlier predictions that magnetic fields suppress spin accumulation induced by SOC, thereby producing positive magnetoresistance [266]. In addition, Pt shows an ordinary magnetoresistance that is typically smooth and approximately quadratic in field over the range relevant here. In practice, both HMR and ordinary magnetoresistance are treated as Pt-dominated backgrounds whose magnitude can vary between Hall bars due to thickness, microstructure, and geometry, motivating device-to-device comparisons and explicit background modeling in field scans [265].

5.2.3. Hall pickup, misalignment, and geometric contributions

Finite contact misalignment and wiring asymmetries mix transverse voltages into the nominal longitudinal channel. This is particularly relevant when extracting small resistive modulations from a large baseline resistance, because a small transverse signal can mimic longitudinal magnetoresistance. A complementary issue is that interfacial proximity-induced magnetism can generate anisotropic magnetoresistance and anomalous Hall-like contributions in Pt that coexist with SMR in magnetic insulator heterostructures, and can be separated only by combining longitudinal and transverse symmetries and their systematic trends [267]. For this reason, we analyze R_{xx} and R_{xy} in parallel and use the α, β, γ protocol as a geometry-independent symmetry test, rather than relying on a single scan.

5.2.4. Out of plane field effects: ordinary Hall and transverse mixing

OOP magnetic field components generate an ordinary Hall voltage in Pt, which can leak into the measured resistance through geometric pickup. This mixing is most evident in field scans, where the transverse response increases linearly with field strength, whereas the true longitudinal backgrounds vary more slowly. In our devices, the γ scan plays a particular role because it provides a control condition in which the genuine SMR contribution is expected to be constant, so any residual modulation can be attributed to Pt-dominated backgrounds or transverse mixing. Therefore, OOP data are interpreted only after applying the same symmetrization procedure used throughout the thesis, and after verifying that the angular harmonics satisfy the expected SMR selection rules [124, 125, 145, 265].

5.2.5. Control checks (current reversal, reference devices, thickness dependence)

To validate the separation of SMR from nonmagnetic and geometric backgrounds, we employ a set of control checks. Current reversal is used to confirm that the extracted magnetoresistance is symmetric with respect to current and to identify offsets caused by thermoelectric pickup. Reference devices are used to quantify Pt-dominated backgrounds, in particular HMR, under the same measurement conditions as Ref. [265]. Thickness dependence provides an additional discriminator because SMR and HMR scale differently with the Pt spin diffusion length and interfacial transparency, whereas purely geometric pickup is thickness-independent to leading order. Together, these controls ensure that the symmetry assignment and the subsequent extraction of reorientation trends are based on a background-corrected SMR component rather than on Pt intrinsic magnetotransport.

5.3. Electrical tracking of field-driven reorientation in orthoferrites

SMR provides a direct electrical readout of the equilibrium orientation of the antiferromagnetic order parameter at the Pt, orthoferrite interface. In insulating canted AFMs, the measured response is governed predominantly by the Néel vector orientation rather than by the small emergent weak moment, which enables a quantitative tracking of reorientation processes via simple transport measurements [125, 268]. In orthoferrites, an applied magnetic field couples first to the canted component and thereby exerts an effective torque on the antiferromagnetic configuration. Because this torque competes with the magnetocrystalline anisotropy and the DMI induced canting constraints, the reorientation proceeds smoothly over a finite field interval instead of occurring as an abrupt jump.

Figure **5.3** summarizes the field dependence of the basic SMR used in this thesis; however, the easiest protocol to eliminate monotonic spurious contributions is the field derivative.

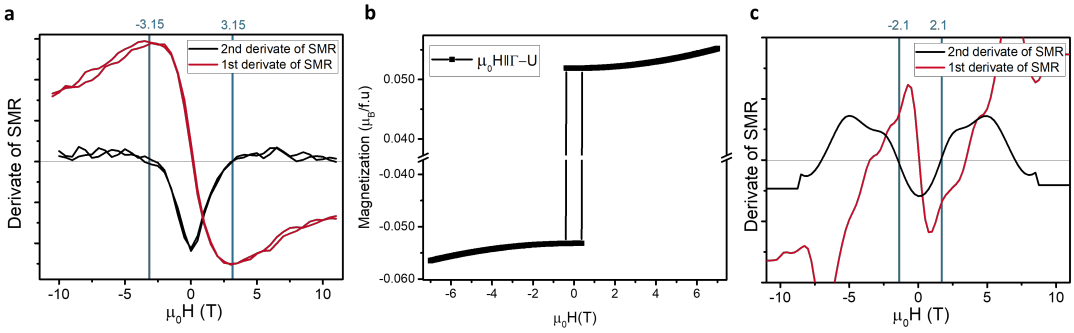

Figure 5.3.: **Analysis of the saturation magnetic field in orthoferrites via spin Hall magnetoresistance. a.** First and second derivatives of the SMR signal in $LuFeO_3$ signal with the current along the Γ–U axis; saturation is determined from the zero-crossing of the second derivative. **b.** Canted magnetic moment versus applied magnetic field along the Γ–U direction, indicating a transition from Néel alignment to enhanced canting after 3 T. **c.** First and second derivatives of the SMR in $YFeO_3$ signal with the current along the Γ–X axis; saturation is determined from the zero-crossing of the second derivative. The external magnetic field is always oriented along the current channel. Error bars not visible, representing 1×10^{-3}%. Adapted from Galíndez et al., arXiv:2508.14569 (2025), licensed under CC BY 4.0 [115].

The derivative representation provides a robust, geometry-independent method for identifying the characteristic reorientation scale because its roots are insensitive to constant offsets and to linear or quadratic Pt backgrounds. Operationally, we define the critical field H_c as the field where the SMR first derivative reaches its maximum high field plateau and where the second derivative approaches zero within the experimental uncertainty, corresponding to a fully established high field magnetic configuration in the device volume relevant for interfacial spin absorption.

From this analysis we extract the critical fields of $H_c = 3.15(3)\,\mathrm{T}$ for $LuFeO_3$ and $H_c = 7.1(1)\,\mathrm{T}$ for $YFeO_3$. These values set the field scale over which the maximum change in smooth reorientation occurs, and, beyond this point, the field evolution is expected to be dominated by spurious contributions as the interfacial order parameter effectively saturates in our device geometry. After knowing the critical field, a background can be safely subtracted at $H_{SF} = 1.5H_c$. This is consistent with the field range over which the sigmoidal evolution of the thermal non-local response R_{th} is maximum in the following chapters [97, 115].

5.3.1. Angular scans at fixed field: identifying the equilibrium configuration

To identify the equilibrium configuration relevant for interfacial spin absorption, we perform angular-dependent SMR scans at a fixed magnetic field. At sufficiently high fields, well above the saturation scale extracted from the derivative analysis, the magnetic configuration becomes single valued in the measurement history, and the SMR harmonics are governed primarily by the saturated orientation of the order parameter at the interface. In this regime, the longitudinal and transverse responses exhibit reproducible sinusoidal modulations with the expected phase relation, and the extracted extrema provide a direct electrical criterion for assigning the equilibrium orientation relative to the orthorhombic axes. Conversely, at fields below the saturation scale, the angular response can be distorted by partial rotation, which can shift extrema and reduce the apparent amplitude. We therefore use the high-field angular scans as the reference state that anchors the symmetry assignment used throughout this chapter and in the interpretation of the non-local transport data, even when those contain a higher Pt contribution [97, 115]. The magnitude of the longitudinal SMR in $YFeO_3$ and $LuFeO_3$ is in the 10^{-5} range in the 200-300 K temperature zone.

5.3.2. Field scans: continuous rotation and characteristic fields

Field-dependent SMR traces provide a complementary view of the reorientation process. Instead of an abrupt transition, the SMR evolves smoothly with the field, reflecting a continuous rotation of the magnetic configuration under competition among Zeeman coupling, anisotropy, and canting constraints. At low fields, the response is sensitive to the reversal of the weak canted moment, which can generate a small "loop" around zero field in both longitudinal and transverse channels. This low-field feature is a signature of the weak ferromagnetic component and its reversal, while the dominant high-field evolution tracks the progressive reorientation of the antiferromagnetic order parameter toward its saturated configuration. The characteristic field scale is quantified by the saturation field H_c extracted from the field derivative of the background corrected SMR, as introduced above.

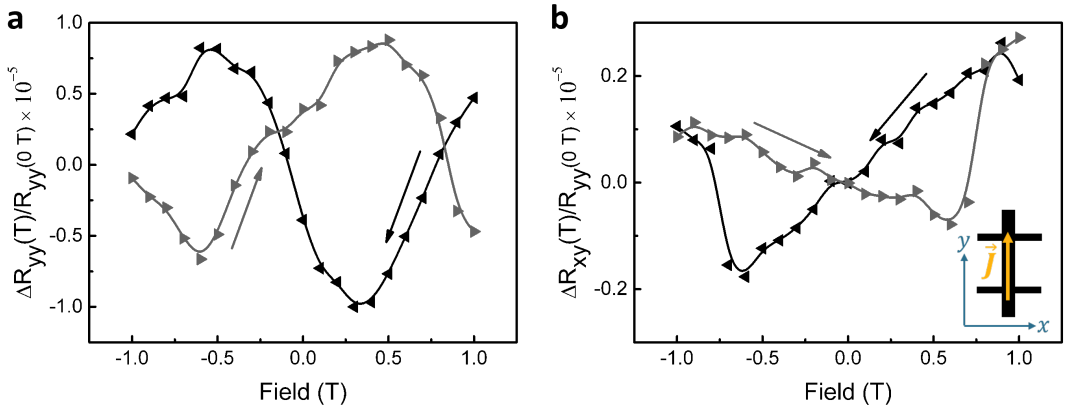

Figure 5.4.: Low field behaviour of the longitudinal and transverse SMR. **a** Longitudinal and **b** transverse SMR response showing a small loop around zero field associated with reversal of the weak canted moment.

5.3.3. Consistency with injector and detector selection rules in non-local transport

The same interfacial spin transparency that produces SMR governs the efficiency of spin injection and detection in non-local magnon-transport experiments. In particular, the current-induced interfacial spin polarization selects which components of the magnetic order parameter absorb spin angular momentum, and this selection rule controls both the SMR amplitude and the sign and magnitude of the electrically and thermally generated non-local signals. Therefore, the SMR-based symmetry assignment provides a starting point for the non-local measurements. In the saturated field regime, the angular positions of extrema in SMR coincide with the angular conditions that maximize non-local injection and detection efficiency, and the field scale over which SMR saturates matches the field range where the sigmoidal evolution of the thermal signal R_{th} saturates. This agreement establishes that the non-local response is interpreted within a consistent interfacial spin polarization framework, rather than being dominated by device-specific artifacts or Pt intrinsic magnetotransport [97, 115].

5.4. Summary

In this chapter, we established SMR as a local electrical probe of the magnetic configuration in insulating orthoferrites. After fixing the crystallographic conventions for $YFeO_3$ and $LuFeO_3$, we used angular-dependent SMR as a symmetry-selective readout of the equilibrium orientation of the order parameter at the Pt, orthoferrite interface. We then identified and separated non-SMR contributions that can mask the signal in Pt, insulator bilayers, including Hanle magnetoresistance and ordinary magnetoresistance in Pt, geometric pickup and Hall mixing, and OOP field-induced transverse leakage.

Using the background corrected SMR, we electrically tracked the field-driven reorientation in both materials and showed that the evolution is continuous rather than abrupt. From the derivative analysis we extracted characteristic saturation fields of

$H_c = 3.15(3)\,\mathrm{T}$ for $LuFeO_3$ and $H_c = 7.1(1)\,\mathrm{T}$ for $YFeO_3$, which define the field scale over which the interfacial configuration relevant for spin absorption becomes saturated in our devices [97, 115]. Finally, we demonstrated that the SMR-based symmetry assignment is consistent with the injector- and detector-selection rules underlying the non-local magnon transport experiments discussed in the following chapters, thereby providing a self-consistent local probe for interpreting direction-dependent non-local signals.

6. Anisotropic non-local magnon transport in orthoferrites

Magnon-mediated spin transport provides an experimental route to access the collective spin excitations in insulating magnets, without invoking charge motion in the magnetic medium. In a non-local geometry [47, 48], a charge current in a heavy-metal injector generates a spin accumulation via the SHE and a local temperature rise via Joule heating [101, 269]. Both pathways create a non-equilibrium magnon population in the adjacent magnet. This population diffuses and is detected electrically in a second metal strip through the ISHE. Injector–detector measurements have therefore become a standard probe of magnon diffusion, relaxation, and polarization selection rules in magnetic insulators [105, 106, 174].

In compensated magnets, magnon transport is particularly sensitive to mode polarization and symmetry [107, 261, 270]. In a collinear AFM, the two low-energy magnon branches carry opposite angular momentum and, in equilibrium, their contributions cancel [107]. A finite detected signal, therefore, requires controlled symmetry breaking, for example, by injected polarized magnons, an applied magnetic field, or internal interactions that lift degeneracies. Long-distance non-local transport has been established experimentally in AFMs, demonstrating that antiferromagnetic order can support diffusive magnon spin currents over micrometer scales under suitable conditions [48, 49, 271, 272]. These results motivate the use of non-local measurements not only as a transport metric, but also as a spectroscopic tool that reveals which magnon modes carry angular momentum under a given symmetry setting.

This chapter establishes the starting point for non-local magnon transport in orthoferrites by using $YFeO_3$ as the reference system, following Ref. [97], where magnons propagate in an orthorhombic anisotropy landscape, and the weak canting enables reproducible reorientation of the Néel order. Rather than reviewing the background on orthoferrite materials here, the crystallographic and magnetic context, together with the corresponding local transport phenomenology, is introduced in the orthoferrite-focused section of the Chapter 5. In the present chapter, the emphasis is on non-local response functions and how their field and distance dependencies encode anisotropic magnon generation, propagation, and detection. In this chapter, the theoretical model used to fit the experimental data was developed by Dr. Helen Gomonay in the group of Prof. Dr. Jairo Sinova at JGU-Mainz. Details of the model can be found in Appendix G.1. The experiments in this chapter where leaded by Dr. S. Das with assistance in the measurements and analysis by the author.

A central experimental reference point is the anisotropic long-range non-local magnon transport reported in $YFeO_3$, where the detected non-local signal depends strongly on crystallographic direction and on the field-driven reorientation of the Néel order [97]. Building on this, the chapter develops the non-local detection formalism, separates thermal and spin-bias contributions through polarity analysis, and extracts anisotropic

magnon decay lengths from distance-dependent datasets. These results provide the starting point that will be used in the subsequent chapter on altermagnetic magnon transport, where the same non-local observables are reinterpreted in a symmetry-classified framework and extended to nonconventional transport directions [115].

This chapter presents the non-local magnon spin transport in the canted antiferromagnetic orthoferrite $YFeO_3$ from Ref. [97]. The emphasis is placed on injector–detector measurements with Pt strips patterned along selected crystallographic directions, on the separation of polarity-odd (spin-bias) and polarity-even (thermal) contributions, and on the extraction of anisotropic magnon propagation lengths from distance-dependent datasets. These results establish $YFeO_3$, and potentially the orthoferrite family, as a promising starting point for nonconventional transport directions and symmetry-selected responses discussed in the next chapter (Chapter 7).

6.1. Experimental overview

Since orthoferrites are insulating, the relevant low-energy transport channel is magnonic. The Chapter 2 establishes that altermagnetic symmetry constraints can imprint a momentum-dependent alternation on the different magnon branches, yielding nodal manifolds where the magnon branches remain degenerate and generic directions where a finite splitting is allowed. Figure **2.8b** summarizes this fingerprint for orthoferrites. In the present chapter, this symmetry input is used operationally. Rather than reconstructing the full dispersion, we focus on transport-level consequences, namely directional selectivity in magnon propagation and detection, encoded in the orientation dependence of the non-local signals.

Non-local Pt injector–detector devices were fabricated on $YFeO_3$ single crystals with well-defined orientations relative to the orthorhombic axes, and with a systematic set of injector–detector separations to enable quantitative distance-dependent analyses. Electrical non-local transport measurements were performed over a range of magnetic fields and device orientations relevant to the canted antiferromagnetic state. The detector voltages were decomposed into polarity-even and polarity-odd components under current reversal, thereby isolating thermal-gradient-driven and spin-bias-driven responses within the same protocol. Magnon propagation lengths were obtained by fitting the separation dependence of the non-local response to an exponential decay model, and the resulting decay lengths were compared across crystallographic directions to quantify the transport anisotropy [97].

The experiments employ a standard non-local geometry with two parallel Pt strips acting as injector and detector on the $YFeO_3$ surface. A charge current in the injector generates a spin accumulation at the Pt|$YFeO_3$ interface via the SHE, which excites a nonequilibrium magnon population in the magnetic insulator. The resulting magnon spin current diffuses to the detector, where it is converted into a voltage via the ISHE.

The general injection and detection mechanisms are introduced in the Chapter 2 (Sec. 2.2.1). At the same time, the crystallographic alignment, device fabrication, and electrical readout procedure are described in the Chapter 3.

The measured detector voltage is decomposed under current reversal (Sec. 3.2.3) into a polarity odd component, V_{el}, and a polarity even component, V_{th}. In this convention, R_{el} captures spin Hall-driven spin-bias injection (non-local spin-bias resistance), whereas R_{th} captures thermally generated signals driven by Joule heating (non-local

thermal resistance).

In $YFeO_3$, the magnetic order in the temperature range relevant for the non-local transport experiments is well described by the Γ_4 configuration (Fig. **2.9(a)**), with the Néel vector predominantly aligned along the orthorhombic **a** axis and a weak ferromagnetic canting along **c** [97, 121, 273].To quantify directional anisotropy in magnon propagation, the injector–detector separation vector was aligned along the orthorhombic **a** axis (easy axis) or along the orthorhombic **c** axis (intermediate axis), enabling a direct comparison of amplitudes and decay lengths between two inequivalent crystallographic directions [97].

6.2. Field dependence of the non-local response

To disentangle current-driven spin bias injection from Joule heating-driven magnon generation, the non-local voltage is decomposed into a polarity-odd component, R_{el}, and a polarity-even component, R_{th}. The latter scales with I^2 and is reported in units of $\mathrm{V\,A^{-2}}$, consistent with a thermal origin. Figure **6.1** compares both contributions for the two crystallographic transport configurations under a magnetic field applied along the orthorhombic easy axis.

A pronounced anisotropy is observed between the two device configurations. The magnitude and field evolution of R_{el} differ qualitatively depending on how the device axes are oriented with respect to the magnetic easy axis. This anisotropy reflects two coupled effects that are specific to canted AFMs in the weak ferromagnetic phase of $YFeO_3$. First, the applied field drives a continuous reorientation of the Néel vector within the orthorhombic anisotropy landscape [97, 274, 275]. Second, the field also modifies the magnon eigenmode polarization, which controls how efficiently angular momentum can be carried by magnons and therefore how efficiently a spin-bias can be injected, transported, and detected [97, 276]. In the following, this experimentally established field response is used as the starting point against which symmetry-selected directions in the altermagnetic analysis are compared in Chapter 7. The thermal signal provides an internal control that ensures magnon generation and detection remain robust across the full field range, even when the electrical signal is suppressed by symmetry and mode polarization. In particular, R_{th} exhibits a pronounced field dependence with characteristic features around the reorientation field scale, and it remains finite at high fields, consistent with a thermally generated non-equilibrium magnon population whose coupling to the detector depends on the field-controlled magnetic configuration [97]. For completeness, measurements with the magnetic field applied along the orthorhombic **c**-axis show no reorientation of the Néel vector and little to no detectable electrical non-local signal across the full field range, whereas the thermal response remains finite; see Appendix G.2.

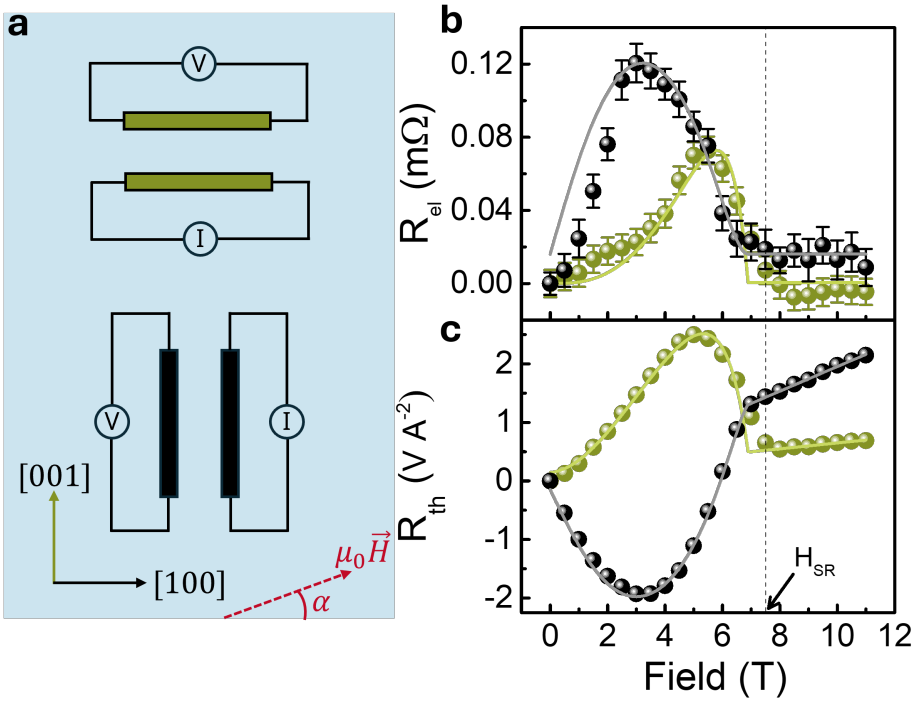

Figure 6.1.: **Field dependence of the non-local magnon spin transport in $YFeO_3$.** **a** Schematics of the two *orthorhombic* devices orientations used in this chapter: patterned along **a**-axis (green) and along **c**-axis (black). **b** Non-local spin-bias resistance R_{el} **b** non-local thermal resistance R_{th}; measured as a function of magnetic field (along the **a**-axis) for devices probing the two principal crystallographic transport configurations, patterned along the **a**-(green) and the **c**-axis(black). Adapted from S. Das et al., *Nat. Commun.* **13**, 6140 (2022), licensed under CC BY 4.0 [97].

The characteristic field dependence of the polarity odd non-local response R_{el} can be rationalized using the two-sublattice theory developed in the Supplementary Information of Das et al. [97]. The essential ingredients are a field-driven reorientation of the equilibrium Néel vector $\mathbf{n}^{(0)}(H)$ within the orthorhombic anisotropy landscape, together with a field-induced ellipticity of the magnon eigenmodes that sets the spin angular momentum carried by each branch and therefore the efficiency of spin bias injection and detection [52, 277]. Operationally, the non-local signal factorizes into a geometric projection term and a field-dependent amplitude,

$$R_{\mathrm{el}}(H,d) = \mathcal{A}_{\mathrm{el}}(H)\exp\left(-\frac{d}{\lambda_{\mathrm{m}}(H)}\right)\left(\hat{\boldsymbol{\mu}}_s \cdot \mathbf{n}^{(0)}(H)\right)^2, \tag{6.1}$$

where $\hat{\boldsymbol{\mu}}_s$ is the interfacial spin accumulation direction set by the Pt current, $\lambda_{\mathrm{m}}(H)$ is the magnon decay length, and $\mathcal{A}_{\mathrm{el}}(H)$ collects the field dependence originating from the magnon mode polarization and thermal occupation [97]. The full derivation, including the equilibrium reorientation, the definition of the critical field, and the relation between ellipticity and dynamical magnetization, is provided in Appendix G.1.

6.2.1. Angular dependence under in-plane field rotation

Having established the characteristic field dependence for fixed crystallographic transport directions, the symmetry of the non-local response can be further tested by rotating the magnetic field in the sample plane. This measurement probes how the electrical and thermal non-local signals evolve as the Néel vector continuously reorients and the weak canting moment varies within the orthorhombic anisotropy landscape.

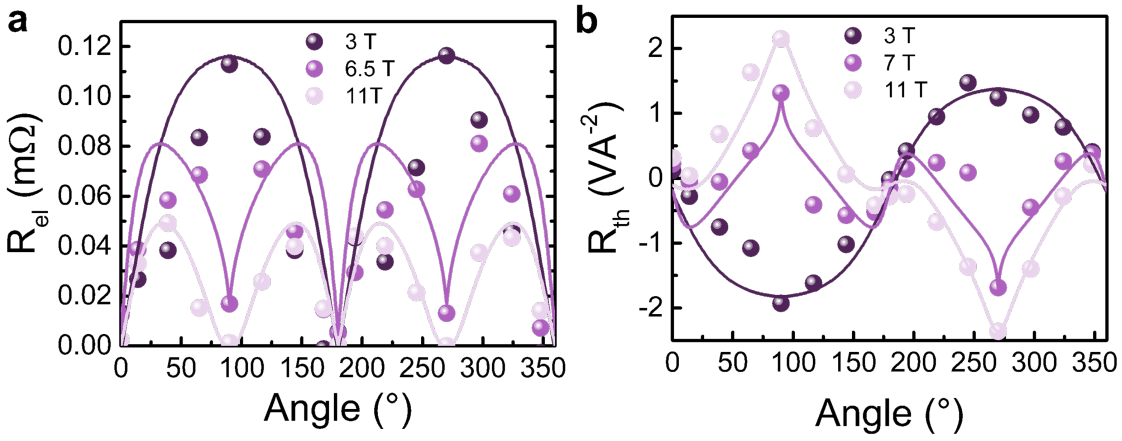

Figure 6.2.: **Angular dependence of non-local responses in $YFeO_3$.** Angular dependence of the **a** polarity odd signal R_{el} and the **b** polarity even signal R_{th} for several magnetic field magnitudes under IP rotation. Solid lines represent fits based on the magnon-dynamics model used in the original work, with a constant offset subtracted from the experimental data. Wires are oriented along the **c**-axis, and the angle is defined as 0 along the wire and increments counterclockwise. Adapted from S. Das et al., *Nat. Commun.* **13**, 6140 (2022), licensed under CC BY 4.0 [97].

Both R_{el} and R_{th} show clear angular modulations whose phase and amplitude evolve with field magnitude, consistent with the fact that the injected spin accumulation, the detector sensitivity axis, and the field controlled Néel vector are coupled through projection factors and through field dependent magnon polarization. The agreement with the model fits supports the interpretation that the anisotropic transport is not purely geometric; instead, it reflects field-controlled mode ellipticity and reorientation of the equilibrium order parameter, which together set the efficiency of magnon spin injection and detection [97].

6.3. Distance dependence and extraction of the magnon decay length

With the field and angular dependencies establishing the symmetry-controlled injection and detection efficiency, the spatial decay with injector–detector separation provides the quantitative metric for anisotropic magnon propagation through the extracted decay length λ. To quantify the characteristic propagation length of the non-equilibrium magnon population, the injector–detector separation d was systematically varied across

multiple devices while keeping the Pt thickness, strip width, and measurement protocol fixed (Sec. 6.2). Figure **6.3** shows the distance dependence of the polarity-odd, spin-bias-driven non-local response R_{el} for the two high-symmetry transport directions. A clear decay with increasing d is observed, enabling an extraction of the characteristic magnon decay length.

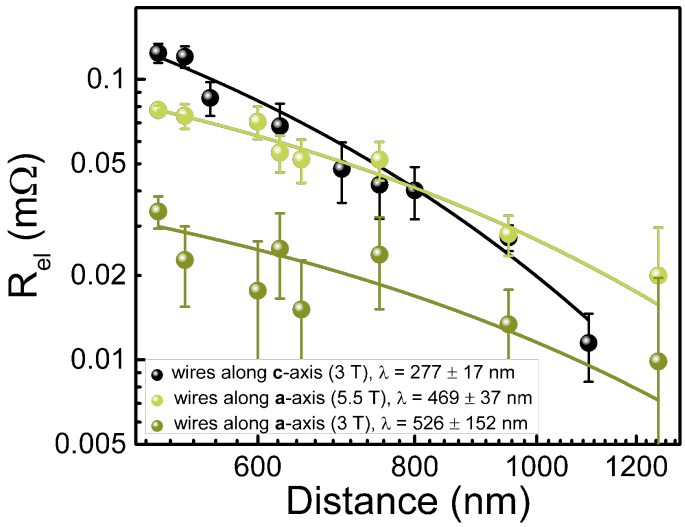

Figure 6.3.: **Distance dependence of the non-local spin-bias signal in $YFeO_3$.** Non-local electrical (polarity-odd) response R_{el} measured as a function of injector–detector separation d for devices probing the two principal crystallographic transport configurations (Green is for wires patterned along **a**-axis, black is for wires patterned along **c**-axis). Solid lines are fits to an exponential decay used to extract the magnon decay length λ. Adapted from S. Das et al., *Nat. Commun.* **13**, 6140 (2022), licensed under CC BY 4.0 [97].

In the non-local geometry, the injector generates a non-equilibrium magnon chemical potential (or, equivalently, a non-equilibrium magnon spin accumulation) that diffuses away from the injector and is detected via the ISHE at the remote Pt strip. In the steady-state diffusive limit, the relevant non-equilibrium magnon density $\delta n_{\mathrm{m}}(\mathbf{r})$ (or $\mu_{\mathrm{m}}(\mathbf{r})$) satisfies a diffusion–relaxation equation of the form [97, 106]

$$D_{\mathrm{m}}\,\nabla^2\mu_{\mathrm{m}} - \frac{\mu_{\mathrm{m}}}{\tau_{\mathrm{m}}} = 0, \qquad \lambda \equiv \sqrt{D_{\mathrm{m}}\tau_{\mathrm{m}}}, \tag{6.2}$$

where D_{m} is an effective magnon diffusion constant and τ_{m} the magnon relaxation time. For injector–detector separations larger than the strip width and in the regime where a single length scale dominates, the non-local electrical response is well captured by an exponential attenuation with distance [97, 106]

$$R_{\mathrm{el}}(d) \;\propto\; \exp\!\left(-\frac{d}{\lambda}\right). \tag{6.3}$$

In practice, the measured non-local signal includes a geometry- and interface-dependent prefactor. A convenient fitting form is therefore

$$R_{\mathrm{el}}(d) = R_0\,\exp\!\left(-\frac{d}{\lambda}\right), \tag{6.4}$$

with R_0 absorbing the injector efficiency, the detector transduction efficiency, and the effective cross-sectional coupling between Pt and the magnon system. For each crystallographic orientation, $R_{\mathrm{el}}(d)$ was determined at a fixed magnetic field where the electrical signal is well developed, and the magnetic configuration is reproducible [97]. The extracted λ values are obtained by fitting Eq. (6.4) to the distance series across multiple nominally identical devices, where the fit uncertainty captures both the electrical noise floor and the device-to-device scatter. Because injector and detector fabrication, Pt thickness, and the measurement electronics are identical for the two orientations, systematic differences in R_0 primarily reflect orientation-dependent interfacial spin conversion and are not sufficient to mimic an apparent change in λ over the full distance range. The extracted values demonstrate an apparent crystallographic anisotropy: the magnon decay length λ is significantly larger when the transport direction is aligned with the magnetic easy axis than when it is perpendicular to it [97]. Importantly, this anisotropy cannot be accounted for by purely geometric factors of the lithographic design (strip widths, separation definition, or current distribution), since those are nominally identical by construction and would affect R_0 more directly than the exponential slope. The orientation dependence of the *slope* in a semilog plot of $R_{\mathrm{el}}(d)$ therefore indicates an intrinsic direction selectivity of magnon propagation in $YFeO_3$. Within the diffusive picture of Eq. (6.2), the anisotropy of λ implies that either D_{m} and/or τ_{m} is direction dependent in $YFeO_3$. Microscopically, such anisotropy is expected in orthorhombic orthoferrites due to the combination of anisotropic exchange pathways (set by the orthorhombic tilts), magnetocrystalline anisotropy, and the symmetry-selected magnon polarization discussed in the Chapter 2. In particular, if the propagating magnon modes that couple most efficiently to the interfacial spin accumulation have different group velocities and/or scattering rates along inequivalent crystallographic directions, the effective transport length λ becomes intrinsically direction dependent. The experimentally extracted anisotropy of λ in Fig. **6.3** is therefore consistent with symmetry-constrained spin-wave dynamics in orthoferrites and provides an experimentally start point for the altermagnetic symmetry analysis developed later in Chapter 7 [97].

6.4. Temperature dependence of the non-local electrical signal

The temperature dependence provides an additional constraint on the transport mechanism, since the non-local signal depends on both the thermal magnon occupation and on the relaxation processes that determine the magnon propagation length and mode polarization. To isolate this effect experimentally, the electrical non-local response was measured as a function of temperature at a fixed magnetic field, in the configuration in which the Pt wires are perpendicular to the easy axis.

The systematic temperature evolution demonstrates that electrically detected magnon spin transport remains measurable across a broad temperature range in $YFeO_3$. Within the diffusive picture, the observed change of $R_{\mathrm{el}}(T)$ reflects a combined temperature dependence of the effective propagation length and the mode-resolved spin angular momentum, which enters through the field-controlled ellipticity and the branch imbalance factor in the electrical injection pathway [97].

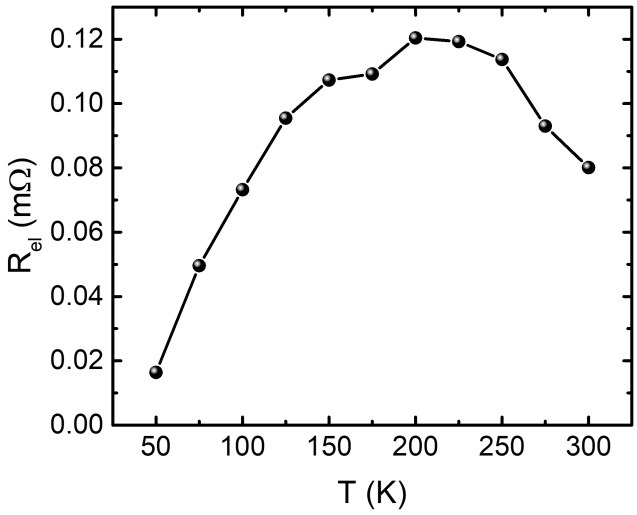

Figure 6.4.: **Temperature dependence of the non-local electrical response in $YFeO_3$.** Polarity odd non-local signal R_{el} as a function of temperature at $H = 3$ T for devices in which the Pt wires are perpendicular to the easy axis. Reproduced from S. Das et al., *Nat. Commun.* **13**, 6140 (2022), licensed under CC BY 4.0 [97].

6.5. Summary

Non-local transport measurements in $YFeO_3$ establish a start point for magnon-mediated spin transport in canted antiferromagnetic orthoferrites. First, electrically detected magnon spin transport persists over several hundred nanometres at experimentally accessible temperatures and magnetic fields, demonstrating that the orthoferrite magnon system can sustain diffusive spin currents on sub-micrometre length scales [48, 97, 106]. Second, both the field dependence and the extracted magnon decay length are strongly crystallographically anisotropic, consistent with the combined role of orthorhombic anisotropy and field-controlled magnon mode polarization in setting the efficiency of injection, propagation, and detection [97].

These results define the conventional reference case along high-symmetry directions (easy-axis versus perpendicular transport) and provide the experimental observables used throughout the remainder of this thesis, namely the polarity-separated responses R_{el} and R_{th} and the corresponding decay length λ. In the following Chapter 7, the same non-local observables are measured along nonconventional crystallographic directions and reinterpreted in terms of altermagnetic symmetry, enabling field-free transport and direction-dependent sign reversals that are absent in the high-symmetry directions [115].

7. Altermagnetic magnon transport in d-wave orthoferrites

Magnon transport along the high symmetry orthorhombic axes established in Chapter 6 provides the starting point for anisotropic non-local propagation in orthoferrites, where the field controlled reorientation of the Néel order and the mode polarization determine the magnitude and decay length of R_{el} and R_{th} [97]. In this chapter, we move beyond these high symmetry directions and probe crystallographic orientations in the **a**–**c** plane where altermagnetic spin splitting is symmetry allowed, as identified in the Chapter 2 and summarized for orthoferrites in Fig. **2.8**, namely the reciprocal space paths Γ–U and Γ–U' that has its corresponding direction in real space [19,88,95,115]. This chapter includes theoretical input spanning atomistic spin modelling, linear spin-wave theory, and atomistic spin-dynamics simulations. Calculations were carried out by the group of Prof. Dr. Ulrich Nowak at Universität Konstanz. Computational details, including model construction, the implementation of the altermagnetic exchange splitting, and the simulation protocols for transport and hysteresis, are provided in Appendix E.2 [88, 98, 118, 278–285].

The underlying connection between reciprocal and real space is analogous to the diffraction picture in X-ray scattering, a chosen $\vec{k}$ direction selects a family of lattice planes and their normal, while magnons with wave-vector $\vec{k}$ propagate as plane wave excitations relative to these planes, so that selecting the transport direction amounts to selecting the symmetry allowed or symmetry forbidden sectors of the magnon spectrum. Experimentally, we implement this selection by patterning Pt injector detector devices at fixed IP angles ϕ with respect to the orthorhombic **a** axis, using $\phi_{\mathrm{AM}} = \arctan(a/c)$ for the altermagnetic directions, $\phi_{\mathrm{AM}}^{\mathrm{YFeO_3}} \approx 34.77°$ and $\phi_{\mathrm{AM}}^{\mathrm{LuFO}} \approx 34.36°$, and adopting a common design value $\phi = \pm 34.5°$ given the experimental constraints from the XRD azimuthal resolution of 0.1° and a typical lithographic alignment uncertainty of about 0.5°. We call to $+34°$ the $\Gamma - U'$ direction and to $-34°$ the $\Gamma - U$ direction, the two altermagnetic directions illustrated in Fig. **7.1a**.

Transport along the orthorhombic **a** and **c** axes is retained as a control, where altermagnetic contributions cancel by symmetry, and the response reduces to the conventional behavior discussed previously. Similar as the previous chapter, the non-local electrical and thermal response functions are reported as R_{el} (non-local spin bias resistance) and R_{th} (non-local thermal resistance) defined in Eq. 3.27. The experimental readout scheme, Delta mode protocol, and the treatment of offsets and background contributions are as described in the Chapter 3. The $YFeO_3$ measurements performed within this chapter were made as a part of a Mr. Jonas Köhler Master thesis, with the supervision and assistance of the author.

7.1. Thermally excited magnons along altermagnetic directions

We begin by probing thermally generated magnons in the nonlocal geometry, using the polarity even response R_{th} defined in Eq. 3.27. In this channel, the injector current produces Joule heating and a local temperature gradient, which excites a nonequilibrium magnon population in the orthoferrite, and the resulting magnon spin current is converted into a detector voltage via the ISHE in Pt [48, 97, 106]. Because the thermal excitation does not impose a selected spin polarization, a finite electrical detection requires that the magnons arriving at the detector carry a nonzero net spin angular momentum density, meaning that the contributions of opposite helicities do not fully cancel when integrated over the thermally occupied modes [95, 98, 107].

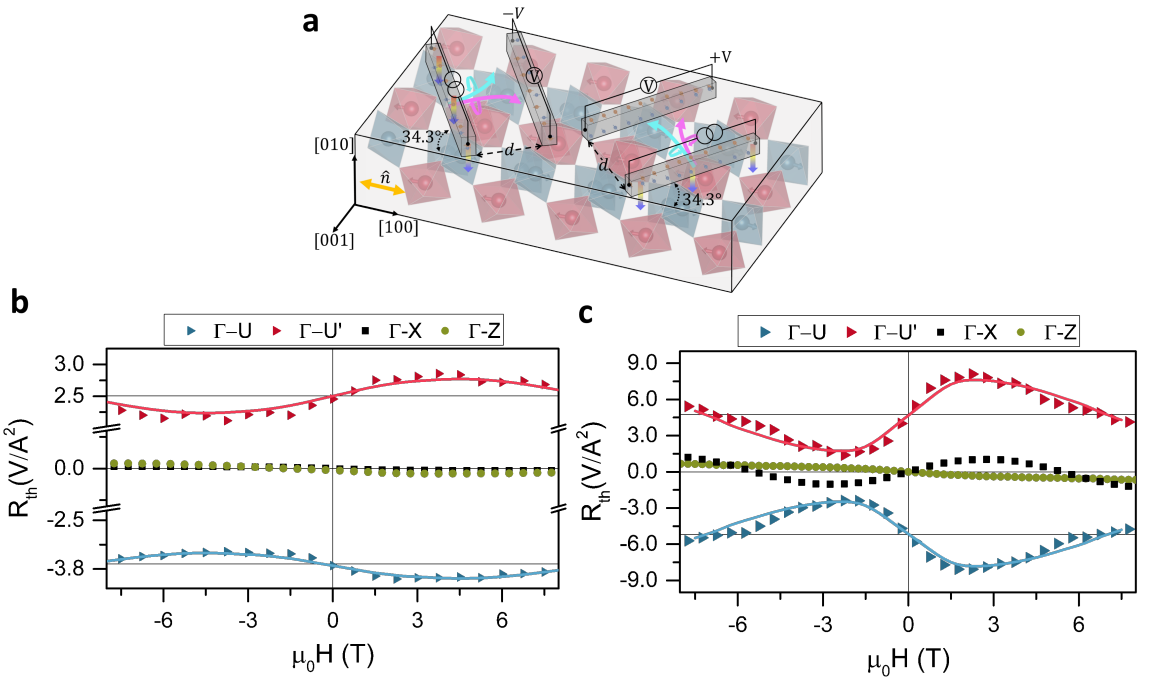

Figure 7.1.: **Altermagnetic non-local thermal magnon transport. a** Schematic of the non-local geometry and the crystallographic transport directions used to test altermagnetic symmetry, where the altermagnetic directions in the orthorhombic **a**–**c** plane correspond to the reciprocal space paths Γ–U and Γ–U'. Non-local thermal resistance $R_{\mathrm{th}} = V_{\mathrm{th}}/I^2$ in **b** $LuFeO_3$ and **c** $YFeO_3$ measured along the two altermagnetic directions, compared to the high symmetry control directions along the **a**-axis and **c**-axis. A linear background was subtracted to account for Pt-related contributions. The solid lines represent the projection factor associated with the field-controlled Néel vector configuration, weighted by the simulated magnon magnetization in the corresponding direction. Adapted from Galíndez et al., arXiv:2508.14569 (2025), licensed under CC BY 4.0 [115].

Figure **7.1** summarizes the central experimental observation of this section. For both $LuFeO_3$ and $YFeO_3$, the nonlocal thermal signal measured along the two symmetry-

related altermagnetic directions has opposite sign, even though the measurement geometry and the detector transduction are otherwise equivalent. This sign inversion between Γ–U and Γ–U' indicates that the net magnon spin angular momentum reaching the detector reverses between the two directions, namely the imbalance between opposite magnon modes changes sign when the propagation direction is rotated by 90° within the **a**–**c** plane. At the same time, transport along the high symmetry **a** and **c** directions yields only a strongly reduced response, establishing these orientations as internal controls where the symmetry allowed altermagnetic contribution cancels or is suppressed [97, 115]. Consistent with the symmetry argument, reversing the propagation direction along the same crystallographic orientation (i.e., $\vec{k} \rightarrow -\vec{k}$) does not invert the thermal signal sign, whereas rotating the transport axis between Γ–U and Γ–U' does.

A second key feature is that the thermal signal along the altermagnetic directions remains finite at zero applied magnetic field. This is in qualitative contrast to the conventional high-symmetry directions of Chapter 6, where a sizable nonlocal response typically requires a field to tune the magnon polarization and the injection and detection efficiency [97]. Here, the persistence of R_{th} at $H = 0$ shows that a symmetry allowed imbalance of thermally occupied magnon modes can generate a measurable net magnon spin angular momentum without relying on external Zeeman splitting. In addition, the very small magnitude of the **c** axis control signal demonstrates that the weak ferromagnetic canting, while present in orthoferrites, cannot account for the dominant response, consistent with the separation between a low field canting related contribution and the much larger altermagnetic signal discussed below and in the literature [97, 115, 286].

The field evolution of R_{th} follows a sigmoidal trend with a characteristic saturation scale H_{c}. In the next subsection, we connect this behavior to a smooth IP rotation of $\mathbf{n}^{(0)}(H)$ and to the independently extracted H_{c} values from SMR.

7.1.1. Field dependence and Néel vector rotation

The sigmoidal field dependence reflects a smooth field-driven reorientation of the equilibrium Néel vector within the orthorhombic anisotropy landscape of the Γ_4 phase, rather than an abrupt spin flop [97, 287]. In this regime, the external field continuously rotates $\mathbf{n}^{(0)}(H)$ towards its high field orientation until a saturation scale H_{c} is reached, beyond which further field increase predominantly enhances the canting response, while the Néel vector orientation changes only weakly [97].

Operationally, the field dependence enters the detected nonlocal signals primarily through the projection of $\mathbf{n}^{(0)}(H)$ onto the spin accumulation axis of the Pt detector. For thermal magnons, the detected voltage is proportional to a field-dependent magnon magnetization imbalance weighted by a projection,

$$R_{\mathrm{th}}(H) \propto \Delta m_{\mathrm{th}}(H)\big(\mathbf{n}^{(0)}(H) \cdot \hat{\boldsymbol{\mu}}\big), \tag{7.1}$$

whereas for spin bias injection, it is weighted by the squared projection,

$$R_{\mathrm{el}}(H) \propto \Delta m_{\mathrm{el}}(H)\big(\mathbf{n}^{(0)}(H) \cdot \hat{\boldsymbol{\mu}}\big)^2, \tag{7.2}$$

consistent with the injection and detection symmetry discussed in Chapter 6 and in Ref. [97]. In Fig. **7.1**, the solid line trends are obtained by combining these projection factors with the simulated equilibrium orientation $\mathbf{n}^{(0)}(H)$ and the corresponding

mode weighted magnon magnetization terms. The extraction of H_c from SMR, which provides an experimental cross check of the saturation scale, is described in Chapter 5, and the simulation details used to obtain $\mathbf{n}^{(0)}(H)$ are given in Appendix E while the simulated values are in Appendix E.2.1.

7.1.2. Low field canting related contributions

In addition to the dominant altermagnetic transport response discussed above, orthoferrites also host a weak ferromagnetic canting driven by relativistic interactions, which can produce small transport features at low magnetic fields when the canted moment reverses. To isolate and quantify this contribution in $LuFeO_3$, we measured the nonlocal thermal channel R_{th} in a narrow field window around zero field, where a magnetic reversal of the canted moment is expected in bulk magnetometry.

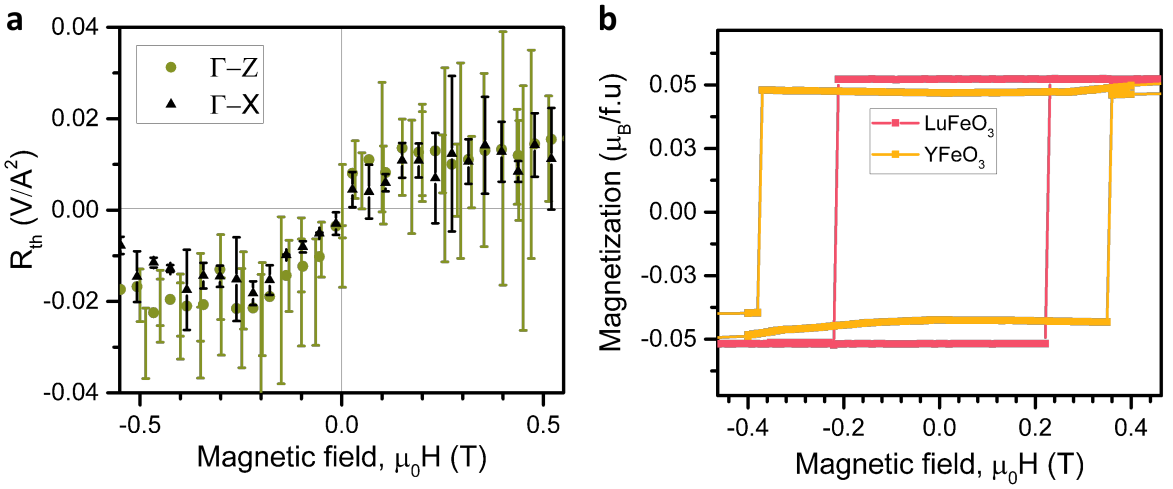

Figure 7.2.: Low field canting related contributions in $LuFeO_3$. **a** Nonlocal thermal resistance R_{th} measured at low magnetic fields, showing a small step-like feature associated with the reversal of the weak ferromagnetic canting. **b** Magnetization curves measured along the **c** axis at room temperature, illustrating the corresponding low field switching of the canted moment. Adapted from Galíndez et al., arXiv:2508.14569 (2025) [115].

Figure **7.2a** shows that R_{th} exhibits a small discontinuity close to the low field switching scale, consistent with a canting-related contribution to thermally generated magnon transport. Such low field signatures have also been reported in local longitudinal SSE measurements in $LuFeO_3$, where the signal follows the reversal of the weak ferromagnetic moment [286]. In our nonlocal geometry, this contribution is clearly present but remains much smaller than the altermagnetic response observed at higher fields along the Γ–U and Γ–U' directions [115].

Crucially, the canting-related low-field feature does not reproduce the defining symmetry signatures of the altermagnetic transport. The low field step is tied to a reversal of the weak ferromagnetic component and therefore provides a common sign change associated with the canting direction, whereas the altermagnetic signal shows an opposite sign between Γ–U and Γ–U' even at zero field, and remains strongly suppressed along the high symmetry **a** and **c** control directions [97, 115]. We therefore treat the

low-field canting contribution as a separate, small background that can coexist with, but cannot explain, the large direction-dependent sign inversion that is the focus of this chapter.

7.2. Magnon spin bias transport

We now turn to current-driven magnon injection and detection, quantified by the polarity odd response R_{el} defined in Eq. 3.27. In this channel, the charge current in the Pt injector generates an interfacial spin accumulation via the SHE, which selectively excites magnon modes whose dynamical magnetization can absorb the injected angular momentum [48, 97, 106]. The resulting nonequilibrium magnon population propagates to the remote Pt strip and is converted into a detector voltage by the inverse SHE [48,106]. Unlike the thermal channel, the injected spin accumulation provides a defined polarization axis, so the sign and magnitude of R_{el} encode which magnon branch carries the dominant transported angular momentum for a given crystallographic direction and magnetic configuration.

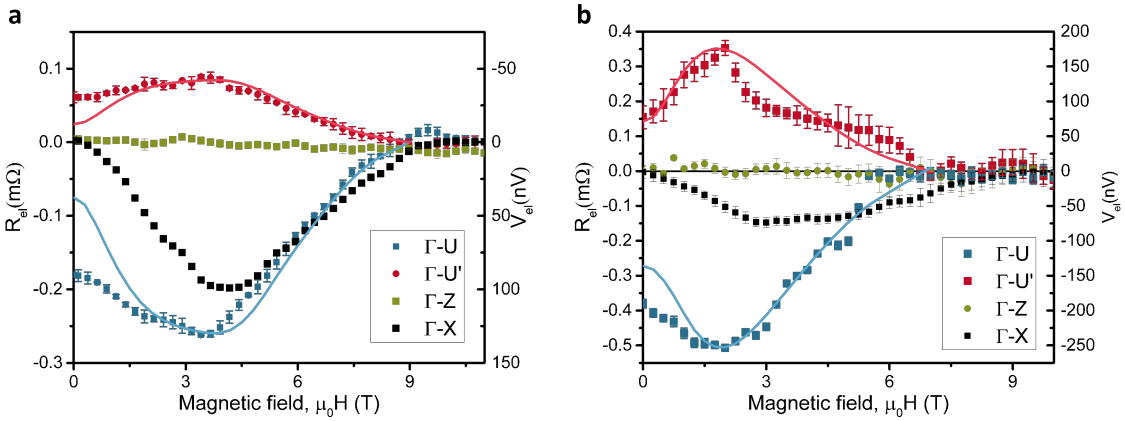

Figure 7.3.: **Nonlocal spin bias transport along altermagnetic directions.** Nonlocal spin bias resistance $R_{\mathrm{el}} = V_{\mathrm{el}}/I$ measured along the two non equivalent altermagnetic directions Γ–U and Γ–U', compared to the high symmetry control directions along the **a** axis (Γ–X) and **c** axis (Γ–Z), for **a** $LuFeO_3$ and **b** $YFeO_3$. Adapted from Galíndez et al., arXiv:2508.14569 (2025), licensed under CC BY 4.0 [115].

Figure **7.3** demonstrates that the spin bias response contains altermagnetic features that cannot be explained by the weak ferromagnetic canting alone. First, a finite R_{el} is observed at zero applied magnetic field along the altermagnetic directions for both $LuFeO_3$ and $YFeO_3$ [115]. In the conventional directions (Chapter 6), a sizable electrical signal typically requires an external field to tune the mode polarization and the injection and detection efficiency through field-induced ellipticity [97] or circular polarized modes. Here, the persistence of R_{el} at $H = 0$ shows that the altermagnetic splitting enables a symmetry-allowed net angular momentum transport without relying on external Zeeman control [95, 98, 115].

Second, the spin bias signal reverses sign between the two altermagnetic directions Γ–U and Γ–U' [115]. This sign inversion indicates that the dominant transported magnon angular momentum reaching the detector has opposite sign when the propagation direction is rotated by 90° within the **a**–**c** plane, consistent with a direction-dependent magnon spin splitter response. Importantly, such a reversal is not expected from a canting dominated mechanism, because a contribution tied primarily to the weak ferromagnetic component would not generically change sign between two tilted directions of the same plane, and it would instead be expected to be most visible along the **c** axis direction where the canting is oriented [97,115,286]. The experimentally observed suppression along **c**, therefore, provides a direct internal control against a canting-only interpretation.

Third, transport along the high symmetry directions **a** (Γ–X) and **c** (Γ–Z) is strongly reduced, in particular at zero field [115]. In these control geometries, the symmetry allowed altermagnetic contributions to cancel, or the relevant low-energy magnons are effectively linearly polarized so that opposite helicities compensate in the transported angular momentum, making field-free transport symmetry suppressed [95,98,107]. This behavior provides the clean bridge to Chapter 6, where the remaining finite signals in high symmetry directions are recovered only when an external field modifies the mode polarization and the equilibrium order parameter configuration [97].

In practice, the spin bias response can be summarized by the same ingredients used in the conventional directions: a geometric projection factor, a propagation factor, and a mode-dependent amplitude, as follows:

$$R_{\mathrm{el}}(H,d) \propto \Delta m_{\mathrm{el}}(H)\, \exp\!\left(-\frac{d}{\lambda_{\mathrm{m}}(H)}\right) \left(\mathbf{n}^{(0)}(H)\cdot\hat{\boldsymbol{\mu}}\right)^2, \tag{7.3}$$

where $\mathbf{n}^{(0)}(H)$ is the equilibrium Néel vector, $\hat{\boldsymbol{\mu}}$ is the interfacial spin accumulation axis set by the Pt current, λ_{m} is the effective magnon decay length, and Δm_{el} denotes the net mode weighted magnon magnetization relevant for spin bias injection and detection [97, 115]. The crucial difference relative to the high symmetry directions is that along Γ–U and Γ–U' the altermagnetic splitting makes Δm_{el} finite already at $H = 0$ and with opposite sign for the two directions, while along Γ–X and Γ–Z this field free contribution is suppressed by symmetry [115].

7.2.1. Defining signatures of altermagnetic spin bias transport

The spin bias measurements establish three defining experimental signatures that we use throughout this chapter. (i) A robust sign reversal of R_{el} between the two altermagnetic directions Γ–U and Γ–U' in both $LuFeO_3$ and $YFeO_3$ [115]. (ii) A strong suppression of the field-free signal along the high symmetry axes Γ–X and Γ–Z, consistent with cancellation or nearly linear polarization in these directions [95,107,115]. (iii) The persistence of a finite response at zero applied field along the altermagnetic directions, demonstrating that external magnetic fields are not required to enable electrical nonlocal transport once symmetry-allowed altermagnetic splitting selects a dominant magnon branch [98,115]. Together, these signatures go beyond a canting-based picture and provide the experimental bridge from the conventional magnon transport in Chapter 6 to the symmetry-selected altermagnetic transport directions that are the focus of this chapter [97, 115].

7.3. Distance dependence: nonmonotonic transport and sign reversal with distance

A stringent test of the transport mechanism is provided by the dependence on the injector–detector separation d. In conventional non-local magnon transport in ferro- and AFMs, the detected signal typically decays monotonically with d and is well described by an exponential attenuation set by a single effective propagation length [48, 97, 106]. This behavior follows directly from a diffusion–relaxation picture, in which the non-equilibrium magnon density obeys a steady-state diffusion equation with a decay length $\lambda = \sqrt{D_{\mathrm{m}}\tau_{\mathrm{m}}}$ [106]. In contrast, along the altermagnetic directions of orthoferrites, we observe a qualitatively different evolution of the thermal non-local response with distance.

Figure **7.4a** shows that $R_{\mathrm{th}}(d)$ does not follow a single monotonic attenuation with distance, but exhibits a crossover in sign as the injector–detector spacing is increased [115]. The sign reversal implies that the dominant net magnon spin angular momentum reaching the detector changes sign at a characteristic distance scale, meaning that the relative weight of opposite modes in the arriving magnon population evolves with propagation.

This non-monotonic behavior is a natural consequence of altermagnetic magnon band splitting, which makes the relevant transport quantities mode-dependent and direction-dependent. Along Γ–U and Γ–U', magnons of opposite modes are non-degenerate and therefore can differ simultaneously in group velocity $v_{\mathrm{g}}(k)$, lifetime $\tau(k)$, and thermal occupation $n(\omega)$, leading to distinct effective decay lengths $\lambda(k) = v_{\mathrm{g}}(k)\tau(k)$ for the two magnon branches [95, 98, 115, 186]. Because the thermal channel samples a broad range of wave vectors up to energies of order $k_{\mathrm{B}}T$, the net magnon magnetization detected at a distance d reflects a competition between branch-dependent propagation and branch-dependent population, rather than a single exponential attenuation. As d increases, the contribution of the shorter-lived or slower branch is progressively filtered out, so that a different mode can dominate at the detector, producing a sign change in the net transported angular momentum [115].

The same physics is reproduced by atomistic spin dynamics simulations that explicitly compute the magnon magnetization generated by a temperature gradient and evaluate its spatial evolution along different transport directions [115,283]. Figure **7.4b** shows that a finite magnon magnetization develops along altermagnetic directions and that its sign and spatial evolution depend on the chosen altermagnetic direction [115,283]. The key consequence, the disappearance of this effect upon removing the altermagnetic exchange splitting, is discussed explicitly in the next section Sec. 7.3.1.

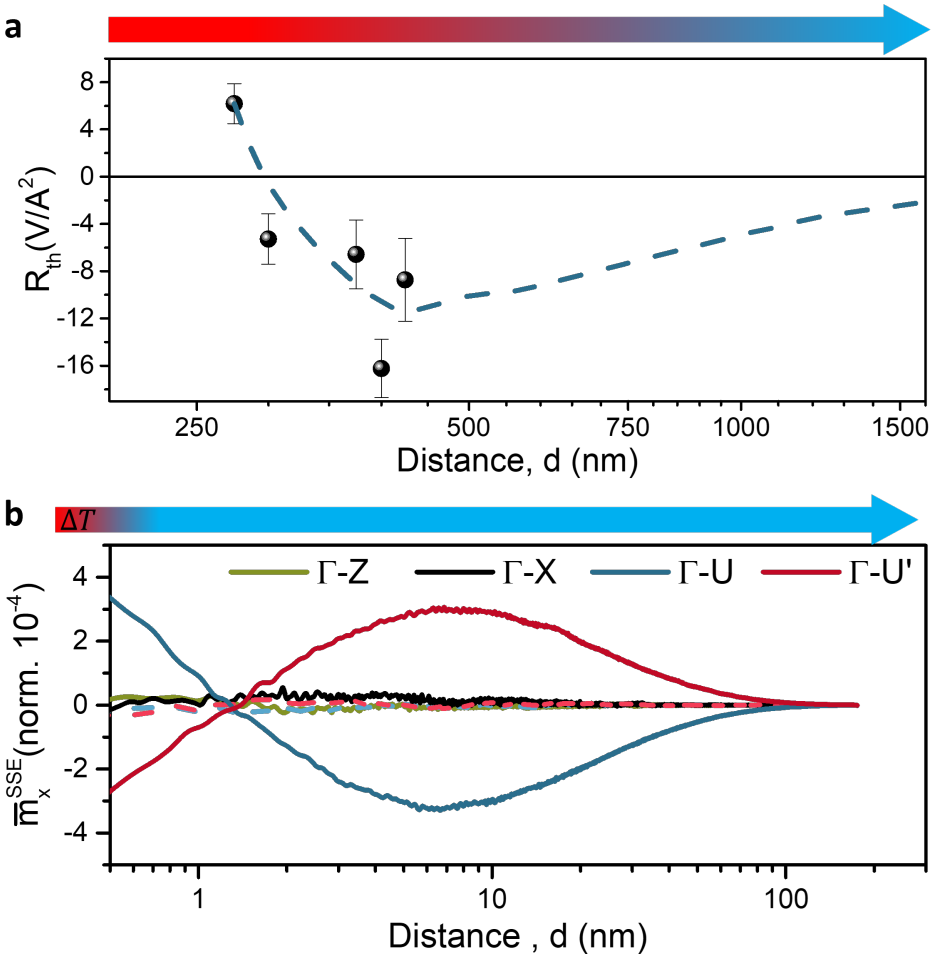

Figure 7.4.: Non-monotonic distance dependence and sign reversal of the altermagnetic thermal signal. a Non-local thermal resistance R_{th} as a function of injector–detector separation d measured along an altermagnetic transport direction in $LuFeO_3$, showing a non-monotonic evolution and a sign change as d is increased. **b** Atomistic spin dynamics simulations of the local magnon magnetization generated by a temperature gradient for different transport directions, illustrating the emergence of a finite, direction-dependent magnon magnetization along altermagnetic directions and its suppression in a non-altermagnetic reference model. Adapted from Galíndez et al., arXiv:2508.14569 (2025) [115].

7.3.1. Magnon mode competition mechanism

The non-monotonic distance dependence in Fig. **7.4a** can be understood from a minimal, mode-resolved transport picture in which the detected thermal signal reflects a weighted sum over the thermally occupied magnon eigenmodes. In the thermal channel, the injector creates a local temperature gradient and therefore excites magnons over a broad range of energies of order $k_{\mathrm{B}}T$. The resulting net magnon spin-angular-momentum density reaching the detector is then set by the imbalance between opposite modes after propagation over a distance d, rather than by a single effective diffusion length.

A compact way to express this is to write the transport-relevant magnon magnetization at distance d as a branch-resolved sum,

$$\Delta m_{\mathrm{th}}(d) \;\propto\; \sum_{\nu=\pm} \int \mathrm{d}k\; s_\nu(k)\, n\big(\omega_\nu(k), T\big)\, W_\nu(k)\, \exp\left[-\frac{d}{\lambda_\nu(k)}\right], \tag{7.4}$$

where $\nu = \pm$ labels the two opposite magnon-modes branches, $s_\nu(k) = \pm 1$ encodes the sign of the spin angular momentum carried by the mode, $n(\omega, T)$ is the Bose occupation, and $\lambda_\nu(k) = v_{\mathrm{g},\nu}(k)\tau_\nu(k)$ is the mode-resolved propagation length written in terms of group velocity $v_{\mathrm{g},\nu}(k) = \partial\omega_\nu/\partial k$ and lifetime $\tau_\nu(k)$. The factor $W_\nu(k)$ collects mode-dependent injection and detection efficiencies (including polarization ellipticity and interfacial coupling), which can vary with k but is not required to introduce a sign reversal by itself [97,107,115]. Equation (7.4) makes the essential point: as d increases, the exponential filtering is branch-dependent and k-dependent, so the dominant contribution to Δm_{th} can switch from one mode to the other, producing a sign change in the detected thermal signal.

The required input for this mechanism is that the two modes are genuinely nondegenerate along altermagnetic directions, so that $n(\omega)$, v_{g}, and τ can differ between $\nu = +$ and $\nu = -$ at the same wave vector. These mode-resolved quantities were obtained from linear spin-wave theory calculations based on an atomistic spin model developed and evaluated in collaboration with the group of Prof. Dr. Ulrich Nowak (Universität Konstanz); computational details are given in Appendix E and Ref. [115]. The resulting branch-resolved occupation, velocity, lifetime, and decay length directly visualize why a single-length-scale exponential decay fails in the altermagnetic directions.

Figure **7.5** highlights the decisive ingredients of the mode-competition mechanism. Along altermagnetic directions, the two modes are split and therefore acquire different dispersions and slopes, leading to distinct group velocities, lifetimes, and thus distinct $\lambda_\nu(k)$ for the modes that are most strongly thermally populated [115]. Consequently, even if both modes are excited near the injector, their relative contributions at the detector are reshuffled with distance. Modes with relatively large $n(\omega)$ but short λ dominate at small d, while modes with longer λ increasingly dominate at larger d, enabling a crossover in the sign of $\Delta m_{\mathrm{th}}(d)$ and thus of R_{th}.

A key consequence is that this entire phenomenology disappears when the altermagnetic exchange splitting is removed from the model. In the atomistic simulations shown in Fig. **7.4b**, symmetrizing the exchange interactions (thereby eliminating the altermagnetic splitting while retaining the remaining ingredients of the spin model) suppresses the finite magnon magnetization along the altermagnetic directions [115]. This provides the cleanest link between symmetry and observation: without altermagnetic exchange splitting, the branch-resolved differences in $\omega_\nu(k)$, $v_{\mathrm{g},\nu}(k)$, and $\tau_\nu(k)$ collapse, the helicity imbalance cancels in Eq. (7.4), and the direction-dependent sign reversal with distance is lost. The experimental sign change in Fig. **7.4a** is therefore most naturally understood as a direct consequence of altermagnetic, direction-dependent magnon band splitting and the resulting competition of mode-resolved population and propagation.

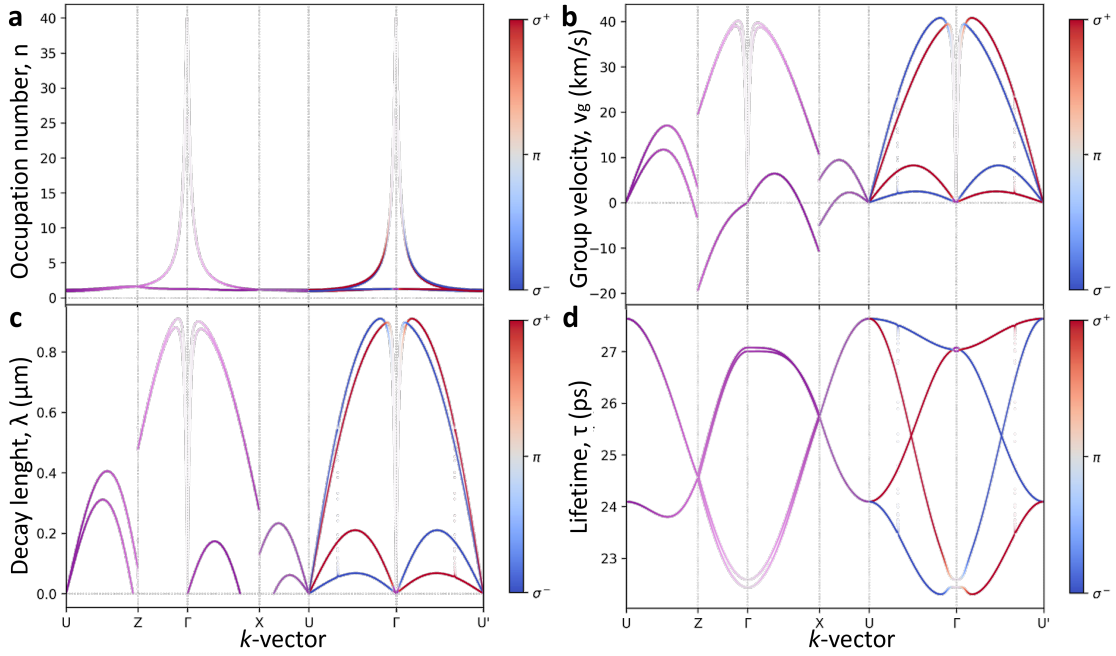

Figure 7.5.: Mode-resolved magnon transport quantities underpinning the distance-driven sign reversal. Branch-resolved quantities from linear spin-wave theory calculations for $LuFeO_3$ along representative reciprocal-space directions, including the altermagnetic paths (Γ–U and Γ–U') and the high-symmetry controls (Γ–X and Γ–Z). **a** Bose occupation $n(\omega)$, **b** group velocity $v_g = \partial\omega/\partial k$, **c** decay length $\lambda = v_g\tau$, and **d** lifetime τ. The color scale indicates the magnon polarization state (right-circular σ^+, left-circular σ^-, linear π). These calculations were performed by collaborators in the group of Prof. Dr. Ulrich Nowak (Universität Konstanz); see Appendix E and Ref. [115]. Reproduced from Galíndez et al., arXiv:2508.14569 (2025), licensed under CC BY 4.0 [115].

7.3.2. Current scaling of the non-local resistances

A key consistency check of the non-local protocol is the current scaling of the separated channels. Because the polarity-even thermal voltage is driven by Joule heating, it must scale as $V_{th} \propto I^2$, whereas the spin Hall-driven spin-bias voltage must scale as $V_{el} \propto I$ [48, 97, 106, 115].

Figure **7.6c** shows that the thermal channel follows $V_{th} \propto I^2$, confirming that R_{th} is governed by the injected thermal power, as expected for thermally generated magnons. Conversely, Fig. **7.6a** shows that the spin-bias channel follows $V_{el} \propto I$, consistent with injection driven by the spin Hall-induced interfacial spin accumulation [48, 97]. Together, these trends validate the polarity decomposition used throughout this chapter and strongly constrain artifact scenarios: any direct electrical cross-talk between injector and detector would predominantly scale linearly with I and would not appear selectively in the polarity-even channel, while static thermoelectric offsets would not reproduce the observed parity separation and current-power scaling.

For completeness, Fig. **7.6b** also illustrates that, at zero magnetic field, the spin-bias response decays exponentially with injector–detector separation, consistent with diffu-

sive magnon transport in the regime probed here and enabling a robust extraction of an effective propagation length in the altermagnetic directions [106,115]. Fitting the zero-field distance dependence yields an effective propagation length of $\lambda_m \approx 600(59)$ nm along both altermagnetic directions (Γ–U and Γ–U'), exceeding the values along the high-symmetry controls Γ–X (280(20) nm) and Γ–Z (470(40) nm) [115].

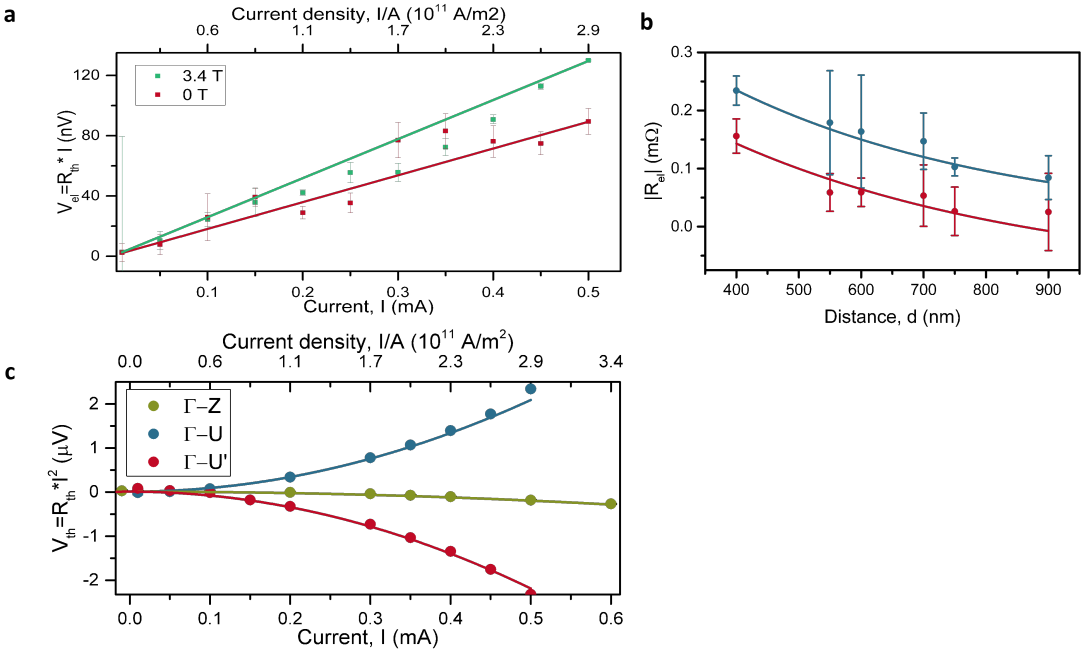

Figure 7.6.: **Current scaling and distance decay cross checks.** **a** Non-local spin-bias voltage V_{el} for transport along an altermagnetic direction as a function of injector current, demonstrating the expected linear scaling ($V_{el} \propto I$) at zero field and at finite field. **b** Non-local spin-bias resistance R_{el} as a function of injector–detector separation at zero field, showing the expected exponential attenuation with distance. **c** Non-local thermal voltage V_{th} at zero field as a function of injector current, demonstrating the expected quadratic scaling with current ($V_{th} \propto I^2$). Adapted from Galíndez et al., arXiv:2508.14569 (2025), licensed under CC BY 4.0 [115].

7.4. Summary

This chapter establishes altermagnetic magnon transport in insulating d-wave orthoferrites by extending the non-local magnon transport of Chapter 6 to nonconventional crystallographic directions where symmetry allows a magnon spin-splitter response [97,115]. The central experimental signatures are observed consistently in both $LuFeO_3$ and $YFeO_3$: (i) a robust sign inversion of the non-local thermal signal R_{th} between the two altermagnetic directions Γ–U and Γ–U', (ii) a finite field-free response along these altermagnetic directions that persists at $H = 0$, and (iii) a strong suppression of field-free transport along the high-symmetry control axes **a** (Γ–X) and **c** (Γ–Z), where symmetry constrains the net transported spin angular momentum to cancel or the relevant magnons are effectively linearly polarized [95,98,115]. These observations

demonstrate that the dominant transport response is not set by the weak ferromagnetic canting, which produces only small low-field features and does not reproduce the direction-dependent sign inversion that defines the altermagnetic effect [115, 286].

Mechanistically, the data are captured by a projection-controlled detection picture in which the external magnetic field primarily tunes the equilibrium Néel vector orientation and therefore the injector–detector efficiency through symmetry-required projection factors, while the transported magnon magnetization is governed by the direction-dependent imbalance of spin-split magnon modes [97, 115, 287]. A distinctive consequence of the spin-split altermagnetic magnon spectrum is the non-monotonic distance dependence of the thermal response, including a sign reversal as a function of injector–detector separation. This behavior follows naturally from mode competition: the measured signal is a weighted sum over non-degenerate magnon branches with different magnon modes, group velocities, thermal occupations, and decay lengths, so that the dominant contributing mode can change with propagation distance [107, 115, 186]. Atomistic spin-dynamics simulations and linear spin-wave calculations reproduce the observed sign changes and anisotropies, and, critically, demonstrate that the finite magnon magnetization and the sign-reversal behavior vanish when the exchange interactions are symmetrized to remove altermagnetic splitting. This provides a direct consequence: the observed field-free transport and its directional selectivity require altermagnetic exchange splitting rather than DMI-related canting alone [115, 281, 283].

Finally, current-scaling checks validate the experimental separation of thermal and spin-bias channels: the thermal voltage scales as I^2, whereas the spin-bias signal scales linearly with I, as expected for Joule-heating-driven and spin Hall-driven injection mechanisms, respectively [48, 106, 115]. Taken together, these results demonstrate that d-wave orthoferrites host symmetry-selected, field-free magnon spin transport governed by altermagnetic band splitting, providing a concrete experimental platform for altermagnetic magnonics and a low-power route to direction-programmable spin transport without external symmetry breaking.

8. Conclusions and Perspectives

This thesis set out to establish how altermagnetic symmetry can be harnessed to generate, guide, and detect spin transport in compensated magnets, with particular focus on insulating platforms in which magnons serve as the natural information carriers. The central outcome is that altermagnetism is not only an electronic band structure concept, but also a practical principle governing spin transport, enabling symmetry-selected signals that are absent in conventional ferro and antiferromagnetic cases [16, 19, 21, 115].

8.1. Summary of Key Findings

(1) Symmetry-controlled transverse transport and real-space imaging in hematite. In Ti-doped hematite, angle-dependent Hall measurements show that an odd transverse response appears only when the spin configuration is driven into a symmetry-allowed regime across the spin flop transition, and that the transverse signal exhibits crystallographic sign inversions that cannot be explained by a fixed canted moment picture alone [41]. Synchrotron XPEEM imaging resolves the 180° ambiguity of XMLD by combining XMLD and XMCD contrast, enabling a reconstruction of the absolute Néel vector orientation and correlating the transport pseudovector with real-space reversal of the order parameter [41]. Together, these results establish a symmetry-consistent route for diagnosing altermagnetic order using complementary reciprocal-space-sensitive transport and nanoscale imaging observables.

(2) SMR as a local electrical probe for orthoferrites. Spin Hall magnetoresistance was established as a robust local probe of the interfacial magnetic configuration in insulating orthoferrites [97, 115]. This chapter presents the symmetry-grounded local readout required to interpret non-local transport, as it fixes the injector- and detector-selection rules via the orientation of the Néel vector at the interface.

(3) An anisotropic magnon mediated non-local transport in $YFeO_3$. Non-local measurements along high symmetry axes establish the expected reference behavior for diffusive magnon spin transport in a canted antiferromagnetic orthoferrite. Signals persist over sub-micrometer length scales, and the decay lengths and field dependences are strongly crystallographically anisotropic, consistent with anisotropy-controlled mode polarization and interface projection effects [48, 97, 106]. This transport generation-detection technique defines the key observables, the polarity-separated R_{el} and R_{th}, and the exponential decay length λ, which are used to isolate genuinely altermagnetic behavior in the subsequent chapter.

(4) Altermagnetic magnon transport in d-wave orthoferrites. The core experimental result of the thesis is the demonstration of symmetry-selected, field-free magnon

spin transport in insulating d wave orthoferrites [115]. Along the altermagnetic directions Γ–U and Γ–U', the non-local thermal signal R_{th} exhibits a robust sign inversion between the two directions, and a finite response persists at $H = 0$, while the high symmetry control axes **a** (Γ–X) and **c** (Γ–Z) show strong suppression of field free transport [95, 98, 115]. These observations are incompatible with a canting-dominated interpretation and directly reflect symmetry-imposed mode selectivity in a compensated magnet.

(5) Magnon-mode competition as cause of the distance-dependent sign reversal: a altermagnonic fingerprint. A distinctive consequence of altermagnetic exchange splitting is a non-monotonic distance dependence of R_{th}, including a sign reversal as a function of injector detector separation. This behavior follows from different magnon-modes competing, where non-degenerate modes carry different magnetization, group velocity, thermal occupation, and decay length, so that the dominant contribution can change with distance [107, 115, 186]. Atomistic spin dynamics and linear spin wave calculations reproduce the anisotropies and sign changes and provide a controlled study: the field-free magnon magnetization and sign reversal vanish when exchange interactions are symmetrized to remove altermagnetic splitting [115, 281, 283]. This directly links the transport phenomenology to the altermagnetic band splitting rather than to DMI-induced canting alone.

(6) A reproducible experimental and analysis pipeline. Across materials and device geometries, the thesis establishes a protocol from device preparation and structural vetting to symmetry-aware harmonic transport protocols and domain-sensitive XPEEM, enabling cross-validation between local probes, non-local transport, and microscopic modelling. This integration is relevant for insulator altermagnets, in which the relevant order parameter is encoded in reciprocal space but must be accessed via real-space interfaces and device-level symmetry constraints.

8.2. Perspectives and Outlook

The results of this thesis establish a symmetry-dependent protocol in which altermagnetism can be diagnosed and exploited in both electrical and magnon-mediated transport. In hematite, we demonstrated that the emergence and angular sign inversions of the odd transverse response are related to the symmetry allowed from the magnetic point group, and we corroborated the transport-derived order parameter configuration by real-space XPEEM reconstruction of the absolute Néel vector orientation (Chapter 4) [41]. In insulating orthoferrites, we established SMR as a local probe which probe the interfacial magnetic configuration and quantify the efficiency of the spin conversion (Chapter 5) [97, 115]. Based in this as a test for the interface charge-spin conversion efficiency, non-local measurements first defined a measurement protocol along high symmetry axes (Chapter 6) [48, 97, 106], and then revealed the central altermagnetic signatures, namely direction selective sign inversions and finite responses at zero magnetic field along Γ–U and Γ–U', together with a non-monotonic distance dependence that arises from mode competition in a spin split magnon spectrum (Chapter 7) [115, 186]. Atomistic and spin wave modeling predicts that these

features vanish when the exchange is symmetrized to remove altermagnetic splitting, directly linking the observed transport to altermagnetism rather than to weak canting alone [115, 281, 283].

With this experimental and theoretical foundation, the most pressing next step is to move from symmetry-based identification to manipulation of the altermagnetic magnon transport. In particular, it is now timely to ask which external parameters can reversibly select the active altermagnetic magnon modes, set the sign and magnitude of the transported spin angular momentum, and stabilize a desired functionality at zero field. Three routes are especially natural in the context of this thesis, because they act directly on the symmetry and projection ingredients that govern the measured nonlocal response, ferroic order as an electrical switch of the altermagnetic texture, strain as a symmetry selective tuning field for the exchange split spectrum and its lifetimes, and orbitronics as an alternative angular momentum source that may offer distinct injection symmetries and reduced dissipation compared with heavy metal spin Hall transducers [288–295].

For hematite, moving beyond the hopping-dominated regime is essential to enable quantitative comparison between measured conductivities and first-principles Berry curvature predictions and to maximize the magnitude of transverse responses [41]. For insulating orthoferrites, electrostatic control will likely target interfaces and magnon chemical potential rather than bulk carrier density. However, gating can still tune interfacial transparency and heating profiles, providing a device-level route to modulate the balance between magnon modes, therefore the sign and amplitude of R_{th} [47, 48].

This thesis provides an experimentally grounded bridge between symmetry-based altermagnetism and magnon-mediated spin transport in wide-gap magnetically compensated insulators. This bridge is essential for extending altermagnetic spintronics beyond metallic systems toward energy-efficient magnonic circuits, and it provides a template for validating altermagnetic functionality in systems that conventional magnetometry cannot probe. Looking forward, combining symmetry diagnostics, real-space imaging, and branch-sensitive transport in a single platform will be a key route to explore predicted phenomena such as altermagnons, giant lifetime anisotropies, and efficient spin caloritronic responses in altermagnets [95, 98, 186].

In summary, this thesis establishes that the consequences of altermagnetic symmetry can be exploited for practical experimental exploration for both particular electrical and magnon-mediated transport properties. The demonstrated field-free, direction-sensitive, variable sign magnon transport in orthoferrites, together with symmetry-dependent Hall transport and domain imaging in hematite, defines a concrete foundation for altermagnetic magnonics and for device concepts that operate without external symmetry-breaking fields [41, 115].

8.3. Open Questions and Future Research Directions

These findings raise a set of open questions that naturally follow from the experimental pipeline developed here: local SMR as an interfacial order-parameter probe; non-local spin bias and thermal transport as symmetry diagnostics; PEEM as real-space domain verification; and atomistic and spin-wave modelling to understand the mechanisms.

A central perspective is that the next stage of altermagnetic magnonics should shift from observation to control, with three complementary routes that remain largely unex-

plored experimentally in insulating systems: electrical control via ferroic order, symmetry engineering via strain, and alternative multipolar order angular-momentum sources beyond the conventional spin Hall effect.

8.3.1. Ferroic control of altermagnetism, from electrically switchable spin splitting to magnonic readout

Recent theory has proposed that ferroelectric or antiferroelectric order can act as a electrical switch for altermagnetic spin splitting, because polarization reversal can change the magnetic space group constraints that define the momentum-dependent spin texture [288, 289]. In two-dimensional settings, the same concept has been extended to a dual switching scenario, where ferroelectric reversal is predicted to invert not only electronic spin splitting, but also the magnonic spin splitting [296]. In parallel, ferroelastic reorientation has been proposed as a multistate, non-volatile tuator for altermagnetic spin splitting via strain states that are encoded mechanically rather than magnetically [297].

Within the scope of the present thesis, the immediate open question is how such ferroic switching can be translated into the non-local magnon transport observables used here. Concretely, the key prediction to target is a control of the sign and amplitude hierarchy of R_{th} and R_{el} at fixed device geometry, driven solely by an electric field through ferroic switching. At the same time, the SMR readout confirms the associated interfacial order parameter configuration. A minimal experimental program would combine (i) an insulating altermagnet channel with the non-local architecture of Chapters 6–7, (ii) a gate stack or ferroic substrate enabling reliable polarization or ferroelastic state control, and (iii) domain resolved imaging, for example XMLD based PEEM, to correlate ferroic state, domain population, and transport symmetry class. In this way, the thesis methodology serves as a direct testbed for multiferroic altermagnetism, with magnon transport providing a functional readout channel that is closer to device operation than purely spectroscopic signatures.

8.3.2. Strain as a symmetry selective tuning parameter for altermagnons and their transport

The orthoferrite results in this thesis motivate strain as a targeted, symmetry-selective perturbation, because the non-local response is sensitive to the altermagnetic mode splitting and to the competition between magnon modes with distinct velocities, occupations, and lifetimes. A set of recent works makes this connection explicit by showing that strain can tune the altermagnetic symmetry class and activate or reshape spin-splitter responses in prototypical altermagnets [290, 291]. The most relevant implication for the present thesis is that strain can, in principle, reweight the competing magnon modes that underlie the non-monotonic distance dependence and sign reversals reported in Chapter 7, thereby offering a route to engineer the crossover length scales and to stabilize a desired sign over a target device distance.

A compact way to frame the experimental objective is to treat strain as a controlled handle on the magnetoelastic anisotropy of the collinear order parameter, and to ask how specific strain components ε_{ij} modify three directly measurable quantities: the

critical fields extracted from SMR, the field-free offset and sign of R_{th} along Γ–U and Γ–U', and the distance-dependent mode competition encoded in $R_{\mathrm{th}}(d)$.

Experimentally, this points to piezo-controlled uniaxial strain on single crystals, or epitaxial strain in thin film orthoferrites, combined with the same SMR-guided symmetry assignment used in Chapter 5. On the theoretical side, the open question is to identify which microscopic parameters govern the strain sensitivity of the relevant altermagnon splittings and lifetimes in orthoferrites, and whether a predictive mapping can be constructed that connects ab initio strain-induced modifications in exchange to the effective decay lengths extracted from non-local transport.

8.3.3. Orbitronics as an alternative injection and torque platform for insulating altermagnets

All magnon transport chapters in this thesis relied on Pt as a combined injector and detector via the spin Hall and inverse spin Hall effects. An important open question is whether orbital currents can provide a lower-loss, and potentially symmetry-distinct, route to drive and detect altermagnetic magnons. The orbital Hall effect has been predicted to be large even in light transition metals, and has been observed directly in Ti using magneto-optical detection [292, 293]. This suggests a practical materials set, such as Ti or V, in which strong orbital currents can be generated with reduced spin-orbit damping relative to heavy metals [294, 295].

For altermagnetic insulators, the central unknown is the efficiency and symmetry of orbital-to-magnon angular-momentum transfer at realistic interfaces. A direct extension of the present thesis methodology is therefore to fabricate otherwise identical non-local devices where Pt is replaced, or complemented, by an orbital Hall metal, and to benchmark (i) the magnitude of R_{el} and R_{th}, (ii) the robustness of the field free response along altermagnetic directions, and (iii) the injector and detector selection rules inferred from SMR. Beyond efficiency, orbitronics may enable qualitatively new probes, for example, torque symmetries that are suppressed for conventional spin Hall injection, or domain wall dynamics driven by orbital accumulations in symmetry-lowered regions. Establishing an orbital mixing conductance basis for metal|altermagnet interfaces, analogous to the spin mixing conductance used throughout the theory chapter, remains an essential theoretical task for making this route predictive rather than empirical.

Bibliography

[1] J. Puebla, J. Kim, K. Kondou, and Y. Otani. Spintronic devices for energy-efficient data storage and energy harvesting. *Communications Materials*, 1(1):1–9, May 2020.

[2] Global Business Development Team. Spintronics Market Expected to Exceed USD 2.7 billion by 2033 | Driven by Technological Advancements and Growing Demand for Energy-efficient Electronic Devices, February 2024.

[3] Goldman Sachs. AI to drive 165% increase in data center power demand by 2030, February 2025.

[4] H. Tahir, K. Liu, Y.-F. Yang, K. Baruah, B. M. Savoie, and B. W. Boudouris. Verdazyl radical polymers for advanced organic spintronics. *Nature Communications*, 16(1):652, January 2025.

[5] P. Gu, C. Wang, D. Su, Z. Dong, Q. Wang, Z. Han, K. Watanabe, T. Taniguchi, W. Ji, Y. Sun, and Y. Ye. Multi-state data storage in a two-dimensional stripy antiferromagnet implemented by magnetoelectric effect. *Nature Communications*, 14(1):1–8, June 2023.

[6] P. Barla, V. K. Joshi, and S. Bhat. Spintronic devices: a promising alternative to CMOS devices. *Journal of Computational Electronics*, 20(2):805–837, April 2021.

[7] C. H. Marrows, J. Barker, T. A. Moore, and T. Moorsom. Neuromorphic computing with spintronics. *npj Spintronics*, 2(1):1–7, April 2024.

[8] S. Reimers, Y. Lytvynenko, Y. R. Niu, E. Golias, B. Sarpi, L. S. I. Veiga, T. Denneulin, A. Kovács, R. E. Dunin-Borkowski, J. Bläßer, M. Kläui, and M. Jourdan. Current-driven writing process in antiferromagnetic Mn_2Au for memory applications. *Nature Communications*, 14(1):1861, April 2023.

[9] A. Dal Din, O. J. Amin, P. Wadley, and K. W. Edmonds. Antiferromagnetic spintronics and beyond. *npj Spintronics*, 2(1):1–8, July 2024.

[10] D. Burrow, J. C. Toscano-Figueroa, V. H. Guarochico-Moreira, K. Omari, I. V. Grigorieva, T. Thomson, and I. J. Vera-Marun. Spin polarised quantised transport via one-dimensional nanowire-graphene contacts. *Communications Materials*, 6(1):1–8, February 2025.

[11] D. Jo, D. Go, G.-M. Choi, and H.-W. Lee. Spintronics meets orbitronics: Emergence of orbital angular momentum in solids. *npj Spintronics*, 2(1):1–9, June 2024.

[12] E. A. Montoya, X. Pei, and I. N. Krivorotov. Anomalous Hall spin current drives self-generated spin–orbit torque in a ferromagnet. *Nature Nanotechnology*, 20(3):353–359, March 2025.

[13] B. H. Rimmler, B. Pal, and S. S. P. Parkin. Non-collinear antiferromagnetic spintronics. *Nature Reviews Materials*, 10(2):109–127, February 2025.

[14] C. Cookson. New magnetic flow has potential to revolutionise electronic devices. *Financial Times*, December 2024.

[15] T. Jungwirth, X. Marti, P. Wadley, and J. Wunderlich. Antiferromagnetic spintronics. *Nature Nanotechnology*, 11(3):231–241, March 2016.

[16] I. Mazin. Altermagnetism Then and Now. *Physics*, 17(1):4, January 2024.

[17] Paolo G. Radaelli. Tensorial approach to altermagnetism. *Physical Review B*, 110(21):214428, December 2024.

[18] C. Song, H. Bai, Z. Zhou, L. Han, H. Reichlova, J. H. Dil, J. Liu, X. Chen, and F. Pan. Altermagnets as a new class of functional materials. *Nature Reviews Materials*, 10(6):473–485, June 2025.

[19] L. Šmejkal, J. Sinova, and T. Jungwirth. Emerging Research Landscape of Altermagnetism. *Physical Review X*, 12(4):040501, December 2022.

[20] L. Šmejkal, J. Sinova, and T. Jungwirth. Beyond Conventional Ferromagnetism and Antiferromagnetism: A Phase with Nonrelativistic Spin and Crystal Rotation Symmetry. *Physical Review X*, 12(3):031042, September 2022.

[21] L. Šmejkal, R. González-Hernández, T. Jungwirth, and J. Sinova. Crystal time-reversal symmetry breaking and spontaneous Hall effect in collinear antiferromagnets. *Science Advances*, 6(23):eaaz8809, June 2020.

[22] Z. Feng, X. Zhou, L. Šmejkal, L. Wu, Z. Zhu, H. Guo, R. González-Hernández, X. Wang, H. Yan, P. Qin, X. Zhang, H. Wu, H. Chen, Z. Meng, L. Liu, Z. Xia, J. Sinova, T. Jungwirth, and Z. Liu. An anomalous Hall effect in altermagnetic ruthenium dioxide. *Nature Electronics*, 5(11):735–743, November 2022.

[23] R. González-Hernández, L. Šmejkal, K. Výborný, Y. Yahagi, J. Sinova, T. Jungwirth, and J. Železný. Efficient Electrical Spin Splitter Based on Nonrelativistic Collinear Antiferromagnetism. *Physical Review Letters*, 126(12):127701, March 2021.

[24] L. Šmejkal, A. H. MacDonald, J. Sinova, S. Nakatsuji, and T. Jungwirth. Anomalous Hall antiferromagnets. *Nature Reviews Materials*, 7(6):482–496, June 2022.

[25] J. Krempaský, L. Šmejkal, S. W. D'Souza, M. Hajlaoui, G. Springholz, K. Uhlířová, F. Alarab, P. C. Constantinou, V. Strocov, D. Usanov, W. R. Pudelko, R. González-Hernández, A. Birk Hellenes, Z. Jansa, H. Reichlová, Z. Šobáň, R. D. Gonzalez Betancourt, P. Wadley, J. Sinova, D. Kriegner, J. Minár, J. H. Dil, and T. Jungwirth. Altermagnetic lifting of Kramers spin degeneracy. *Nature*, 626(7999):517–522, February 2024.

[26] R.D. Gonzalez Betancourt, J. Zubáč, R. Gonzalez-Hernandez, K. Geishendorf, Z. Šobáň, G. Springholz, K. Olejník, L. Šmejkal, J. Sinova, T. Jungwirth, S. T. B. Goennenwein, A. Thomas, H. Reichlová, J. Železný, and D. Kriegner. Spontaneous Anomalous Hall Effect Arising from an Unconventional Compensated Magnetic Phase in a Semiconductor. *Physical Review Letters*, 130(3):036702, January 2023.

[27] R. Zarzuela, R. Jaeschke-Ubiergo, O. Gomonay, L. Šmejkal, and J. Sinova. Transport theory and spin-transfer physics in d-wave altermagnets. *Physical Review B*, 111(6):064422, February 2025.

[28] H. Ohldag. Hidden in not-so-plain sight: altermagnets. *npj Spintronics*, 2(1):1–1, November 2024.

[29] H. Reichlova, R. Lopes Seeger, R. González-Hernández, I. Kounta, R. Schlitz, D. Kriegner, P. Ritzinger, M. Lammel, M. Leiviskä, A. Birk Hellenes, K. Olejník, V. Petříček, P. Doležal, L. Horak, E. Schmoranzerova, A. Badura, S. Bertaina, A. Thomas, V. Baltz, L. Michez, J. Sinova, S. T. B. Goennenwein, T. Jungwirth, and L. Šmejkal. Observation of a spontaneous anomalous Hall response in the Mn_5Si_3 d-wave altermagnet candidate. *Nature Communications*, 15(1):4961, June 2024.

[30] T. Osumi, S. Souma, T. Aoyama, K. Yamauchi, A. Honma, K. Nakayama, T. Takahashi, K. Ohgushi, and T. Sato. Observation of a giant band splitting in altermagnetic MnTe. *Physical Review B*, 109(11):115102, March 2024.

[31] A. Hariki, A. Dal Din, O.J. Amin, T. Yamaguchi, A. Badura, D. Kriegner, K.W. Edmonds, R.P. Campion, P. Wadley, D. Backes, L.S.I. Veiga, S.S. Dhesi, G. Springholz, L. Šmejkal, K. Výborný, T. Jungwirth, and J. Kuneš. X-Ray Magnetic Circular Dichroism in Altermagnetic α-MnTe. *Physical Review Letters*, 132(17):176701, April 2024.

[32] I. Gray, Q. Deng, Q. Tian, M. Chilcote, J. S. Dodge, M. Brahlek, and L. Wu. Time-resolved magneto-optical effects in the altermagnet candidate MnTe. *Applied Physics Letters*, 125(21):212404, November 2024.

[33] O. J. Amin, A. Dal Din, E. Golias, Y. Niu, A. Zakharov, S. C. Fromage, C. J. B. Fields, S. L. Heywood, R. B. Cousins, F. Maccherozzi, J. Krempaský, J. H. Dil, D. Kriegner, B. Kiraly, R. P. Campion, A. W. Rushforth, K. W. Edmonds, S. S. Dhesi, L. Šmejkal, T. Jungwirth, and P. Wadley. Nanoscale imaging and control of altermagnetism in MnTe. *Nature*, 636(8042):348–353, December 2024.

[34] T. Aoyama and K. Ohgushi. Piezomagnetic properties in altermagnetic MnTe. *Physical Review Materials*, 8(4):L041402, April 2024.

[35] N. N. Orlova, A. A. Avakyants, A. V. Timonina, N. N. Kolesnikov, and E. V. Deviatov. Crossover from Relativistic to Non-Relativistic Net Magnetization for MnTe Altermagnet Candidate. *Journal of Experimental and Theoretical Physics Letters*, 120(5):360–366, September 2024.

[36] D. Y. Kazmin, V. D. Esin, Y. S. Barash, A. V. Timonina, N. N. Kolesnikov, and E. V. Deviatov. Andreev reflection for MnTe altermagnet candidate. *Physica B: Condensed Matter*, 696(1):416602, January 2025.

[37] Y. Bai, X. Xiang, S. Pan, S. Zhang, H. Chen, X. Chen, Z. Han, G. Xu, and F. Xu. Nonlinear field dependence of Hall effect and high-mobility multi-carrier transport in an altermagnet CrSb. *Applied Physics Letters*, 126(4):042402, January 2025.

[38] T. Urata, W. Hattori, and H. Ikuta. High mobility charge transport in a multi-carrier altermagnet CrSb. *Physical Review Materials*, 8(8):084412, August 2024.

[39] J. Ding, Z. Jiang, X. Chen, Z. Tao, Z. Liu, T. Li, J. Liu, J. Sun, J. Cheng, J. Liu, Y. Yang, R. Zhang, L. Deng, W. Jing, Y. Huang, Y. Shi, M. Ye, S. Qiao, Y. Wang, Y. Guo, D. Feng, and D. Shen. Large Band Splitting in g-Wave Altermagnet CrSb. *Physical Review Letters*, 133(20):206401, November 2024.

[40] S. Reimers, L. Odenbreit, L. Šmejkal, V. N. Strocov, P. Constantinou, A. B. Hellenes, R. Jaeschke Ubiergo, W. H. Campos, V. K. Bharadwaj, A. Chakraborty, T. Denneulin, W. Shi, R. E. Dunin-Borkowski, S. Das, M. Kläui, J. Sinova, and M. Jourdan. Direct observation of altermagnetic band splitting in CrSb thin films. *Nature Communications*, 15(1):2116, March 2024.

[41] E. Galindez-Ruales, R. Gonzalez-Hernandez, C. Schmitt, S. Das, F. Fuhrmann, A. Ross, E. Golias, A. Akashdeep, L. Lünenbürger, E. Baek, W. Yang, L. Šmejkal, V. Krishna, R. Jaeschke-Ubiergo, J. Sinova, A. Rothschild, C.-Y. You, G. Jakob, and M. Kläui. Revealing the Altermagnetism in Hematite via XMCD Imaging and Anomalous Hall Electrical Transport. *Advanced Materials*, 37(41):e05019, July 2025.

[42] D. Jost, R. B. Regmi, S. Sahel-Schackis, M. Scheufele, M. Neuhaus, R. Nickel, F. Yakhou, K. Kummer, N. Brookes, L. Shen, G. L. Dakovski, N. J. Ghimire, S. Geprägs, and M. F. Kling. Chiral Altermagnon in MnTe, January 2025. arXiv:2501.17380 [cond-mat].

[43] C.-Y. Tan, Z.-F. Gao, H.-C. Yang, Z.-X. Liu, K. Liu, P.-J. Guo, and Z.-Y. Lu. Crystal valley Hall effect. *Physical Review B*, 111(9):094411, March 2025.

[44] D. S. Antonenko, R. M. Fernandes, and J. W. F. Venderbos. Mirror Chern Bands and Weyl Nodal Loops in Altermagnets. *Physical Review Letters*, 134(9):096703, March 2025.

[45] I. Khan, D. Bezzerga, B. Marfoua, and J. Hong. Altermagnetism, piezovalley, and ferroelectricity in two-dimensional Cr_2SeO altermagnet. *npj 2D Materials and Applications*, 9(1):1–9, February 2025.

[46] G. Yang, Z. Li, S. Yang, J. Li, H. Zheng, W. Zhu, Z. Pan, Y. Xu, S. Cao, W. Zhao, A. Jana, J. Zhang, M. Ye, Y. Song, L.-H. Hu, L. Yang, J. Fujii, I. Vobornik, M. Shi, H. Yuan, Y. Zhang, Y. Xu, and Y. Liu. Three-dimensional mapping of the altermagnetic spin splitting in CrSb. *Nature Communications*, 16(1):1442, February 2025.

[47] R. Lebrun, A. Ross, O. Gomonay, V. Baltz, U. Ebels, A.-L. Barra, A. Qaiumzadeh, A. Brataas, J. Sinova, and M. Kläui. Long-distance spin-transport across the Morin phase transition up to room temperature in ultra-low damping single crystals of the antiferromagnet α-Fe2O3. *Nature Communications*, 11(1):6332, December 2020.

[48] R. Lebrun, A. Ross, S. A. Bender, A. Qaiumzadeh, L. Baldrati, J. Cramer, A. Brataas, R. A. Duine, and M. Kläui. Tunable long-distance spin transport in a crystalline antiferromagnetic iron oxide. *Nature*, 561(7722):222–225, September 2018.

[49] A. Ross, R. Lebrun, O. Gomonay, D. A. Grave, A. Kay, L. Baldrati, S. Becker, A. Qaiumzadeh, C. Ulloa, G. Jakob, F. Kronast, J. Sinova, R. Duine, A. Brataas, A. Rothschild, and M. Kläui. Propagation Length of Antiferromagnetic Magnons Governed by Domain Configurations. *Nano Letters*, 20(1):306–313, January 2020.

[50] A. V. Chumak, A. A. Serga, and B. Hillebrands. Magnon transistor for all-magnon data processing. *Nature Communications*, 5(1):4700, August 2014.

[51] A. El Kanj, O. Gomonay, I. Boventer, P. Bortolotti, V. Cros, A. Anane, and R. Lebrun. Antiferromagnetic magnon spintronic based on nonreciprocal and nondegenerated ultra-fast spin-waves in the canted antiferromagnet α-Fe_2O_3. *Science Advances*, 9(32):eadh1601, August 2023.

[52] T. Wimmer, A. Kamra, J. Gückelhorn, M. Opel, S. Geprägs, R. Gross, H. Huebl, and M. Althammer. Observation of Antiferromagnetic Magnon Pseudospin Dynamics and the Hanle Effect. *Physical Review Letters*, 125(24):247204, December 2020.

[53] G. R. Hoogeboom and B. J. van Wees. Nonlocal spin Seebeck effect in the bulk easy-plane antiferromagnet NiO. *Physical Review B*, 102(21):214415, December 2020.

[54] P. Muduli, R. Schlitz, T. Kosub, R. Hübner, A. Erbe, D. Makarov, and S. T. B. Goennenwein. Local and nonlocal spin Seebeck effect in lateral Pt–Cr2O3–Pt devices at low temperatures. *APL Materials*, 9(2):021122, February 2021.

[55] S. Hayami, Y. Yanagi, and H. Kusunose. Momentum-Dependent Spin Splitting by Collinear Antiferromagnetic Ordering. *Journal of the Physical Society of Japan*, 88(12):123702, December 2019.

[56] K.-H. Ahn, A. Hariki, K.-W. Lee, and J. Kuneš. Antiferromagnetism in RuO_2 as d-wave Pomeranchuk instability. *Physical Review B*, 99(18):184432, May 2019.

[57] K. Samanta, M. Ležaić, M. Merte, F. Freimuth, S. Blügel, and Y. Mokrousov. Crystal Hall and crystal magneto-optical effect in thin films of SrRuO3. *Journal of Applied Physics*, 127(21):213904, June 2020.

[58] L.-D. Yuan, Z. Wang, J.-W. Luo, and A. Zunger. Prediction of low-Z collinear and noncollinear antiferromagnetic compounds having momentum-dependent spin splitting even without spin-orbit coupling. *Physical Review Materials*, 5(1):014409, January 2021.

[59] I. Mazin, K. Koepernik, M. D. Johannes, R. González-Hernández, and L. Šmejkal. Prediction of unconventional magnetism in doped FeSb2. *Proceedings of the National Academy of Sciences*, 118(42):e2108924118, October 2021.

[60] H.-Y. Ma, M. Hu, N. Li, J. Liu, W. Yao, J.-F. Jia, and J. Liu. Multifunctional antiferromagnetic materials with giant piezomagnetism and noncollinear spin current. *Nature Communications*, 12(1):2846, May 2021.

[61] L. Šmejkal, A. B. Hellenes, R. González-Hernández, J. Sinova, and T. Jungwirth. Giant and Tunneling Magnetoresistance in Unconventional Collinear Antiferromagnets with Nonrelativistic Spin-Momentum Coupling. *Physical Review X*, 12(1):011028, February 2022.

[62] L.-D. Yuan, Z. Wang, J.-W. Luo, E. I. Rashba, and A. Zunger. Giant momentum-dependent spin splitting in centrosymmetric low-Z antiferromagnets. *Physical Review B*, 102(1):014422, July 2020.

[63] S. Hayami, Y. Yanagi, and H. Kusunose. Bottom-up design of spin-split and reshaped electronic band structures in antiferromagnets without spin-orbit coupling: Procedure on the basis of augmented multipoles. *Physical Review B*, 102(14):144441, October 2020.

[64] M. Roig, A. Kreisel, Y. Yu, B. M. Andersen, and D. F. Agterberg. Minimal models for altermagnetism. *Physical Review B*, 110(14):144412, October 2024.

[65] O. Fedchenko, J. Minár, A. Akashdeep, S. W. D'Souza, D. Vasilyev, O. Tkach, L. Odenbreit, Q. Nguyen, D. Kutnyakhov, N. Wind, L. Wenthaus, M. Scholz, K. Rossnagel, M. Hoesch, M. Aeschlimann, B. Stadtmüller, M. Kläui, G. Schönhense, T. Jungwirth, A. B. Hellenes, G. Jakob, L. Šmejkal, J. Sinova, and H.-J. Elmers. Observation of time-reversal symmetry breaking in the band structure of altermagnetic RuO2. *Science Advances*, 10(5):eadj4883, January 2024.

[66] S. Lee, S. Lee, S. Jung, J. Jung, D. Kim, Y. Lee, B. Seok, J. Kim, B. G. Park, L. Šmejkal, C.-J. Kang, and C. Kim. Broken Kramers Degeneracy in Altermagnetic MnTe. *Physical Review Letters*, 132(3):036702, January 2024.

[67] Q. Faure, D. Bounoua, V. Balédent, A. Gukasov, V. O. Garlea, A. Ribeiro, J. G. Rau, S. Petit, and P. McClarty. Altermagnetism revealed by polarized neutrons in MnF_2, September 2025.

[68] V. C. Morano, Z. Maesen, S. E. Nikitin, J. Lass, D. G. Mazzone, and O. Zaharko. Absence of Altermagnetic Magnon Band Splitting in MnF_2. *Physical Review Letters*, 134(22), June 2025.

[69] F. Zhang, X. Cheng, Z. Yin, C. Liu, L. Deng, Y. Qiao, Z. Shi, S. Zhang, J. Lin, Z. Liu, M. Ye, Y. Huang, X. Meng, C. Zhang, T. Okuda, K. Shimada, S. Cui, Y. Zhao, G.-H. Cao, S. Qiao, J. Liu, and C. Chen. Crystal-symmetry-paired spin–valley locking in a layered room-temperature metallic altermagnet candidate. *Nature Physics*, 21(5):760–767, May 2025.

[70] B. Jiang, M. Hu, J. Bai, Z. Song, C. Mu, G. Qu, W. Li, W. Zhu, H. Pi, Z. Wei, Y.-J. Sun, Y. Huang, X. Zheng, Y. Peng, L. He, S. Li, J. Luo, Z. Li, G. Chen, H. Li, H. Weng, and T. Qian. A metallic room-temperature d-wave altermagnet. *Nature Physics*, 21(5):754–759, May 2025.

[71] M. Sprague, M. I. Mondal, A. P. Sakhya, R. B. Regmi, S. Sadhukhan, A. K. Kumay, H. Sheokand, I. I. Mazin, N. J. Ghimire, and M. Neupane. Observation of altermagnetic spin splitting in an intercalated transition metal dichalcogenide, August 2025. 2508.12985 [cond-mat].

[72] D. Takegami, T. Aoyama, T. Okauchi, T. Yamaguchi, S. Tippireddy, S. Agrestini, M. García-Fernández, T. Mizokawa, K. Ohgushi, Ke-Jin Zhou, J. Chaloupka, J. Kuneš, A. Hariki, and H. Suzuki. Circular dichroism in resonant inelastic x-ray scattering: Probing altermagnetic domains in MnTe. *Physical Review Letters*, 135(19):196502, November 2025.

[73] Z. Liu, M. Ozeki, S. Asai, S. Itoh, and T. Masuda. Chiral Split Magnon in Altermagnetic MnTe. *Physical Review Letters*, 133(15):156702, October 2024.

[74] A. Badura, W. H. Campos, V. K. Bharadwaj, I. Kounta, L. Michez, M. Petit, J. Rial, M. Leiviskä, V. Baltz, F. Krizek, D. Kriegner, J. Železný, J. Zemen, S. Telkamp, S. Sailler, M. Lammel, R. Jaeschke-Ubiergo, A. B. Hellenes, R. González-Hernández, J. Sinova, T. Jungwirth, S. T. B. Goennenwein, L. Šmejkal, and H. Reichlova. Observation of the anomalous Nernst effect in altermagnetic candidate Mn_5Si_3. *Nature Communications*, 16(1):7111, August 2025.

[75] A. Badura, D. Kriegner, E. Schmoranzerová, K. Výborný, M. Leiviskä, R. L. Seeger, V. Baltz, D. Scheffler, S. Beckert, I. Kounta, L. Michez, L. Šmejkal, J. Sinova, S. T. B. Goennenwein, J. Železný, and H. Reichlová. Even-in-magnetic field part of transverse resistivity as a probe of magnetic transitions. *Applied Physics Letters*, 126(17):172404, April 2025.

[76] M. Hiraishi, H. Okabe, A. Koda, R. Kadono, T. Muroi, D. Hirai, and Z. Hiroi. Nonmagnetic Ground State in RuO_2 revealed by muon spin rotation. *Physical Review Letters*, 132(16):166702, April 2024.

[77] P. Keßler, L. Garcia-Gassull, A. Suter, T. Prokscha, Z. Salman, D. Khalyavin, P. Manuel, F. Orlandi, I. I. Mazin, R. Valentí, and S. Moser. Absence of magnetic order in RuO_2: insights from μ_{SR} spectroscopy and neutron diffraction. *npj Spintronics*, 2(1):50, October 2024.

[78] G. Yumnam, P. R. Raghuvanshi, J. D. Budai, L. Bocklage, D. Abernathy, Y. Cheng, A. H. Said, I. I. Mazin, H. Zhou, B. A. Frandsen, D. S. Parker, L. R. Lindsay, V. R. Cooper, M. E. Manley, and R. P. Hermann. Constraints on magnetism and correlations in RuO_2 from lattice dynamics and Mössbauer spectroscopy. *Cell Reports Physical Science*, 6(10):102852, October 2025.

[79] M. Wang, J. Zhang, D. Tian, P. Yu, and F. Kagawa. Unveiling an in-plane Hall effect in rutile RuO_2 films. *Communications Physics*, 8(1):28, January 2025.

[80] T. Osumi, K. Yamauchi, S. Souma, P. Shubhankar, A. Honma, K. Nakayama, K. Ozawa, M. Kitamura, K. Horiba, H. Kumigashira, C. Bigi, F. Bertran, T. Oguchi, T. Takahashi, Y. Maeno, and T. Sato. Spin-degenerate bulk bands and topological surface states associated with Dirac nodal lines in RuO_2. *Physical Review B*, 00(00):00, January 2026.

[81] W. Lu, S. Feng, Y. Wang, D. Chen, Z. Lin, X. Liang, S. Liu, W. Feng, K. Yamagami, J. Liu, C. Felser, Q. Wu, and J. Ma. Signature of Topological Surface Bands in Altermagnetic Weyl Semimetal CrSb. *Nano Letters*, 25(18):7343–7350, May 2025.

[82] M. Zeng, M.-Y. Zhu, Y.-P. Zhu, X.-R. Liu, X.-M. Ma, Y.-J. Hao, P. Liu, G. Qu, Y. Yang, Z. Jiang, K. Yamagami, M. Arita, X. Zhang, T.-H. Shao, Y. Dai, K. Shimada, Z. Liu, M. Ye, Y. Huang, Q. Liu, and C. Liu. Observation of Spin Splitting in Room-Temperature Metallic Antiferromagnet CrSb. *Advanced Science*, 11(43):2406529, September 2024.

[83] S. Zeng and Y.-J. Zhao. Bilayer stacking *A*-type altermagnet: A general approach to generating two-dimensional altermagnetism. *Physical Review B*, 110(17):174410, November 2024.

[84] Z. Zhou, X. Cheng, M. Hu, R. Chu, H. Bai, L. Han, J. Liu, F. Pan, and C. Song. Manipulation of the altermagnetic order in CrSb via crystal symmetry. *Nature*, 638(8051):645–650, February 2025.

[85] N. Biniskos, M. dos Santos Dias, S. Agrestini, D. Sviták, K.-J. Zhou, J. Pospíšil, and P. Čermák. Systematic mapping of altermagnetic magnons by resonant inelastic X-ray circular dichroism. *Nature Communications*, 16(1):9311, October 2025.

[86] Q. Sun, J. Guo, D. Wang, D. L. Abernathy, W. Tian, and C. Li. Observation of chiral magnon band splitting in altermagnetic hematite. *Physical Review Letters*, 135(18):186703, October 2025.

[87] J. Luo, X. Zhou, J. Liang, L. Wang, Q. Zhou, Y. Jiang, W. Wang, Y. Yao, L. Yang, and W. Jiang. Symmetry-driven giant magneto-optical Kerr effects in altermagnetic insulator. *Chinese Physics Letters*, 43(2):020713, February 2026.

[88] L. Bai, W. Feng, S. Liu, L. Šmejkal, Y. Mokrousov, and Y. Yao. Altermagnetism: Exploring New Frontiers in Magnetism and Spintronics. *Advanced Functional Materials*, 34(49):2409327, September 2024.

[89] Z.-F. Gao, S. Qu, B. Zeng, Y. Liu, J.-R. Wen, H. Sun, P.-J. Guo, and Z.-Y. Lu. AI-accelerated discovery of altermagnetic materials. *National Science Review*, 12(4):nwaf066, April 2025.

[90] S.-B. Zhang, L.-H. Hu, and T. Neupert. Finite-momentum Cooper pairing in proximitized altermagnets. *Nature Communications*, 15(1):1801, February 2024.

[91] D. Zhu, Z.-Y. Zhuang, Z. Wu, and Z. Yan. Topological superconductivity in two-dimensional altermagnetic metals. *Physical Review B*, 108(18):184505, November 2023.

[92] C. W. J. Beenakker and T. Vakhtel. Phase-shifted Andreev levels in an altermagnet Josephson junction. *Physical Review B*, 108(7):075425, August 2023.

[93] S. A. A. Ghorashi, T. L. Hughes, and J. Cano. Altermagnetic Routes to Majorana Modes in Zero Net Magnetization. *Physical Review Letters*, 133(10):106601, September 2024.

[94] Y.-X. Li and C.-C. Liu. Majorana corner modes and tunable patterns in an altermagnet heterostructure. *Physical Review B*, 108(20):205410, November 2023.

[95] L. Šmejkal, A. Marmodoro, K.-H. Ahn, R. González-Hernández, I. Turek, S. Mankovsky, H. Ebert, S. W. D'Souza, O. Šipr, J. Sinova, and T. Jungwirth. Chiral Magnons in Altermagnetic RuO_2. *Physical Review Letters*, 131(25):256703, December 2023.

[96] R. M. Fernandes, V. S. de Carvalho, T. Birol, and R. G. Pereira. Topological transition from nodal to nodeless Zeeman splitting in altermagnets. *Physical Review B*, 109(2):024404, January 2024.

[97] S. Das, A. Ross, X. X. Ma, S. Becker, C. Schmitt, F. van Duijn, E. F. Galindez-Ruales, F. Fuhrmann, M.-A. Syskaki, U. Ebels, V. Baltz, A.-L. Barra, H. Y. Chen, G. Jakob, S. X. Cao, J. Sinova, O. Gomonay, R. Lebrun, and M. Kläui. Anisotropic long-range spin transport in canted antiferromagnetic orthoferrite YFeO3. *Nature Communications*, 13(1):6140, October 2022.

[98] Q. Cui, B. Zeng, P. Cui, T. Yu, and H. Yang. Efficient spin Seebeck and spin Nernst effects of magnons in altermagnets. *Physical Review B*, 108(18):L180401, November 2023.

[99] R. Hoyer, P. P. Stavropoulos, A. Razpopov, R. Valentí, L. Šmejkal, and A. Mook. Altermagnetic splitting of magnons in hematite α-Fe_2O_3. *Physical Review B*, 112(6):064425, August 2025.

[100] R. Hoyer, R. Jaeschke-Ubiergo, K.-H. Ahn, L. Šmejkal, and A. Mook. Spontaneous crystal thermal Hall effect in insulating altermagnets. *Physical Review B*, 111(2):L020412, January 2025.

[101] J. Sinova, S. O. Valenzuela, J. Wunderlich, C.H. Back, and T. Jungwirth. Spin Hall effects. *Reviews of Modern Physics*, 87(4):1213–1260, October 2015.

[102] E. Saitoh, M. Ueda, H. Miyajima, and G. Tatara. Conversion of spin current into charge current at room temperature: Inverse spin-Hall effect. *Applied Physics Letters*, 88(18):182509, May 2006.

[103] K. Uchida, S. Takahashi, K. Harii, J. Ieda, W. Koshibae, K. Ando, S. Maekawa, and E. Saitoh. Observation of the spin Seebeck effect. *Nature*, 455(7214):778–781, October 2008.

[104] K.-I. Uchida, H. Adachi, T. Ota, H. Nakayama, S. Maekawa, and E. Saitoh. Observation of longitudinal spin-Seebeck effect in magnetic insulators. *Applied Physics Letters*, 97(17):172505, October 2010.

[105] A. V. Chumak, V. I. Vasyuchka, A. A. Serga, and B. Hillebrands. Magnon spintronics. *Nature Physics*, 11(6):453–461, June 2015.

[106] L. J. Cornelissen, K. J. H. Peters, G. E. W. Bauer, R. A. Duine, and B. J. van Wees. Magnon spin transport driven by the magnon chemical potential in a magnetic insulator. *Physical Review B*, 94(1):014412, July 2016.

[107] S. M. Rezende, A. Azevedo, and R. L. Rodríguez-Suárez. Introduction to antiferromagnetic magnons. *Journal of Applied Physics*, 126(15):151101, October 2019.

[108] O. Gomonay, V. P. Kravchuk, R. Jaeschke-Ubiergo, K. V. Yershov, T. Jungwirth, L. Šmejkal, J. van den Brink, and J. Sinova. Structure, control, and dynamics of altermagnetic textures. *npj Spintronics*, 2(1):35, July 2024.

[109] T. Jungwirth, R. M. Fernandes, J. Sinova, and L. Smejkal. Altermagnets and beyond: Nodal magnetically-ordered phases, September 2024. arXiv:2409.10034 [cond-mat].

[110] I. Mazin. Altermagnetism in MnTe: Origin, predicted manifestations, and routes to detwinning. *Physical Review B*, 107(10):L100418, March 2023.

[111] A. B. Hellenes, T. Jungwirth, R. Jaeschke-Ubiergo, A. Chakraborty, J. Sinova, and L. Šmejkal. P-wave magnets, July 2024. arXiv:2309.01607 [cond-mat].

[112] B. Brekke, P. Sukhachov, G. H. Giil, A. Brataas, and J. Linder. Minimal Models and Transport Properties of Unconventional p-Wave Magnets. *Physical Review Letters*, 133(23), December 2024.

[113] A. Chakraborty, A. Birk Hellenes, R. Jaeschke-Ubiergo, T. Jungwirth, L. Šmejkal, and J. Sinova. Highly efficient non-relativistic Edelstein effect in nodal p-wave magnets. *Nature Communications*, 16(1):7270, August 2025.

[114] Q. N. Meier, A. Carta, C. Ederer, and A. Cano. (Anti-)Altermagnetism from Orbital Ordering in the Ruddlesden-Popper Chromates $Sr_{n+1}Cr_nO_{3n+1}$, February 2025. arXiv:2502.01515 [cond-mat].

[115] E. Galindez-Ruales, W. Yang, T. Dannegger, M. Kundu, J. Köhler, C. Schmitt, F. Fuhrmann, A. Akashdeep, D. M. Tran, X. Ma, G. Jakob, S. Cao, U. Nowak, and M. Kläui. Altermagnetic magnon transport in the d-wave altermagnet $LuFeO_3$, August 2025. arXiv:2508.14569 [cond-mat.mtrl-sci].

[116] Paul A. McClarty and J. G. Rau. Landau Theory of Altermagnetism. *Physical Review Letters*, 132(17):176702, April 2024.

[117] R. Cheng, J. Xiao, Q. Niu, and A. Brataas. Spin Pumping and Spin-Transfer Torques in Antiferromagnets. *Physical Review Letters*, 113(5):057601, July 2014.

[118] S. A. Bender and Y. Tserkovnyak. Interfacial spin and heat transfer between metals and magnetic insulators. *Physical Review B*, 91(14):140402(R), April 2015.

[119] Y. Tserkovnyak, A. Brataas, and G. E. W. Bauer. Spin pumping and magnetization dynamics in metallic multilayers. *Physical Review B*, 66(22):224403, December 2002.

[120] C. Kittel. Theory of Antiferromagnetic Resonance. *Physical Review*, 82(4):565, May 1951.

[121] R. L. White. Review of Recent Work on the Magnetic and Spectroscopic Properties of the Rare-Earth Orthoferrites. *Journal of Applied Physics*, 40(3):1061–1069, March 1969.

[122] T. Yamaguchi. Theory of spin reorientation in rare-earth orthochromites and orthoferrites. *Journal of Physics and Chemistry of Solids*, 35(4):479–500, January 1974.

[123] X. H. Verbeek, D. Voderholzer, S. Schären, Y. Gachnang, N. A. Spaldin, and S. Bhowal. Nonrelativistic ferromagnetotriakontadipolar order and spin splitting in hematite. *Physical Review Research*, 6(4):043157, November 2024.

[124] A. Ross, R. Lebrun, C. Ulloa, D. A. Grave, A. Kay, L. Baldrati, F. Kronast, S. Valencia, A. Rothschild, and M. Kläui. Structural sensitivity of the spin Hall magnetoresistance in antiferromagnetic thin films. *Physical Review B*, 102(9):094415, September 2020.

[125] R. Lebrun, A. Ross, O. Gomonay, S. A. Bender, L. Baldrati, F. Kronast, A. Qaiumzadeh, J. Sinova, A. Brataas, R. A. Duine, and M. Kläui. Anisotropies and magnetic phase transitions in insulating antiferromagnets determined by a Spin-Hall magnetoresistance probe. *Communications Physics*, 2(1):50, May 2019.

[126] T. Dannegger, A. Deák, L. Rózsa, E. Galindez-Ruales, S. Das, E. Baek, M. Kläui, L. Szunyogh, and U. Nowak. Magnetic properties of hematite revealed by an *ab initio* parameterized spin model. *Physical Review B*, 107(18):184426, May 2023.

[127] M. Białek, J. Zhang, H. Yu, and J.-Ph. Ansermet. Antiferromagnetic resonance in α-Fe_2O_3 up to its Néel temperature. *Applied Physics Letters*, 121(3):032401, July 2022.

[128] T. Moriya. Anisotropic Superexchange Interaction and Weak Ferromagnetism. *Physical Review*, 120(1):91–98, October 1960.

[129] I. Dzyaloshinsky. A thermodynamic theory of "weak" ferromagnetism of antiferromagnetics. *Journal of Physics and Chemistry of Solids*, 4(4):241–255, January 1958.

[130] H. Liu, H. Zhang, J. Keagy, Q. Gao, L. Li, J. Li, R. Cheng, and J. Shi. Anisotropic field suppression of Morin transition temperature in epitaxially grown hematite thin films. *Physical Review Materials*, 9(3):034410, March 2025.

[131] H. Qiu, T. S. Seifert, L. Huang, Y. Zhou, Z. Kašpar, C. Zhang, J. Wu, K. Fan, Q. Zhang, D. Wu, T. Kampfrath, C. Song, B. Jin, J. Chen, and P. Wu. Terahertz Spin Current Dynamics in Antiferromagnetic Hematite. *Advanced Science*, 10(18):2300512, April 2023.

[132] J. O. Artman, J. C. Murphy, and S. Foner. Magnetic Anisotropy in Antiferromagnetic Corundum-Type Sesquioxides. *Physical Review*, 138(3A):A912–A917, May 1965.

[133] P. J. Besser, A. H. Morrish, and C. W. Searle. Magnetocrystalline Anisotropy of Pure and Doped Hematite. *Physical Review*, 153(2):632–640, January 1967.

[134] M. Scheufele, J. Gückelhorn, M. Opel, A. Kamra, H. Huebl, R. Gross, S. Geprägs, and M. Althammer. Impact of growth conditions on magnetic anisotropy and magnon Hanle effect in α-Fe_2O_3. *APL Materials*, 11(9):091115, September 2023.

[135] S.-H. Park, H. Jang, J.-Y. Kim, B.-G. Park, T.-Y. Koo, and J.-H. Park. Strain control of Morin temperature in epitaxial α-Fe_2O_3(0001) film. *Europhysics Letters*, 103(2):27007, August 2013.

[136] D. Kan, T. Moriyama, R. Aso, S. Horai, and Y. Shimakawa. Triaxial magnetic anisotropy and Morin transition in α-Fe_2O_3 epitaxial films characterized by spin Hall magnetoresistance. *Applied Physics Letters*, 120(11):112403, March 2022.

[137] N. Shimomura, S. P. Pati, Y. Sato, T. Nozaki, T. Shibata, K. Mibu, and M. Sahashi. Morin transition temperature in (0001)-oriented α-Fe_2O_3 thin film and effect of Ir doping. *Journal of Applied Physics*, 117(17):17C736, April 2015.

[138] H. Jani, J. Linghu, S. Hooda, R. V. Chopdekar, C. Li, G. J. Omar, S. Prakash, Y. Du, P. Yang, A. Banas, K. Banas, S. Ghosh, S. Ojha, G. R. Umapathy, D. Kanjilal, A. Ariando, S. J. Pennycook, E. Arenholz, P. G. Radaelli, J. M. D. Coey, Y. P. Feng, and T. Venkatesan. Reversible hydrogen control of antiferromagnetic anisotropy in α-Fe_2O_3. *Nature Communications*, 12(1):1668, March 2021.

[139] A. M. Glazer. The classification of tilted octahedra in perovskites. *Acta Crystallographica Section B: Structural Crystallography and Crystal Chemistry*, 28(11):3384–3392, November 1972.

[140] P. M. Woodward. Octahedral Tilting in Perovskites. I. Geometrical Considerations. *Acta Crystallographica Section B: Structural Science*, 53(1):32–43, February 1997.

[141] D. Treves. Magnetic Studies of Some Orthoferrites. *Physical Review*, 125(6):1843–1853, March 1962.

[142] D. Treves. Studies on Orthoferrites at the Weizmann Institute of Science. *Journal of Applied Physics*, 36(3):1033–1039, March 1965.

[143] Y.-T. Chen, S. Takahashi, H. Nakayama, M. Althammer, S. T. B. Goennenwein, E. Saitoh, and G. E. W. Bauer. Theory of spin Hall magnetoresistance. *Physical Review B*, 87(14):144411, April 2013.

[144] T. Hajiri, L. Baldrati, R. Lebrun, M. Filianina, A. Ross, N. Tanahashi, M. Kuroda, W. L. Gan, T. O. Menteş, F. Genuzio, A. Locatelli, H. Asano, and M. Kläui. Spin structure and spin Hall magnetoresistance of epitaxial thin

films of the insulating non-collinear antiferromagnet $SmFeO_3$. *Journal of Physics: Condensed Matter*, 31(44):445804, August 2019.

[145] J. Fischer, M. Althammer, N. Vlietstra, H. Huebl, S. T.B. Goennenwein, R. Gross, S. Geprägs, and M. Opel. Large Spin Hall Magnetoresistance in Antiferromagnetic α-Fe_2O_3/pt Heterostructures. *Physical Review Applied*, 13(1):014019, January 2020.

[146] K. P. Belov, A. K. Zvezdin, A. M. Kadomtseva, and R. Z. Levitin. Spin-reorientation transitions in rare-earth magnets. *Soviet Physics Uspekhi*, 19(7):574, July 1976.

[147] M. Marezio, J. P. Remeika, and P. D. Dernier. The crystal chemistry of the rare earth orthoferrites. *Acta Crystallographica Section B*, 26(12):2008–2022, December 1970.

[148] X. Li, D. Kim, Y. Liu, and J. Kono. Terahertz spin dynamics in rare-earth orthoferrites. *Photonics Insights*, 1(2):R05, January 2023.

[149] M. Eibschütz. Lattice constants of orthoferrites. *Acta Crystallographica*, 19(3):337–339, September 1965.

[150] P. K. Pradhan, A. B. Panda, G. K. Mishra, and N. K. Mohanty. Rare earth orthoferrites ($RFeO_3$, R= rare earth elements): A comprehensive review of structural, dielectric, and magnetic properties. *Smart Materials in Manufacturing*, 3:100082, January 2025.

[151] J. Jensen and A. R. Mackintosh. Elements Of Rare Earth Magnetism. In *Rare Earth Magnetism: Structures and Excitations*, page 1–67. Oxford University Press, June 1991.

[152] N. E. Massa, L. del Campo, V. T. Phuoc, P. Kayser, and J. A. Alonso. Low-temperature terahertz spectroscopy of $LaFeO_3$, $PrFeO_3$, $ErFeO_3$, and $LuFeO_3$: Quasimagnon resonances and ground-state multiplet transitions. *Physical Review B*, 108(11):115116, September 2023.

[153] M. C. Weber, M. Guennou, H. J. Zhao, J. Íñiguez, R. Vilarinho, A. Almeida, J. A. Moreira, and J. Kreisel. Raman spectroscopy of rare-earth orthoferrites $RFeO_3$ (r=la, sm, eu, gd, tb, dy). *Physical Review B*, 94(21):214103, December 2016.

[154] C. Ritter, M. Ceretti, and W. Paulus. Determination of the magnetic structures in orthoferrite $CeFeO_3$ by neutron powder diffraction: first order spin reorientation and appearance of an ordered Ce-moment. *Journal of Physics: Condensed Matter*, 33(21):215802, April 2021.

[155] L. Hou, L. Shi, J. Zhao, S. Pan, Y. Xin, and X. Yuan. Spin-Reorientation Transition Driven by Double Exchange in $CeFeO_3$ Ceramics. *The Journal of Physical Chemistry C*, 124(28):15399–15405, July 2020.

[156] E. Li, Z. Feng, B. Kang, J. Zhang, W. Ren, and S. Cao. Spin switching in single crystal $PrFeO_3$ and spin configuration diagram of rare earth orthoferrites. *Journal of Alloys and Compounds*, 811(1):152043, November 2019.

[157] J. Jiang, G. Song, D. Wang, Z. Jin, Z. Tian, X. Lin, J. Han, G. Ma, S. Cao, and Z. Cheng. Magnetic-field dependence of strongly anisotropic spin reorientation transition in $NdFeO_3$: a terahertz study. *Journal of Physics: Condensed Matter*, 28(11):116002, February 2016.

[158] S. Cao, H. Zhao, B. Kang, J. Zhang, and W. Ren. Temperature induced Spin Switching in $SmFeO_3$ Single Crystal. *Scientific Reports*, 4(1):5960, August 2014.

[159] X.-H. Zhu, X.-B. Xiao, X.-R. Chen, and B.-G. Liu. Electronic structure, magnetism and optical properties of orthorhombic $GdFeO_3$ from first principles. *RSC Advances*, 7(7):4054–4061, January 2017.

[160] B.-G. Park, S. B. Kim, H.-J. Lee, Y. H. Jeong, J.-H. Park, and C.-S. Kim. Magnetic Properties of the Orthoferrites $TbFeO_3$ and $ErFeO_3$. *Journal of the Korean Physical Society*, 53(2):758–762, August 2008.

[161] T. N. Stanislavchuk, Y. Wang, S.-W. Cheong, and Sirenko A. A. Far-IR magnetospectroscopy of magnons and electromagnons in $TbFeO_3$ single crystals at low temperatures. *Physical Review B*, 95(5):054427, February 2017.

[162] C. Ritter, R. Vilarinho, J. A. Moreira, M. Mihalik, M. Mihalik, and S. Savvin. The magnetic structure of $DyFeO_3$ revisited: Fe spin reorientation and Dy incommensurate magnetic order. *Journal of Physics: Condensed Matter*, 34(26):265801, April 2022.

[163] B. Biswas, V. F. Michel, Ø. S. Fjellvåg, G. Bimashofer, M. Döbeli, M. Jambor, L. Keller, E. Müller, V. Ukleev, E. V. Pomjakushina, D. Singh, U. Stuhr, C. A. F. Vaz, T. Lippert, and C. W. Schneider. Role of Dy on the magnetic properties of orthorhombic $DyFeO_3$. *Physical Review Materials*, 6(7):074401, July 2022.

[164] K. Dey, A. Indra, S. Mukherjee, S. Majumdar, J. Strempfer, O. Fabelo, E. Mossou, T. Chatterji, and S. Giri. Natural ferroelectric order near ambient temperature in the orthoferrite $HoFeO_3$. *Physical Review B*, 100(21):214432, December 2019.

[165] A. K. Ovsyanikov, I. A. Zobkalo, W. Schmidt, S. N. Barilo, S. A. Guretskii, and V. Hutanu. Neutron inelastic scattering study of rare-earth orthoferrite $HoFeO_3$. *Journal of Magnetism and Magnetic Materials*, 507(1):166855, August 2020.

[166] A. K. Ovsianikov, O. V. Usmanov, I. A. Zobkalo, V. Hutanu, S. N. Barilo, N. A. Liubachko, K. A. Shaykhutdinov, K. Yu Terentjev, S. V. Semenov, T. Chatterji, M. Meven, P. J. Brown, G. Roth, L. Peters, H. Deng, and A. Wu. Magnetic phase diagram of $HoFeO_3$ by neutron diffraction. *Journal of Magnetism and Magnetic Materials*, 557(1):169431, September 2022.

[167] T. Chatterji, M. Meven, and P. J. Brown. Temperature evolution of magnetic structure of $HoFeO_3$ by single crystal neutron diffraction. *AIP Advances*, 7(4):045106, April 2017.

[168] K. Yamaguchi, T. Kurihara, Y. Minami, M. Nakajima, and T. Suemoto. Terahertz Time-Domain Observation of Spin Reorientation in Orthoferrite $ErFeO_3$ through magnetic free induction decay. *Physical Review Letters*, 110(13):137204, March 2013.

[169] G. Deng, P. Guo, W. Ren, S. Cao, H. E. Maynard-Casely, M. Avdeev, and G. J. McIntyre. The magnetic structures and transitions of a potential multiferroic orthoferrite $ErFeO_3$. *Journal of Applied Physics*, 117(16):164105, April 2015.

[170] K. Zhang, K. Xu, X. Liu, Z. Zhang, Z. Jin, X. Lin, B. Li, S. Cao, and G. Ma. Resolving the spin reorientation and crystal-field transitions in $TmFeO_3$ with terahertz transient. *Scientific Reports*, 6(1):23648, March 2016.

[171] X. Ma, N. Yuan, X. Luo, Y. Chen, B. Kang, W. Ren, J. Zhang, and S. Cao. Field tunable spin switching in perovskite $YbFeO_3$ single crystal. *Materials Today Communications*, 27(1):102438, June 2021.

[172] S. E. Hahn, A. A. Podlesnyak, G. Ehlers, G. E. Granroth, R. S. Fishman, A. I. Kolesnikov, E. Pomjakushina, and K. Conder. Inelastic neutron scattering studies of $YFeO_3$. *Physical Review B*, 89(1):014420, January 2014.

[173] Z. Jin, Z. Mics, G. Ma, Z. Cheng, M. Bonn, and D. Turchinovich. Single-pulse terahertz coherent control of spin resonance in the canted antiferromagnet $YFeO_3$, mediated by dielectric anisotropy. *Physical Review B*, 87(9):094422, March 2013.

[174] L. J. Cornelissen, J. Liu, R. A. Duine, J. Ben Youssef, and B. J. van Wees. Long-distance transport of magnon spin information in a magnetic insulator at room temperature. *Nature Physics*, 11(12):1022–1026, December 2015.

[175] Y. Tserkovnyak, A. Brataas, G. E. W. Bauer, and B. I. Halperin. Nonlocal magnetization dynamics in ferromagnetic heterostructures. *Reviews of Modern Physics*, 77(4):1375–1421, December 2005.

[176] P. Liu, J. Li, J. Han, X. Wan, and Q. Liu. Spin-Group Symmetry in Magnetic Materials with Negligible Spin-Orbit Coupling. *Physical Review X*, 12(2):021016, April 2022.

[177] J. Xiao, G. E. W. Bauer, K.-C. Uchida, E. Saitoh, and S. Maekawa. Theory of magnon-driven spin Seebeck effect. *Physical Review B*, 81(21):214418, June 2010.

[178] S. Murakami, N. Nagaosa, and S.-C. Zhang. Dissipationless Quantum Spin Current at Room Temperature. *Science*, 301(5638):1348–1351, September 2003.

[179] N. Nagaosa, J. Sinova, S. Onoda, A. H. MacDonald, and N. P. Ong. Anomalous Hall effect. *Reviews of Modern Physics*, 82(2):1539–1592, May 2010.

[180] J. Barker and G. E.W. Bauer. Thermal Spin Dynamics of Yttrium Iron Garnet. *Physical Review Letters*, 117(21):217201, November 2016.

[181] S. M. Rezende, R. L. Rodríguez-Suárez, and A. Azevedo. Diffusive magnonic spin transport in antiferromagnetic insulators. *Physical Review B*, 93(5):054412, February 2016.

[182] A. Brataas, Y. V. Nazarov, and G. E. W. Bauer. Finite-Element Theory of Transport in Ferromagnet–Normal Metal Systems. *Physical Review Letters*, 84(11):2481–2484, March 2000.

[183] S. Takei, B. I. Halperin, A. Yacoby, and Tserkovnyak1 Y. Superfluid spin transport through antiferromagnetic insulators. *Physical Review B*, 90(9):094408, September 2014.

[184] B. Flebus, S. A. Bender, Y. Tserkovnyak, and R. A. Duine. Two-Fluid Theory for Spin Superfluidity in Magnetic Insulators. *Physical Review Letters*, 116(11):117201, March 2016.

[185] H.-M. Tang, X.-T. Jia, and S.-Z. Wang. Thermal spin transfer torque in Fe|Ag|YIG multilayers. *Frontiers of Physics*, 12(3):128501, June 2017.

[186] A. Costa, J. C. G. Henriques, and J. Fernández-Rossier. Giant spatial anisotropy of magnon Landau damping in altermagnets. *SciPost Physics*, 18(4):125, April 2025.

[187] S. A. Bender, H. Skarsvåg, A. Brataas, and R. A. Duine. Enhanced Spin Conductance of a Thin-Film Insulating Antiferromagnet. *Physical Review Letters*, 119(5):056804, August 2017.

[188] R. Cheng, S. Okamoto, and D. Xiao. Spin Nernst Effect of Magnons in Collinear Antiferromagnets. *Physical Review Letters*, 117(21):217202, November 2016.

[189] A. Kamra and W. Belzig. Spin Pumping and Shot Noise in Ferrimagnets: Bridging Ferro- and Antiferromagnets. *Physical Review Letters*, 119(19):197201, November 2017.

[190] F. Keffer and C. Kittel. Theory of antiferromagnetic resonance. *Physical Review*, 85:329–337, Jan 1952.

[191] Vladimir A. Zyuzin and Alexey A. Kovalev. Magnon Spin Nernst Effect in Antiferromagnets. *Physical Review Letters*, 117(21):217203, November 2016.

[192] H. V. Gomonay and V. M. Loktev. Spin transfer and current-induced switching in antiferromagnets. *Physical Review B*, 81(14):144427, April 2010.

[193] J.-H. Moon, S.-M. Seo, K.-J. Lee, K.-W. Kim, J. Ryu, H.-W. Lee, R. D. McMichael, and M. D. Stiles. Spin-wave propagation in the presence of interfacial Dzyaloshinskii-Moriya interaction. *Physical Review B*, 88(18):184404, November 2013.

[194] H. Nakayama, M. Althammer, Y.-T. Chen, K. Uchida, Y. Kajiwara, D. Kikuchi, T. Ohtani, S. Geprägs, M. Opel, S. Takahashi, R. Gross, G. E. W. Bauer, S. T. B. Goennenwein, and E. Saitoh. Spin Hall Magnetoresistance Induced by a Nonequilibrium Proximity Effect. *Physical Review Letters*, 110(20):206601, May 2013.

[195] E. Cho, K. Klyukin, T. Su, A. Kaczmarek, and C. A. Ross. Composition-Dependent Ferroelectricity of $LuFeO_3$ Orthoferrite Thin Films. *Advanced Electronic Materials*, 9(7):2300059, May 2023.

[196] Y. Niu, N. Vinogradov, A. Preobrajenski, C. Struzzi, B. Sarpi, L. Zhu, E. Golias, and A. Zakharov. MAXPEEM: a spectromicroscopy beamline at MAX IV laboratory. *Journal of Synchrotron Radiation*, 30(2):468–478, March 2023.

[197] D. A. Grave, H. Dotan, Y. Levy, Y. Piekner, B. Scherrer, K. D. Malviya, and A. Rothschild. Heteroepitaxial hematite photoanodes as a model system for solar water splitting. *Journal of Materials Chemistry A*, 4(8):3052–3060, February 2016.

[198] M. Todeschini, A. Bastos da Silva Fanta, F. Jensen, J. B. Wagner, and A. Han. Influence of Ti and Cr Adhesion Layers on Ultrathin Au Films. *ACS Applied Materials & Interfaces*, 9(42):37374–37385, October 2017.

[199] P. R. Willmott and J. R. Huber. Pulsed laser vaporization and deposition. *Reviews of Modern Physics*, 72(1):315–328, January 2000.

[200] G. J. H. M. Rijnders, G. Koster, D. H. A. Blank, and H. Rogalla. In situ monitoring during pulsed laser deposition of complex oxides using reflection high energy electron diffraction under high oxygen pressure. *Applied Physics Letters*, 70(14):1888–1890, April 1997.

[201] T. Ohnishi, T. Yamamoto, S. Meguro, H. Koinuma, and M. Lippmaa. Pulsed laser ablation and deposition of complex oxides. *Journal of Physics: Conference Series*, 59(1):514, April 2007.

[202] Y.-L. Huang, H.-J. Liu, C.-H. Ma, P. Yu, Y.-H. Chu, and J.-C. Yang. Pulsed laser deposition of complex oxide heteroepitaxy. *Chinese Journal of Physics*, 60(1):481–501, August 2019.

[203] H. M. Christen and G. Eres. Recent advances in pulsed-laser deposition of complex oxides. *Journal of Physics: Condensed Matter*, 20(26):264005, June 2008.

[204] S. M. Koohpayeh, D. Fort, and J. S. Abell. The optical floating zone technique: A review of experimental procedures with special reference to oxides. *Progress in Crystal Growth and Characterization of Materials*, 54(3):121–137, September 2008.

[205] Naoki Kikugawa. Recent Progress of Floating-Zone Techniques for Bulk Single-Crystal Growth. *Crystals*, 14(6):552, June 2024.

[206] S. M. Koohpayeh, D. Fort, A. Bradshaw, and J. S. Abell. Thermal characterization of an optical floating zone furnace: A direct link with controllable growth parameters. *Journal of Crystal Growth*, 311(8):2513–2518, April 2009.

[207] P. J Kelly and R. D Arnell. Magnetron sputtering: a review of recent developments and applications. *Vacuum*, 56(3):159–172, March 2000.

[208] N. Savvides and B. Window. Unbalanced magnetron ion-assisted deposition and property modification of thin films. *Journal of Vacuum Science & Technology A*, 4(3):504–508, May 1986.

[209] J. E. Greene. Review Article: Tracing the recorded history of thin-film sputter deposition: From the 1800s to 2017. *Journal of Vacuum Science & Technology A*, 35(5):05C204, September 2017.

[210] M. Althammer, S. Meyer, H. Nakayama, M. Schreier, S. Altmannshofer, M. Weiler, H. Huebl, S. Geprägs, M. Opel, R. Gross, D. Meier, C. Klewe, T. Kuschel, J.-M. Schmalhorst, G. Reiss, L. Shen, A. Gupta, Y.-T. Chen, G. E. W. Bauer, E. Saitoh, and S. T. B. Goennenwein. Quantitative study of the spin Hall magnetoresistance in ferromagnetic insulator/normal metal hybrids. *Physical Review B*, 87(22):224401, June 2013.

[211] E. Sagasta, Y. Omori, M. Isasa, M. Gradhand, L. E. Hueso, Y. Niimi, Y.-C. Otani, and F. Casanova. Tuning the spin Hall effect of Pt from the moderately dirty to the superclean regime. *Physical Review B*, 94(6):060412, August 2016.

[212] B. D. Cullity and S. R. Stock. *Elements of X-ray Diffraction*. Prentice Hall, March 2001.

[213] J. Als-Nielsen and D. McMorrow. *Diffraction by perfect crystals*. John Wiley & Sons, Ltd, March 2011.

[214] D. M. Mattox. Thin film metallization of oxides in microelectronics. *Thin Solid Films*, 18(2):173–186, November 1973.

[215] M. Kawamura, T. Mashima, Y. Abe, and K. Sasaki. Formation of ultra-thin continuous Pt and Al films by RF sputtering. *Thin Solid Films*, 377-378:537–542, December 2000.

[216] H. Hölscher. AFM, Tapping Mode. In *Encyclopedia of Nanotechnology*, page 99. Springer, Dordrecht, 2012.

[217] S. Kohli, C. D. Rithner, P. K. Dorhout, A. M. Dummer, and C. S. Menoni. Comparison of nanometer-thick films by x-ray reflectivity and spectroscopic ellipsometry. *Review of Scientific Instruments*, 76(2):023906, January 2005.

[218] P. Dutta and P. M. Horn. Low-frequency fluctuations in solids: $1/f$ noise. *Reviews of Modern Physics*, 53(3):497–516, July 1981.

[219] M. B. Weissman. $1/f$ noise and other slow, nonexponential kinetics in condensed matter. *Reviews of Modern Physics*, 60(2):537–571, April 1988.

[220] R. Kiely. Understanding and eliminating $1/f$ noise. *Analog Dialogue*, May 2017.

[221] Keithley Instruments, a Tektronix company. *Low Level Measurements Handbook, 7th Edition: Precision DC Current, Voltage, and Resistance Measurements*, January 2016.

[222] Tektronix. *Low-Voltage/Low-Resistance Measurement Techniques*, January 2013.

[223] Tektronix. *Making Precision Low Voltage and Low Resistance Measurements*, September 2013.

[224] Stanford Research Systems. *About Lock-In Amplifiers, Application Note #3*, May 2004.

[225] Lake Shore Cryotronics. *The Lock-in Amplifier Explained and Reimagined*, August 2021.

[226] A. Mandelis. Signal-to-noise ratio in lock-in amplifier synchronous detection: A generalized communications systems approach with applications to frequency, time, and hybrid (rate window) photothermal measurements. *Review of Scientific Instruments*, 65(11):3309–3323, November 1994.

[227] Keithley Instruments. *Model 2182/2182A Nanovoltmeter User's Manual*, May 2017. Document 2182A-900-01 Rev. B.

[228] J. B. Johnson. Thermal agitation of electricity in conductors. *Physical Review*, 32(1):97–109, July 1928.

[229] H. Nyquist. Thermal agitation of electric charge in conductors. *Physical Review*, 32(1):110–113, July 1928.

[230] F. N. Hooge. $1/f$ noise is no surface effect. *Physics Letters A*, 29(3):139–140, April 1969.

[231] Robin S. Smith. Electrical characterization of GaAs materials and devices. *Advanced Materials*, 5(4):314–315, April 1993.

[232] W. Li, C. Xu, M. Wang, M.and Zou, W. Li, H. Wang, W. Jiang, and B. Wang. Large anomalous Nernst effect in a metallic altermagnet CrSb single crystal. *Physical Review B*, 112(10):L100401, September 2025.

[233] E. Arenholz, G. van der Laan, R. V. Chopdekar, and Y. Suzuki. Anisotropic x-ray magnetic linear dichroism at the Fe $l_{2,3}$ edges in Fe_3O_4. *Physical Review B*, 74(9):094407, September 2006.

[234] G. van der Laan, N. D. Telling, A. Potenza, S. S. Dhesi, and E. Arenholz. Anisotropic x-ray magnetic linear dichroism and spectromicroscopy of interfacial Co/NiO(001). *Physical Review B*, 83(6):064409, February 2011.

[235] O. Bezencenet, D. Bonamy, R. Belkhou, P. Ohresser, and A. Barbier. Origin and Tailoring of the Antiferromagnetic Domain Structure in α-Fe_2O_3 thin films unraveled by statistical analysis of dichroic spectromicroscopy (x-ray photoemission electron microscopy) images. *Physical Review Letters*, 106(10):107201, March 2011.

[236] K. Fabian, P. Robinson, S. A. McEnroe, F. Heidelbach, and A. M. Hirt. *Experimental Study of the Magnetic Signature of Basal-Plane Anisotropy in Hematite*, pages 311–320. Springer Netherlands, Dordrecht, January 2011.

[237] P. Giannozzi, O. Baseggio, P. Bonfà, D. Brunato, R. Car, I. Carnimeo, C. Cavazzoni, S. de Gironcoli, P. Delugas, F. Ferrari R., A. Ferretti, N. Marzari, I. Timrov, A. Urru, and S. Baroni. Quantum ESPRESSO toward the exascale. *The Journal of Chemical Physics*, 152(15):154105, April 2020.

[238] G. Pizzi, V. Vitale, R. Arita, S. Blügel, F. Freimuth, G. Géranton, M. Gibertini, D. Gresch, C. Johnson, T. Koretsune, J. Ibañez-Azpiroz, H. Lee, J.-M. Lihm, D. Marchand, A. Marrazzo, Y. Mokrousov, J. I. Mustafa, Y. Nohara, Y. Nomura, L. Paulatto, S. Poncé, T. Ponweiser, J. Qiao, F. Thöle, S. S. Tsirkin, M. Wierzbowska, N. Marzari, D. Vanderbilt, I. Souza, A. A. Mostofi, and J. R. Yates. Wannier90 as a community code: new features and applications. *Journal of Physics: Condensed Matter*, 32(16):165902, January 2020.

[239] X. Wang, J. R. Yates, I. Souza, and D. Vanderbilt. *Ab initio* calculation of the anomalous Hall conductivity by Wannier interpolation. *Physical Review B*, 74(19):195118, November 2006.

[240] M. I. Aroyo, A. Kirov, C. Capillas, J. M. Perez-Mato, and H. Wondratschek. Bilbao Crystallographic Server. II. Representations of crystallographic point groups and space groups. *Acta Crystallographica Section A: Foundations of Crystallography*, 62(2):115–128, March 2006.

[241] S. V. Gallego, J. M. Perez-Mato, L. Elcoro, E. S. Tasci, R. M. Hanson, K. Momma, M. I. Aroyo, and G. Madariaga. MAGNDATA: towards a database of magnetic structures. I. The commensurate case. *Journal of Applied Crystallography*, 49(5):1750–1776, October 2016.

[242] G. Kresse and J. Furthmüller. Efficient iterative schemes for *ab initio* total-energy calculations using a plane-wave basis set. *Physical Review B*, 54(16):11169–11186, October 1996.

[243] P. E. Blöchl. Projector augmented-wave method. *Physical Review B*, 50(24):17953–17979, December 1994.

[244] G. Kresse and D. Joubert. From ultrasoft pseudopotentials to the projector augmented-wave method. *Physical Review B*, 59(3):1758–1775, January 1999.

[245] J. P. Perdew, K. Burke, and M. Ernzerhof. Generalized Gradient Approximation Made Simple. *Physical Review Letters*, 77(18):3865–3868, October 1996.

[246] H. J. Monkhorst and J. D. Pack. Special points for Brillouin-zone integrations. *Physical Review B*, 13(12):5188–5192, June 1976.

[247] N. Marzari and D. Vanderbilt. Maximally localized generalized Wannier functions for composite energy bands. *Physical Review B*, 56(20):12847–12865, November 1997.

[248] I. Souza, N. Marzari, and D. Vanderbilt. Maximally localized Wannier functions for entangled energy bands. *Physical Review B*, 65(3):035109, December 2001.

[249] A. A. Mostofi, J. R. Yates, Y.-S. Lee, I. Souza, D. Vanderbilt, and N. Marzari. wannier90: A tool for obtaining maximally-localised Wannier functions. *Computer Physics Communications*, 178(9):685–699, May 2008.

[250] Y. Yao, L. Kleinman, A. H. MacDonald, J Sinova, T Jungwirth, D.-S. Wang, E. Wang, and Q. Niu. First Principles Calculation of Anomalous Hall Conductivity in Ferromagnetic bcc Fe. *Physical Review Letters*, 92(3):037204, January 2004.

[251] D. Xiao, M.-C. Chang, and Q. Niu. Berry phase effects on electronic properties. *Reviews of Modern Physics*, 82(3):1959–2007, July 2010.

[252] K. D. Malviya, H. Dotan, D. Shlenkevich, A. Tsyganok, H. Mor, and A. Rothschild. Systematic comparison of different dopants in thin film hematite (α-Fe_2O_3) photoanodes for solar water splitting. *Journal of Materials Chemistry A*, 4(8):3091–3099, December 2016.

[253] Allan H. Morrish. *Canted Antiferromagnetism: Hematite*. World Scientific, December 1994.

[254] A. Ross, R. Lebrun, L. Baldrati, A. Kamra, O. Gomonay, S. Ding, F. Schreiber, D. Backes, F. Maccherozzi, D. A. Grave, A. Rothschild, J. Sinova, and M. Kläui. An insulating doped antiferromagnet with low magnetic symmetry as a room temperature spin conduit. *Applied Physics Letters*, 117(24):242405, December 2020.

[255] F. J. Morin. Magnetic susceptibility of α-Fe_2O_3 and α-Fe_2O_3 with added titanium. *Physical Review*, 78(6):819–820, June 1950.

[256] Y. L. Zhao, W. M. Lv, Z. Q. Liu, S. W. Zeng, M. Motapothula, S. Dhar, Ariando, Q. Wang, and T. Venkatesan. Variable range hopping in TiO2 insulating layers for oxide electronic devices. *AIP Advances*, 2(1):012129, January 2012.

[257] B. Zhao, T. C. Kaspar, T. C. Droubay, J. McCloy, M. E. Bowden, V. Shutthanandan, S. M. Heald, and S. A. Chambers. Electrical transport properties of Ti-doped Fe_2O_3(0001) epitaxial films. *Physical Review B*, 84:245325, December 2011.

[258] E. Gharibi, A. Hbika, B. Dupre, and C. Gleitzer. ChemInform abstract: Electrical properties of pure and titanium-doped hematite single crystals, in the basal plane, at low oxygen pressure. *ChemInform*, 21(43), October 1990.

[259] A. J. E. Rettie, W. D. Chemelewski, B. R. Wygant, J. Lindemuth, J.-F. Lin, D. Eisenberg, C. S. Brauer, T. J. Johnson, T. N. Beiswenger, R. D. Ash, X. Li, J. Zhou, and C. B. Mullins. Synthesis, electronic transport and optical properties of Si:α-Fe_2O_3 single crystals. *Journal of Materials Chemistry C*, 4:559–567, December 2016.

[260] G. A. Acket and J. Volger. Electric transport in N-type Fe_2O_3. *Physica*, 32(9):1543–1550, September 1966.

[261] V. Baltz, A. Manchon, M. Tsoi, T. Moriyama, T. Ono, and Y. Tserkovnyak. Antiferromagnetic spintronics. *Reviews of Modern Physics*, 90(1):015005, February 2018.

[262] S. Geprägs, M. Opel, J. Fischer, O. Gomonay, P. Schwenke, M. Althammer, H. Huebl, and R. Gross. Spin Hall magnetoresistance in antiferromagnetic insulators. *Journal of Applied Physics*, 127(24):243902, June 2020.

[263] W. Zhu, L. Pi, S. Tan, and Y. Zhang. Anisotropy and extremely high coercivity in weak ferromagnetic $LuFeO_3$. *Applied Physics Letters*, 100(5):052407, February 2012.

[264] A. Akashdeep, E. M. Ababneh, C. Schmitt, E. Galíndez-Ruales, F. Fuhrmann, T. Kuschel, M. Kläui, V. Amin, and G. Jakob. Angle-dependent magnetoresistance induced by interface-generated spin current in RuO_2/permalloy heterostructures. *Physical Review Applied*, 24(5):054018, November 2025.

[265] S. Vélez, V. N. Golovach, A. Bedoya-Pinto, M. Isasa, E. Sagasta, M. Abadia, C. Rogero, L. E. Hueso, F. S. Bergeret, and F. Casanova. Hanle Magnetoresistance in Thin Metal Films with Strong Spin-Orbit Coupling. *Physical Review Letters*, 116(1):016603, January 2016.

[266] M. I. Dyakonov. Magnetoresistance due to Edge Spin Accumulation. *Physical Review Letters*, 99(12):126601, September 2007.

[267] X. Zhou, L. Ma, Z. Shi, W. J. Fan, Jian-Guo Zheng, R. F. L. Evans, and S. M. Zhou. Magnetotransport in metal/insulating-ferromagnet heterostructures: Spin Hall magnetoresistance or magnetic proximity effect. *Physical Review B*, 92(6):060402, August 2015.

[268] S. Becker, A. Ross, R. Lebrun, L. Baldrati, S. Ding, F. Schreiber, F. Maccherozzi, D. Backes, M. Kläui, and G. Jakob. Electrical detection of the spin reorientation transition in antiferromagnetic $TmFeO_3$ thin films by spin Hall magnetoresistance. *Physical Review B*, 103(2):024423, January 2021.

[269] J. E. Hirsch. Spin Hall Effect. *Physical Review Letters*, 83(9):1834–1837, August 1999.

[270] T. Jungwirth, J. Sinova, A. Manchon, X. Marti, J. Wunderlich, and C. Felser. The multiple directions of antiferromagnetic spintronics. *Nature Physics*, 14(3):200–203, March 2018.

[271] Christian Hahn, Grégoire de Loubens, Vladimir V. Naletov, Jamal Ben Youssef, Olivier Klein, and Michel Viret. Conduction of spin currents through insulating antiferromagnetic oxides. *Europhysics Letters*, 108(5):57005, December 2014.

[272] Hailong Wang, Chunhui Du, P. Chris Hammel, and Fengyuan Yang. Spin transport in antiferromagnetic insulators mediated by magnetic correlations. *Physical Review B*, 91(22):220410, June 2015.

[273] V. M. Judin, A. B. Sherman, and I. E. Myl'nikova. Magnetic properties of $YFeO_3$. *Physics Letters*, 22(5):554–555, September 1966.

[274] I. S. Jacobs, Hugh F. Burne, and Lionel M. Levinson. Field-Induced Spin Reorientation in $YFeO_3$ and $YCrO_3$. *Journal of Applied Physics*, 42(4):1631–1632, March 1971.

[275] G. W. Durbin, C. E. Johnson, and M. F. Thomas. Direct observation of field-induced spin reorientation in $YFeO_3$ by the Mossbauer effect. *Journal of Physics C: Solid State Physics*, 8(18):3051, September 1975.

[276] J. Han, P. Zhang, Z. Bi, Y. Fan, T. S. Safi, J. Xiang, J. Finley, L. Fu, R. Cheng, and L. Liu. Birefringence-like spin transport via linearly polarized antiferromagnetic magnons. *Nature Nanotechnology*, 15(7):563–568, July 2020.

[277] Gen Tatara and Christian Ortiz Pauyac. Theory of spin transport through an antiferromagnetic insulator. *Physical Review B*, 99(18):180405, May 2019.

[278] B. Flebus, K. Shen, T. Kikkawa, K.-I. Uchida, Z. Qiu, E. Saitoh, R. A. Duine, and G. E. W. Bauer. Magnon-polaron transport in magnetic insulators. *Physical Review B*, 95(14):144420, April 2017.

[279] A. Vansteenkiste, J. Leliaert, M. Dvornik, M. Helsen, F. Garcia-Sanchez, and B. Van Waeyenberge. The design and verification of MuMax3. *AIP Advances*, 4(10):107133, October 2014.

[280] B. Skubic, J. Hellsvik, L. Nordström, and O. Eriksson. A method for atomistic spin dynamics simulations: implementation and examples. *Journal of Physics: Condensed Matter*, 20(31):315203, July 2008.

[281] M. A. Weiss, A. Herbst, J. Schlegel, T. Dannegger, M. Evers, A. Donges, M. Nakajima, A. Leitenstorfer, S. T. B. Goennenwein, U. Nowak, and T. Kurihara. Discovery of ultrafast spontaneous spin switching in an antiferromagnet by femtosecond noise correlation spectroscopy. *Nature Communications*, 14(1):7651, November 2023.

[282] S. Toth and B. Lake. Linear spin wave theory for single-Q incommensurate magnetic structures. *Journal of Physics: Condensed Matter*, 27(16):166002, March 2015.

[283] U. Ritzmann, D. Hinzke, and U. Nowak. Thermally induced magnon accumulation in two-sublattice magnets. *Physical Review B*, 95(5):054411, February 2017.

[284] R. F. L. Evans, W. J. Fan, P. Chureemart, T. A. Ostler, M. O. A. Ellis, and R. W. Chantrell. Atomistic spin model simulations of magnetic nanomaterials. *Journal of Physics: Condensed Matter*, 26(10):103202, February 2014.

[285] D. Hinzke and U. Nowak. Domain Wall Motion by the Magnonic Spin Seebeck Effect. *Physical Review Letters*, 107(2):027205, July 2011.

[286] J. Xu, J. He, J.-S. Zhou, D. Qu, S.-Y. Huang, and C. L. Chien. Observation of vector spin seebeck effect in a noncollinear antiferromagnet. *Physical Review Letters*, 129(11):117202, September 2022.

[287] Alexander Moskvin. Structure–property relationships for weak ferromagnetic perovskites. *Magnetochemistry*, 7(8):111, August 2021.

[288] M. Gu, Y. Liu, H. Zhu, K. Yananose, X. Chen, Y. Hu, A. Stroppa, and Q. Liu. Ferroelectric Switchable Altermagnetism. *Physical Review Letters*, 134(10):106802, March 2025.

[289] X. Duan, J. Zhang, Z. Zhu, Y. Liu, Z. Zhang, I. Žutić, and T. Zhou. Antiferroelectric Altermagnets: Antiferroelectricity Alters Magnets. *Physical Review Letters*, 134(10):106801, March 2025.

[290] B. Karetta, X. H. Verbeek, R. Jaeschke-Ubiergo, L. Šmejkal, and J. Sinova. Strain-controlled g- to d-wave transition in altermagnetic CrSb. *Physical Review B*, 112(9):094454, September 2025.

[291] M. Khodas, S. Mu, I. I. Mazin, and K. D. Belashchenko. Tuning of altermagnetism by strain, July 2025. arXiv:2506.06257 [cond-mat].

[292] D. Go, D. Jo, C. Kim, and H.-W. Lee. Intrinsic Spin and Orbital Hall Effects from Orbital Texture. *Physical Review Letters*, 121(8):086602, August 2018.

[293] Y.-G. Choi, D. Jo, K.-H. Ko, D. Go, K.-H. Kim, H. G. Park, C. Kim, B.-C. Min, G.-M. Choi, and H.-W. Lee. Observation of the orbital Hall effect in a light metal Ti. *Nature*, 619(7968):52–56, July 2023.

[294] I. Baek, S. Han, and H.-W. Lee. Magnetic octupole Hall effect in heavy transition metals. *Physical Review B*, 112(6):064421, August 2025.

[295] S. Han, D. Jo, I. Baek, S. Cheon, P. M. Oppeneer, and H.-W. Lee. Harnessing Magnetic Octupole Hall Effect to Induce Torque in Altermagnets. *Physical Review Letters*, 135:076705, August 2025.

[296] S.-Y. Wang, W.-W. Wang, J. Fan, X. Zhou, X.-P. Li, and L. Wang. Two-Dimensional Dual-Switchable Ferroelectric Altermagnets: Altering Electrons and Magnons. *Nano Letters*, 25(40):14618–14624, October 2025.

[297] R. Peng, S. Fang, P. Ho, F. Liu, T. Zhou, J. Liu, and Y. S. Ang. Ferroelastic altermagnetism. *npj Quantum Materials*, 11(1):5, December 2025.

[298] J. O. Ledesma-Martin, E. Galindez-Ruales, S. Krishnia, F. Fuhrmann, M. D. Tran, R. Gupta, M. Gasser, D. Go, A. Kamra, G. Jakob, Y. Mokrousov, and M. Kläui. Nonreciprocity in Magnon Mediated Charge-Spin-Orbital Current Interconversion. *Nano Letters*, 25(8):3247–3252, February 2025.

A. Appendix: Experimental evidence on altermagnetism or altermagnetic hallmarks

Table A.1.: **Summary of recent experimental demonstrations of altermagnetic properties in different materials**. Techniques include ARPES, spin-resolved ARPES, magneto-transport (AHE/ANE/IPHE), neutron and RIXS spectroscopy, x-ray dichroism microscopy, and optical probes.

Material	Year	Observation	Technique
CrSb	2024	Surface Fermi arcs due to topological Weyl physics in altermagnetic phase [81]	ARPES
	2024	Spin-split metallic state [82]	ARPES
	2024	Giant momentum-dependent spin splitting (∼0.8 eV) at room temperature [83]	SR-ARPES
	2025	3D mapping of g-wave spin-split bands [46]	SR-ARPES
	2025	Room-temperature AHE controlled by crystal symmetry/DMI locking [84]	Magneto-transport (AHE)
	2025	Large anomalous Nernst effect in single crystals [232]	Magneto-transport (ANE)
	2025	Systematic mapping of altermagnons by circular dichroism RIXS; domain-resolved protocol [85]	CD-RIXS
Mn_5Si_3	2024	Spontaneous anomalous Hall effect at zero net magnetization [29]	Magneto-transport (AHE)
	2025	Spontaneous anomalous Nernst effect with Berry-curvature analysis [74]	Magneto-transport (ANE)
	2025	Even-in-field transverse resistivity diagnostic of symmetry phase [75]	Magneto-transport

Continued on next page

Table A.1.: Summary of recent experimental demonstrations of altermagnetic properties in different materials (continued)

Material	Year	Observation	Technique
MnTe	2024	Giant band spin splitting (∼0.3–0.8 eV) [25, 30, 66]	(SR-)ARPES
	2025	Chiral altermagnon mode [42]	CD-RIXS
	2025	Domain readout via circular dichroism RIXS [72]	CD-RIXS
	2025	Polarized neutron protocol to probe magnon chirality [73]	Polarized INS
	2024	Direct imaging of nanoscale altermagnetic domains [33]	XMCD-PEEM
	2024	Spontaneous AHE in epitaxial films [26]	Magneto-transport (AHE)
	2025	Unconventional Andreev reflection in AM state [36]	Transport spectroscopy
MnF_2	2025	Direct observation of spin-split magnons and chirality reversal between branches [67]	Polarized INS
	2025	Null result: no detectable splitting within 0.4 meV resolution [68]	INS
$LuFeO_3$	2025	Direction-dependent, sign-reversing non-local SSE signals [115]	Non-local magnon transport
α-Fe_2O_3	2023	Crystal-axis dependent AHE [41]	Magneto-transport (AHE)
	2025	XMCD/XMLD-PEEM imaging of 180° AM domains correlated with AHE [41]	XPEEM (XMLD + XMCD)
	2025	Observation of chiral magnon band splitting in altermagnetic hematite [86]	CD-RIXS
	2026	Symmetry-driven giant magneto-optical Kerr effect (MOKE) in altermagnetic hematite, enabling optical imaging of altermagnetic domains and reversible domain-wall motion [87]	Magneto-optics (MOKE), optical domain imaging
RuO_2	2024	TRS-breaking dichroism in ARPES [65]	MCD-ARPES
	2024–25	Multiple μSR/neutron/Mössbauer works find no static AM order [76–78]	μSR, INS, Mössbauer

Continued on next page

Table A.1.: Summary of recent experimental demonstrations of altermagnetic properties in different materials (continued)

Material	Year	Observation	Technique
	2025	Clarification: IPHE is symmetry-forbidden, observed only on low-symmetry planes [79]	Magneto-transport (IPHE)
	2025	ARPES finds bulk bands spin-degenerate, with surface topological states [80]	ARPES
Layered AM	2025	$Rb_{1-\delta}V_2Te_2O$: Spin-valley locked, oppositely polarized valleys at RT [69]	SR-ARPES, STM/STS
	2025	KV_2Se_2O: d-wave spin–momentum locking at RT [70]	SR-ARPES
	2025	Observation of altermagnetic spin splitting in an intercalated TMD ($CoNb_4Se_8$) [71]	(SR-)ARPES

B. Appendix: Altermagnetic candidates

Table B.1.: Candidate altermagnets grouped by the symmetry class of the reciprocal space spin splitting. The listed space groups are the nonmagnetic crystallographic space groups (international number in parentheses). The labels *d*-, *g*-, and *i*-wave denote the angular character of the altermagnetic spin polarization in momentum space as defined by the spin Laue group of the collinear compensated magnetic state. Because the $d/g/i$ classification is fixed by magnetic (spin) symmetry rather than by the nonmagnetic space group alone, these assignments should be interpreted as candidate classifications and may depend on the realized magnetic order and Néel vector orientation. The asterisk in the conduction column indicates the electronic character inferred from material family [88, 89].

Candidate	Space group (nonmagnetic)	Crystal system	Anisotropy (d,g,*i*-wave)	Conduction
$OsNNaSCl_5$	$P2_1$ (4)	Monoclinic	*d*-wave	*insulator
KV_2Se_2O	$P4/mmm$ (123)	Tetragonal	*d*-wave	metal
$V_2ClBrI_2O_2$	Cm (8)	Monoclinic	*d*-wave	*insulator
$Rb_{1-\delta}V_2Te_2O$	$P4/mmm$ (123)	Tetragonal	*d*-wave	metal
RuF_4	$P2_1/c$ (14)	Monoclinic	*d*-wave	*Semicon.
RuO_2	$P4_2/mnm$ (136)	Tetragonal	*d*-wave	metal
VF_4	$P2_1/c$ (14)	Monoclinic	*d*-wave	*Semicon.
AgF_2	$P2_1/c$ (14)	Monoclinic	*d*-wave	Semicon.
OsF_4	$P2_1/c$ (14)	Monoclinic	*d*-wave	*insulator
$LiFeP_2O_7$	$P2_1$ (4)	Monoclinic	*d*-wave	insulator
$SrRuO_3$ (010)	$P2_1/c$ (14)	Monoclinic	*d*-wave	metal
$MnTeMoO_6$	$P2_12_12$ (18)	Orthorhombic	*d*-wave	insulator
$CaLaFeAgO_6$	Pc (7)	Monoclinic	*d*-wave	metal
$Mn_4Nb_2O_9$	Cc (9)	Monoclinic	*d*-wave	insulator
FeS (110)	$Pmma$ (51)	Orthorhombic	*d*-wave	Semicon.
$CaFe_5O_7$	$P2_1/m$ (11)	Monoclinic	*d*-wave	insulator
FeSe (110)	$Pmma$ (51)	Orthorhombic	*d*-wave	metal
$Fe_3F_8(H_2O)_2$	$C2/m$ (12)	Monoclinic	*d*-wave	*insulator

Continued on next page

Table B.1.: Candidate altermagnets grouped by the symmetry class of the reciprocal space spin splitting. (continued)

Candidate	Space group (nonmagnetic)	Crystal system	Anisotropy (d,g,*i*-wave)	Conduction
$RbMnF_4$	$P2_1/a$ (14)	Monoclinic	*d*-wave	insulator
Fe_2WTe_4	$P\bar{4}2m$ (111)	Tetragonal	*d*-wave	*Semicon.
$Li_2Co(SO_4)_2$	$P2_1/c$ (14)	Monoclinic	*d*-wave	insulator
Fe_2MoS_4	$P\bar{4}2m$ (111)	Tetragonal	*d*-wave	*Semicon.
Fe_2MoSe_4	$P\bar{4}2m$ (111)	Tetragonal	*d*-wave	*Semicon.
Fe_2MoTe_4	$P\bar{4}2m$ (111)	Tetragonal	*d*-wave	*Semicon.
$LiFe(SO_4)_2$	$P2_1/c$ (14)	Monoclinic	*d*-wave	insulator
$LuCrO_3$	$Pnma$ (62)	Orthorhombic	*d*-wave	metal
$Ca(CoN)_2$	$P\bar{4}m2$ (115)	Tetragonal	*d*-wave	*insulator
$Li_2Mn(SO_4)_2$	$P2_1/c$ (14)	Monoclinic	*d*-wave	insulator
$TaCoB_2$	$Pnma$ (62)	Orthorhombic	*d*-wave	metal
$Ca(FeN)_2$	$P\bar{4}m2$ (115)	Tetragonal	*d*-wave	*insulator
$Fe_3(PO_4)_2(OH)_2$	$P2_1/c$ (14)	Monoclinic	*d*-wave	insulator
$NbRuO_3$	$Pnma$ (62)	Orthorhombic	*d*-wave	metal
CrO	$P4/mmm$ (123)	Tetragonal	*d*-wave	half-metallic
CuF_2	$P2_1/c$ (14)	Monoclinic	*d*-wave	insulator
V_2Se_2O	$P4/mmm$ (123)	Tetragonal	*d*-wave	metal
$Li_2Ni(SO_4)_2$	$P2_1/c$ (14)	Monoclinic	*d*-wave	insulator
V_2Te_2O	$P4/mmm$ (123)	Tetragonal	*d*-wave	metal
K_2ReI_6	$P2_1/n$ (14)	Monoclinic	*d*-wave	insulator
$NaFeO_2$	$P4_12_12$ (92)	Tetragonal	*d*-wave	insulator
Sr_2CoTeO_6	$P2_1/n$ (14)	Monoclinic	*d*-wave	*insulator
Cr_2Se_2O	$P4/mmm$ (123)	Tetragonal	*d*-wave	Semicon.
Sr_2ScOsO_6	$P2_1/n$ (14)	Monoclinic	*d*-wave	*insulator
Fe_2Se_2O	$P4/mmm$ (123)	Tetragonal	*d*-wave	Semicon.
Sr_2YRuO_6	$P2_1/n$ (14)	Monoclinic	*d*-wave	insulator
$Ca_3Cr_2O_7$	$Cmc2_1$ (36)	Orthorhombic	*d*-wave	insulator
FeSe (001)	$P4/nmm$ (129)	Tetragonal	*d*-wave	metal
Sr_2TbIrO_6	$P2_1/n$ (14)	Monoclinic	*d*-wave	*insulator
$ZrCrO_3$	$Pnma$ (62)	Orthorhombic	*d*-wave	insulator
Sr_2LuRuO_6	$P2_1/n$ (14)	Monoclinic	*d*-wave	*insulator
Sr_2YbRuO_6	$P2_1/n$ (14)	Monoclinic	*d*-wave	*insulator
Sr_2TmRuO_6	$P2_1/n$ (14)	Monoclinic	*d*-wave	*insulator
Sr_2TbRuO_6	$P2_1/n$ (14)	Monoclinic	*d*-wave	*insulator
Sr_2HoRuO_6	$P2_1/n$ (14)	Monoclinic	*d*-wave	*insulator
Sr_2DyRuO_6	$P2_1/n$ (14)	Monoclinic	*d*-wave	*insulator

Continued on next page

Table B.1.: Candidate altermagnets grouped by the symmetry class of the reciprocal space spin splitting. (continued)

Candidate	Space group (nonmagnetic)	Crystal system	Anisotropy (d,g,*i*-wave)	Conduction
Mn_2ScSbO_6	$P2_1/n$ (14)	Monoclinic	*d*-wave	insulator
$CuAg(SO_4)_2$	$P2_1/n$ (14)	Monoclinic	*d*-wave	insulator
La_2LiRuO_6	$P2_1/n$ (14)	Monoclinic	*d*-wave	insulator
Ca_2CoTeO_6	$P2_1/c$ (14)	Monoclinic	*d*-wave	insulator
$Sr_2Co_{0.9}Mg_{0.1}TeO_6$	$P2_1/n$ (14)	Monoclinic	*d*-wave	*insulator
Sr_2CoOsO_6	$B2/c$ (15)	Monoclinic	*d*-wave	Semicon.
$Ba_3CoIr_2O_9$	$C2/c$ (15)	Monoclinic	*d*-wave	insulator
$FeSO_4F$	$C2/c$ (15)	Monoclinic	*d*-wave	*insulator
$FeOHSO_4$	$C2/c$ (15)	Monoclinic	*d*-wave	*insulator
$CaMnO_3$	$Pnma$ (62)	Orthorhombic	*d*-wave	insulator
$BiCrO_3$	$C2/c$ (15)	Monoclinic	*d*-wave	insulator
$CaVO_3$	$Pnma$ (62)	Orthorhombic	*d*-wave	insulator
$BaCrF_5$	$P2_12_12_1$ (19)	Orthorhombic	*d*-wave	*insulator
$FeHO_2$	$Pmn2_1$ (31)	Orthorhombic	*d*-wave	*insulator
$LaVO_3$	$Pnma$ (62)	Orthorhombic	*d*-wave	insulator
$CaLaCr_2O_6$	$Pmn2_1$ (31)	Orthorhombic	*d*-wave	metal
$MnSeO_4$	$Pnma$ (62)	Orthorhombic	*d*-wave	insulator
$MnPr_2OsO_6$	$P2_1/c$ (14)	Monoclinic	*d*-wave	insulator
$Y_2Cu_2O_5$	$Pna2_1$ (33)	Orthorhombic	*d*-wave	*Semicon.
$NaPr_2RuO_6$	$P2_1/c$ (14)	Monoclinic	*d*-wave	insulator
$NaFeO_2$	$Pna2_1$ (33)	Orthorhombic	*d*-wave	insulator
$[C(ND_2)_3]Cu(DCOO)_3$	$Pna2_1$ (33)	Orthorhombic	*d*-wave	*insulator
$NdRhO_3$	$Pnma$ (62)	Orthorhombic	*d*-wave	insulator
$PrRuO_3$	$Pnma$ (62)	Orthorhombic	*d*-wave	insulator
$Ca_3Mn_2O_7$	$Cmc2_1$ (36)	Orthorhombic	*d*-wave	insulator
$ScVO_3$	$Pnma$ (62)	Orthorhombic	*d*-wave	insulator
$SmRhO_3$	$Pnma$ (62)	Orthorhombic	*d*-wave	insulator
$CaLaCrMoO_6$	Pc (7)	Monoclinic	*d*-wave	insulator
$ErGe_{1.83}$	$Cmc2_1$ (36)	Orthorhombic	*d*-wave	*metal
La_2MnRhO_6	$P2_1/c$ (14)	Monoclinic	*d*-wave	insulator
$Cu_2V_2O_7$	$Fdd2$ (43)	Orthorhombic	*d*-wave	insulator
$LiFeF_4$	$P2_1/c$ (14)	Monoclinic	*d*-wave	insulator
$ZnFeF_5(H_2O)_2$	$Imm2$ (44)	Orthorhombic	*d*-wave	*insulator
Sr_2MnGaO_5	$Ima2$ (46)	Orthorhombic	*d*-wave	*Semicon.
$[C(ND_2)_3]Co(DCOO)_3$	$Pnna$ (52)	Orthorhombic	*d*-wave	*insulator
$[C(ND_2)_3]Mn(DCOO)_3$	$Pnna$ (52)	Orthorhombic	*d*-wave	*insulator
$CrSb_2$	$Pnnm$ (58)	Orthorhombic	*d*-wave	Semicon.
$CaCrO_3$	$Pbnm$ (62)	Orthorhombic	*d*-wave	metal
$YCrO_3$	$Pbnm$ (62)	Orthorhombic	*d*-wave	insulator
$TbCrO_3$	$Pbnm$ (62)	Orthorhombic	*d*-wave	insulator
$DyCrO_3$	$Pbnm$ (62)	Orthorhombic	*d*-wave	insulator

Continued on next page

Table B.1.: Candidate altermagnets grouped by the symmetry class of the reciprocal space spin splitting. (continued)

Candidate	Space group (nonmagnetic)	Crystal system	Anisotropy (d,g,*i*-wave)	Conduction
$ErCrO_3$	P*bnm* (62)	Orthorhombic	*d*-wave	insulator
$CeFeO_3$	P*bnm* (62)	Orthorhombic	*d*-wave	insulator
$SmFeO_3$	P*bmn* (62)	Orthorhombic	*d*-wave	insulator
$TbFeO_3$	P*bnm* (62)	Orthorhombic	*d*-wave	insulator
$DyFeO_3$	P*bnm* (62)	Orthorhombic	*d*-wave	insulator
$ErVO_3$	P*bnm* (62)	Orthorhombic	*d*-wave	*insulator
$TbCr_{0.5}Mn_{0.5}O_3$	P*bnm* (62)	Orthorhombic	*d*-wave	*insulator
κ-Cl	P*nma* (62)	Orthorhombic	*d*-wave	Semicon.
YVO_3	P*nma* (62)	Orthorhombic	*d*-wave	insulator
$NdVO_3$	P*nma* (62)	Orthorhombic	*d*-wave	insulator
$LaCrO_3$	P*nma* (62)	Orthorhombic	*d*-wave	insulator
$YRuO_3$	P*nma* (62)	Orthorhombic	*d*-wave	*Semicon.
$LaMnO_3$	P*nma* (62)	Orthorhombic	*d*-wave	insulator
$NdMnO_3$	P*nma* (62)	Orthorhombic	*d*-wave	*insulator
$PrMnO_3$	P*nma* (62)	Orthorhombic	*d*-wave	*insulator
$LaFeO_3$	P*nma* (62)	Orthorhombic	*d*-wave	insulator
$NdFeO_3$	P*nma* (62)	Orthorhombic	*d*-wave	insulator
$NaOsO_3$	P*nma* (62)	Orthorhombic	*d*-wave	Semicon.
α-Fe_2PO_5	P*nma* (62)	Orthorhombic	*d*-wave	*insulator
$Mn_2SeO_3F_2$	P*nma* (62)	Orthorhombic	*d*-wave	*insulator
MnO_2	P*nma* (62)	Orthorhombic	*d*-wave	insulator
$KMnF_3$	P*nma* (62)	Orthorhombic	*d*-wave	insulator
Ca_2MnGaO_5	P*nma* (62)	Orthorhombic	*d*-wave	insulator
$Ca_2PrCr_2TaO_9$	P*nma* (62)	Orthorhombic	*d*-wave	*insulator
$Ca_2PrCr_2NbO_9$	P*nma* (62)	Orthorhombic	*d*-wave	*insulator
$Ho_{0.2}Bi_{0.8}FeO_3$	P*nma* (62)	Orthorhombic	*d*-wave	*insulator
$Ho_{0.15}Bi_{0.85}FeO_3$	P*nma* (62)	Orthorhombic	*d*-wave	*insulator
$La_{0.95}Ba_{0.05}Mn_{0.95}Ti_{0.05}O_3$	P*nma* (62)	Orthorhombic	*d*-wave	*Semicon.
$La_{0.5}Sr_{0.5}FeO_{2.5}F_{0.5}$	P*nma* (62)	Orthorhombic	*d*-wave	*Semicon.
$BiFe_{0.5}Sc_{0.5}O_3$	P*nma* (62)	Orthorhombic	*d*-wave	*insulator
$Bi_{0.85}Ca_{0.15}Fe_{0.55}Mn_{0.45}O_3$	P*nma* (62)	Orthorhombic	*d*-wave	*Semicon.
$Ca_2Fe_{0.875}Cr_{0.125}GaO_5$	P*nma* (62)	Orthorhombic	*d*-wave	*insulator
$Pb_2Mn_{0.6}Co_{0.4}WO_6$	P*mcn* (62)	Orthorhombic	*d*-wave	insulator
$Tb_2Ir_3Ga_9$	C*mcm* (63)	Orthorhombic	*d*-wave	metal
$CaIrO_3$	C*mcm* (63)	Orthorhombic	*d*-wave	insulator
$CoFe_3O_5$	C*mcm* (63)	Orthorhombic	*d*-wave	Semicon.
$YBaMn_2O_{5.5}$	I*bam* (72)	Orthorhombic	*d*-wave	Semicon.
$Y_2SrCu_{0.6}Co_{1.4}O_{6.5}$	I*bam* (72)	Orthorhombic	*d*-wave	Semicon.
$Bi_{0.8}La_{0.2}Fe_{0.5}Mn_{0.5}O_3$	I*mma* (74)	Orthorhombic	*d*-wave	*insulator
$K_yFe_{2-x}Se_2$	I4/*m* (87)	Tetragonal	*d*-wave	Semicon.
$Rb_yFe_{2-x}Se_2$	I4/*m* (87)	Tetragonal	*d*-wave	Semicon.

Continued on next page

Table B.1.: Candidate altermagnets grouped by the symmetry class of the reciprocal space spin splitting. (continued)

Candidate	Space group (nonmagnetic)	Crystal system	Anisotropy (d,g,*i*-wave)	Conduction
$SrMn_2V_2O_8$	$I4_1cd$ (110)	Tetragonal	*d*-wave	insulator
$Ba_2MnSi_2O_7$	$P\bar{4}2_1m$ (113)	Tetragonal	*d*-wave	*insulator
$Ba_2CoGe_2O_7$	$P\bar{4}2_1m$ (113)	Tetragonal	*d*-wave	insulator
$Ca_2CoSi_2O_7$	$P\bar{4}2_1m$ (113)	Tetragonal	*d*-wave	insulator
$CuFeS_2$	$I\bar{4}2d$ (122)	Tetragonal	*d*-wave	Semicon.
$ZrMn_2Ge_4O_{12}$	$P4/nbm$ (125)	Tetragonal	*d*-wave	*insulator
$CeMn_2Ge_4O_{12}$	$P4/nbm$ (125)	Tetragonal	*d*-wave	*insulator
$CeMnCoGe_4O_{12}$	$P4/nbm$ (125)	Tetragonal	*d*-wave	*insulator
MnF_2	$P4_2/mnm$ (136)	Tetragonal	*d*-wave	insulator
CoF_2	$P4_2/mnm$ (136)	Tetragonal	*d*-wave	insulator
ReO_2	$P4_2/mnm$ (136)	Tetragonal	*d*-wave	metal
$LiFe_2F_6$	$P4_2/mnm$ (136)	Tetragonal	*d*-wave	insulator
$La_2O_3FeMnSe_2$	$I4/mmm$ (139)	Tetragonal	*d*-wave	Semicon.
$Sr_{0.7}Tb_{0.3}CoO_{2.9}$	$I4/mmm$ (139)	Tetragonal	*d*-wave	Semicon.
$Sr_{0.7}Er_{0.3}CoO_{2.8}$	$I4/mmm$ (139)	Tetragonal	*d*-wave	Semicon.
$Sr_{0.7}Ho_{0.3}CoO_{2.7}$	$I4/mmm$ (139)	Tetragonal	*d*-wave	Semicon.
$Co_2(PO_4)O$	$I4_1/amd$ (141)	Tetragonal	*d*-wave	*Semicon.
$MnTiO_3$	$R3c$ (161)	Trigonal	*d*-wave	*Semicon.
$GaFeO_3$	$R3c$ (161)	Trigonal	*d*-wave	*insulator
$ScFeO_3$	$R3c$ (161)	Trigonal	*d*-wave	*insulator
$CoNb_3S_6$	$P6_322$ (182)	Hexagonal	*d*-wave	metal
VNb_3Sb_6	$P6_322$ (182)	Hexagonal	*d*-wave	metal
$Fe_2Mo_3O_8$	$P6_3mc$ (186)	Hexagonal	*d*-wave	Semicon.
UNiGa	$P\bar{6}2m$ (189)	Hexagonal	*d*-wave	metal
FeS	$P\bar{6}2c$ (190)	Hexagonal	*d*-wave	insulator
$BaMnO_3$	$P6_3/mmc$ (194)	Hexagonal	*d*-wave	Semicon.
$CrNb_4S_8$	$P6_3/mmc$ (194)	Hexagonal	*d*-wave	*metal
$Ba_3NiRu_2O_9$	$P6_3/mmc$ (194)	Hexagonal	*d*-wave	*Semicon.
$Ba_5Co_5ClO_{13}$	$P6_3/mmc$ (194)	Hexagonal	*d*-wave	insulator
$CsNiCl_3$	$P6_3/mmc$ (194)	Hexagonal	*d*-wave	*insulator
$MnSe_2$	$Pa\bar{3}$ (205)	Cubic	*d*-wave	*insulator
Ce_4Sb_3	$I\bar{4}3d$ (220)	Cubic	*d*-wave	metal

Continued on next page

Table B.1.: Candidate altermagnets grouped by the symmetry class of the reciprocal space spin splitting. (continued)

Candidate	Space group (nonmagnetic)	Crystal system	Anisotropy (d,g,*i*-wave)	Conduction
Tb_2C_3	I$\bar{4}3d$ (220)	Cubic	*d*-wave	*metal
$LiTi_2O_4$	F$d\bar{3}m$ (227)	Cubic	*d*-wave	metal
$Er_2Ru_2O_7$	F$d\bar{3}m$ (227)	Cubic	*d*-wave	insulator
NdB_2C_2	P4/*mbm* (127)	Tetragonal	*g*-wave	metal
Mn_5Si_3	P6_3/*mcm* (193)	Hexagonal	*g*-wave	metal
$Mg_2FeIr_5B_2$	P4/*mbm* (127)	Tetragonal	*g*-wave	metal
CrSb	P6_3/*mmc* (194)	Hexagonal	*g*-wave	metal
$Mg_2MnIr_5B_2$	P4/*mbm* (127)	Tetragonal	*g*-wave	metal
MnTe	P6_3/*mmc* (194)	Hexagonal	*g*-wave	Semicon.
$Mg_2NiIr_5B_2$	P4/*mbm* (127)	Tetragonal	*g*-wave	metal
$Sc_2MnIr_5B_2$	P4/*mbm* (127)	Tetragonal	*g*-wave	metal
$VP_2H_8(NO_4)_2$	P4*bm* (100)	Tetragonal	*g*-wave	*insulator
GdB_2C_2	P4/*mbm* (127)	Tetragonal	*g*-wave	metal
HoB_2C_2	P4/*mbm* (127)	Tetragonal	*g*-wave	metal
MnO	P6_3mc (186)	Hexagonal	*g*-wave	insulator
$CaMnN_2$	P6_3/*mmc* (194)	Hexagonal	*g*-wave	insulator
$Ba_2FeGe_2O_7$	P$\bar{4}2_1m$ (113)	Tetragonal	*g*-wave	insulator
$Ba_2CoSi_2O_7$	P$\bar{4}2_1m$ (113)	Tetragonal	*g*-wave	insulator
$Sr_2CoGe_2O_7$	P$\bar{4}2_1m$ (113)	Tetragonal	*g*-wave	insulator
GdAlSi	I4_1md (109)	Tetragonal	*g*-wave	metal
$CsCoF_4$	I$\bar{4}c2$ (120)	Tetragonal	*g*-wave	*insulator
Nb_2FeB_2	P4/*mbm* (127)	Tetragonal	*g*-wave	metal
Ta_2FeB_2	P4/*mbm* (127)	Tetragonal	*g*-wave	metal
$FeBO_3$	R$\bar{3}c$ (167)	Trigonal	*g*-wave	insulator
FeF_3	R$\bar{3}c$ (167)	Trigonal	*g*-wave	insulator
α-Fe_2O_3	R$\bar{3}c$ (167)	Trigonal	*g*-wave	insulator
Ca_3LiRuO_6	R$\bar{3}c$ (167)	Trigonal	*g*-wave	insulator
Sr_3LiRuO_6	R$\bar{3}c$ (167)	Trigonal	*g*-wave	*insulator
Sr_3NaRuO_6	R$\bar{3}c$ (167)	Trigonal	*g*-wave	*insulator
Ca_3LiOsO_6	R$\bar{3}c$ (167)	Trigonal	*g*-wave	insulator
$Co_2Mo_3O_8$	P6_3mc (186)	Hexagonal	*g*-wave	insulator
$CsCoCl_3$	P6_3/*mmc* (194)	Hexagonal	*g*-wave	*insulator
$RbCoBr_3$	P6_3/*mmc* (194)	Hexagonal	*g*-wave	*insulator
$MnTeLi_{0.003}$	P6_3/*mmc* (194)	Hexagonal	*g*-wave	*Semicon.

Continued on next page

Table B.1.: Candidate altermagnets grouped by the symmetry class of the reciprocal space spin splitting. (continued)

Candidate	Space group (nonmagnetic)	Crystal system	Anisotropy (d,g,*i*-wave)	Conduction
$NiFe_3$	R$\bar{3}c$ (167)	Trigonal	*i*-wave	metal
2H-$FeBr_3$	P$\bar{6}2m$ (189)	Hexagonal	*i*-wave	*insulator
$ZrMnO_3$	R3*c* (161)	Trigonal	*i*-wave	insulator
VF_3	R$\bar{3}c$ (167)	Trigonal	*i*-wave	insulator
C_3F_3	R$\bar{3}c$ (167)	Trigonal	*i*-wave	insulator
$Fe_{1.5}Mn_{1.5}BO_5$	P*bam* (55)	Orthorhombic	*i*-wave	*insulator
$Mn(N(CN)_2)_2$	P*nnm* (58)	Orthorhombic	*i*-wave	*insulator
$FeSb_2$	P*nnm* (58)	Orthorhombic	*i*-wave	Semicon.
$Eu_3In_2As_4$	P*nnm* (58)	Orthorhombic	*i*-wave	*Semicon.
Fe_2WO_6	P*bcn* (60)	Orthorhombic	*i*-wave	*insulator
Ca_2RuO_4	P*bca* (61)	Orthorhombic	*i*-wave	Semicon.
$NdCoO_3$	P*bnm* (62)	Orthorhombic	*i*-wave	Semicon.
$ScCrO_3$	P*nma* (62)	Orthorhombic	*i*-wave	insulator
$InCrO_3$	P*nma* (62)	Orthorhombic	*i*-wave	insulator
$TlCrO_3$	P*nma* (62)	Orthorhombic	*i*-wave	*insulator
$Ca_{1-x}Ce_xMnO_3$	P*nma* (62)	Orthorhombic	*i*-wave	*Semicon.
$NiFePO_5$	P*nma* (62)	Orthorhombic	*i*-wave	*insulator
$CuFePO_5$	P*nma* (62)	Orthorhombic	*i*-wave	*insulator
$La_{0.75}Bi_{0.25}Fe_{0.5}Cr_{0.5}O_3$	P*nma* (62)	Orthorhombic	*i*-wave	Semicon.
Nd_2PdGe_6	C*mce* (64)	Orthorhombic	*i*-wave	*metal
$LaCaFeO_4$	C*mce* (64)	Orthorhombic	*i*-wave	*insulator
$Sr_4Fe_4O_{11}$	C*mmm* (65)	Orthorhombic	*i*-wave	Semicon.
UCr_2Si_2C	P4/*mmm* (123)	Tetragonal	*i*-wave	metal
NiF_2	P4_2/*mnm* (136)	Tetragonal	*i*-wave	insulator
La_2NiO_4	P4_2/*ncm* (138)	Tetragonal	*i*-wave	insulator
β-$Fe_2(PO_4)O$	I4_1/*amd* (141)	Tetragonal	*i*-wave	metal
Co_2Mo_3N	P$4_1$32 (213)	Cubic	*i*-wave	metal
Bi_2RuMnO_7	F*d*$\bar{3}$*m* (227)	Cubic	*i*-wave	metal

C. Appendix: Noise pre-characterization of the set-up

This appendix documents the baseline voltage noise of the cryostat, wiring, and readout chain, using the same acquisition modes employed throughout this thesis. Unless explicitly stated as 300 K, all resistive loads were mounted at the sample position inside the variable temperature insert (VTI), such that the measured noise includes the relevant cryogenic wiring and environmental contributions. The purpose is to define a quantitative pre noise floor, to motivate the choice of detection protocol, and to provide practical criteria for identifying non stationary measurement conditions.

C.1. Noise versus excitation method and dissipated power

Figure **C.1** compares three acquisition modes, delta mode, lock in detection at 14 Hz, and a slow switching pseudo DC protocol. The voltage fluctuations are defined as 2σ, where σ is the standard deviation of the measured voltage time trace, as a function of dissipated electrical power. The monotonic increase with power sets the practical trade off between signal amplitude and baseline uncertainty. The relative separation between the protocols provides a direct sensitivity basis for the same dissipated power, and motivates the use of phase sensitive detection for weak signals.

The low frequency background is consistent with slow drift and $1/f$ type contributions, while narrow interference lines are visible at 50 Hz and its harmonics, reflecting mains pickup. These spectral features define preferred operating windows for narrow band detection and provide a reference for interpreting narrowband peaks in experimental datasets.

At low Fourier frequencies, the noise spectral density of precision voltage measurements frequently follows a power law, $S_V(f) \propto f^{-\alpha}$ with $\alpha \approx 1$, commonly referred to as $1/f$ (flicker) noise. This behavior is ubiquitous in condensed matter and electronic instrumentation, and is usually interpreted as the superposition of many independent fluctuators with a broad distribution of activation energies and relaxation times, which naturally yields an approximately scale free spectrum in the measurement band, as reviewed by Dutta and Horn (1981) [218] and Weissman (1988) [219]. In practical low level transport measurements, the observed $1/f$ background can originate from resistance fluctuations of the device under test, from contact and interface fluctuations, and from the front end electronics flicker noise, therefore it is expected to dominate below the white noise floor set by Johnson Nyquist noise and amplifier noise at sufficiently low f [220, 221].

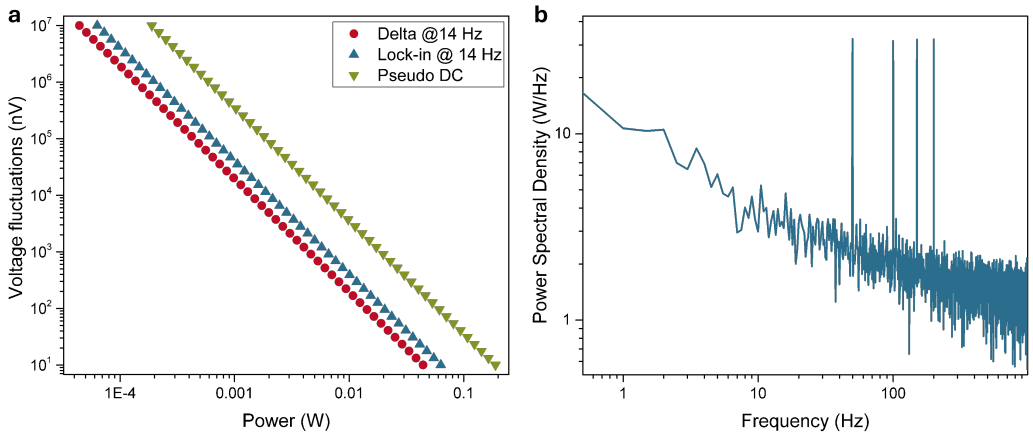

Figure C.1.: **Acquisition mode basis and mains pickup.** Baseline voltage noise for different acquisition modes. **a** Voltage fluctuations, defined as 2σ of the voltage time trace, as a function of dissipated power for delta mode at 14 Hz, lock in detection at 14 Hz, and a slow switching pseudo DC protocol. **b** Voltage noise amplitude spectral density in the frequency range of interest, highlighting the low frequency background and discrete interference peaks at 50 Hz and harmonics.

Delta mode implements polarity reversal and synchronous averaging to extract the signal while suppressing additive offsets and slow drift. In low voltage measurements, thermoelectric electromotive forces, input offset drift, and low frequency environmental pickup can produce apparent voltages that are comparable to, or larger than, the target signal. Current reversal based offset compensation strongly reduces these contributions because constant offsets cancel in the difference between opposite polarity readings, and the three step delta technique also suppresses linearly drifting offsets when the switching is fast compared to the drift time scale [222, 223]. In contrast, pure DC measurements integrate directly at $f \to 0$, where drift and $1/f$ noise are largest, while lock in detection shifts the measurement to a chosen reference frequency and rejects out of band noise through phase sensitive detection and a narrow effective bandwidth [224–226]. Delta mode sits between both approaches, it preserves a quasi DC measurement of the transport coefficient, while introducing a controlled modulation through polarity reversal, therefore it can outperform slow switching DC in the presence of offsets and drift, and can be more robust than lock in for purely resistive signals where one aims to minimize phase dependent systematic errors [221, 227].

Figure **C.2** assesses whether delta mode voltage fluctuations are consistent with a Gaussian distribution. Under stable conditions, the histogram is well described by a Gaussian, indicating stationary fluctuations and justifying uncertainty estimates based on σ and 2σ. In contrast, when the sample heater is set to higher values, the distribution becomes visibly non Gaussian, with skewness and long tails. This behaviour is consistent with intermittent perturbations, for example vibration sensitivity, microphonic pickup, or sporadic electrical disturbances, which violate the stationarity assumption.

Operationally, this figure provides a diagnostic criterion used throughout this work: a non Gaussian delta histogram indicates that standard deviation based error bars

underestimate the probability of rare excursions, and that mechanical mounting, cable strain relief, and electromagnetic shielding should be improved before acquiring quantitative datasets. Within this thesis, the kurtosis of each averaging was estimated, a kurtosis outside the ± 2 range, was considered not normal, and instead of the standard 2σ error, a 3σ was considered.

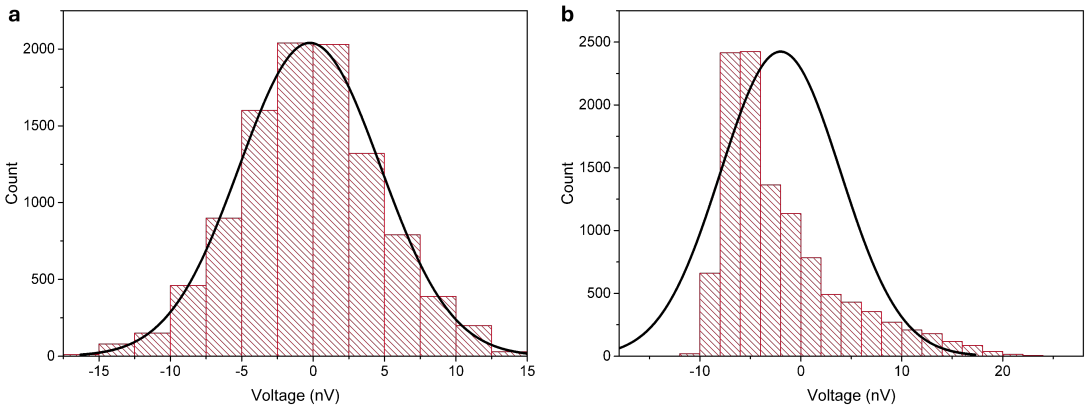

Figure C.2.: **Gaussianity test and nonstationary noise diagnostic.** Delta mode noise distribution and Gaussianity criterion. **a** Example of a Gaussian voltage histogram in delta mode, consistent with stationary noise. **b** Example of a non Gaussian distribution observed for a sample heather value of 8%.

C.2. Noise spectral density versus resistance and temperature

Figure **C.3** shows the baseline voltage noise amplitude spectral density as a function of frequency for different resistances and temperatures. Panel a demonstrates that the voltage noise floor increases systematically with the resistive load, consistent with the expected scaling of thermal noise and input referred amplifier noise when expressed as a voltage. Panel b highlights the temperature dependence for two representative resistances, with an overall reduction of the noise floor upon cooling. Across all conditions, narrowband peaks at 50 Hz and harmonics persist, indicating residual mains pickup that is largely independent of resistance and temperature.

These spectra define the relevant pre noise level for transport measurements in this thesis, and they provide the reference against which small signals and frequency dependent features should be compared.

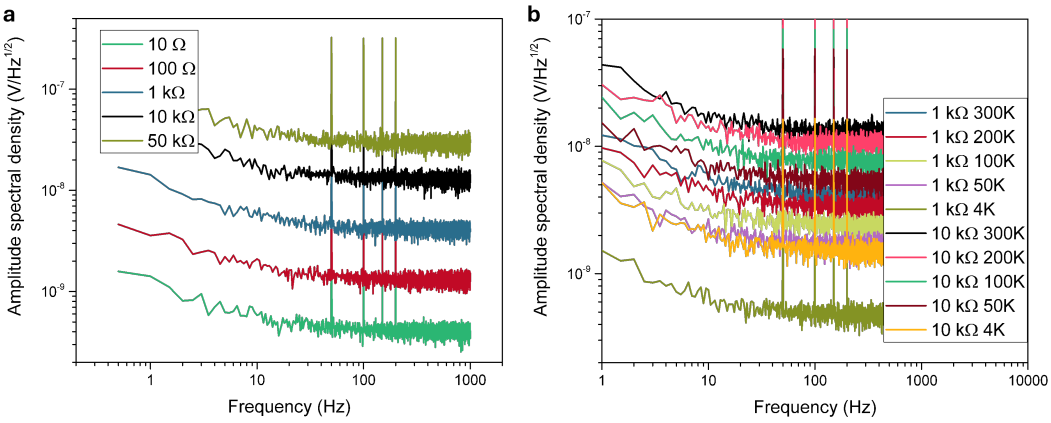

Figure C.3.: Baseline noise scaling with resistance and temperature. Amplitude spectral density of the baseline voltage noise. **a** Frequency dependent amplitude spectral density for different resistive loads mounted at the VTI sample position, showing an increasing noise floor with resistance and discrete interference peaks. **b** Temperature dependence of the amplitude spectral density for two representative resistances, demonstrating a systematic reduction of the baseline noise upon cooling, together with persistent interference peaks at 50 Hz and harmonics.

The resistance and temperature dependence of the measured voltage noise follows directly from fundamental and instrumental contributions. The irreducible thermal noise of a resistor is the Johnson Nyquist noise, with a white spectral density $S_V^{\mathrm{th}} = 4k_B T R$, therefore the voltage noise floor increases linearly with both T and R [228, 229]. In addition, the total input referred noise of a voltmeter or preamplifier typically combines a voltage noise term e_n^2 and a current noise term $(i_n R)^2$, implying that increasing R can drive a crossover from voltage noise dominated to current noise dominated operation, even at fixed temperature [221]. Finally, low frequency excess noise frequently scales with the device resistance fluctuations, often described phenomenologically by Hooge type relations $S_R/R^2 \propto 1/(Nf)$, so that under current bias the corresponding voltage noise scales as $S_V(f) = I^2 S_R(f)$ and can increase strongly with R and with microscopic disorder [218, 230]. Temperature can further modify the $1/f$ amplitude and slope because the fluctuator kinetics are thermally activated, so changes in T can change both the number of active fluctuators in the measurement band and their characteristic times, consistent with the Dutta Horn work [218, 219].

D. Experimental run-table

For clarity and reproducibility, a comprehensive run table is provided, summarizing all experimental measurement parameters used throughout this thesis. For each run, the table specifies the sample and device identifiers, measurement geometry, excitation and detection schemes, temperature, magnetic field magnitude and orientation, electrical biasing conditions, and relevant acquisition parameters. This systematic documentation allows direct comparison between different experiments, ensures traceability of all reported datasets, and provides a transparent reference for reproducing the measurements.

Table D.1.: Overview of the experimental procedures and measurement runs performed in this thesis. For each procedure, the internal eLabFTW identifier, associated figures, experimental equipment, and relevant measurement parameters are listed to ensure traceability and reproducibility of the reported results.

Technique	eLabFTW	Figure(s)	Equipment	Key parameters
XRD	5899	4.1, 5.1	Bruker D8	Monochromator; slit 1: 0.2 mm; slit 2: 0.25 mm; aluminium sample holder (2 mm thickness)
SQUID	7536	5.3b, 7.2b	Quantum Design MPMS XL	Standard DC magnetometry
SQUID	7536	4.2a	Quantum Design MPMS XL5	Standard DC magnetometry
AFM	7874	3.4	Veeco Dimension 3100	Tapping mode; tip: TESP-V2
EBL	3520	3.6	Raith Pioneer	Aperture: 7.5 μm; beam current: 16 pA; step size: 4 nm
EBL	6509	3.6	Raith Pioneer	Aperture: 30 μm; beam current: 348 pA; step size: 100 nm
Optical lithography	4545	–	ML3 mask aligner	Exposure dose: 140 mJ cm^{-2}

Continued on next page

Technique	eLabFTW	Figure(s)	Equipment	Key parameters
Transport experiment	505	4.2a, 4.3–4.6	Out-of-plane holder	8 electrical contacts + additional Cernox sensor; temperature: 295 K (unless stated); heater power: 5%; magnet: 12 T; pseudo-DC mode (Keithley 2400, 5 s pulses) + Keithley 2182A nanovoltmeter
Transport experiment	505	5.2c	Variable-angle holder	Temperature: 200 K; heater power: 5%; magnet: 12 T; delta mode (Keithley 6221 + Keithley 2182A)
Transport experiment	505	5.2a, 5.4, 6.1b–6.4	In-plane holder	12 electrical contacts; temperature: 200 K (unless stated); heater power: 2%; magnet: 12 T; delta mode (Keithley 6221 + Keithley 2182A)
Transport experiment	505	7.1b–7.4a, 7.6	In-plane holder	12 electrical contacts; temperature: 295 K; heater power: 2%; magnet: 12 T; delta mode (Keithley 6221 + Keithley 2182A)
PEEM imaging	-	4.9–4.11	MAXPEEM beamline	5 mm wide sample holder

Table **D.2** summarizes all material samples investigated in this thesis, including their identifiers, fabrication provenance, and corresponding internal eLabFTW records. For each sample, the table documents the material composition, sample ID used throughout the manuscript, the fabricating collaborator, and the experimental context in which the sample was employed. This overview provides traceability between the physical samples, the experimental datasets, and the corresponding chapters or figures where the results are discussed.

Table D.2.: Overview of the samples investigated in this thesis. The table lists the material composition, sample identifiers used throughout the manuscript, fabrication source, experimental usage, and corresponding internal eLabFTW records for both sample preparation and measurement documentation.

Sample	**Sample ID**	**eLabFTW (sample)**	**Fabricator**	**Used for**	**eLabFTW**
Ti-doped α-Fe_2O_3 (1%)	15K	3899	A. Rothschild	Chapter 4	4937
R-cut α-Fe_2O_3	A149	6509	A. Akashdeep	Fig. **4.8**	6509
$YFeO_3$ single crystal	YFO Das	7884	X. Ma	Chapter 6	12218
$YFeO_3$ single crystal	YFO Jonas	6806	W. Yang	Chapter 7	17243
$LuFeO_3$ single crystal	LuFO big	3575	W. Yang	Chapter 7	13194
$LuFeO_3$ single crystal	LuFO small	3525	W. Yang	Chapter 7	13194

E. Appendix: Computational details

The computational workflow integrates first–principles electronic-structure theory with symmetry analysis and continuum-to-mesoscopic transport modeling to quantify spin transport in insulating collinear magnets, with emphasis on altermagnets. Ground-state and spin–orbit–coupled band structures are obtained from plane–wave density functional theory (DFT) and density-functional perturbation theory, followed by Wannier tight-binding projections for efficient Brillouin-zone interpolation of Berry curvature and anomalous Hall conductivity [177, 237–239]. Magnetic space-group constraints, order-parameter irreducible representations, and literature magnetic structures are incorporated via the Bilbao Crystallographic Server and MAGNDATA to ensure that model Hamiltonians and transport tensors respect the relevant magnetic symmetries [240, 241]). Exchange parameters and anisotropies extracted from first principles parameterize linear spin-wave theories and atomistic spin-dynamics simulations, which in turn inform micromagnetic and drift–diffusion descriptions of magnon-mediated non-local transport, including interfacial boundary conditions for spin transfer [118, 278–280]. Where applicable, we leverage recent altermagnetic theory to guide the identification of symmetry-protected magnon modes and their thermoelectric responses, providing quantitative links between ab initio symmetry indicators and measured anisotropic spin signals [88, 98].

E.1. First-principles calculations for band structure.

First–principles calculations were carried out within Kohn–Sham density functional theory (DFT) using the projector–augmented–wave (PAW) formalism as implemented in VASP [242–244]. Exchange–correlation effects were treated with the Perdew–Burke–Ernzerhof (PBE) generalized gradient approximation [245]. To account for electron correlation in localized d states, we employed the Dudarev DFT+U approach with spherical corrections (Dudarev et al., 1998), applying U_{eff} on the transition–metal $3d$ manifold as appropriate for each compound [41]. A plane–wave kinetic–energy cutoff of 520 eV ensured convergence of total energies and band eigenvalues, and Brillouin–zone sampling used Monkhorst–Pack meshes of $11 \times 11 \times 11$ for self–consistent calculations [246]. Spin–orbit coupling was included in noncollinear calculations for all Berry curvature–related properties.

Maximally localized Wannier functions (MLWFs) were constructed with WANNIER90 to obtain compact tight–binding representations suitable for fine k–space interpolation [238, 247–249]. The intrinsic anomalous Hall conductivity (AHC) was evaluated from the Berry curvature on dense uniform meshes up to $240 \times 240 \times 240$, following the modern theory of the AHE [239, 250, 251]. Explicitly,

$$\sigma_{ij} \;=\; -\frac{e^2}{\hbar} \sum_{n} \int_{\mathrm{BZ}} \frac{d^3k}{(2\pi)^3}\; f_{n\mathbf{k}}\; \Omega^{n}_{ij}(\mathbf{k}), \tag{E.1}$$

with the band Berry curvature

$$\Omega_{ij}^{n}(\mathbf{k}) \;=\; -2\,\mathrm{Im}\sum_{m\neq n}\frac{\langle u_{n\mathbf{k}}|\hat{v}_i|u_{m\mathbf{k}}\rangle\langle u_{m\mathbf{k}}|\hat{v}_j|u_{n\mathbf{k}}\rangle}{(E_{m\mathbf{k}}-E_{n\mathbf{k}})^2}, \tag{E.2}$$

where $\hat{v}_i$ are velocity operators and $f_{n\mathbf{k}}$ are Fermi–Dirac occupations [177, 250]. The Wannier–interpolated formulation [238, 239] allows converged Brillouin–zone integrals at tractable cost while preserving the magnetic–space–group symmetry used to define the collinear antiferro-/altermagnetic order. All k–systematic convergence checks of total energy, band gaps, and AHC plateaus validated mesh and cutoff parameters reported here.

E.2. Simulations of transport phenomena in altermagnetic orthoferrites

Spin model for orthoferrites. We employ an atomistic spin Hamiltonian tailored to orthorhombic orthoferrites and adapted from a model previously developed for $Sm_{0.7}Er_{0.3}FeO_3$ [281]. The structural prototype implies identical symmetry constraints on the Dzyaloshinskii–Moriya (DM) vectors and exchange pathways in $LuFeO_3$ or $YFeO_3$; the essential difference is the absence of a spin-reorientation transition in the mentioned orthoferrites, whose easy axis lies along a over the whole temperature range relevant here. Accordingly, we exchange the roles (signs/magnitudes) of onsite and two–ion anisotropies relative to $Sm_{0.7}Er_{0.3}FeO_3$ to stabilize the a–axis ground state. To capture altermagnetic physics beyond a purely bipartite antiferromagnet, we introduce a symmetry–allowed splitting of the isotropic exchange on the fourth Fe–Fe shell, $J_4 \to J_4 \pm \Delta J_4$ with $\Delta J_4 = 1$ meV, which tunes the alternating spin splitting in k–space; setting $\Delta J_4 = 0$ recovers the antiferromagnetic limit [281]. The working Hamiltonian reads

$$\mathcal{H} = -\sum_{\langle ij\rangle} J_{ij}\,\mathbf{S}_i\mathbf{S}_j - \sum_{\langle ij\rangle}\mathbf{D}_{ij}\cdot(\mathbf{S}_i\times\mathbf{S}_j) - K_{\mathrm{on}}\sum_i(\mathbf{S}_i\hat{\mathbf{a}})^2 - K_2\sum_{\langle ij\rangle}(\mathbf{S}_i\hat{\mathbf{a}})(\mathbf{S}_j\hat{\mathbf{a}}) - \mu_s\sum_i \mathbf{B}\cdot\mathbf{S}_i, \tag{E.3}$$

where $\hat{\mathbf{a}}$ denotes the crystallographic easy axis, μ_s the local spin moment, and the 4th–shell bonds are split into two symmetry–inequivalent classes by ΔJ_4.

Linear spin–wave theory (LSWT). Small–amplitude dynamics about the numerically determined ground state are obtained by linearizing the Landau–Lifshitz–Gilbert (LLG) equation, Fourier transforming to momentum space, and solving the resulting non–Hermitian eigenproblem for each $\mathbf{k}$ [282]. The eigenfrequencies give the dispersions and damping–limited lifetimes, while the eigenvectors encode the relative phase of sublattices, from which we extract the polarization (left/right circular or linear). In practice, we diagonalize the dynamical matrix of transverse fluctuations $\delta\mathbf{S}_{\mathbf{k}}$,

$$\partial_t\,\delta\mathbf{S}_{\mathbf{k}} = \mathsf{A}(\mathbf{k})\,\delta\mathbf{S}_{\mathbf{k}} \;\;\Rightarrow\;\; \mathsf{A}(\mathbf{k})\,\mathbf{v}_{\mathbf{k},\nu} = (-i\omega_{\mathbf{k},\nu})\,\mathbf{v}_{\mathbf{k},\nu}, \tag{E.4}$$

with ν labeling magnon branches; $\omega_{\mathbf{k},\nu}$ and $\mathbf{v}_{\mathbf{k},\nu}$ yield energies, linewidths, and polarization content [282].

Atomistic spin–dynamics (ASD) simulations. To simulate finite–temperature transport and hysteresis, we integrate the stochastic LLG equation using a predictor–corrector Heun scheme [280, 283, 284]:

$$\frac{d\mathbf{S}_i}{dt} = -\gamma\,\mathbf{S}_i \times \left[\mathbf{H}_i^{\text{eff}} + \mathbf{h}_i(t)\right] + \frac{\alpha}{S}\,\mathbf{S}_i \times \frac{d\mathbf{S}_i}{dt}, \qquad \langle h_{i\mu}(t) h_{j\nu}(t')\rangle = \frac{2\alpha k_{\mathrm{B}} T_i}{\gamma \mu_s}\,\delta_{ij}\delta_{\mu\nu}\delta(t-t'), \tag{E.5}$$

where $\mathbf{H}_i^{\text{eff}} = -\partial\mathcal{H}/\partial\mathbf{S}_i$ includes exchange, DM, anisotropies, and Zeeman terms, and α is the Gilbert damping. For spin–Seebeck–driven transport, we initialize an elongated simulation cell of 16 nm × 16 nm × 140 nm in its ground state; the long axis is aligned along a crystallographic transport direction (e.g., Γ–U, Γ–U′, Γ–Z, Γ–X). A temperature profile $T(z)$ is imposed by coupling the first 10% of the length to a 348 K heat bath while the remainder is at $T = 0$ K; periodic boundary conditions are used transverse to transport, while an absorbing boundary at the cold end minimizes back–reflections [283, 285]. For field–cycling hysteresis, the external field $\mathbf{B}$ is applied parallel to the transport axis.

Observables and analysis. We compute (i) magnon accumulation and spin current profiles along the long axis, (ii) the spectral function from the temporal and spatial Fourier transform of spin–spin correlations, and (iii) polarization maps from the phase relation of sublattice precession. The simulated non–equilibrium steady state yields a length–scale for magnon decay that we compare to experimental diffusion lengths; its anisotropy as the axis rotates between alternating crystal directions quantifies the altermagnetic splitting encoded by ΔJ_4. The temperature– and field–dependence of these quantities provides input parameters and validation targets for the drift–diffusion description used to interpret non–local transport.

E.2.1. Simulation results

This appendix summarizes the atomistic spin-dynamics simulations used to support the interpretation of the non-local altermagnetic magnon-transport experiments in orthoferrites. The simulations and the associated linear spin-wave analysis were performed in collaboration with the group of Prof. Dr. Ulrich Nowak (Universität Konstanz). The goal of this appendix is to document the simulated equilibrium response of the Néel vector and the sublattice magnetizations under an applied magnetic field, which is used as an input for the projection-based description of the experimental non-local signals in Chapter 7. Further methodological details of the atomistic model, numerical implementation, and parameter choices are provided in Ref. [115].

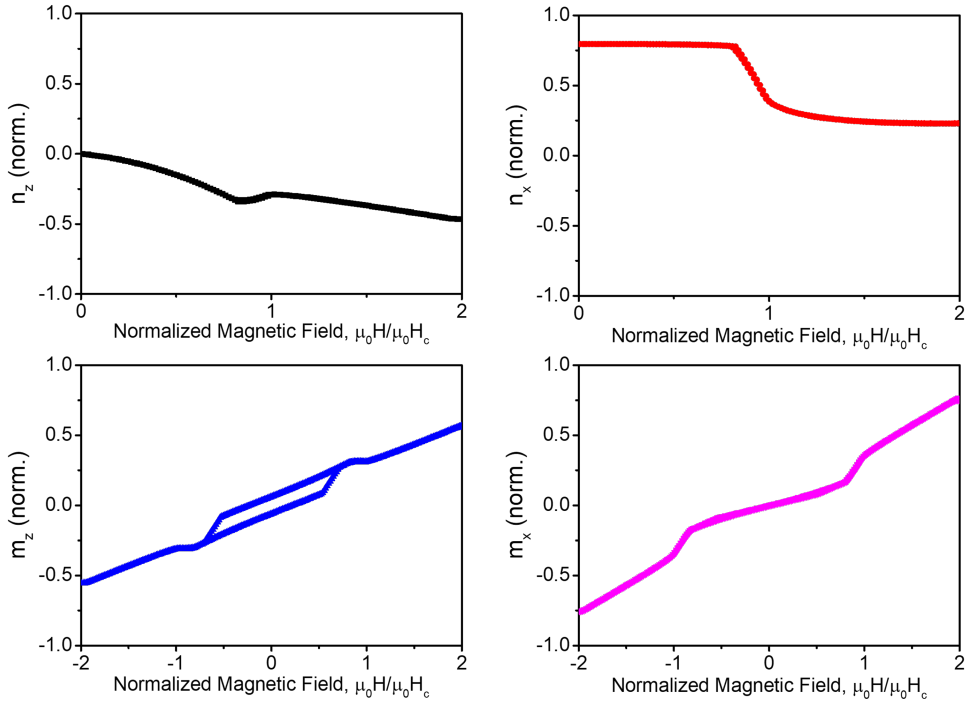

Figure E.1.: **Atomistic spin-dynamics simulations of the field-driven magnetic reorientation in an orthoferrite.** Simulation results for an external magnetic field applied along an altermagnetic direction (here taken along Γ–U). **a,c** Equilibrium Néel-vector components as a function of a normalized magnetic field, illustrating a smooth reorientation regime at intermediate fields. **b,d** Corresponding evolution of the four-sublattice magnetization components under the same field protocol, highlighting the redistribution of sublattice contributions during the reorientation. The displayed curves were used to obtain the field-dependent equilibrium configuration $\mathbf{n}^{(0)}(H)$ employed in the projection-based fits of the experimental non-local signals in Chapter 7. Simulations were performed by collaborators in the group of Prof. Dr. Ulrich Nowak (Universität Konstanz); see Ref. [115] for computational details.

The non-local transport signals discussed in Chapter 7 depend on the magnetic configuration through projection factors involving the equilibrium Néel vector $\mathbf{n}^{(0)}(H)$ and the spin accumulation direction $\hat{\boldsymbol{\mu}}$ of the Pt detector. In orthoferrites, the relevant field range is characterized by a smooth in-plane reorientation of $\mathbf{n}^{(0)}(H)$ within the anisotropy landscape of the Γ_4 phase, followed by an approach to a high-field configuration that defines an experimental saturation scale H_c [97, 287]. The simulations summarized in Fig. **E.1** provide a microscopic determination of this equilibrium reorientation under controlled field conditions and thereby supply the $\mathbf{n}^{(0)}(H)$ input used for the solid-line trends shown in the experimental figures of Chapter 7.

Figure **E.1a,c** shows the simulated components of the Néel vector as the field increases. The evolution is continuous, indicating a gradual reorientation rather than an

abrupt spin-flop transition, consistent with the phenomenology of orthoferrites in the relevant geometry [97,287]. The corresponding sublattice magnetization components in Fig. **E.1b,d** provide additional microscopic insight into how the four-sublattice structure accommodates the reorientation. In the field range where the Néel vector rotates most strongly, the sublattice contributions redistribute accordingly. In contrast, at higher fields the Néel-vector orientation changes only weakly and further field increase predominantly enhances the canting response.

The simulated equilibrium configuration $\mathbf{n}^{(0)}(H)$ is used in Chapter 7 to capture the measured sigmoidal field dependence of the non-local resistances through projection relations of the form

$$R_{\mathrm{th}}(H) \propto \Delta m_{\mathrm{th}}(H)\big(\mathbf{n}^{(0)}(H)\cdot\hat{\boldsymbol{\mu}}\big), \qquad R_{\mathrm{el}}(H) \propto \Delta m_{\mathrm{el}}(H)\big(\mathbf{n}^{(0)}(H)\cdot\hat{\boldsymbol{\mu}}\big)^2, \tag{E.6}$$

where Δm_{th} and Δm_{el} denote the corresponding mode-weighted magnon magnetization imbalances for thermal and spin-bias injection, respectively [97, 115]. In this way, the simulations provide an independent microscopic constraint on the field-dependent magnetic configuration used to interpret the experimental transport data, while the experimentally extracted saturation fields from SMR serve as an additional cross-check within the same material platform.

F. Appendix: Symmetry-controlled Hall conductivity in hematite, from angle-dependent transport to Néel vector imaging

This appendix section documents the complete Hall bar array dataset used to extract the angular dependence of the field odd transverse response discussed in Section 4.2. The figure separates the measured transverse conductivity into its total response, its antisymmetric field-odd component, and its symmetric field-even component across all patterned Hall bar orientations.

F.1. Complete Hall bar array dataset and odd, even decomposition

This appendix provides additional temperature-dependent transport data across the Morin transition, along with a corresponding first-principles comparison that supports the phase-selective appearance of anomalous Hall conductivity contributions. These datasets are consistent with the phase window and symmetry arguments used in chapter 4, but are not required for the main flow of the chapter.

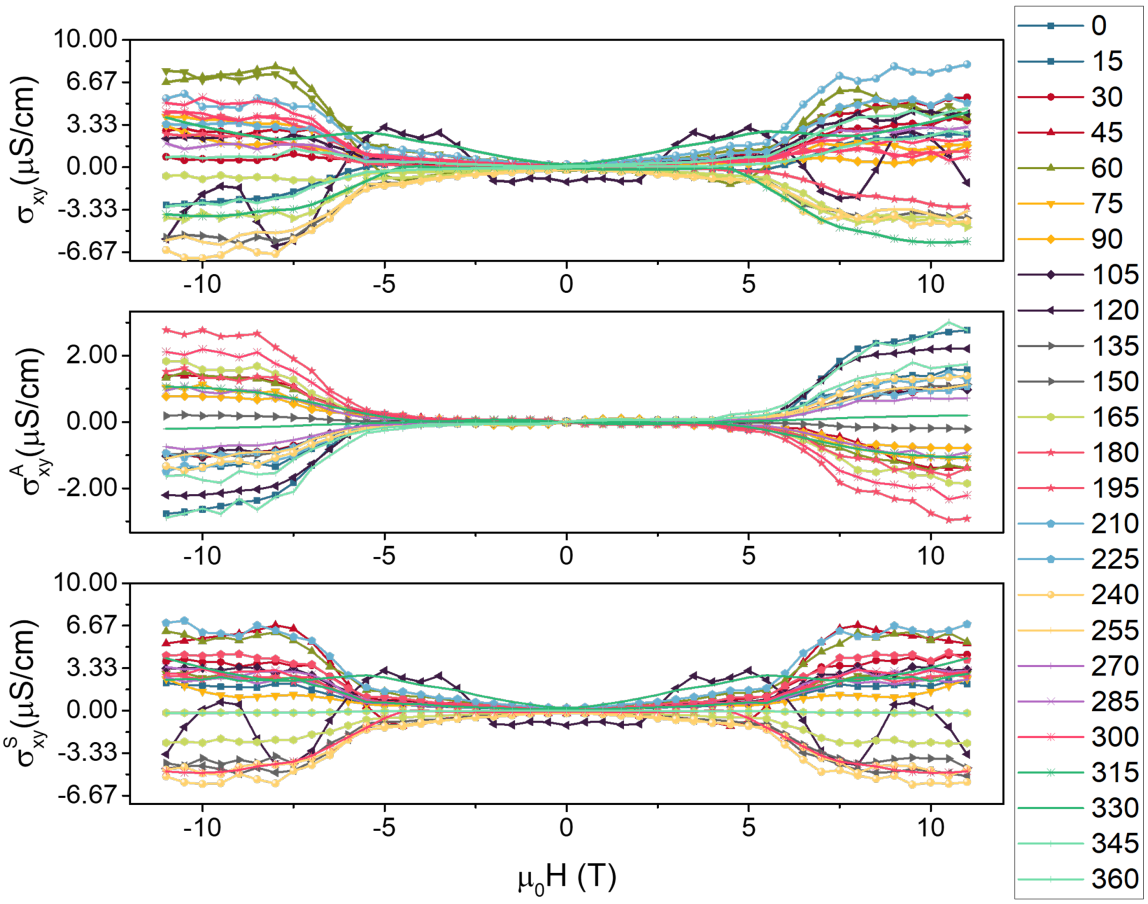

Figure F.1.: Dataset for all 24 different Hall bars on hematite. Transverse conductivity σ_{xy} as a function of out-of-plane magnetic field for 24 Hall bars patterned at different in-plane angles ϕ in 15° steps. **a** Total transverse conductivity. **b** Antisymmetric, field odd component used as the Hall-like signal in the main chapter. **c** Symmetric, field even component, which contains non-Hall contributions such as geometric pickup of longitudinal resistance. Adapted from Galíndez et al., *Adv. Mater.* **37**(2025): e05019, licensed under CC BY 4.0 [41].

F.2. Hall response below and above the Morin transition

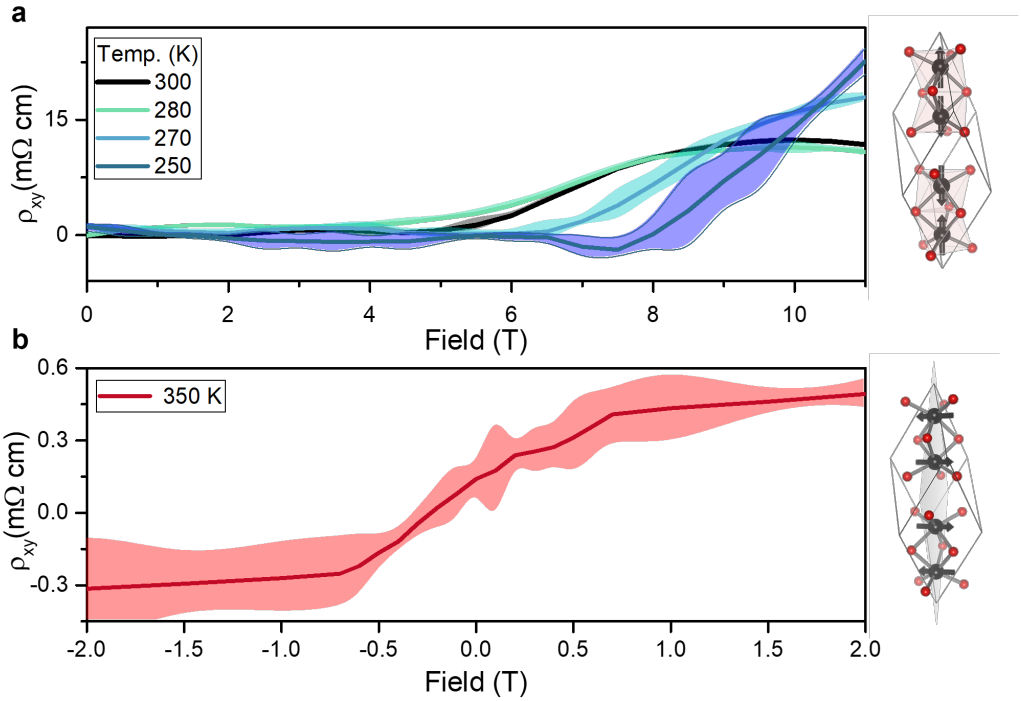

Figure F.2.: **Temperature dependence of the Hall-resistivity.** Hall resistivity as a function of out-of-plane magnetic field for temperatures below and above the Morin transition. The shaded bands denote the standard deviation across repeated field cycles. The shift of the characteristic onset field with temperature follows the spin-reorientation scale associated with Morin-transition physics. Adapted from Galíndez et al., *Adv. Mater.* **37**(2025): e05019, licensed under CC BY 4.0 [41].

F.3. First principles AHC comparison for in-plane and out-of-plane Néel orientations

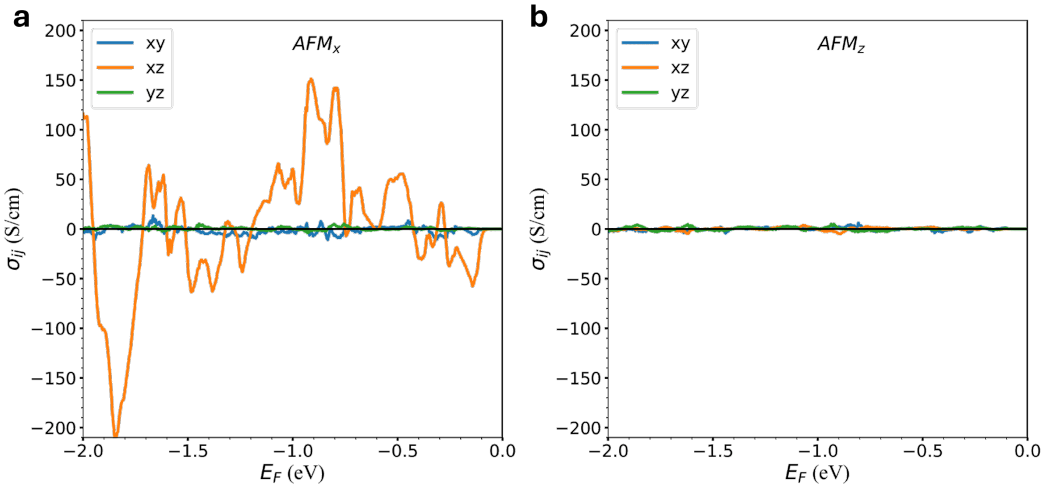

Figure F.3.: First principles anomalous Hall conductivity comparison for Néel vector orientations on opposite sides of the Morin transition. **a** In the high temperature regime, the Néel vector prefers the in-plane easy axis orientation, and a finite anomalous Hall conductivity is obtained. **b** When the Néel vector aligns with the out-of-plane easy axis below the Morin transition, the anomalous Hall conductivity contribution is strongly suppressed. Reproduced from Galíndez et al., *Adv. Mater.* **37**(2025): e05019, licensed under CC BY 4.0 [41].

G. Appendix: $YFeO_3$ spin transport

G.1. Two-sublattice model for the field dependence of the non-local spin bias response in $YFeO_3$

This appendix summarizes the theoretical model used to interpret the characteristic field dependence of the polarity odd non-local response R_{el} in $YFeO_3$. The model and its application to $YFeO_3$ are developed in the Supplementary Information of Das et al. [97] by Dr. Helen Gomonay. The core ingredients are (i) a field-driven reorientation of the equilibrium Néel vector in the orthorhombic anisotropy landscape and (ii) a field-induced ellipticity of the magnon eigenmodes, which sets the dynamical magnetization carried by each branch and thus the efficiency of spin bias injection, transport, and detection.

G.1.1. Equation of motion and free energy density

The dynamics are formulated in a two-sublattice description in terms of the Néel vector $\mathbf{n}$ and the small net magnetization $\mathbf{m}$. The linearized equation of motion for the Néel order parameter can be written as [97]

$$\mathbf{n} \times \left(\ddot{\mathbf{n}} - 2\gamma\, \dot{\mathbf{n}} \times \mathbf{H} + \gamma^2\, \mathbf{H} \times (\mathbf{n} \times \mathbf{H}) + \gamma^2\, H_{\mathrm{ex}}\, \frac{\partial w}{\partial \mathbf{n}} \right) = -\alpha\, H_{\mathrm{ex}}\, \mathbf{n} \times \dot{\mathbf{n}}, \tag{G.1}$$

where γ is the gyromagnetic ratio, α is the Gilbert damping, H_{ex} is the exchange field, $\mathbf{H}$ is the applied field, and $w(\mathbf{n})$ is the magnetic free energy density per unit magnetization that encodes anisotropy and Dzyaloshinskii–Moriya interaction.

For fields applied along the magnetic easy axis, the free energy density used in Ref. [97] is

$$w(\mathbf{n}) = \frac{H_D}{H_{\mathrm{ex}}}\, \mathbf{H} \cdot (\mathbf{e}_x \times \mathbf{n}) + \frac{H_a}{2}\, n_x^2 + \frac{H_c}{2}\, n_z^2, \tag{G.2}$$

where H_D is the effective Dzyaloshinskii field, H_a and H_c are anisotropy fields, and $\mathbf{e}_x$ is a unit vector fixed by the crystallographic and device orientation convention [97].

G.1.2. Equilibrium reorientation and critical field

Minimization of $w(\mathbf{n})$ yields a continuous rotation of the equilibrium Néel vector $\mathbf{n}^{(0)}(H)$. The field dependence of the equilibrium component $n_y^{(0)}$ is [97]

$$n_y^{(0)}(H) = \begin{cases} \sqrt{1 - \left(\dfrac{H}{H_{\mathrm{cr}}} \right)^2}, & H \le H_{\mathrm{cr}}, \\ 0, & H > H_{\mathrm{cr}}, \end{cases} \tag{G.3}$$

where the critical field is [97]

$$H_{\mathrm{cr}} = \frac{H_c H_{\mathrm{ex}}}{H_D}. \tag{G.4}$$

The weak ferromagnetic response follows from $\mathbf{m}^{(0)} \propto \mathbf{H} \times \mathbf{n}^{(0)}$ and the corresponding field dependent net moment component becomes [97]

$$m_x^{(0)}(H) = \begin{cases} \dfrac{H_D}{H_{\mathrm{ex}}}\, n_y^{(0)}(H), & H \le H_{\mathrm{cr}}, \\ 0, & H > H_{\mathrm{cr}}. \end{cases} \tag{G.5}$$

G.1.3. Magnon eigenmodes, ellipticity, and dynamical magnetization

Small oscillations $\delta\mathbf{n}$ about $\mathbf{n}^{(0)}$ are introduced and plane wave solutions $\delta\mathbf{n}(t,\mathbf{k}) \propto e^{-i\omega t + i\mathbf{k}\cdot\mathbf{r}}$ lead to an eigenvalue problem for the transverse components of $\delta\mathbf{n}$ [97]. For the uniform mode, the two magnon branch eigenfrequencies are [97]

$$\omega_{\pm}^2(0) = \frac{\omega_1^2 + \omega_2^2}{2} + \omega_3^2 \pm \sqrt{\left(\frac{\omega_1^2 - \omega_2^2}{2}\right)^2 + \omega_3^2\,(\omega_1^2 + \omega_2^2) + \omega_4^4}, \tag{G.6}$$

where ω_1 to ω_4 denote field dependent combinations of exchange, anisotropy, Dzyaloshinskii–Moriya, and Zeeman contributions [97].

A key point for non-local transport is that each branch carries a finite dynamical magnetization that is proportional to its ellipticity. The branch magnetization per mode is [97]

$$m_{\pm} = \frac{\omega_{\pm}\,\varepsilon_{\pm}}{\gamma H_{\mathrm{ex}}}\, M_s, \tag{G.7}$$

where M_s is the sublattice saturation magnetization and $\varepsilon_{\pm}$ is the ellipticity parameter. The ellipticity is given by [97]

$$\varepsilon_{\pm} = \frac{\omega_1^2 + \omega_2^2 - \omega_{\pm}^2}{\omega_3 \omega_4}. \tag{G.8}$$

Equations (G.6)–(G.8) make explicit that a finite transport relevant dynamical magnetization requires $\varepsilon_{\pm} \neq 0$, such that magnons carry spin angular momentum and can mediate a spin bias in a compensated magnet [97].

G.1.4. From branch imbalance to the non-local spin bias response

A spin Hall-driven spin bias generates an imbalance between the two magnon branches, which can be expressed in terms of an average magnetization $\mathbf{m}_{\mathrm{ave}}$ aligned with the equilibrium Néel axis and weighted by the opposite angular momentum of the two branches [97, 107]. In linear response, this yields

$$\mathbf{m}_{\mathrm{ave}} \;\propto\; \left(\hat{\boldsymbol{\mu}}_s \cdot \mathbf{n}^{(0)}\right) \mathbf{n}^{(0)}\, \frac{\gamma\hbar\, G_s^{\mathrm{curr}}}{\alpha} \left[\frac{m_+}{T}\, f\big(\omega_+(0)\big) - \frac{m_-}{T}\, f\big(\omega_-(0)\big)\right], \tag{G.9}$$

where $\hat{\boldsymbol{\mu}}_s$ is the unit vector of the interfacial spin accumulation, G_s^{curr} is the spin conductance associated with the current induced spin bias, and $f(\omega) = \left(e^{\hbar\omega/k_BT} - 1\right)^{-1}$ is the Bose occupation factor [97]. The sign difference reflects the opposite angular momentum carried by the two branches.

The detected non-local electrical signal is proportional to the projection of the arriving $\mathbf{m}_{\mathrm{ave}}$ onto the inverse spin Hall detection axis and to the spatial decay between injector and detector. For identical injector and detector strips, this leads to the commonly used product form [97]

$$R_{\mathrm{el}}(H,d) = \mathcal{A}_{\mathrm{el}}(H)\,\exp\!\left(-\frac{d}{\lambda_{\mathrm{m}}(H)}\right)\left(\hat{\boldsymbol{\mu}}_s \cdot \mathbf{n}^{(0)}(H)\right)^2, \tag{G.10}$$

where $\lambda_{\mathrm{m}}(H)$ is the magnon decay length and $\mathcal{A}_{\mathrm{el}}(H)$ collects the ellipticity and thermal population factors implied by Eq. (G.9) [97]. Within this model, the suppression and recovery of $R_{\mathrm{el}}(H)$ can be traced to the field evolution of $\mathbf{n}^{(0)}(H)$ and to the field induced ellipticity that enables magnons to carry spin angular momentum. At the same time, the crystallographic device orientation enters through the projection factor and the field dependent equilibrium configuration.

G.2. Non-local transport for magnetic field along the orthorhombic c axis

To test whether the electrical non-local response requires a field-induced magnon ellipticity aligned with the injection and detection geometry, the non-local signals were measured with the magnetic field applied perpendicular to the easy axis, along the orthorhombic **c** direction. For both transport configurations, no polarity odd signal is observed across the full field range, whereas the polarity even thermal response remains finite.

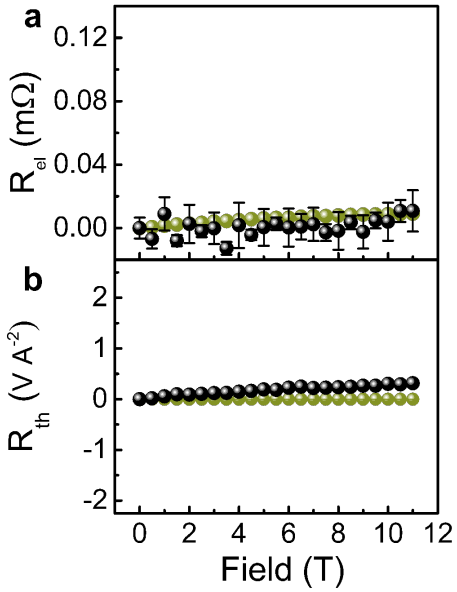

Figure G.1.: Suppressed electrical non-local response for field along c-axis. Field dependence of **a** R_{el} and **b** R_{th} for magnetic field applied perpendicular to the easy axis, along the orthorhombic **c** axis. No polarity odd signal is detected over 0 to 11 T in either wiring configuration, while R_{th} remains finite and shows a weak field dependence. Adapted from S. Das et al., *Nat. Commun.* **13**, 6140 (2022), licensed under CC BY 4.0 [97].

The persistence of a finite thermal response while the electrical signal vanishes supports the interpretation that the absence of R_{el} is not caused by device failure or loss of magnon generation; instead it reflects symmetry and polarization constraints on the electrically injected branch imbalance for this field orientation [97].

H. Appendix: Additional Information

H.1. Contributions: Detailed individual contributions to this work.

This section details the contributions of the author and co-workers (from JGU-Mainz if not noted otherwise) to the results presented in this work.

Symmetry-controlled Hall conductivity in hematite

i Experiment conceiving by Prof. Dr. Mathias Kläui, Prof. Dr. Gerhard Jakob and Dr. Libor Šmejkal.

ii Electronic band calculations were done by Prof. Dr. Rafael González-Hernández (Universidad del Norte, Barranquilla, Colombia) with Dr. Libor Šmejkal's help and support from Dr. Venkata Krishna and Rodrigo Jaeschke-Ubiergo.

iii The hematite growth sample recipe was developed and optimized by Dr. Eunchong Baek (PhD visitor from DGIST, Daegu, Republic of Korea) under the author's supervision. Akashdeep Akashdeep helped with the grow process and optimization.

iv Ti-doped hematite samples were fabricated by Prof. Dr. Avner Rothschild (Technion-Israel Institute of Technology, Haifa, Israel).

v Undoped samples were fabricated by Akashdeep Akashdeep.

vi The author and Dr. Shubhankar Das patterned the samples and fabricate the devices with the help of Dr. Eunchong Baek and Christin Schmitt.

vii The author performed the electrical measurements and analysis, magnetic and structural characterization with the help of Christin Schmitt, Dr. Shubhankar Das, and Felix Fuhrmann.

viii The X-PEEM measurements were fabricated in the MAX IV Laboratory (Sweeden) by the author, Christin Schmitt, Felix Fuhrmann, Laura Lünenbürger and Wanting Yang. Measurements were performed in the MAXPEEM beamline under proposal No. 20231423 and supervision and help from Dr. Evangelos Golias.

ix The author, Christin Schmitt, Felix Fuhrmann, Laura Lünenbürger and Wanting Yang processed the data and XPEEM images.

x the data was analyzed and discussed between the author and Christin Schmitt, Felix Fuhrmann, Dr. Libor Šmejkal, Prof. Dr. Jairo Sinova, Prof. Dr. Gerhard Jakob, and Prof. Dr. Mathias Kläui.

$YFeO_3$ and $LuFeO_3$ single crystals samples

i $YFeO_3$ single crystals were grown by Dr. Xiaoxuan Ma and Haiyang Chen under the supervision of Prof. Dr. Shixun Cao (all from Shanghai University, Shanghai, China). The samples were grown according from specifications sent by Dr. Shubhankar Das and Dr. Sven Becker.

ii $LuFeO_3$ single crystals were grown by Wanting Yang with the help of Dr. Xiaoxuan Ma under the supervision of Prof. Dr. Shixun Cao (all from Shanghai University, Shanghai, China). The samples were grown according from specifications sent by the author.

iii Laue diffraction measurements were performed by Wanting Yang and Dr. Xiaoxuan Ma under the supervision of Prof. Dr. Shixun Cao.

iv Magnetic and structural characterization was performed by the author, Dr. Shubhankar Das, Dr. Sven Becker, Jonas Köhler and Wanting Yang.

v All single crystal samples were polished commercially by MaTeck Material Technologie & Kristalle GmbH.

vi SMR and non-local devices were patterned by Dr. Shubhankar Das and the author with the help of Tobias Reimer.

vii Cleaning pre-etching and Pt deposition was performed by Maria Andromachi Syskaki and Duc Mihn Tran under the author specifications.

viii Contact pads were patterned by the author and Dr. Shubhankar Das.

ix Bilayers of Ti/Au and Cr/Au were deposited by the author and Dr. Shubhankar Das with help of Tobias Reimer, Mona Bhukta and Duc Mihn Tran.

$YFeO_3$ and $LuFeO_3$ magnon transport.

i Electrical measurements were performed by the author, Jonas Köhler, and Dr. Shubhankar Das with the help of Akashdeep Akashdeep, Christin Schmitt, Felix Fuhrmann, Wanting Yang (as a visior PhD student in JGU-Mainz), Dr. Sven Becker.

ii The theoretical transport model is developed by Helen Gomonay at the group of Prof. Dr. Jairo Sinova.

iii The data was analyzed by the author, Dr. Shubhankar Das, Dr. Andrew Ross, and Jonas Köhler.

Altermagnetic spin transport model

i Tobias Tobias Dannegger., Moumita Kundu, and prof. Dr. Ulrich Nowak (all from Universität Konstanz) did the altermagnetic theoretical calculations and altermagnetic modeling.

H.2. List of tools and aids used

Attachment to statutory declaration (§12(3e)): List of tools and aids used

Category	Tool (version optional)	Purpose in preparing the dissertation
Manuscript preparation	LaTeX (Overleaf / TEXmaker)	Writing and compiling the dissertation text, equations, tables, and figure references.
Bibliography	Zotero, BibTeX	Reference management, citation handling, and bibliography generation.
Bibliography search	Connected Papers	Literature discovery, mapping related works, and identifying relevant references.
Data analysis	Python (NumPy, SciPy, pandas)	Processing raw datasets, numerical analysis, error propagation, and parameter extraction.
Plotting	Python (Matplotlib) and OriginPro	Generating plots used in figures, publication quality export.
Curve fitting	SciPy (optimize) and OriginPro	Fitting experimental data and extracting fit parameters with uncertainties.
Figure layout	Adobe Illustrator and Inkscape	Multi-panel figure assembly, annotations, consistent formatting.
Image handling	ImageJ/Fiji	Cropping, contrast and brightness adjustment, adding scale bars, no manipulation of scientific content.
Instrument software	LabVIEW	Data acquisition, instrument control, and export of raw measurement files.
Language editing	Grammarly	Grammar and style corrections only, no scientific content generation.
Language editing	ChatGPT	Grammar, readability, and style polishing only, no scientific content generation, all technical content verified by the author.
Translation	DeepL	Translation of papers and technical text from other languages for comprehension, no insertion of translated text without author verification.
Brainstorming, concept clarification	Consensus AI	Brainstorming and concept clarification during literature reading, no direct generation of scientific claims without verification in primary sources.
Outline organization	Perplexity	Outline organization and structuring support for the thesis, all final structure and content decisions made by the author.

Note: All scientific interpretations, numerical results, and conclusions are the author's own. The AI-based tools listed above were used solely for language editing, translation support, literature exploration, brainstorming, and outline organization; any resulting text or ideas were checked against primary sources and the author's analysis.

H.3. List of Publications: Papers derived from this thesis.

- E. Galindez-Ruales, R. Gonzalez-Hernandez, C. Schmitt, et al. Revealing the Altermagnetism in Hematite via XMCD Imaging and Anomalous Hall Electrical Transport. Adv. Mater. 37, no. 41 (2025): e05019 [41].
- Das, S., Ross, A., Ma, X.X. et al. Anisotropic long-range spin transport in canted antiferromagnetic orthoferrite $YFeO_3$. Nat Commun 13, 6140 (2022) [97].
- Galindez-Ruales, E., Yang, W., Dannegger, T., Kundu, M., Köhler, J., Schmitt, C., Fuhrmann, F., Akashdeep, A., Tran, D.-M. Ma, X., Jakob, G., Cao, S., Nowak, U., Kläui, M. Altermagnetic magnon transport in the *d*-wave altermagnet $LuFeO_3$. arXiv:2508.14569 [cond-mat.mtrl-sci] (2025) [115].
- Ledesma-Martin, J.-O., Galindez-Ruales, E., Krishnia, S., Fuhrmann, F., Tran, D.-M., Gupta, R., Gasser, M., Go, D., Kamra, A., Jakob, G., Mokrousov, Y., and Kläui, M. Nonreciprocity in Magnon Mediated Charge-Spin-Orbital Current Interconversion. Nano Letters 25 (8), 3247-3252 (2025) [298].
- Dannegger, T., Deák, A., Rózsa, L., Galindez-Ruales, E., Das, S., Baek, E., Kläui, M., Szunyogh, L., Nowak, U. Magnetic properties of hematite revealed by an ab initio parameterized spin model. Phys. Rev. B 107, 184426 (2023) [126].
- Akashdeep, A., Ababneh, E.-M., Schmitt, C., Galíndez-Ruales, E., Fuhrmann, F., Kuschel, T., Kläui, M., Amin, V., Jakob, G. Angle-dependent magnetoresistance induced by interface-generated spin current in RuO_2/permalloy heterostructures. Phys. Rev. Applied 24, 054018 (2025) [264].

H.4. Acknowledgments

Removed under data protection law

H.5. Curriculum Vitae

Removed under data protection law